BOND OF GLASS FIBRE REINFORCED POLYMER BARS IN HIGH STRENGTH CONCRETE

Najia Mohammed SALEH

Submitted for the Degree of
Doctor of Philosophy

Faculty of Engineering and Informatics
University of Bradford

2018

BOND OF GLASS FIBRE REINFORCED POLYMER BARS IN HIGH STRENGTH CONCRETE

PhD Thesis,

School of Engineering and Informatics

University of Bradford, UK

Najia Mohammed Saleh

Signature: …… Date: ……

PAPERS PRODUCED FROM THIS THESIS

1. Saleh N., Ashour A. F., Lam D. and Sheehan T., “Bond Performance of helically wrapped GFRP bars in High Strength Concrete”, Proceeding of the 8th international conference on Advanced Composites in Construction, 5th – 7th September 2017, University of Sheffield, U.K.

2. Saleh N., Ashour A. F., Lam D. and Sheehan T., “Bond Strength of sand-coated GFRP re-bars in High - Strength Concrete”, Proceeding of the 8th international conference on Advanced Composites in Construction, 5th – 7th September 2017, University of Sheffield, U.K.

3. Saleh N., Ashour A. F., Lam D. and Sheehan T., “Experimental investigation of bond behaviour of two common GFRP bar types in high - strength concrete”, Construction and Building Materials, 2017. (Article in Press).

Abstract

Najia Mohammed Saleh
UNIVERSITY OF BRADFORD, UK, 2018

BOND OF GLASS FIBRE REINFORCED POLYMER BARS IN HIGH STRENGTH CONCRETE

Keywords: GFRP bars, Concrete, Pull-out test, Hinged beam test, Bond

Very limited research studies have been conducted to examine bond of glass fibre reinforced polymer (GFRP) bars with high concrete strength. The current research project aims to compare between bond measured from a pull-out test and a hinged beam test for GFRP bars embedded in high strength concrete. Different parameters influencing bond such as GFRP bar diameter, embedment length and surface configuration were investigated in both test methods, while the bar position, i.e. top or bottom, was only studied in hinged beams.

Seventy-two pull-out cubes, eight pull-out prisms and twenty-four hinged beams reinforced with GFRP bars were constructed and tested to failure. Twelve pull-out cubes and four hinged beams reinforced with steel bars were also tested for comparison purposes. The results showed that bond stress – slip curves obtained from various testing methods were similar, consisting of high initial stiffness, followed by nonlinear ascending and softening branches. In addition, it was found that the experimental bond strength obtained from hinged beams was higher than both bond strengths measured by the pull-out cube and pull-out prism. However, when a finite element analysis was conducted for hinged beams, it was shown that the tensile force in the reinforcing bar estimated by equilibrium conditions is overestimated as the large deformation of hinged beams at failure was not considered. Therefore, if the tensile force obtained from the finite element analysis is used to calculate the bond strength, it would be similar to that obtained from pull-out cube and prism. Moreover, it was found that the distribution of tensile and bond stresses was nonlinear along the GFRP embedment length and bond stress

at the vicinity of the free end increased with increasing the load due to redistribution of bond stresses along the embedment length.

Bond strengths were compared against the prediction methods provided in ACI-440.1R, CSA-S806, CSA-S6 and JSCE 1997. In general, all design codes showed conservative results for all specimens tested and ACI predictions gave a good agreement with experimental data compared to other codes.

Artificial neural network models were developed to predict bond strength of GFRP bars in concrete. These models used bar diameter, embedment length, concrete compressive strength and concrete cover as input variables. The developed ANN models showed to be able to predict bond strength of GFRP bars in concrete and, therefore, were used to conduct a parametric study.

Declaration

I declare that this thesis is the result of my own work except where references have been made to the work related to others. This thesis has not been submitted anywhere for the application of another degree, diploma, or other qualification.

Najia M. Saleh

Acknowledgments

It is a pleasure to thank those who made this thesis possible. First and foremost, I would like to thank **Allah**; our Lord, the All-Knowing, the Almighty, the most Merciful and the most Compassionate.

I would like to express my sincere appreciation and special thanks to my supervisors **Prof. Ashraf Ashour, Prof. Dennis Lam and Dr. Therese Sheehan** for their excellent supervision, constant encouragement and approachability throughout the period of this work. I deeply appreciate **Prof. Ashour** for his great support and help, especially throughout the difficult time course of the fighting in my country, Libya.

Special thanks go to the **Laboratory staff** who were always ready to help in times of needs. I would like to particularly thank **Steve Robinson**, **Owen Baines** and **Michael Procter** for their expert advice and help during the experimental investigation.

I am forever deeply grateful to my dear family, **my parents, my husband Yasir and my son Mustafa, my brothers and my sisters** for their moral support, help and understanding during the whole period of this work.

I take the chance to thank and express my gratitude to all **my friends** for their encouragement, advice and understanding.

I do appreciate the grant and financial support provided by the Higher Education Institute in the **Libyan Government** needed to finish this research.

Finally, I would like to thank everybody who was involved in this work as well as expressing my apology to those I did not mention in this acknowledgment.

Table of Contents

List of Figures

List of Tables

Notations

The following symbols are used in the present thesis:

d_b = Bar diameter (mm)

L_e = Embedment length (mm)

L_{db} = Development length (mm)

A_b = Cross sectional area of bar (mm^2)

A_t = Cross-sectional area of transverse reinforcement (mm^2)

f_c' = Cylinder compressive strength of concrete (MPa)

f_{cu} = Cube compressive strength of concrete (MPa)

f_c = Prism compressive strength of concrete (MPa)

f_t = Tensile strength of concrete (MPa)

f_{cr} = Cracking strength of concrete (MPa)

f_{fu} = Ultimate tensile strength of FRP rebar (MPa)

f_{fr} = Required bar stress (MPa)

E_{frp} = Elastic modulus of FRP rebar (GPa)

E_s = Elastic modulus of steel rebar (GPa)

σ_{max}= Maximum normal stress (MPa)

σ_{min}= Minimum normal stress (MPa)

σ_{av}= Average normal stress (MPa)

α' = Bar surface factor

α_1 = Confinement modification factor

α_2 = Modification factor for bond strength

f_d = Design tensile strength of the reinforcement (MPa)

f_{bod} = Design bond strength of concrete (MPa)

E_t = Young's modulus of elasticity for the transverse reinforcement (MPa)

f_{yt} = Yield stress in transverse reinforcement (MPa)

k_1 = Top bar modification factor

k_2 = Concrete density factor

k_3 = Bar size factor

k_4 = Bar fibre factor

k_5 = Surface profile factor

k_6 = Bar surface factor

k_m = Bar location modification factor

k_{tr} = Transverse reinforcement index

c = The lesser of the concrete cover to the centre of the bar or one-half of the centre-to-centre spacing of the bars being developed (mm)

d_{cs} = The smaller of the distance from the closest concrete surface to the centre of the bar or two-thirds of the centre to centre spacing of the bars (mm)

s = Maximum spacing centre to centre of transverse bars within l_{db} (mm)

N = Number of bars being developed along the potential plane of bond splitting

σ_f = Stress of FRP reinforcing bar (MPa)

σ = Confining axisymmetric radial pressure

τ_{max} = Peak bond stress (MPa)

τ = Bond stress (MPa)

τ_f = Frictional bond stress (MPa)

τ_{pred} = Predicted bond strength (MPa)

τ_{exp} = Experimental bond strength (MPa)

s_1 = Slip at the peak bond stress (mm)

s_r, α, β, ρ= Curve fitting parameters

β_0, β_1, r_0, r_1, τ_0, τ_1, m_0, m_1, α_0 and α_1 = Curve fitting parameters

A, B, C, D, E, F and G = Empirical constants

$A_{\tau 1}$ = Area underneath the ascending branch

F = Concentrated load (KN)

D_o = Diameter of plastic sleeve (mm)

s = Slip at bond stress τ (mm)

s_{le} = Loaded end slip at the peak bond stress (mm)

s_{ul} = Unloaded end slip at the peak bond stress (mm)

s_e = Elongation of the bar (mm)

σ_c = Compressive stress of concrete (MPa)

ε_c = Compressive strain of concrete at any stress σ_c

ε_{c1} = Strain at peak stress of concrete

ε_{cu1} = Ultimate strain of concrete

ε_{cr} = Cracking strain of concrete

σ_1 = Tensile stress of concrete (MPa)

ε_1 = Tensile strain at any stress

ψ = Dilation angle

ϵ = Flow potential eccentricity

K_c = The ratio of the second stress invariant in tension to that in compression

f_b/f_c = The ratio of initial equibiaxial compressive yield stress to initial compressive yield stress

t_n= Nominal traction in the normal direction

t_s and t_t = Nominal stresses in the two local shear directions

δ_n = Displacement in normal direction

δ_s and δ_t = Displacements in shear directions

k_{nn} = Stiffness in normal direction

k_{tt} and k_{ss} = Stiffness in tangential directions

$\mathrm{T_{exp}}$ = Experimental ultimate tensile force acting on the bar (kN)

$\mathrm{T_{pred}}$ = Predicted ultimate tensile force acting on the bar (kN)

$\mathrm{F_{exp}}$ = Experimental failure load (kN)

$\mathrm{F_{pred}}$ = Predicted failure load (kN)

w_i = Weight of input x_i

x_i = Input

y_i = Output signal of neuron

s_i = Net input signal of neurons

b = Bias

n = Number of neurons in a layer

t_k = Actual output

x_k = Predicted output

I_n and I = Normalized and unnormalized values of the training set

I_{min} and I_{max} = Minimum and maximum values of the data set

R = Regression value

Abbreviations

The following abbreviations are used in the present thesis:

GFRP = Glass Fibre Reinforced Polymers

CFRP = Carbon Fibre Reinforced Polymers

AFRP = Aramid Fibre Reinforced Polymers

BFRP = Basalt Fibre Reinforced Polymers

HFRP = Hybrid (Glass + Carbon) Fibre Reinforced Polymers

HW-SC = Helical Wrapping with slightly Sand Coating

SC = Sand Coating

RC = Reinforced Concrete

NSC = Normal Strength Concrete

HSC = High Strength Concrete

FE = Finite Element

ANNs = Artificial Neural Networks

ACI = American Concrete Institute

ASTM = American Society for Testing and Materials

BS = British Standards

CEB = Comite Euro-international du Beton

FIB = Federation International du Beton

EC = Eurocode

JSCE = Japanese Society of Civil Engineers

CHBDC = Canadian Highway Bridge Design Code

CSA = Canadian Standards Association

SD = Standard Deviation

COV = Coefficient of Variation

LVDT = Linear Variable Displacement Transducer

MAPE = Mean Absolute Percentage Error

CFRM = Continuous Fibre Reinforcing Materials

CDPM = Concrete Damage Plasticity Model

Chapter 1

Introduction

1.1 Background

In construction, steel reinforcement is the most widely used structural material in the world, but premature deterioration of the steel reinforced concrete structures especially in aggressive environments due to corrosion of steel re-bars has become a serious problem. Therefore, epoxy coated steel re-bars were introduced to overcome the corrosive problem associated with the use of steel reinforcing bars; however, they were ineffective to resist the corrosion in real structures (Tighiouart et al., 1999). A lot of efforts were spent to repair and strengthen reinforced concrete structures that have deteriorated because of corrosion. In the last two decades, fiber reinforced polymer (FRP) re-bars have been introduced as an alternative to the conventional steel reinforcement in concrete structures owing to their excellent corrosion resistance, high tensile strength to weight ratio, good non-magnetic properties, good fatigue properties and ease of handling. FRP bars used successfully in concrete structures susceptible to aggressive environments namely chemical and wastewater treatment plants, sea walls, floating docks, and under water structures. However, FRP reinforced concrete members behave differently from those reinforced with steel bars because of non-ductility of FRP bars, lower modulus of elasticity and bond strength which influence the performance of FRP reinforced concrete members. The bond mechanism between FRP re-bars and concrete is a critical design parameter that controls the performance of reinforced concrete members

at serviceability limit state. The bond behaviour of FRP re-bars embedded in concrete is different compared to that of steel re-bars because of different mechanical properties and surface deformations (ACI-440.1R, 2015). From the literature, several research investigations have been carried out to understand the bond properties of FRP re-bars embedded in normal strength concrete (NSC), but they are not completely understood yet, because of the complexity of the parameters influencing the bond behaviour such as bar diameter, embedment length, concrete compressive strength, concrete cover, surface configuration, bar position, transverse reinforcement and FRP type.

In recent years, a marked increase in the use of high-strength concrete (HSC) has been evident in construction projects around the world. HSC offers significantly better structural engineering properties, namely better durability, higher compressive and tensile strengths, higher stiffness compared with conventional normal-strength concrete. The bond behaviour of GFRP-reinforced bars in high strength concrete is of particular interest and is the focus of the current research.

1.2 Research significance

In recent years, the use of high strength concrete has been increased in construction and the mechanism of bond stress transfer between FRP bars and concrete is a fundamental requirement to guarantee their successful application in concrete members. The literature shows that several studies have focused on investigating the bond behaviour of fiber-reinforced polymer (FRP) bars in normal strength concrete (NSC), but very limited experimental investigations have been conducted to investigate the bond behaviour of FRP bars embedded in high

strength concretes using a pull-out test. Moreover, very limited experimental data have been available in the literature regarding bond behaviour of FRP re-bars in normal strength concrete using hinged beams, as they are more challenging to prepare and test. Despite this, hinged beams are more realistic and representative of stress conditions in RC members in bending than pull-out specimens. However, no investigation has been implemented to measure the bond properties of FRP bars in HSC using a hinged beam test. Therefore, the contribution of high strength concrete in bond behaviour of GFRP bars will be tested using pull-out and hinged beam tests in the current research. In addition, the literature illustrates that few authors have investigated the FRP bar position effect on bond strength using pull-out specimens and lap splice beams, however, it has not been studied using hinged beams. Thus, the aim of the present research is to investigate the influence of bar position on bond strength. Furthermore, the present investigation intends to compare the experimental results (bond stress-slip relationship, failure mode and bond strength) obtained from testing hinged beams with those obtained from testing pull-out cubes and prisms for finding the correlation between two different test methods. The information will be valuable for designers, who use GFRP re-bars to reinforce high strength concrete structures as it will provide structural engineers with more understanding of bond behaviour of GFRP re-bars in HSC, as well as for the development of design guidelines. Subsequently, the use of GFRP reinforcement will be a more effective option than conventional steel reinforcement.

1.3 Aims and objectives of the research

This research aims to investigate the bond behaviour of two common GFRP types in high strength concrete using pull-out and hinged beam tests. The main objectives are summarized as follows:

- To experimentally investigate the bond behaviour of two GFRP types (helical wrapping with slight sand coating and sand coating) in high strength concrete using pull-out cubes, pull-out prisms and hinged beams in comparison with pull-out cubes and hinged beams reinforced with steel bars.
- To compare bond performed by hinged beams with that performed by pull-out specimens.
- To develop a three-dimensional nonlinear finite element model using ABAQUS to estimate the tensile force acting on the bar in a hinged beam and also to investigate the tensile and bond stress distributions along the bonded length.
- To propose three-dimensional nonlinear finite element models for pull-out cube and pull-out prism using ABAQUS to investigate the distribution of tensile and bond stresses along the embedment length.
- To examine the applicability of design guidelines in predicting bond strength of GFRP bars against the experimental results of pull-out specimens and hinged beams, in the case of high strength concrete.
- To develop an artificial neural network model using MATLAB to predict bond strength of GFRP bars in concrete and conduct a series of parametric studies.

1.4 Research methodology

To achieve the above objectives, the following research strategy approaches have been employed:

- Seventy-two pull-out cubes, eight pull-out prisms and twenty-four hinged beams reinforced with GFRP bars were constructed and tested to study the effect of different parameters such as bar diameter, embedment length and surface configuration on bond behaviour of GFRP bars in high strength concrete including bond stress-slip relationship, failure mode and bond strength. The bar position, i.e. top or bottom, was only studied in hinged beams. Twelve pull-out cubes and four hinged beams reinforced with steel bars were also tested for comparison purposes.
- A three-dimensional nonlinear finite element model for a hinged beam has been developed using ABAQUS package 6.14 to determine the ultimate tensile forces in the reinforcing bars. These predicted forces were compared with the experimental ultimate tensile forces obtained from testing pull-out cubes and prisms to find the correlation between two different test methods. In addition, the FE models developed for the pull-out cube, pull-out prism and hinged beam have been used to investigate the distribution of tensile and bond stresses along the bonded length.
- The design guidelines (ACI-440.1R, 2015, CAN/CSA-S806, 2012, CAN/CSA-S6, 2014, JSCE, 1997) for predicting the bond strength were assessed against the experimental results of pull-out specimens and hinged beams.

- An artificial neural network model has been developed to predict bond strength of GFRP bars embedded in concrete. Then, a parametric study has been conducted to investigate the generalization ability of the developed NN model within the range of inputs considered in the current study and examine the influence of the main input parameters on the bond strength.

1.5 Outline of the thesis

This chapter presents a general introduction about the necessity to investigate the bond behaviour between FRP bars and concrete. Research significance, the aims and objectives of this research and research methodology are also presented.

Chapter 2 contains a comprehensive review of the literature regarding bond behaviour of FRP bars to concrete, including summary of mechanical properties of FRP re-bars, bond mechanism and bond failures, as well as different main factors influencing bond strength and bond tests. Bond stress – slip analytical models and empirical models to evaluate bond strength and development length of FRP bars are described in this chapter as well. Literature review also focuses on design guidelines for calculating the bond strength of FRP bars in concrete. Previous numerical studies regarding a finite element analysis and artificial neural network are also reviewed. This detailed review is to present relevant research work and address the research gaps.

Chapter 3 describes the experimental program including test specimens, material properties, specimen preparation, and experimental set – up and testing procedure.

Chapter 4 presents the experimental results of seventy-two pull-out cubes and eight pull-out prisms reinforced with GFRP bars, as well as twelve pull-out cubes reinforced with steel bars for comparison purposes. The results and discussions include bond stress-slip curves and bond failure, as well as the investigation of effect of main parameters on bond strength. Comparisons between bond strengths obtained from pull-out cubes and those obtained from pull-out prisms are also presented.

Chapter 5 presents the experimental results and discussions of twenty-four HSC hinged beams reinforced with GFRP bars, including bond stress-slip curves, bond failures and analysis of effect of various parameters on bond strength. Four hinged beams reinforced with steel bars are also presented for comparison purposes.

Chapter 6 provides comparisons between results obtained from a pull-out test and those obtained from a hinged beam test, including bond strength, bond stress-slip relationship and bond failure. Also, three-dimensional nonlinear finite element models for a hinged beam, pull-out cube and prism using ABAQUS software are proposed in this chapter. The validation of these models is developed against the experimental test results obtained from this study, in terms of load-slip curve and failure mode. In addition, the validated FE model for hinged beams is used to predict the pull-out force acting on the bar. The FE models developed for pull-out

cube and prism as well as hinged beam are used to investigate the distribution of tensile and bond stresses along the embedment length.

Chapter 7 aims to evaluate design code equations against the experimental results of pull-out specimens and hinged beams tested.

Chapter 8 presents the neural network models developed using MATLAB for predicting the bond strength of helical wrapped with slight sand coated GFRP and sand coated GFRP reinforcing bars embedded in concrete. A parametric study using the developed ANN models is also reported in this chapter.

Finally, chapter 9 summarizes the main conclusions of the research presented in this thesis and gives some recommendations and suggestions for future work.

Chapter 2

Literature Review

2.1 Introduction

This chapter introduces a comprehensive review on the bond behaviour of fibre reinforced polymer (FRP) bars embedded in concrete, including the mechanical properties of FRP bars, bond mechanism and failure modes, as well as parameters which influence the bond strength of FRP bars and the bond stress-slip analytical models. Additionally, the empirical models and the design code equations developed to calculate the bond strength and development length of FRP re-bars in concrete will be reviewed. Bond test methods are also described. Moreover, numerical methods are presented in this chapter to predict bond strength of FRP bars.

2.2 Mechanical properties of FRP re-bar

The most common fibres are carbon, glass, aramid and basalt. FRP reinforcing bars are manufactured with different diameters and different surface treatments such as ribbed, helical wrapping, sand coating, surface texture and grooves to improve the bond strength between FRP and concrete. FRP re-bars are anisotropic unlike the steel re-bars. Therefore, their mechanical properties differ in the two directions, where the longitudinal direction parallel to the fibres is stronger than the transverse direction. This difference depends on fibre type, matrix and manufacturing process. In addition, the nature and volume of fibres in the cross section of FRP reinforcing bars, the mechanical properties of resin and

the fibre orientation are responsible for determining the FRP bar characteristics (Ehsani et al., 1993). Subsequently, it is very complicated to determine the universal values of the mechanical characteristics of FRP re-bars.

2.2.1 Tensile strength and elongation at failure

Unidirectional FRP re-bars are manufactured by a pultrusion method that provides FRP re-bars with the maximum tensile strength and stiffness in the axial direction of FRP bars. FRP reinforcing bars develop a tensile strength that is higher than that of the conventional steel reinforcement, for example glass fibre reinforced polymer reinforcement (GFRP) offers a tensile strength two times higher than that of steel re-bars, while the tensile strength of carbon and aramid fibre reinforced polymer re-bars is three times more than that of steel bars as shown in Figure 2.1. It was stated that the ultimate tensile strength is sensitive to the FRP re-bar diameters, where it is reduced rapidly with increasing the bar diameter, especially for GFRP reinforcing bars (Faza and Gangarao, 1990, Ehsani et al., 1995, Ehsani et al., 1996b) because of shear lag as explained by Ehsani et al. (1996b). However, Rossetti et al. (1995) concluded that there is no sign of any dependence of the mechanical properties monitored (ultimate tensile strength, ultimate strain and elastic modulus) on the diameter and the surface type of GFRP re-bars. Furthermore, it was mentioned that the change of bar diameter does not seem to influence the tensile strength of twisted CFRP strands (ACI-440.1R, 2006). The stress-strain relationship for FRP reinforcement does not illustrate any plastic behaviour or a yield point; otherwise the elastic behaviour is continuous up to failure. The elongation of FRP re-bars depends on the nature of fibres, for

example the maximum elongation for CFRP bars is less than that for GFRP and AFRP bars as demonstrated in Figure 2.1.

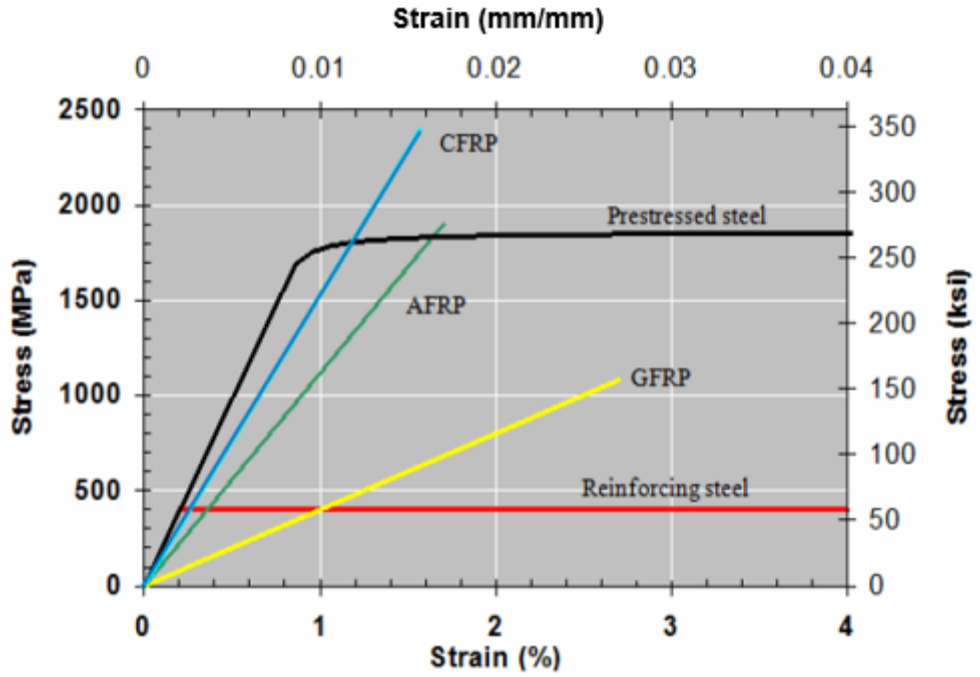

Figure 2.1 - Stress versus strain for FRP and steel re-bars (ACI-440R, 1996)

2.2.2 Compressive strength of FRP

Although FRP reinforcement has a low compressive strength, because of the low buckling strength of the individual fibres, this is not usually a concern because the majority of civil engineering applications use FRP reinforcing bars only in tension. Compressive strengths of GFRP, CFRP, and AFRP bars are 55, 78, and 20% of the tensile strength, respectively. In general, compressive strengths are higher for bars having higher tensile strengths, except AFRP bars, where the fibres exhibit nonlinear behaviour in compression at a relatively low level of stress (ACI-440.1R, 2006).

2.2.3 Modulus of elasticity

It is well known that the behaviour of FRP re-bars is elastic; subsequently the elastic modulus remains constant until the failure point (brittle failure), whereas the behaviour of steel re-bars is ductile. The elastic modulus of FRP re-bars is less than that of steel reinforcement. The modulus of elasticity of CFRP re-bars is the highest one, followed by AFRP re-bars, then GFRP re-bars as shown in Figure 2.1. The elastic modulus of FRP materials used in construction generally varies between 20% of that of steel for glass fibres to 75% of that of steel for carbon fibres. As a result, more flexible RC elements are obtained which develop higher strains in tension and reach higher overall deformations. Rossetti et al. (1995) concluded that the elastic modulus of GFRP re-bars ranged from one-fifth to one-seventh of that of steel re-bars, while, it was found to be about one-quarter of that of mild steel (Faza and Gangarao, 1990).

2.2.4 Shear strength

The shear strength of FRP re-bars is very low in the transverse direction. Standard test methods to measure the shear properties of FRP re-bars have not been established yet. For design purposes, the shear strength properties can be obtained from the bar manufacturer. The manufacturer will provide the test method that is used to investigate the shear strength (ACI-440.1R, 2006).

2.3 Bond mechanism

The bond strength of FRP re-bars to concrete is the main factor to be considered in the use of FRP as reinforcing bars for concrete structures because the forces

are transferred between the two materials across the interface. Bond stresses, also known as shear stresses, are parallel to FRP re-bar and act on the interface between the two materials as shown in Figure 2.2. Bond stress is calculated by dividing the pull-out force by the bonded surface area of the bar. The bond strength of FRP reinforcing bars embedded in concrete depends on several factors, namely concrete strength, bar diameter, embedment length, surface configuration, fibre type, bar position, concrete cover and transverse reinforcement, which will be explained in more detail in section 2.6.

According to CEB-Bulletin-151 (1982), the interaction mechanism between a steel bar subjected to a pull-out force and the surrounding concrete mainly depends on three components: chemical adhesion, friction and mechanical interlock. The chemical adhesion takes place between the mortar paste and the bar surface, and the friction resistance arises from the roughness of the interface between the concrete and the bar. The mechanical bearing (wedging effect) is a major source of the bond for steel bars and acts between surface deformations and concrete. Also, the bond mechanism of FRP re-bars consists of three components as steel re-bars. The first component is chemical adhesion, then friction resistance and mechanical interlock, which depends on the surface type of FRP bars (Pecce et al., 2001, Xue et al., 2008). At the initial loading, the chemical adhesion is dominant. The adhesion resistance reduces gradually with increasing the applied loads. As a result, slippage occurs. After that the friction takes place to resist the slip of FRP re-bars subjected to tensile forces, and then the mechanical interlock is the controlled part (Xue et al., 2008). Moreover, it was stated that the resistance of chemical adhesion was extremely low, and friction and mechanical interlock

played an important role in transferring stresses between CFRP re-bars and concrete (Xue et al., 2008). In contrast to steel reinforcement, plain steel bars mainly depended on adhesion and friction, while deformed steel bars depended more on the mechanical interlock (Xue et al., 2008). On the other hand, Chaallal and Benmokrane (1993) and Tighiouart et al. (1998) deduced that adhesion and friction governed the bond strength of GFRP re-bars, because their surface deformations did not have the same properties as steel reinforcing bars such as high shear strength, high rigidity and deformation geometry, which provide sufficient lateral confinement over rib bearing, while the bond strength of steel re-bars mainly depends on the mechanical interlock. Tighiouart et al. (1998) and Larralde and Silva-Rodriguez (1993) concluded that the GFRP re-bars illustrated lower bond strength compared to steel re-bars due to the difference of surface deformations and mechanical properties. GFRP bars have different surface treatments such as helical wrapping, ribbing, sand coating and spiral wrapping and therefore, their bearing force owing to mechanical interlock is usually smaller than that for ribbed steel bars.

Okelo (2007) investigated beam specimens reinforced with CFRP, GFRP and steel re-bars in normal strength concrete (NSC) and found that the bond strength of GFRP and CFRP was less than that of steel reinforcing bars. Furthermore, the CFRP re-bars developed a bond strength more than 85% of that of the deformed steel re-bars (Rafi et al., 2007) and the GFRP bar bond strength varied from 62% to 84% of that of deformed steel re-bars (Chaallal and Benmokrane, 1993). Also, Okelo and Yuan (2005) concluded that the bond strength of FRP re-bars was typically 40 to 100% of that of steel re-bars for pull-out failure. It was reported that

the bond strength of FRP varied owing to the difference of mechanical characteristics in the longitudinal and transverse direction and surface deformations (Cosenza, et. al 1997). Also, it was stated that the modulus of elasticity for FRP reinforcement is an essential variable affecting bond strength (Mosley et al., 2008).

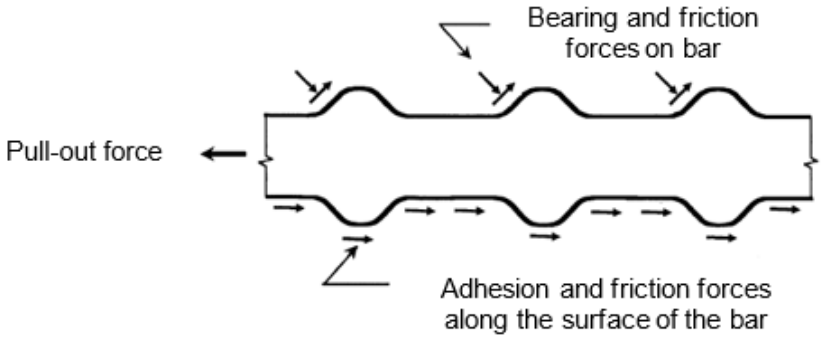

Figure 2.2 - Bond force transfer mechanisms (ACI-408R, 2003)

2.4 Shear lag

When the FRP re-bar is pulled in tension, there will be differential movement between the core and surface fibres that results in a non-uniform distribution of normal stresses through the cross section of the bar. Thus, this shear lag leads to higher surface normal stresses (Achillides and Pilakoutas, 2004). In addition, it was mentioned that fibres close to the centre of the bar cross section are not so highly stressed as fibres close to the outer surface of the bar because of the shear lag (Faza and GangaRao, 1993). The idealized stress distribution is shown in Figure 2.3.

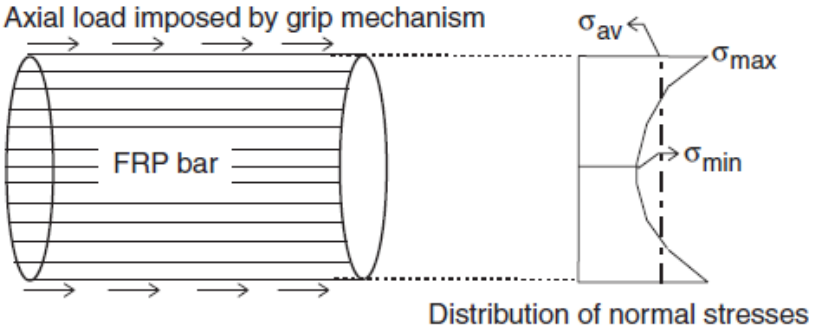

Figure 2.3 - Indicative distribution of normal stresses on a FRP rebar cross section subjected to axial tensile force (Tepfers, 2006)

2.5 Bond failures

Two types of failures are observed through the investigations of the pull-out and beam specimens reinforced with FRP re-bars. These failures are pull-out and splitting. They are described in more detail below.

2.5.1 Pull out failure

The definition of this failure is to pull the reinforcing bar out of the concrete specimen without crushing concrete or rupturing reinforcement. In other words, pull-out failure is shearing off the interface between the concrete and the rebar as illustrated in Figure 2.4. The pull-out failure occurs when radial forces propagating from rebar subjected to tensile force, are lower than the resistance of the surrounding concrete and /or transverse reinforcement, but tangential forces are higher than what the concrete can resist. From previous experimental investigations, pull-out failure usually occurs at the interface between concrete and surface deformations or between the bar core and surface deformation. For example, Robert and Benmokrane (2010) split the pull-out specimens reinforced

with sand coated GFRP bars after testing to investigate the bond failure mode. They found that pull-out mode occurred at the interface between the sand coating and bar core due to high shear strength of concrete, which exceeded the interface strength between bar core and bar surface. In addition, Hao et al. (2007) observed the type of failure for each test. The results showed that most pull-out specimens failed by the shearing of concrete between the ribs of the GFRP bar, and the shear off of the ribs was also observed, which is called pull-out failure.

Bond failures are majorly associated with bar diameter, embedment length, concrete strength, concrete cover and transverse reinforcement. It was stated that the bond failure mainly depended on compressive strength of concrete, rebar surface, embedment length and concrete cover (Okelo and Yuan, 2005). Ehsani et al. (1996b) reported that the specimens having shorter embedment lengths failed in a pull-out mode, and the experimental observations noted that the loaded and free end slips quickly increased, despite the increase of the applied tension load being slight. Furthermore, it was reported that the specimens having shorter embedment lengths with low concrete compressive strengths were failed in a pull-out mode (Okelo and Yuan, 2005). In specimens with a clear concrete cover of twice the rebar diameter, depending on the embedment length, either pull-out or rebar fracture occurred (Ehsani et al., 1996b). The ultimate bond stresses in specimens with a clear concrete cover of twice the rebar diameter were higher than those in specimens with a clear concrete cover of one rebar diameter (Ehsani et al., 1996b). It means that pull out failure occurs at a higher bond strength than the splitting failure as the concrete is well confined and therefore, the radial splitting cracks need more energy to reach the outer surface of the concrete. Yan

et al. (2016) reported that higher concrete cover provides higher confinement to the reinforcing bar, which in turn decreases from the possibility of developing cracks and then pull-out failure takes place. Achillides and Pilakoutas (2004) found that bond failure happened at the surface of the FRP bar, when the concrete compressive strength was more than 30 MPa, while concrete cracks took place in the case of lower concrete compressive strength (around 15 MPa). Karlsson (1997) also found that failure was owing to the rupture of the surrounding concrete, whereas the deformed bar remained undamaged in the case of low concrete compressive strength (less than 30 MPa). For a higher concrete compressive strength (greater than 55 MPa), failure was owing to the damage of the ribs of the FRP bar and the damage of the surrounding concrete was negligible. Yan et al. (2016) reported that a pull-out failure occurred with smaller bar diameters.

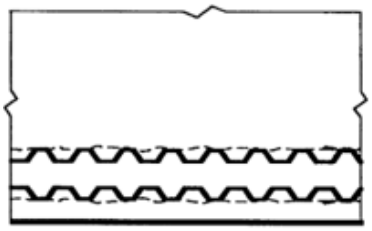

Figure 2.4 - A side view of a member showing shear crack and/or local concrete crushing due to bar pull out (ACI-408R, 2003)

2.5.2 Splitting failure

This type of failure takes place in the concrete surrounding the reinforcement subjected to tensile force. When the bars are loaded, the bars exert radial pressure on the surrounding concrete. If concrete cover and/or transverse reinforcement are not sufficient to resist this pressure, splitting cracks occur at the

interface between the concrete and the bar. These cracks propagate towards the outer surface resulting in a concrete failure by splitting the concrete cover. Cracks generate in the perpendicular and parallel planes to the reinforcement, as shown in Figure 2.5. In other words, splitting is due to normal tensile stresses reaching or exceeding the tensile strength of the concrete. This occurs at a much lower load than the pull-out failure and the bond stress in the bar is lost suddenly. Ehsani et al. (1996b) pointed out that splitting failure occurred in specimens with a small concrete cover as the concrete cannot resist the tensile stresses. However, the specimens reinforced with longer embedment lengths of FRP re-bars and having sufficient concrete cover failed by rebar rupture due to the tensile stresses in the cross section of the rebar reaching the ultimate strength. Furthermore, it was reported that the bond failure was strongly dependent on the concrete cover. The specimens with a clear concrete cover of one rebar diameter failed in splitting (Ehsani et al., 1996b). Moreover, the ACI-408R (2003) code stated that bond failure occurs by splitting the concrete when the member does not have an adequate concrete cover, while the splitting failure will be prevented or delayed when the provided concrete cover is sufficient. Embedment lengths are also reported to affect the bond failure. Longer embedment lengths result in splitting failure, whereas sufficiently shorter embedment lengths lead to pull-out failure. Xue et al. (2014) found that the sand-coated GFRP reinforced specimens having embedment lengths less than 5 times the rebar diameter failed by a pull-out mode; whilst the specimens whose embedment lengths were more than 5 times the bar diameter failed by concrete splitting, but the specimens having embedment lengths equal to 5 times the bar diameter, failed in either pull-out or splitting. It

was reported that for the shorter embedment lengths with high compressive strength and longer embedment lengths with low concrete compressive strength, splitting failure might occur (Okelo and Yuan, 2005). Yan et al. (2016) stated that transverse reinforcement provides confinement to the concrete and this results in preventing or delaying a splitting failure. Subsequently, the likelihood of a pull-out failure will increase. Bar diameters are also reported to influence the failure mode of the specimens. Yan et al. (2016) reported that an increase in the bar diameter increases the tendency towards splitting failures. Achillides and Pilakoutas (2004) and Karlsson (1997) indicated that the dominant bond failure was splitting in the case of lower concrete compressive strength. It can be deduced that the splitting failure was controlled by concrete cover, embedment length, bar diameter, concrete strength and transverse reinforcement.

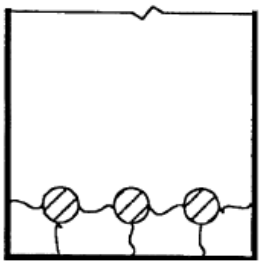

Figure 2.5 - Cross sectional view of a member showing splitting cracks between bars and through the concrete cover (ACI-408R, 2003)

2.6 Factors influencing on bond strength

Extensive research was carried out to investigate the effect of the main factors on bond strength. Pull out and beam tests were used to perform these studies. According to experimental investigations, it was found that the bond strength between FRP reinforcement and concrete depends on several factors, such as

embedment length, bar diameter, compressive strength of concrete, surface type, FRP type, concrete cover, transverse reinforcement and rebar position. It is important to understand the influence of the main parameters on bond strength in order to develop a design equation to estimate the bond strength. As a result, bond failure can be avoided. In the following, the main parameters controlling the performance of bond strength are presented and discussed.

2.6.1 Embedment length

Embedment length is one of the main parameters that influence the bond strength of FRP bars embedded in concrete. In general, bond strength reduces with increasing the bonded length. This is because of the nonlinear distribution of bond stresses along the embedment length (Benmokrane et al., 1996, Achillides and Pilakoutas, 2004). This trend was confirmed by several investigations using a pull-out test and beam test (Makitani et al., 1993, El Refai et al., 2014, Cosenza et al., 1997, Nanni et al., 1995, Yan et al., 2016, Achillides and Pilakoutas, 2004, Tighiouart et al., 1998, Xue et al., 2014). The nonlinear distribution of bond stresses is more obvious with increasing the embedment length, resulting in a decrease of the average bond stress. In addition, the increase of the embedment length leads to increase the applied tensile load, and it was also observed that the tensile stresses decreased quickly from the loaded end towards the unloaded end referring to a non-linear distribution of bond stresses (Tighiouart et al., 1998). Furthermore, Achillides and Pilakoutas (2004) and Pepe et al. (2013) reported that embedment length has a significant effect on the initial bond stiffness of FRP bars, where the increase in the embedment length leads to reduce the initial bond

stiffness. The effect of embedment length on bond performance of GFRP bars embedded in normal strength concrete was studied by Okelo and Yuan (2005), Tighiouart et al. (1998), El Refai et al. (2014), Achillides and Pilakoutas (2004), Tastani and Pantazopoulou (2006) and Achillides (1998), and their results showed that the embedment length was inversely proportional to the bond strength, similar to the steel re-bars. However, few references in the literature have investigated the effect of embedment length of GFRP bars in high strength concrete (HSC). For example, Hossain et al. (2014) tested the bond behaviour of sand-coated GFRP bars in HSC (74 MPa) with considering the embedment length (3, 5, 7 and 10 times bar diameter). The findings showed that the decrease rate in bond strength reduced, as embedment length increased. The investigation performed by Tekle et al. (2016) indicated that the increase of the embedment length of sand-coated GFRP bars in HSC (42 MPa) resulted in reducing in the bond strength. Due to the very limited number of studies available in the literature regarding the bond behaviour of GFRP bars in high strength concrete, the author has decided to investigate the influence of embedment length on bond strength of GFRP bars embedded in HSC using centric pull-out cubes, eccentric pull-out prisms and hinged beams.

2.6.2 Bar diameter

From previous studies, it is deduced that the increase of the FRP rebar diameter results in reducing the average maximum bond stress, similar to steel reinforcement (Tighiouart et al., 1998, Baena et al., 2009, Darwin et al., 1996, Esfahani et al., 2013, Achillides and Pilakoutas, 2004, Okelo and Yuan, 2005, De

Larrard et al., 1993, Soretz, 1972, Faza and Gangarao, 1990, Hao et al., 2007, Benmokrane et al., 1996, Xue et al., 2014). Tighiouart et al. (1998) and Hao et al. (2007) indicated that larger diameter bars developed bond strength less than smaller diameter bars due to the bleeding of water beneath these re-bars and the creation of larger voids, which in turn lead to reduce the contact surface between the rebar and the concrete. Thereby the bond strength decreases. While, Achillides and Pilakoutas (2004) explained the reduction of bond strength for bigger diameters because of three factors: embedment length, Poisson effect and shear lag, which are explained below in more detail.

Larger diameters of FRP re-bars need longer embedment lengths in order to develop the same normal bond stresses. As mentioned above, larger bonded lengths lead to reduce the average bond strength (Achillides and Pilakoutas, 2004). The Poisson effect is able to result in a slight decrease of bar diameter owing to the longitudinal stress. This reduction increases with the size of bar, that can lead to decrease the frictional and mechanical locking stresses (Achillides and Pilakoutas, 2004). Shear lag principally depends on the shear stiffness of the resin and shear strength of the interface between the resin and fibre. When tension force is applied on the cross section of FRP rebar, some differential movement will be propagated between the core and surface fibres. This will result in a non-uniform distribution of normal stresses through the cross section of FRP rebar as shown in section 2.4. This shear lag results in producing the maximum normal stresses at the surface which control the bond strength, while lower average normal stresses are at the middle of the cross section. The difference between the maximum and average normal stresses is higher in large diameters,

subsequently, it is anticipated to decrease the bond strength of FRP rebar (Achillides and Pilakoutas, 2004).

The effect of bar diameter on bond behaviour of GFRP bars in normal strength concrete was investigated using a pull-out test and beam test by many researchers (Achillides and Pilakoutas, 2004, Baena et al., 2009, Tighiouart et al., 1998, Hao et al., 2007, Okelo and Yuan, 2005, Benmokrane et al., 1996, Achillides, 1998). They pointed out that bond strength reduced with increasing bar diameter. However, few references in the literature have investigated the effect of bar diameter of GFRP bars on bond strength in high strength concrete (HSC). Hossain et al. (2014) tested the bond behaviour of sand-coated GFRP bars in HSC (74 MPa) considering two main parameters: bar diameter (15.9 and 19.1 mm) and embedment length (3, 5, 7, 10 times bar diameter). The findings showed that the reduction in bond strength with increasing bar diameter was clear for each embedment length. Lee et al. (2017) investigated the effect of bar diameter (19 and 25mm) on bond behaviour of two types of GFRP bars (sand-coated and spiral-wrapped) in high strength concrete (40 and 60 MPa). It was noted that a reduction rate in bond strength was lower with increasing the bar size in high strength concrete. Therefore, the author has decided to investigate the influence of bar diameter on bond strength of GFRP bars in HSC using centric pull-out cubes, eccentric pull-out prisms and hinged beams.

2.6.3 Concrete strength

The tensile and compressive concrete strengths play an important role in bond performance of FRP bars. The results obtained by Xue et al. (2008) showed that

the higher concrete compressive strength led to the development of higher bond strength for CFRP bars. In addition, Achillides and Pilakoutas (2004) and Achillides (1998) tested the effect of concrete strength on the bond behaviour of the deformed GFRP bars embedded in conventional concrete having cubic compressive strength ranging from 15.5 to 49.5 MPa. Their results revealed that the concrete strength affected the bond failure mode, where specimens with concrete strength greater than 30 MPa failed by a pull-out mode, therefore, the bond strength did not depend much on concrete strength. But, for the lower concrete strengths (around 15 MPa), the bond failure happened in the concrete, subsequently, it was reported that the bond strength was directly proportional to the concrete strength. This trend also has been confirmed by the experimental study conducted by Baena et al. (2009). Although concrete compressive strength was not low enough (almost 30 MPa), complete failure occurred in the concrete. They found that a lower concrete compressive strength of 30 MPa led to less damage in the bar surface and more in the concrete, and vice versa for concrete compressive strengths of 50 MPa. They also reported that a change in the concrete compressive strength led to changes in failure mode and failure surface. Moreover, it was confirmed from collecting database from the literature by Davalos et al. (2008), that the bond strength was proportional to the square root of the concrete compressive strength, as the concrete compressive strength was below 20 MPa, and in this case the concrete splitting was controlled. However, when the concrete compressive strength was more than 30 MPa, this correlation was not apparent and the dominant failure was bar surface damage (pull-out mode). Also, the effect of concrete compressive strength (20, 40 and 60 MPa) on

the bond behaviour of two types of GFRP bars (sand coated and spiral wrapped) was investigated by Lee et al. (2017). The experimental results demonstrated the low increase rate in the bond strength with increasing concrete compressive strength from 40 to 60 MPa. Furthermore, it was stated that the concrete compressive strength did not considerably affect the bond strength of GFRP re-bars in spliced beams (Esfahani et al., 2013). From these discussions, it can be reported that the concrete strength influences the bond strength up to a certain limit beyond which there is no further enhancement of bond strength with the increase of concrete strength, this may be attributed to change in the failure surface.

In contrast, the results obtained by Lee et al. (2008) showed that bond strength of GFRP bars with two different surfaces (sand-coated and helical wrapped) steadily increased with increasing concrete compressive strength (from 25 to 92 MPa) and this improvement in bond strength was greater in steel bars than in GFRP bars. They found that the bond failure did not only occur in the concrete, but also in the outer surface of the bar. In addition, the effect of concrete compressive strengths (25, 40 and 70 MPa) on two types of GFRP bars (sand-coated and helical wrapped) was investigated by Lee et al. (2012), the results showed that the bond strength increased with concrete strength ($f_c'^{1/3}$) and the corresponding slip reduced with a higher concrete compressive strength. This was attributed to the failure of the outer surface of the bar instead of crushing of the concrete. Based on this contradiction, the current study has decided to examine the bond behaviour of two common types of GFRP bars (helical wrapped and sand coated)

embedded in high strength concrete and their bond failure using a pull-out test and hinged beam test, and it would be interesting to combine the authors' findings with those available in the literature with different concrete strengths to gain a better understanding of the extent to which concrete compressive strength plays a significant role in bond. To date, there has been no research about bond behaviour of FRP bars in high strength concrete hinged beams. Subsequently, one of the aims of this research is to investigate bond of GFRP bars in HSC using a hinged beam test.

Several researchers developed models using linear regression analysis to predict bond strength depending on the concrete strength (Pleimann, 1987, Pleimann, 1991, Liu, 2003, Okelo and Yuan, 2005, Wambeke and Shield, 2006, Lee et al., 2008, Xue et al., 2008, Xue et al., 2014). It was noted that these equations had different exponential powers of concrete strengths. It was mentioned that the power of the concrete strength played an important role to present an accurate relationship between concrete strength and bond strength, for example, the square root of compressive concrete strength did not give an accurate representation of the effect of concrete strength on bond strength over the full range of concrete strengths, while a power of 1/4 provided an accurate representation of the relationship between concrete strength and bond strength for concretes with compressive strength between 17 and 110 MPa (Darwin et al., 1996).

2.6.4 Surface deformation

The surface treatment plays an important role in improving the bond strength. Various research studies have been conducted on different types of FRP reinforced bars having different surface deformations such as sand coating, helical wrapping, ribs, grooves and surface texture as illustrated in Figure 2.6 in order to explore the effect of surface treatment on the bond behaviour. Baena et al. (2009) tested the pull-out specimens reinforced with different types of FRP bars with various surface treatments and concrete compressive strengths (30 and 50 MPa). The analysis of the bond behaviour for each bar surface confirmed that different bond mechanisms were observed for different surface configurations, and CFRP bars with sand coated surfaces developed bond strengths higher than other surfaces. In addition, the effect of surface treatment on bond strength was less significant for concretes with low compressive strengths, it was, however, important for concretes with high compressive strengths. As for deformed or indented re-bars, the effect of the surface geometry was analyzed using the geometric ratios such as area to space ratio and concrete lug ratio, obtaining higher bond strength for higher values of geometric ratios (Baena et al., 2009). The bond strength of steel re-bars was from 30% to 50% higher than FRP re-bars (Mosley et al., 2008, Xue et al., 2008, Hao et al., 2007, Okelo and Yuan, 2005, Achillides and Pilakoutas, 2004). This is because of differences in the mechanical properties and surface deformations. Hao et al. (2007) examined 105 pull-out specimens reinforced with GFRP re-bars having different rib geometries. It was concluded that the optimal rib height and spacing that provided higher bond

strength were 6% of the bar diameter and equal to the bar diameter, respectively. Xue et al. (2008) indicated that the bar surfaces with high friction coefficients had high bond strength. Hence, their embedment lengths were smaller than those with low friction coefficients. Also, the bar deformations such as external helicoidal strands and deep dents (grooves) contributed to the improvement of bond strength. Moreover, it was noted that sand coating and surface texture provided a better bond performance than a smooth surface (Okelo and Yuan, 2005). The results obtained by Tighiouart et al. (Tighiouart et al., 1998) indicated that the ratio of the bond strength for a GFRP deformed surface to that of a GFRP spirally wound surface changed from 1.15 to 1.48 depending on bar diameter. Mazaheripour et al. (Mazaheripour et al., 2013) found that the bond strength of the ribbed GFRP bars is higher than that of the sand-coated GFRP bars embedded in self-compacting steel fibre reinforced concrete. In addition, the influence of two types of GFRP bars (sand coated and helical wrapped with slight sand coating) on the bond performance was investigated by Davalos et al. (2008) considering concrete compressive strength in the range of 57 to 63 MPa. They found that sand coated GFRP bars had better bond strength than helically wrapped GFRP bars because of theirs sand coated surface. On the contrary, the results obtained by Lee et al. (2012) indicated that the bond strength for the helically wrapped with slightly sand coated GFRP bars was higher than that for the sand coated GFRP bars for concrete compressive strengths (25, 40 and 70 MPa). The corresponding slip for GFRP (SC) bars was smaller than that for GFRP (HW) bars. Conversely, database analysis showed that the surface configuration did not appear to influence the bond strength of FRP bars in concrete (Wambeke

and Shield, 2006). The CAN/CSA-S806 (2012) and CAN/CSA-S6 (2014) codes acknowledge the influence of surface treatment by suggesting a bar surface factor in their development length equations, whereas the ACI-440.1R (2015) and JSCE (1997) do not have any special provisions for this parameter. Therefore, this study aims to examine and compare the bond behaviour of two common GFRP bar types (helical wrapping with slight sand coating and sand coating).

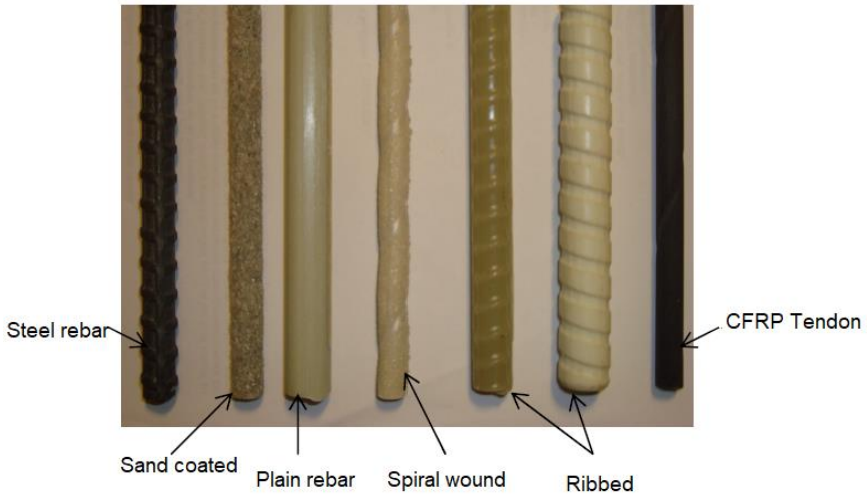

Figure 2.6 - Different surfaces of FRP reinforcing bars (Quayyum, 2010)

2.6.5 Bar position

The literature illustrates that the FRP bar position effect on bond strength was investigated by some authors (Tighiouart et al., 1998, Chaallal and Benmokrane, 1993, Ehsani et al., 1996b, Benmokrane and Masmoudi, 1996, Pay et al., 2014, Golafshani et al., 2014). It was concluded that the top re-bars developed lower bond strengths than the bottom re-bars. Due to this, the development lengths for top bars should be multiplied by the modification factor to become longer than the bottom bars (Rossetti et al., 1995). Chaallal and Benmokrane (1993) defined the top-cast modification factor as the ratio of the pull-out force for the bottom re-bars

to that for the top re-bars. (Tighiouart et al., 1998) used the pull-out test to examine the position effect of GFRP (spirally wound) bars in NSC on bond strength. The results showed that the ratio of the bond strengths of the bottom bars to the top bars was in the range between 1.09 and 1.32 with an average of 1.29, and therefore it was recommended to use a factor of 1.3. In addition, the ratios obtained from the results of pull-out test changed from 1.08 to 1.38 with an average of 1.23 and from 1.11 to 1.22 with an average of 1.18 depending on bar diameter for NSC and HSC, respectively (Chaallal and Benmokrane, 1993). It was noted that the modification factor increased with reducing the rebar diameter for both NSC and HSC (Chaallal and Benmokrane, 1993). Moreover, Ehsani et al. (1996b) reported that the top modification factor was 1.25 from testing pull-out specimens. Furthermore, Benmokrane and Masmoudi (1996) obtained the top modification factor of FRP C-bar equal to 1.1 from pull-out test. CAN/CSA-S806 (2012), CAN/CSA-S6 (2014), ACI-440.1R (2015) and JSCE (1997) codes take the effect of the bar location into consideration by including the bar location factor in the calculations of the development length. The bar location factor is 1.3 in Canadian and Japanese codes and 1.5 in ACI-440.1R-15. It was also stated that the bond strength was lower, when the concrete cover was more than 305 mm below the horizontal bars, because of the bleeding of water and segregation (Wambeke and Shield, 2006). The results obtained from testing pull-out specimens revealed that the reduction of the water to cement ratio and using high cementitious materials decreased the bond strength variation between the upper and lower zones of the specimens (Golafshani et al., 2014). Pay et al. (2014) investigated the bar position effect on bond behaviour using lap splice specimens.

The results reported that the bond strength of the top-cast specimens was slightly lower (average 7% reduction) than that of the bottom-cast specimens due to less water bleeding and a lower concrete slump. However, the effect of bar position on bond strength has not been investigated using a hinged beam. Therefore, the current study aims to investigate the influence of bar position on bond strength. The investigated parameters considered in the previous beam tests are presented in Table 2.1.

Table 2.1 - Investigated parameters in existing hinged beam tests

Reference	Bar diameter	Embedment length	Concrete cover	Surface treatment	Concrete strength	Fibre type	Concrete type
Benmokrane et al. (1996)	✓	-	-	-	-	GFRP	NC
Tighiouart et al. (1998)		✓	-	✓	-	GFRP	NC
Pecce et al. (2001)	-	✓	-	-	✓	GFRP	NC
Okelo (2007)	✓	✓	-	-	-	GFRP, CFRP	NC
Mazaheripour et al. (2013)	✓	✓	✓	✓	-	GFRP	SFRSCC
Ovitigala and Issa (2013)	✓	✓	-	-	-	BFRP	NC
(Kotynia et al. (2017))	✓	-	✓	-	-	GFRP	NC

Note: NC is normal concrete and SFRSCC is steel fibre reinforced self-compacting concrete.

2.6.6 Concrete cover

Concrete cover provides confinement to the reinforcing bars and this leads to an increase in the bond strength between two materials and a reduction in splitting forces (Ehsani et al., 1993, Kanakubu et al., 1993, DeFreese and Roberts-Wollmann, 2002). It is obvious that the bond failure influences the concrete cover. Splitting failure occurs in the specimens having a small concrete cover because the concrete cannot resist the tensile stresses. It was reported that the specimens

with a clear concrete cover equal to one bar diameter failed by concrete splitting (Ehsani et al., 1996b). However, those with a concrete cover of twice the rebar diameter, depending on the embedment length, failed in either pull-out or rebar fracture (Ehsani et al., 1996b). It means that the bond failure strongly depends on a clear concrete cover. The ultimate bond stresses in specimens with the clear concrete cover of twice the rebar diameter were higher than those in specimens having a clear concrete cover of one rebar diameter (Ehsani et al., 1996b). In addition, it was observed that the side concrete cover was more effective in increasing the bond strength than the bottom concrete cover (Aly et al., 2006). Moreover, the ACI-440.1R (2015) code stated that bond failure is caused by splitting the concrete when the member does not have an adequate concrete cover. It can be deduced that splitting failure will be prevented or delayed when the provided concrete cover is sufficient. Furthermore, Aly et al. (2006) investigated six full-scale beams to study the effect of concrete cover on the bond strength of tensile lap splicing of GFRP re-bars with the concrete cover varying from one to four times the bar diameter. It was found that the bond strength increased by 27% when the concrete cover increased from one to four times the bar diameter and the influence of concrete cover on bond strength was nonlinear. Furthermore, the results obtained by Hossain et al. (2014) demonstrated that the increase in bond strength of sand-coated GFRP bars was 10 and 20% for bar diameters of 15.9 mm and 19.1 mm, respectively, when increasing the concrete cover from 40 to 60 mm. Also, ribbed GFRP reinforced hinged beams were tested by Kotynia et al. (2017) to investigate the effect of concrete thickness on bond strength, showing that a reduction in the concrete cover caused a reduction in

bond strength. On the contrary, higher bond strength and lower slip values developed for eccentric pull-out specimens compared to centric ones, and this was more pronounced for lower concrete strengths (Veljkovic et al., 2017). Canadian, American and Japanese codes acknowledge the influence of concrete confinement on bond performance in the equations of the development length calculation.

2.6.7 Transverse reinforcement

The transverse reinforcement (stirrups) are provided along developed and spliced reinforcing bars to confine the concrete in order to increase bond strength between those re-bars and the concrete. The importance of transverse reinforcement in controlling the splitting mode of failure of FRP re-bars in concrete members has been studied by various authors. Aly (2005) stated that transverse reinforcement increased the bond strength of spliced re-bars embedded in concrete, and Harajli and Abouniaj (2010) also mentioned that transverse reinforcement increased the bond strength of GFRP re-bars. In addition, it was reported that the increase of transverse reinforcement along the splice length in beam specimens reinforced with ribbed GFRP re-bars led to improve the bond strength (Esfahani et al., 2013), and this result was similar to that obtained for the steel re-bars by Orangun et al. (1977) and Darwin et al. (1996). However, the transverse reinforcement in those reinforced with sand coated GFRP re-bars had a minor effect on the bond strength (Esfahani et al., 2013). Therefore, it can be concluded that the effect of transverse reinforcement on bond strength depends on the surface properties of rebar (Esfahani et al., 2013). On the contrary,

database analysis revealed that transverse reinforcement provided along the development length had no effect on bond strength between GFRP re-bars and concrete and the bar surface did not seem to have a major influence on the bond stress (Wambeke and Shield, 2006). According to ACI-440.1R (2015), the presence of transverse reinforcement in specimens reinforced with the GFRP bars having a very low relative rib area, does not lead to improvements in the bond strength. Therefore, it is recommended to investigate the effect of transverse reinforcement on bond strength of FRP reinforcing bars using more data (ACI-440.1R, 2015). The importance of transverse reinforcement is also underlined in the codes of practice JSCE (1997) and CAN/CSA-S6 (2014).

2.6.8 Fibre type

As mentioned earlier, the mechanical properties of FRP re-bars are different, because they depend on the manufacturing process, type of resin and type of fibre. Therefore, the bond behaviour of each FRP type should be investigated. Several researchers conducted tests to observe the effect of each FRP type on bond stresses. For example, Okelo and Yuan (2005) tested 151 pull-out specimens reinforced with various reinforcing bar types, such as GFRP, CFRP, AFRP and steel. It was concluded that the bond strength of FRP re-bars varied from 40% to 100% of that of steel re-bars for pull-out failure modes. Also, they stated that the elastic modulus of GFRP, CFRP and AFRP re-bars seems to have some effect on the bond stresses. However, the equation developed by Okelo and Yuan (2005) considered two parameters only (compressive concrete strength and bar diameter) to calculate bond strength and ignored the influence of FRP

type. It means that all FRP re-bars (GFRP, CFRP and AFRP) with the same bar diameter and embedded in the same concrete develop the same bond strength. In addition, it was reported that the GFRP and CFRP re-bars showed the same bond behaviour and both had 72% of the bond strength of steel re-bars (Achillides and Pilakoutas, 2004). Also, AFRP and hybrid (glass and carbon) re-bars illustrated about 85% and 90% of the bond strength of GFRP and CFRP re-bars, respectively (Achillides and Pilakoutas, 2004). CAN/CSA-S806 (2012) code only takes into account the influence of FRP type by including the bar fibre factor in calculations of the development length. According to the Canadian code (CAN/CSA-S806, 2012), the bar fibre factor is equal to 1.0 for CFRP and GFRP and 1.25 for AFRP. This indicates that carbon and glass fibres have the same effect on bond strength, however, aramid fibres have lower bond strength than carbon and glass fibres.

2.7 Bond stress - slip behaviour

In general, the bond stress – slip curve consists of two parts: the first part is ascending (pre-peak) and the second part is descending (post-peak) as illustrated in Figure 2.7. The ascending curve is divided into two branches; the first branch is linear with a high initial stiffness up to a percentage of the ultimate load, and chemical adhesion is controlled at this stage. Then, the second branch becomes non-linear with a small slip before reaching the peak bond stress, at this stage, the bar surface deformation (mechanical interlock) is dominant to resist the pull-out force. At the stage of the post-peak load, the descending branch drops rapidly or gradually depending on an interface failure with increasing the slip and the

bond resistance arises from the friction between the rebar surface and the concrete.

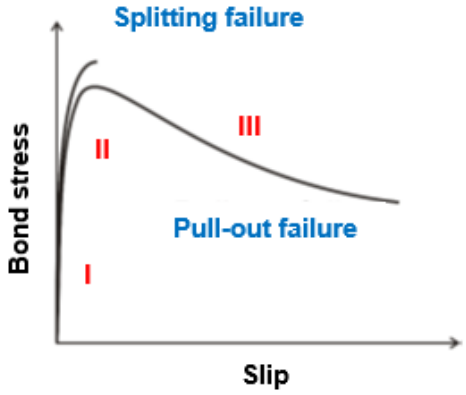

Figure 2.7 - Schematic bond stress-slip curve (Tekle et al., 2016)

2.8 Existing bond stress – slip analytical models

Bond stress – slip relationships are very important in designing the anchoring systems and developing constitutive models of concrete – reinforcing bar interface for the analysis of reinforced concrete structures. Therefore, several FRP bond stress - slip models proposed in the literature will be reviewed in this section. These models were developed based on experimental results to predict the bond stress - slip behaviour of FRP reinforcing bars. Some models described the so-called “complete” relationship law (ascending and descending curve), namely the Eligehausen, Popov and Bertero (BPE) model, the BPE modified model and the Xue et al. (2008) model. Others predicted an ascending curve only such as the CMR model and the Tighiouart et al. (1998) model. The well-known models are introduced in more detail as shown below.

2.8.1 Malvar's model

The first FRP bond stress - slip model was proposed by Malvar (1994) based on the pull-out data. Three different types of FRP surfaces (deformed and indented surface, indented surface, and deformed surface) were investigated in his study. In addition, the effects of confinement and indentation depth on the bond strength were tested. The bond stress - slip model was derived in two steps. The first step is that the peak bond stress τ_{max} and the corresponding slip at the peak bond stress s_1 were defined as a function of confining axisymmetrical radial pressure (σ) as shown in equations 2.1 and 2.2. The second one illustrates the bond stress - slip model which was determined as a function of τ = τ(s, σ) as shown in expression 2.3. Furthermore, seven empirical constants were required to determine the shape of the curve which describes the entire bond stress versus loaded-end slip response.

$$\frac{\tau_{max}}{f_t} = A + B\left(1 - \exp\left(-\frac{C\sigma}{f_t}\right)\right) \tag{2.1}$$

$$s_1 = D + E\sigma \tag{2.2}$$

$$\frac{\tau}{\tau_{max}} = \frac{F\left(\frac{S}{s_1}\right) + (G-1)(\frac{S}{s_1})^2}{1 + (F-2)\left(\frac{S}{s_1}\right) + G(\frac{S}{s_1})^2} \tag{2.3}$$

where τ_{max} is the peak bond stress, s_1 is the slip at the peak bond stress, σ is the confining axisymmetrical radial pressure, f_t defined as the tensile concrete strength and A, B, C, D, E, F and G are empirical constants estimated for each rebar type. In Malvar's study, those empirical constants were evaluated only for GFRP re-bars having two rebar surface treatments, but the effect of fibre type and

rebar diameter were not considered. Another disadvantage is that the value of confining axisymmetrical radial pressure, σ, is difficult to determine when analysing the structures under bending load. Moreover, the Malvar's model was less reliable for modelling the ascending branch of the bond stress-slip curve of the FRP bar (Cosenza et al., 1997).

2.8.2 BPE model

The BPE Model was first proposed for deformed steel bars that failed in pull out by Eligehausen et al. (1983) and it has been the most well-known and commonly used model in analysis of traditional steel-reinforced concrete structures (Monti and Spacone, 2000, Salari and Spacone, 2001, Oliveira et al., 2008, Lundgren et al., 2012). Then this model was applied to represent the local bond stress-slip relationship of FRP re-bars by Rossetti et al. (1995) and Cosenza et al. (1995) by calibrating the parameters based on experimental results. It has an ascending curve that shows the bond mechanism of chemical adhesion, followed by a plateau interval with constant maximum bond stress, then a linear descending branch and a final horizontal branch with a constant frictional response (Gravina and Smith, 2008). This model is adopted by the CEB-FIP (2010) for the use of traditional steel reinforcements based on a series of parameters (i.e. the peak bond stress, τ_{max}, the slip corresponding to the peak bond stress, s_1, and parameters s_2, s_3, α and β), which in turn depend on the amount of confinement, bond conditions and concrete strength. Figure 2.8 and equations 2.4 to 2.7 describe the bond stress-slip curve of this model in which the bond stress is a function of the slip, s.

Figure 2.8 - BPE Model

$$\frac{\tau}{\tau_{max}} = \left(\frac{s}{s_1}\right)^{\alpha} for \quad 0 \le s \le s_1 \tag{2.4}$$

$$\tau = \tau_{max} \quad for \quad s_1 < s \le s_2 \tag{2.5}$$

$$\tau = \tau_{max} - \left(\tau_{max} - \tau_f\right)\left(\frac{s - s_2}{s_3 - s_2}\right) for \qquad s_2 < s \le s_3 \tag{2.6}$$

$$\tau = \tau_f = \beta\tau_{max} \quad for \quad s > s_3 \tag{2.7}$$

The parameters in the BPE model for steel re-bars need to be recalibrated to use them in describing the bond stress - slip behaviour of FRP re-bars. Rossetti et al. (1995) determined the parameters for smooth and rough surface GFRP re-bars embedded in concrete having different compressive strengths. The peak bond stress and the slip corresponding to the peak bond stress were obtained from experimental tests, while the parameters s_2, s_3, α and β were defined by a special identification technique. However, the test results were quite scattered and the rebar diameter had no effect on the bond stress - slip behaviour of GFRP re-bars (Rossetti et al., 1995). In addition, Cosenza et al. (1995) investigated different

fibre types, rebar surfaces and pressure confinements in order to determine the values of parameters in the BPE model. It was found that intended and grain covered re-bars offered good results in terms of bond strength, whereas the bond strength results for spirally wounded re-bars were very scattered.

2.8.3 BPE modified model

The BPE modified model was proposed by Cosenza et al. (1997) and in this model, the effect of different rebar surfaces on the bond strength of FRP reinforcing bars has been considered. This model has been utilized in a number of studies on FRP reinforced concrete structures (Pecce et al., 2001, Focacci et al., 2000, Gravina and Smith, 2008). The second part of the BPE model with a constant peak bond stress deleted to obtain a better representation of the bond stress - slip relationship for FRP re-bars as shown in Figure 2.9. The BPE modified model is more suitable for FRP reinforcing bars, however, this model does not take into account the effect of rebar diameter and fibre type on the bond strength. The following expressions demonstrate the bond stress – slip relationship for each part of the complete curve.

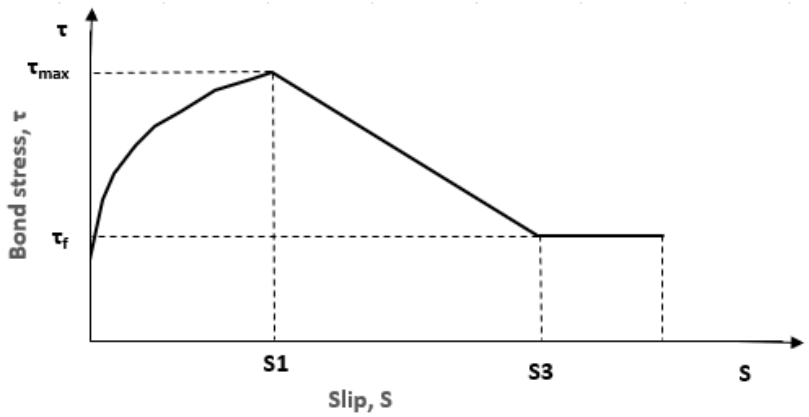

Figure 2.9 - BPE Modified Model

$$\frac{\tau}{\tau_{max}} = \left(\frac{s}{s_1}\right)^{\alpha} \qquad for\ 0 \le s \le s_1 \tag{2.8}$$

$$\frac{\tau}{\tau_{max}} = 1 - \rho\left(\frac{s}{s_1} - 1\right) \qquad for\ s_1 < s \le s_3 \tag{2.9}$$

$$\tau = \tau_f \quad for \quad s > s_3 \tag{2.10}$$

where τ_{max} is maximum bond stress (MPa); τ_f is frictional bond stress (MPa); α and ρ are the curve fitting parameters; α is specified as $\left(= \frac{\tau_{max} s_1}{A_{\tau 1}} - 1\right)$ and $A_{\tau 1}$ is the area underneath the ascending branch.

2.8.4 CMR model and Tighiouart et al.'s model

Cosenza et al. (1995) proposed an alternative model rather than the BPE model and this model is only for the ascending branch of the bond stress - slip curve. In the CMR model, different fibre types and rebar surfaces were investigated to determine the parameters s_r and β. It was noted that some database was very scattered and the effect of the rebar diameter on the bond strength has not been investigated. The CMR model is expressed as:

$$\frac{\tau}{\tau_{max}} = \left(1 - exp\left(-\frac{s}{s_r}\right)\right)^{\beta} \tag{2.11}$$

where s_r and β are parameters based on curve fitting of the experimental data. Tighiouart et al. (1998) used the CMR model and evaluated the parameters (s_r, β) based on the tested database. Thus, the below model was developed for the ascending branch of the bond stress - slip relationship. It is obvious that the model depends on the peak bond stress, τ_{max}, only. However, according to Tighiouart

et al.'s test data, this peak bond stress is influenced by rebar diameter, embedment length and rebar surface treatments:

$$\frac{\tau}{\tau_{max}} = [1 - e^{4s}]^{0.5} \tag{2.12}$$

In addition, it is obvious that in terms of mathematics, equation 2.12 makes sense, $1 - e^{4s} \geq 0 \rightarrow e^{4s} \leq 1 \rightarrow s \leq 0$ but it is impossible for a slip to have a negative value. As a result, there is a mistake in the Tighiouart et al. (1998) model (Lin and Zhang, 2014).

2.8.5 Xue et. al.'s model

Xue et al. (2008) developed a model based on investigating pull-out specimens reinforced with high strength carbon fibre reinforced polymer (CFRP) strands, which were embedded in different bonding agents such as normal concrete, high strength concrete, epoxy resin and grout. The bond stress - slip curves obtained from testing pull-out specimens could be divided into four phases. In the first three phases, the bond stresses increase with the slip and their relationships exhibit a nonlinear response. Therefore, the first three parts were combined to produce the ascending branch. The last phase was subdivided into two branches, where the first branch had a steep descending slope and the other had a slope close to zero. These two branches were renamed as the descending branch and the horizontal branch, respectively. The developed equations were defined as follows:

$$\frac{\tau}{\tau_{max}} = \left(\frac{s}{s_1}\right)^{0.1} \quad \text{for ascending branch} \tag{2.13}$$

$$\tau = \left(\frac{a_1}{s}\right)^{b_1} \text{ for descending branch} \quad (2.14)$$

where: $b_1 = log_{\left(\frac{s_2}{s_1}\right)}\left(\frac{\tau_{max}}{\tau_2}\right), \quad a_1 = s_1(\tau_{max})^{1/b_1}$

$$\tau = \tau_2 \quad \text{for horizontal branch} \quad (2.15)$$

where τ_{max} is the maximum bond stress and s_1 is the corresponding slip at τ_{max}, τ_2 is the inflexion from the descending branch to the horizontal branch, and s_2 is the corresponding slip at τ_2. It was mentioned that this model could provide better understanding for further theoretical researches.

2.8.6 Baena et. al's model

Baena et al. (2009) used the BEP modified model and considered the effect of the bar diameter for estimating the values of the parameters s_1, τ_{max} and α:

$$\tau_{max} = \tau_0 + \tau_1 d_b \quad (2.16)$$

$$s_1 = m_0 e^{m_1 d_b} \quad (2.17)$$

$$\alpha = \alpha_0 . d_b^{\alpha_1} \quad (2.18)$$

where τ_0, τ_1, m_0, m_1, α_0 and α_1 are curve fitting parameters.

In addition, Baena et al. (2009) used the CMR model and considered influencing the bar diameter to calculate the parameters β and s_r. Usually, the parameters of the analytical models are individually curve fitted by the least-square error method. For instance, it is impossible to use the parameters for helically wrapped surfaces for grooved surfaces due to the difference of the bar surface treatment, and furthermore, they cannot be used in cases where the failure type is different (Baena et al., 2009):

$$\beta = \beta_0 e^{\beta_1 d_b} \quad (2.19)$$

$$s_r = r_0 e^{r_1 d_b} \tag{2.20}$$

where β_0, β_1, r_0 and r_1 are curve fitting parameters.

From the bond stress-slip relationships presented in Equations 2.1 to 2.20, it is evident that no specific formulations can predict the bond stress - slip relationship for different types of FRP re-bars. Moreover, all of the proposed formulations need to be validated by comparison with experimental results (Cosenza et al., 1997). Furthermore, these equations were developed based on investigating pull-out specimens reinforced with GFRP bars, except the Xue et al. (2008) model which was developed for CFRP bars.

2.9 Review of existing bond strength and development length models

Some researchers developed equation 2.21 to estimate the development length of FRP re-bars (Pleimann, 1987 and 1991, Faza and Gangarao, 1990, Ehsani et al., 1996a and 1996b, Tighiouart et al., 1998). It is the same equation for steel reinforcing bars as that found in ACI-318 (2005) and it is based on the work done by Orangun et al. (1977). However, the value of factor K is different from one researcher to the other as explained below:

$$\mathrm{l_{db}} = \frac{\mathrm{A_b} f_{fu}}{K\sqrt{f_c'}} \tag{2.21}$$

The increase of the embedment length leads to an increase in the applied tensile load up to the ultimate load capacity. At the ultimate load, the embedment length is referred to as the optimal anchored length, which is defined as the minimum development length required to develop the ultimate tensile strength (Chaallal and

Benmokrane, 1993). Subsequently, rupture failure occurs instead of bond failure. By equating the bond force to the ultimate tensile force, expression 2.22 is formulated and equation 2.23 for calculating the bond strength is extracted by substituting the development length equation 2.21 in the following equation:

$$\tau_{max} = \frac{A_b f_{fu}}{\pi d_b l_{db}} \tag{2.22}$$

$$\tau_{max} = \frac{k\sqrt{f_c'}}{d_b} \tag{2.23}$$

However, some researchers (Xue et al., 2014, Lee et al., 2008) used a regression analysis to develop their equations. Tables 2.2 and 2.3 present the analytical models available in the literature. Most of them were developed based on investigating pull-out specimens owing to their simplicity, while Faza and Gangarao (1990) and Ovitigala and Issa (2013) proposed their models based on beam data. In addition, Ehsani et al. (1996a), Ehsani et al. (1996b), Tighiouart et al. (1998), Liu (2003) and Xue et al. (2014) developed their equations depending on pull-out and beam tests. The majority of these models were derived based on investigating GFRP re-bars. Furthermore, it is noted that each study examined a limited range of bar diameters, embedment lengths, bar surfaces and compressive strengths of concrete for developing the equations in Tables 2.2 and 2.3, consequently, they are valid within the studied range. From Table 2.2, Weichen (1997) and Brown and Bartholomew (1993) reported that the bond strength of GFRP bars was equal to 80% and 66% of the bond strength of steel bars, respectively. It can be seen that bond strength as a function of the bar

diameter and compressive strength of concrete were considered in most of the existing bond strength models, and this means that both parameters play an important role in affecting bond strength. On the other hand, Lee et al. (2008) depended only on the concrete compressive strength to estimate bond strength. The embedment length was only taken into account by Liu (2003) and Xue et al. (2014) to evaluate the bond strength. Furthermore, Xue et al. (2014) only tested the effect of the bar surface on bond strength and this influence is included in their equation.

From Table 2.3, it can be noted that the bar diameter is considered in all models and this is an indicator that bar size is an important factor. Furthermore, all authors specify the required development length to develop the tensile strength of FRP bars because it is easier to implement by designers, except Chaallal et al. (1992) and Ovitigala and Issa (2013). Moreover, two expressions that ignored the influence of the compressive strength of concrete on bond strength are those of Chaallal et al. (1992) and Ovitigala and Issa (2013). Although the bar surface plays an important role in improving bond performance, Xue et al. (2014) only acknowledge this influence by suggesting the bar surface factor in their model. It is obvious that the factor, K, has different numerical values as shown in Pleimann, (1987 and 1991), Faza and Gangarao, (1990), Ehsani et al., (1996a and 1996b), Tighiouart et al., (1998) and Okelo and Yuan, (2005) equations. This difference may be due to the variety of testing methods of bond behaviour and the type of FRP reinforcing bars (Tighiouart et al., 1998). It is found that the factor K for GFRP is higher than that for steel re-bars because GFRP re-bars have lower bond strength than steel reinforcement (Tighiouart et al., 1998). In most models, the

power of the compressive strength of concrete is 0.5, while Lee et al. (2008) used a power of 0.3. It can be reported that the power of concrete strength plays an important role in giving an accurate representation of the effect of concrete strength on bond strength as detailed in section 2.6.3. The concrete tensile strength is indirectly included in the equations below by using the power of the concrete compressive strength, whilst the Xue et al. (2014) model included the concrete tensile strength, which is estimated by $f_t = 0.56(f_c')^{1/2}$(ACI-318, 2005).

Table 2.2 - Bond strength models in the literature

Reference	Model	Tested FRP type
Weichen (1997)	$\tau_{max(deformedGFRP)} = \frac{4}{5}\tau_{max(deformed\ steel)}$ (2.24)	GFRP bars
Brown and Bartholomew (1993)	$\tau_{max(GFRP)} = \frac{2}{3}\tau_{max(steel)}$ (2.25)	GFRP bars
Ehsani et al., (1996a and 1996b)	$\tau_{max} = \frac{k\sqrt{f_c'}}{d_b}$ (2.26) where k = 14.25	GFRP bars
Tighiouart et al. (1998)	$\tau_{max} = \frac{k\sqrt{f_c'}}{d_b}$ (2.27) where k = 10.6	GFRP bars
Liu (2003)	$\tau_{max} = \frac{13.1\sqrt{f_c}}{d_b^{0.555} l_{db}^{0.125}}$ (2.28)	GFRP bars
Okelo and Yuan (2005)	$\tau_{max} = \frac{k\sqrt{f_c'}}{d_b}$ (2.29) where k=14.7	GFRP bars
Xue et al. (2008)	$\tau_{max} = \frac{5.4\sqrt{f_{cu}}}{d_b^{0.52}}$ (2.30)	CFRP bars
Lee et al. (2008)	$\tau_{max} = \alpha(f_c')^{\beta}$ (2.31)	GFRP bars

Xue et al. (2014)	$\tau_{max} = \alpha'(5.27f_t)(1.477 - 0.028d_b)\left[2.59\left(\frac{l_{db}}{d_b}\right)^{-0.62}\right]$ (2.32)	GFRP bars with $d_b < 20mm$ and $l_{db} < 20d_b$

Table 2.3 - Development length models in the literature

Reference	Model	Tested FRP type
Pleimann, (1987 and 1991)	$l_{db} = \frac{A_b f_{fu}}{K\sqrt{f_c'}}$ (2.33) where K= 42 and 38 for GFRP and AFRP, respectively.	GFRP and AFRP bars
Faza and Gangarao (1990)	$l_{db} = \frac{A_b f_{fu}}{K\sqrt{f_c'}}$ (2.34) where 1/K= 0.028	GFRP bars
Chaallal et al. (1992)	$l_{db} = 20d_b$ (2.35)	Sand-coated GFRP bars
Ehsani et al., (1996a and 1996b)	For bottom bars. $l_{db} = \frac{A_b f_{fu}}{K\sqrt{f_c'}} > 0.0508 d_b f_{fu} > 381\ mm$ (2.36) where 1/K= 0.022 $l_{db} = k_m \frac{A_b f_{fu}}{K\sqrt{f_c'}}$ (2.37) where k_m=1.25 and 1.5 for top bars and small concrete covers, respectively.	GFRP bars
Tighiouart et al. (1998)	$l_{db} = \frac{A_b f_{fu}}{K\sqrt{f_c'}}$ (2.38) where 1/k = 0.030	GFRP bars
Xue et al. (2008)	$l_{db} = 0.083 \frac{f_{fu} {d_b}^{1.52}}{\sqrt{f_c'}}$ (2.39)	CFRP bars
Ovitigala and Issa (2013)	$l_{db} = 20d_b$ (2.40)	BFRP bars
Xue et al. (2014)	$l_{db} = \left\lfloor \frac{f_{fu} d_b^{0.38}}{\alpha' 54.6 f_t (1.477 - 0.028 d_b)} \right\rfloor^{1/0.38}$ (2.41)	GFRP bars with $d_b < 20mm$ and $l_{db} < 20d_b$

where A_b is the cross-sectional area of FRP re-bar (mm^2); d_b is the bar diameter (mm); l_{db} is the development length (mm); f_{fu} is the ultimate tensile strength of

FRP re-bar (MPa); f_c' is the cylinder compressive strength of concrete (MPa); f_{cu} is the cube compressive strength of concrete (MPa); f_c is the prism compressive strength of concrete (MPa); τ_{max} is the peak bond strength of reinforcing bar (MPa); f_t is the tensile strength of concrete (MPa); α is a coefficient (= 3.3 and 4.1 for GFRP and steel re-bars, respectively); β is a coefficient (= 0.3 and 0.5 for GFRP and steel re-bars, respectively); and α' is outer surface factor (= 1 for sand coated deformed, = 0.64 for sand coated ribbed and = 0.67 for fabric coated).

2.10 Review of existing FRP reinforced concrete design guidelines

A number of design guidelines have been published for FRP reinforced concrete structures. These include Japanese (JSCE 1997), American (ACI-440.1R 2003, ACI-440.1R 2015) and Canadian (CAN/CSA-S6 2014; CSA/CAN-S806 2012) design codes. Table 2.4 summarizes the equations proposed by different design codes to estimate the development length of FRP reinforcement in order to avoid bond failure. It is clear that design codes describe the development length required to develop the design stress in the FRP bar in such a way as to be easier to apply by designers. Canadian and Japanese equations developed to evaluate the development length were substituted in equation 2.22 to yield the bond strength expressions as shown in Table 2.4, whereas the ACI-440.1R-15 equation was formulated based on a database of 67 beam bond tests collected by Wambeke and Shield (2006), and the concrete compressive strength for these GFRP reinforced concrete beams ranged from 28 to 45 MPa. Splitting failure was only considered in this study and regression analysis of the normalized bond

strength versus the normalized concrete cover and embedment length was conducted to develop the bond strength equation.

Table 2.4 - Code equations for determining development length and bond strength

Code	Development length model	Bond strength model
JSCE (1997)	$l_{db} = \alpha_1 k_1 \frac{f_d}{4 f_{bod}} d_b > 20 d_b$ (2.42) For a splitting controlled failure	$\tau_{max} = \frac{f_{bod}}{\alpha_1}$ (2.43) For all FRP bars
ACI-440.1R (2003)	For a pull-out controlled failure $l_{db} = \frac{d_b f_{fu}}{K_3}$ (2.44) For a splitting controlled failure $l_{db} = k_m \frac{d_b f_{fu}}{K_3}$ (2.45) Where k_3=18.5	$\tau_{max} = 4.63\ MPa$ (2.46) For all FRP bars
CSA-S806 (2012)	$l_{db} = 1.15 \frac{k_1 k_2 k_3 k_4 k_5}{d_{cs}} \frac{f_f}{\sqrt{f_c'}} A_b > 300\ mm$ (2.47)	$\tau_{max} = \frac{d_{cs}\sqrt{f_c'}}{1.15 k_1 k_2 k_3 k_4 k_5 \pi d_b}$ (2.48) For GFRP, CFRP and AFRP bars
CSA-S6 (2014)	$l_{db} = 0.45 \frac{k_1 k_6}{d_{cs} + k_{tr} \frac{E_{frp}}{E_s}} \left(\frac{f_{FRPU}}{f_{cr}}\right) A_b > 250mm$ (2.49)	$\tau_{max} = \frac{\left(d_{cs} + k_{tr} \frac{E_{frp}}{E_s}\right) f_{cr}}{0.45 k_1 k_6 \pi d_b}$ (2.50) For all FRP bars
ACI-440.1R (2015)	$l_{db} = \frac{\alpha \frac{f_{fr}}{0.083\sqrt{f_c'}} - 340}{13.6 + \frac{C}{d_b}} d_b$ (2.51)	$\frac{\tau_{max}}{0.083\sqrt{f_c'}} = 4 + 0.3 \frac{C}{d_b} + 100 \frac{d_b}{l_{db}}$ (2.52) For all FRP bars

where f_d is the design tensile strength of the reinforcement; k_1 is a top bar modification factor (= 1 when less than 300 mm of fresh concrete is cast below the bar and = 1.3 when more than 300 mm of fresh concrete is cast below the bar); f_{bod} is the design bond strength of concrete specified as $f_{bod} = 0.28\alpha_2 f_c'^{2/3}/1.3 \ \leq 3.2\ N/mm^2$. where α_2 is the modification factor for bond strength of CFRM (= 1 when bond strength of CFRM is equal to or greater than that of deformed steel bars); otherwise α_2 shall be decreased according to test

results. α_1 is a confinement modification factor (= 1 when $k_c \leq 1$; 0.9 when $1 < k_c \leq 1.5$; 0.8 when $1.5 < k_c \leq 2$; 0.7 when $2 < k_c \leq 2.5$ and 0.6 when $k_c > 2.5$); k_c is specified as $\left(= \frac{c}{d_b} + \frac{15A_t}{sd_b} + \frac{E_t}{E_s}\right)$; c is the smaller of the bottom clear cover of the main reinforcement or half of the clear space between the reinforcement being developed; A_t is the cross-sectional area of transverse reinforcement (mm^2); s is maximum spacing centre to centre of transverse bars within l_{db} (mm); E_t is Young's modulus of elasticity for the transverse reinforcement (MPa) and E_s is Young's modulus for steel (MPa). k_6 is a bar surface factor representing the ratio of the bond strength of FRP to that of steel rebar provided that both have the same cross section area, it should be less than 1, and = 0.8 if test or manufacturer data is absent; E_{frp} is the modulus of elasticity of FRP re-bars (MPa); d_{cs} is the smaller of the distance from the closest concrete surface to the centre of the bar or two-thirds of the centre to centre spacing of the bars (mm); f_{cr} is the flexural cracking strength of concrete (MPa); k_{tr} is a transverse reinforcement index specified as: $A_t f_{yt}/10.5sN$ where f_{yt} is the yield stress of the transverse reinforcement (MPa); N is the number of bars being developed along the potential plane of bond splitting and the expression ($d_{cs} + k_{tr}\, E_{frp}/E_s$) should be equal to or less than $2.5d_b$. k_2 is the concrete density factor (= 1.3 for structural low-density concrete, = 1.2 for structural semi-low-density concrete and = 1 for normal density concrete); k_3 is the bar size factor (= 0.8 for $A_b \leq 300$ mm^2 and = 1.0 for $A_b > 300$ mm^2); k_4 is the bar fibre factor (= 1.0 for CFRP and GFRP, and = 1.25 for AFRP); k_5 is the bar surface profile factor (= 1.0 for surface-roughened or sand-coated surfaces and braided surfaces, = 1.05 for spiral pattern and ribbed surfaces, and = 1.8 for

indented surfaces); k_m is a bar location modification factor (= 1 for $c_1 > 2d_b$ and $= (4\,d_b - c_1)/2d_b \quad for\ \ d_b \leq c_1 \leq 2d_b$ for bottom bars); (= 1.3 for top bars); and c_1 is a concrete cover, where f_{fr} is a required bar stress (MPa); f_f is the design stress in FRP tension reinforcement at the ultimate limit state (MPa); f_{FRPU} is the stress in the FRP tension reinforcement at the ultimate limit state (MPa); $\frac{C}{d_b}$ should not be taken as more than 3.5 so that the same equation can be used for either splitting or pull-out failure and α is a bar location factor.

The ACI-440.1R (2003) equation is the same as that proposed by Ehsani et al. (1996a) and Gao et al. (1998) for pull out controlled failure rather than concrete splitting, but the value of K_3 is different. Moreover, it was developed with an assumption of an upper limitation of the FRP bond stress of 4.63 MPa, while Ehsani et al. (1996a) and Gao et al. (1998) used a value of 4.93 MPa for the limit of the bond stress. A comparison among design codes is summarized in Table 2.5, to better understand the parameters that influence the bond strength considered in these design guidelines. The key factors, namely concrete strength, bar diameter, concrete cover and bar position, are considered in all of these codes. The bond strength for the bottom bars is higher than that for the top bars owing to bleeding of water and air trapped beneath the top bars (Tighiouart et al., 1998), therefore, the effect of the bar location on bond strength is acknowledged by a factor k_1 of 1.3 in Canadian and Japanese codes and a factor α of 1.5 in ACI 440.1R-15. Embedment length is only taken into account by ACI 440.1R-15. As mentioned in section 2.6.4, the bar surface is one of the main factors which affects bond strength, however, CAN/CSA-S6 (2014) and CAN/CSA-S806 (2012) only

considered this influence by suggesting the bar surface factor in their equations. Although each FRP type has different bond characteristics, all codes neglected the effect of fibre type on bond strength, except Canadian codes. Furthermore, confinement provided by transverse reinforcement (stirrups) along the developed and spliced reinforcing bars, that contributes in increasing bond strength, is considered by Japanese (JSCE) and Canadian (CSA-S6) codes, and it is ignored in other codes.

Table 2.5 - Main factors considered in determining bond strength by design codes

Model	Bar diameter	Concrete strength	Concrete cover	Bar surface	Bar location	Bonded length	Transverse reinforcement	Fibre type
JSCE 1977	✓	✓	✓	x	✓	x	✓	x
CSA-S806-12	✓	✓	✓	✓	✓	x	x	✓
CSA-S6-14	✓	✓	✓	✓	✓	x	✓	✓
ACI 440.1R-15	✓	✓	✓	x	✓	✓	x	x

2.11 Methods of bond test

Various test methods described in standards to measure bond strength are pull-out, hinged beam, end beam, notched beam and splice beam as shown in Figures 2.10 and 2.11. A pull-out test is a widely used method due to its simplicity and a low cost to construct and test. Pull-out tests were employed by several researchers to investigate the effect of the main parameters on bond behaviour of FRP re-bars embedded in concrete. In addition, they are useful to study bond stress – slip relationships and experimental data can be used to compare bond behaviours considering different parameters and materials. However, bond values obtained from pull-out tests are not accurate because the concrete surrounding the rebar is under compression due to a bearing plate, reducing the

cracking and therefore increasing the bond strength (Tighiouart et al., 1998). Thus, ACI-440.3R (2012) recommended to use a pull-out test for only comparative purposes to compare the effect of different parameters on bond strength, and not for establishing design bond values and development lengths for FRP bars in concrete. Very limited literature (Benmokrane et al., 1996, Tighiouart et al., 1998, Ovitigala and Issa, 2013, Xue et al., 2014) have used a hinged beam test to estimate bond strength of FRP bars in concrete, as they are more challenging to prepare and test. Despite this, beams are more realistic and representative of stress conditions in RC members in bending than pull-out specimens, because the concrete surrounding the bar is under tension in the beam test, resulting in cracking under low stress and thus decreasing the bond strength (Tighiouart et al., 1998). Details of the test methods are described in the following sections:

2.11.1 Pull-out test

One of the first set-ups was proposed by Rehm (1961) as illustrated in Figure 2.10 (a). This test arrangement has been adopted by many researchers with minor changes in order to eliminate its weak points. These relate to the friction developed between the concrete specimen and the bearing plate that provides additional confinement to the bonded area and can also assist the development of the arch-effect in the centre of the specimen during the test. For the above reasons, the RILEM/CEB/FIP standard pull-out test arrangement moved the bonded length of the bar away from the centre of the specimen and introduced a

rubber plate between the concrete block and the bearing plate to reduce the friction effects as demonstrated in Figure 2.10 (b).

Eight methods used to investigate bond behaviour of FRP bars embedded in concrete are detailed in Table 2.6. All methods utilize a cube specimen, but with different sizes. A cube size of 150 x 150 x 150 mm is applied by ASTM-C234 (2000), CAN/CSA-S806 (2012) and Losberg (1963), while ACI-440.3R (2012) used 200 x 200 x 200 mm. BS/ISO-10406-1 (2013) and JSCE-E539 (1995) employed 100*100*100 mm for $d_b < 17mm$, and 150*150*150 mm for $17mm \leq d_b \leq 30mm$. RILEM/CEB/FIP (1983) and BG50152 (1992) recommended using dimensions of $10d_b$*$10d_b$*$10d_b$. The embedment length is four times the bar diameter according to CAN/CSA-S806 (2012), BS/ISO-10406-1 (2013) and JSCE-E539 (1995), whereas ACI-440.3R (2012), RILEM/CEB/FIP (1983) and BG50152 (1992) utilized five times the bar diameter. The embedment length of the reinforcing bar changes from $2d_b$ to $10d_b$ according to Losberg (1963) test. All methods used one plastic sleeve at the loaded end except Losberg (1963), which used two plastic sleeves at the unloaded and loaded ends to reduce the effect of area close to the bearing plate (Okelo and Yuan, 2005) and to equalize the stress from the loading plate on the loaded end side (CAN/CSA-S806, 2012). ASTM-C234 (2000) did not use plastic sleeves, therefore the embedment length is to be equal to 150 mm the same as the size of the cube specimen. CAN/CSA-S806 (2012) stated that the increase of the cube size led to avoid splitting of the concrete and the bonded length can be increased, if this length ($4d_b$) is thought to misrepresent the bonding properties of the FRP rebar. In a pull-out test, a bar incorporated in a concrete cube along a defined length is strained at one end by

a tensile load, and the other end remains without stress. The tensile load and the relative displacement between the concrete and the bar will be measured by a load cell and linear variable displacement transducers (LVDTs). The tensile force will be increased up to a bond failure.

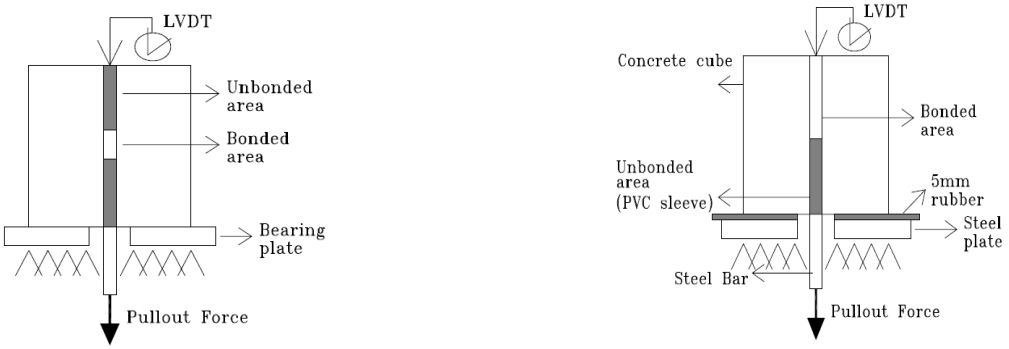

(a) Rehm (1961) **(b) RILEM/CEB/FIP (1983)**

Figure 2.10 - Typical pull-out tests (Achillides, 1998)

Table 2.6 - A comparison among pull-out test methods according to different codes

Code	Specimen shape	Specimen size (mm)	No. of embedded bars	Bar position	No. of plastic sleeves at the ends	Bonded length
ACI-440.3R (2012)	Cube	200*200*200	One	Vertical	One	$5d_b$
ASTM-C234 (2000)	Cube	150*150*150	One	Vertical	N/A	150 mm
CAN/CSA-S806 (2012)	Cube	150*150*150	One	Vertical	One	$4d_b$
BS/ISO-10406-1 (2013)	Cube	100*100*100 For d_b<17mm	One	Vertical	One	$4d_b$
		150*150*150 For 17 mm ≤d_b≤ 30 mm				
RILEM/CEB/FIP (1983)	cube	$10d_b$*$10d_b$*$10d_b$ Min: 200mm	One	Vertical	One	$5d_b$
Losberg (1963)	Cube	150*150*150	One	Vertical	Two	2/4/4.5/5.5/6 /8/$10d_b$
BG50152 (1992)	Cube	$10d_b$*$10d_b$*$10d_b$	One	Vertical	one	$5d_b$
JSCE-E539 (1995)	Cube	100*100*100 For d_b<17mm	One	Vertical	One	$4d_b$
		150*150*150 For 17 mm ≤ d_b≤ 30 mm				

2.11.2 Beam test

Figure 2.11 presents different types of beams which offer various bond strength measurements of FRP reinforcing bars embedded in concrete (ACI-440.3R, 2012, ACI-408R, 2003). The current research will focus on a hinged beam test to measure bond properties of FRP bars. The RILEM/CEB/FIP standard only describes the arrangement for the hinged beam test, which is shown in Figure 2.12. Firstly, this approach was developed to investigate bond behaviour of steel bars and then, utilized also for FRP re-bars. The beam specimen consists of two parallelepiped reinforced concrete blocks, interconnected at the bottom by the bar whose bond is to be investigated and at the top by a steel hinge. It is loaded in simple flexure by two forces of equal magnitude which are disposed symmetrically with regard to the mid span section of the beam. During loading, which should be continued until a complete bond failure occurs in each of the two half-beams, the slip of the two ends of the bar should be measured. Thus, each test provides two results, i.e. two curves representing the slip of the bar as a function of the load applied to the beam. The hinged beam dimensions depend on the bar diameter as illustrated in Figure 2.12.

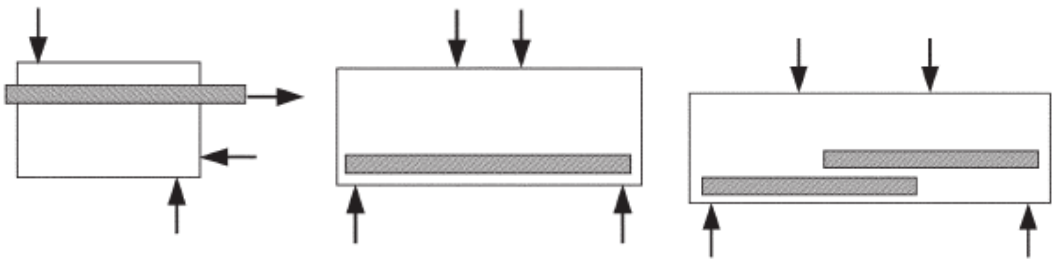

(a) **(b)** **(c)**

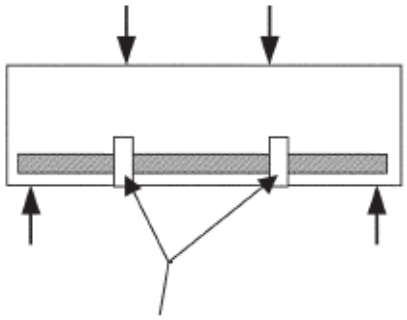

Crack initiators or notches

(d)

Figure 2.11 - Types of test methods for different bond values of FRP reinforcement in concrete (a) beam-end specimen; (b) simple beam specimen; (c) splice specimen; (d) notched beam specimen (ACI-440.3R, 2012)

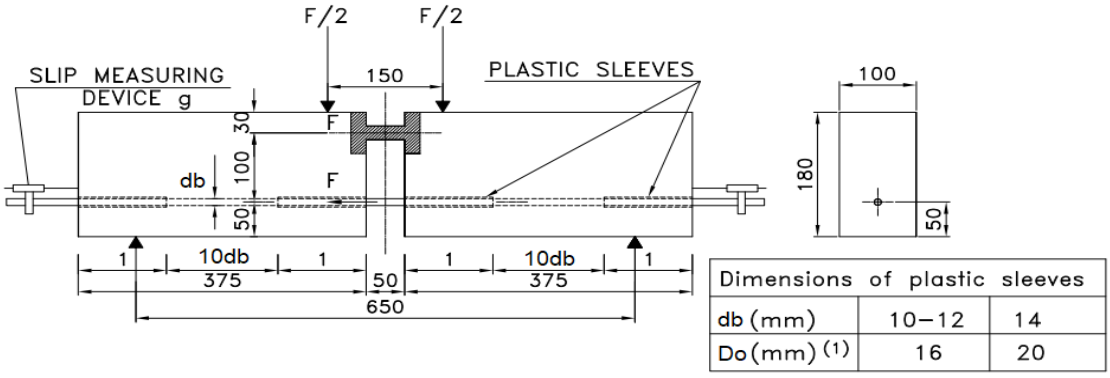

Dimensions of plastic sleeves		
db (mm)	10–12	14
Do(mm) (1)	16	20

Type (I)

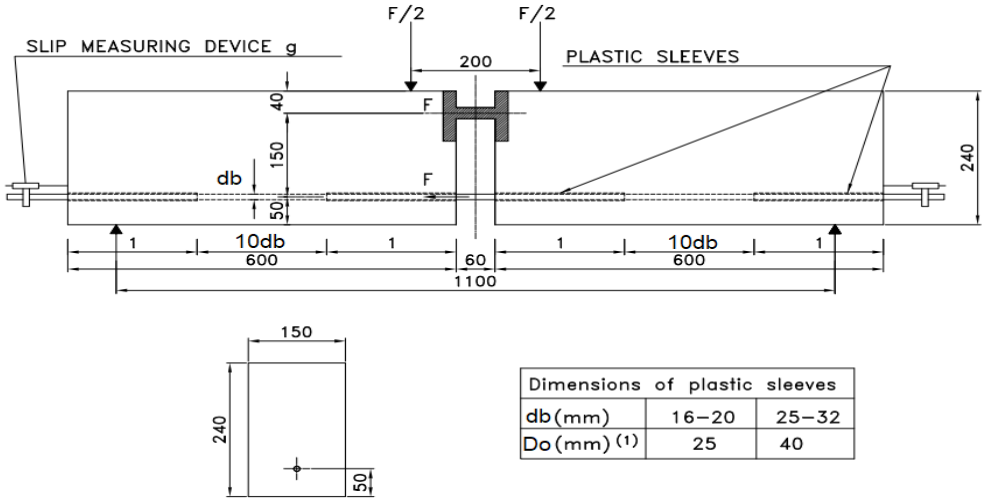

Dimensions of plastic sleeves		
db(mm)	16–20	25–32
Do(mm) (1)	25	40

Type (II)

Figure 2.12 - RC5 Bond test for reinforcement: Beam test - type I and II (RILEM/CEB/FIP, 1982)

2.12 Bond strength obtained from pull-out and hinged beam tests

A few sources published in the literature (Chan, 2012, Ametrano et al., 2011, de Almeida Filho et al., 2008, Tighiouart et al., 1998, Soretz, 1972) have conducted a study for comparing a pull-out test with a hinged beam test. Table 2.7 shows the main parameters considered by each author to perform the experimental investigation. It was reported that the bond strengths measured by the pull-out tests were lower than those measured by the hinged beam tests (Ametrano et al., 2011, Chan, 2012). This might be attributed to unconfined concrete in pull-out specimens, while hinged beams had a large amount of internal reinforcement which in turn provided confinement, thus increasing the bond strength (Ametrano et al., 2011). However, Tighiouart et al. (1998) found that the ratio of the bond strength in pull-out specimen to that in hinged beam changed from 1.05 to 1.84, depending on bar diameter. This was because of the concrete surrounding the bar being subjected to compressive stresses in the pull-out test, thus reducing the cracking and increasing the bond strength. On the other hand, it was subjected to tensile stresses in the hinged beam test and this led to cracking, which in turn decreased the bond strength (Tighiouart et al., 1998). In addition, the results obtained by Soretz (1972) revealed that the bond strengths for pull-out specimens were higher than those for hinged beams. The experimental results (bond stress – slip curves and bond strengths) measured by pull-out tests were similar to those measured by hinged beam tests (de Almeida Filho et al., 2008). The result obtained by Tighiouart et al. (1998) disagrees with that obtained by Ametrano et al. (2011) and Chan (2012), although Tighiouart et al. (1998) also used transverse reinforcement in their hinged beams. This means that the reason provided by

Ametrano et al. (2011) is not enough justified. The behaviour of hinged beams is not similar to normal beams, in other words there are no flexural cracks to reduce the bond strength as reported by Tighiouart et al. (1998). Therefore, this study needs to be investigated. None of the above publications has investigated pull-out specimens having the same size as one concrete block of hinged beam. Moreover, the surface of the GFRP bar has not been investigated as a parameter in the previous studies and no one tested hinged beams without transverse reinforcement to cancel the effect of confinement on bond strength and to become unconfined as pull-out specimens. The comparison between pull-out and hinged beam tests has not been carried out using GFRP bars embedded in high strength concrete.

Table 2.7 - Factors considered in a comparison of pull-out test with hinged beam test

Reference	Bar diameter	Embedment length	Concrete cover	Surface treatment	Concrete strength	Bar type	Concrete used
Soretz (1972)	✓	-	-	-	-	steel	NSC
Tighiouart et al. (1998)	✓	-	-	-	-	GFRP	NSC
de Almeida Filho et al. (2008)	✓	-	-	-	✓	steel	NSC
Ametrano et al. (2011)	✓	✓	-	-	-	GFRP	HP/UHPC
Chan (2012)	-	-	-	✓	-	steel	HSC

Note: NSC is normal strength concrete, HSC is high strength concrete, HPC is high performance concrete and UHPC is ultra-high-performance concrete.

2.13 Numerical investigations on bond behaviour of reinforcing bars

2.13.1 Finite element analysis (FEA)

The slip at the interface between the concrete and the bar occurs due to loss of bond. Therefore, the real bond behaviour at the interface should be modelled using a bond stress - slip response to simulate the structural behaviour of the composite structures, and not be considered as a perfect

bond. Connector elements were employed by Gooranorimi et al. (2017) to define the bond action between the concrete and the GFRP bar in pull-out specimens for predicting the load - slip response and failure mode. Tekle et al. (2016), Tekle et al. (2017a) and Tekle et al. (2017b) also used a three-dimensional finite element analysis to model pull-out specimens, end beams and splice beams by applying cohesive behaviour to simulate the bond interaction between GFRP bars and surrounding concrete in order to investigate the distribution of the tensile and bond stresses along the embedment length. In addition, Henriques et al. (2013) implemented a numerical study to simulate composite beam to reinforced concrete wall joints using a three-dimensional finite element model and they defined the bond interaction between the wall and slab by a cohesive behaviour. The numerical results gave a good agreement with the experimental results. Thus, it was reported that cohesive model highlighted its accuracy to simulate the composite behaviour of reinforced concrete members. Moreover, nonlinear springs were employed to model the bond behaviour of FRP bars to concrete in pull-out specimens (Achillides, 1998) . The numerical results (the load – slip curves and normal and bond stress distributions along the embedment length) showed a reasonable agreement with the experimental results. Furthermore, Pepe et al. (2013) used interface finite elements to simulate the bond behaviour between GFRP bars and steel fibre-reinforced self-compacting concrete in hinged beams. The results revealed that the predicted load – slip responses were very close to the experimental ones. From the literature, cohesive behaviour is preferable to be used rather than connector elements for investigating the contact shear stresses at the interface. Connector

elements link between two nodes, and not two surfaces like the cohesive behaviour, and therefore the interface stresses are not shown. Up to date, no numerical study has been conducted to predict the tensile force acting on the bar in a hinged beam.

2.13.2 Artificial neural networks (ANNs)

Over the last two decades, artificial neural network (ANN) has become popular and has been employed by many researchers for a variety of engineering applications. This section will focus on using ANN to predict the bond strength of reinforcement to concrete. Two ANN models with six and two inputs were developed by Dahou et al. (2009) to predict the bond strength of steel re-bars embedded in concrete based on a pull-out test database, and the results showed that the proposed models exhibited good prediction ability. In addition, Abdalla et al. (2011) investigated the feasibility of applying ANN to predict the ultimate bond strength between FRP plates and concrete prisms. Their proposed model showed a good predictive performance. Golafshani et al. (2015) also modelled the bond strength of GFRP bars in concrete using ANN based on notched, hinged, splice and inverted beam data. The developed model was confirmed to be more reliable than the model proposed using multi-linear regression analysis. Moreover. Gooranorimi et al. (2017) developed the ANN model to predict the bond strength of spliced steel bars in concrete. The results revealed that the proposed model gave a good prediction and generalization capacity with fewer errors. Furthermore, Mashrei et al. (2013) used the ANN to predict the bond strength of FRP plates to concrete prisms. The results illustrated that the developed ANN model has better agreement with test results than those from existing analytical models. From the literature,

the prediction of bond strength of helical wrapped and sand coated GFRP bars in concrete using ANN has not been implemented based on pull-out test data. No study has examined the effect of GFRP bar surface on bond strength using the developed ANN model, except Golafshani et al. (2015).

2.14 Conclusions

An overview of past and recent research on bond behaviour of FRP reinforcing bars embedded in concrete is presented in this chapter. The main attention is given to the bond behaviour of GFRP bars in conventional concrete because this is the main subject in this thesis. From the literature review presented above, the following conclusions can be drawn:

- The majority of the previous experimental studies concentrated on investigating bond behaviour of FRP bars in normal strength concrete using a pull-out test.
- Little research has been conducted to investigate the bond behaviour of GFRP bars in high strength concrete using a pull-out test, but no study has been carried out using a hinged beam test.
- There are several parameters controlling the bond strength of FRP re-bars in concrete. The most important ones are bar diameter, embedment length, concrete compressive strength, surface configuration and bar position.
- The bar diameter and embedment length are inversely proportional to the bond strength of FRP bars in concrete. The concrete compressive strength is directly proportional to the bond strength of FRP bars in concrete.

- The bond strength for bottom bars is higher than that for top bars due to bleeding of water and air trapped beneath the top bars.
- The effect of bar position on bond strength has been investigated using pull-out and spliced beam tests, but it has not been studied using a hinged beam test. Subsequently, the bar position needs to be investigated.
- Analytical models were developed based on experimental results to predict the bond stress - slip behaviour of FRP reinforcing bars. In addition, design codes and some researchers proposed equations to evaluate the bond strength and development length of FRP re-bars.
- The key factors considered in all codes to predict the bond strength are concrete strength, bar diameter, concrete cover and bar position. However, embedment length is only taken into account by ACI 440.1R-15. Also, Canadian codes only acknowledge the effect of the bar surface on bond strength.
- Very limited research work has been implemented to compare bond strengths obtained from hinged beams with those obtained from pull-out specimens, and the results obtained were different from author to other. Therefore, this discrepancy needs to be investigated. In addition, this comparison has not been conducted on GFRP bars in the case of high strength concrete.
- Finite element analysis was done to better understand the bond behaviour and to investigate the distribution of tensile and bond stresses along the embedment length. However, FEA has not been used to estimate the tensile force acting on the bar in hinged beam.

- It is concluded that artificial neural network (ANN) is capable of providing with results close to real-life results. Therefore, ANN is required to predict the bond strength of GFRP bars in concrete based on pull-out test data.

Chapter 3

Experimental program

3.1 Introduction

To achieve the objectives of this research, an experimental program has been conducted to investigate the bond behaviour and failure mode of high strength concrete (HSC) specimens reinforced with glass fiber reinforced polymer (GFRP) bars using pull-out test and hinged beam test. Test parameters included bar diameter, embedment length and surface configuration, as well as bar position examined using hinged beam method only. The effect of concrete strength on bond strength was not studied in the current experimental research as it has been extensively studied in the literature as well as due to the large number of parameters covered in this investigation. A detailed description of the experimental program including test specimens, material properties, specimen preparation, and experimental set – up and testing procedure is presented in this chapter. Test results will be presented and discussed in chapters 4 and 5 for pull-out specimens and hinged beams, respectively.

3.2 Study parameters

Some parameters, such as bar diameter and embedment length, have been widely studied and their effect on bond behaviour is well known, but limited research studies have investigated their effect on bond strength in the case of high strength concrete. In addition, not many studies included bar surface and bar position, therefore they still need to be investigated. Thus, the current study included the following parameters: bar diameter, embedment length and

surface properties to investigate the bond behaviour of GFRP bars using pull-out and hinged beam tests. Also, bar position was only investigated in hinged beam specimens.

Another objective of this research is to compare the experimental results (bond strength, bond stress-slip curve and bond failure) obtained from a pull-out test with those obtained from a hinged beam test. To conduct this study, several parameters that influence bond behaviour need to be investigated and analysed to know the effect of each parameter on the relationship between pull-out test and hinged beam test. Again, these parameters were diameter, embedment length and surface configuration of GFRP bars, as well as the size of a pull-out specimen.

3.3 Test specimens

3.3.1 Pull-out specimens

The test specimens consisted of eighty-four cubes and eight prisms. All pull-out specimens were reinforced with GFRP re-bars, except twelve concrete cubes reinforced with 16 mm steel re-bars as control specimens. The geometrical dimensions of the pull-out cube were 200 x 200 x 200 mm according to ACI-440.3R (2012) as shown in Figure 3.1(a), while the size of the prism as presented in Figure 3.1(b) was 375 x 180 x 100 mm, the same dimensions as those of one concrete block of the (type I) hinged beam described in section 3.3.2. The main parameters investigated in pull-out cubes were bar diameter (9.5 mm, 12.7 mm and 15.9 mm for GFRP bar and 16 mm for steel bar) and embedment length (2.5, 5, 7.5 and 10 times bar diameter). Whilst in the pull-out prisms, bar diameter (9.5 mm and 12.7 mm) and

embedment length (5 and 10 times bar diameter) only were tested with the aim of comparing with (type I) hinged beams detailed in chapter 5. Surface configuration (sand coating and helical wrapping with a slight sand coating) was examined in both pull-out types. The bar location in the concrete cube was centric, while in the concrete prism was eccentric. The influence of these factors on bond strength were analysed and discussed to deeply understand the bond behaviour between GFRP re-bars and concrete. A general overview of the test program of pull-out specimens is shown in Figure 3.3.

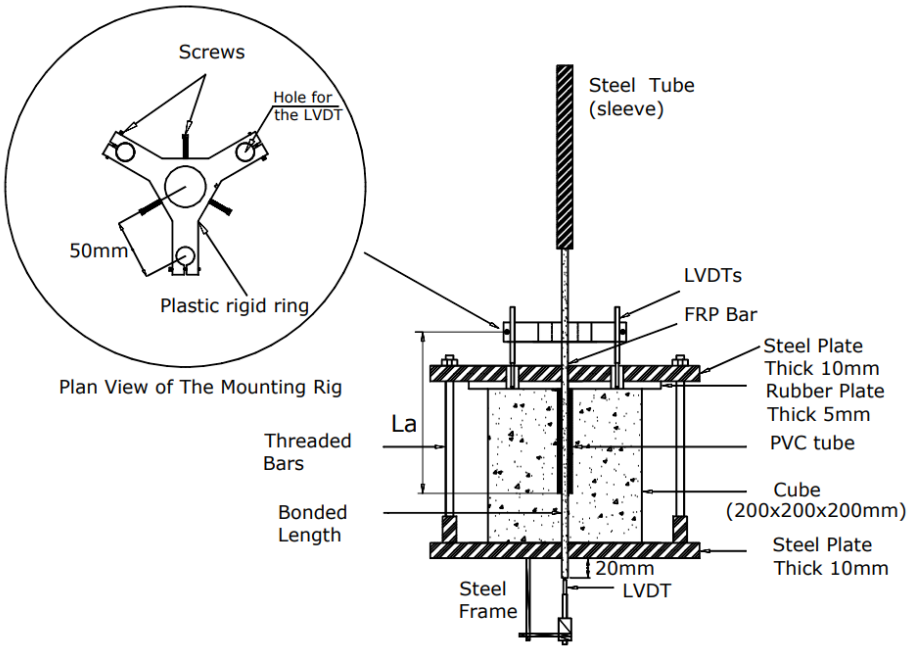

(a) Cube

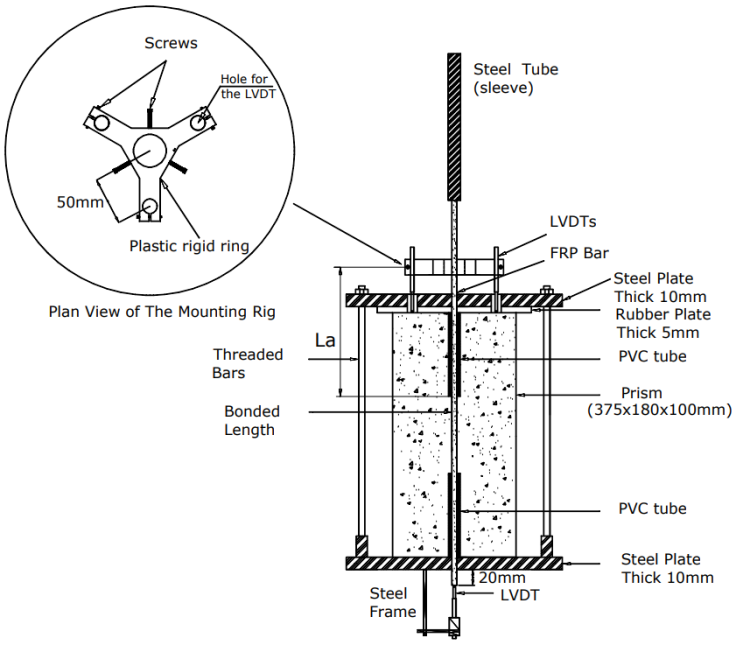

(b) Prism

Figure 3.1 - The details of pull-out specimens

3.3.2 Hinged beam specimens

Twenty-four hinged beams reinforced with GFRP bars and four hinged beams reinforced with steel re-bars as control specimens were tested. The geometrical details of hinged beams are given in Figure 3.2 according to RILEM specification. Hinged beams were classified into two types based on bar diameter: (type I) hinged beams were used for bar diameters less than 16mm, and (type II) hinged beams were used for bar diameters equal to or more than 16mm. The presence of confining reinforcement did not appear to influence the bond strength as reported by ACI-440.1R (2015). Therefore, the current study has aimed to cast the hinged beams without transverse reinforcement, similar to the specimens of Xue et al. (2014) and Mazaheripour et al. (2013). A general overview of the experimental program of hinged beams is described in Figure 3.3. The test specimens for each bar type were classified

into two series: (a) specimens that were cast with the bottom bar position as shown in Figure 3.2, (b) specimens that were cast with the top bar in the same position as that in the sketch of the hinged beam presented in Figure 3.2, but inverted. The parameters investigated were bar diameter (9.5, 12.7 and 15.9 mm for GFRP and 16 mm for steel), embedment length (five and ten times bar diameter), bar position (bottom and top) and surface configuration (helical wrapping with a slight sand coating and sand coating). These parameters need to be investigated to better understand the bond behaviour of GFRP bars embedded in high strength concrete.

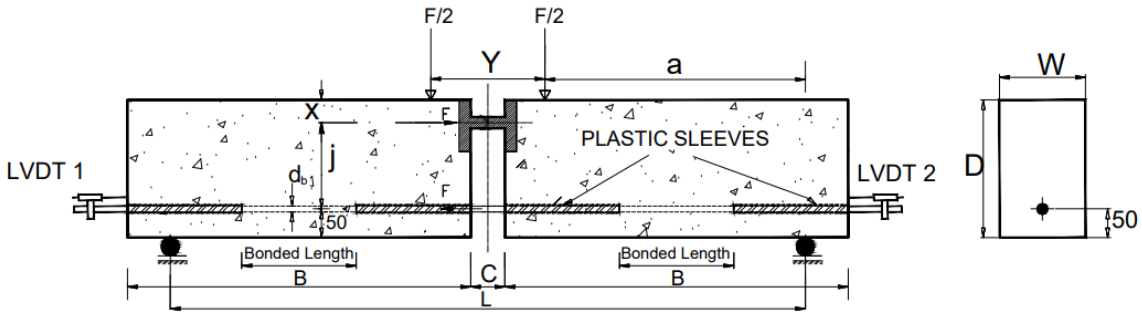

Beam No.	d_b	W	D	L	B	C	X	Y	j
Type I	10-14	100	180	650	375	50	30	150	100
Type II	16-32	150	240	1100	600	60	40	200	150

Figure 3.2 - Hinged beam test arrangement (all dimensions in mm)

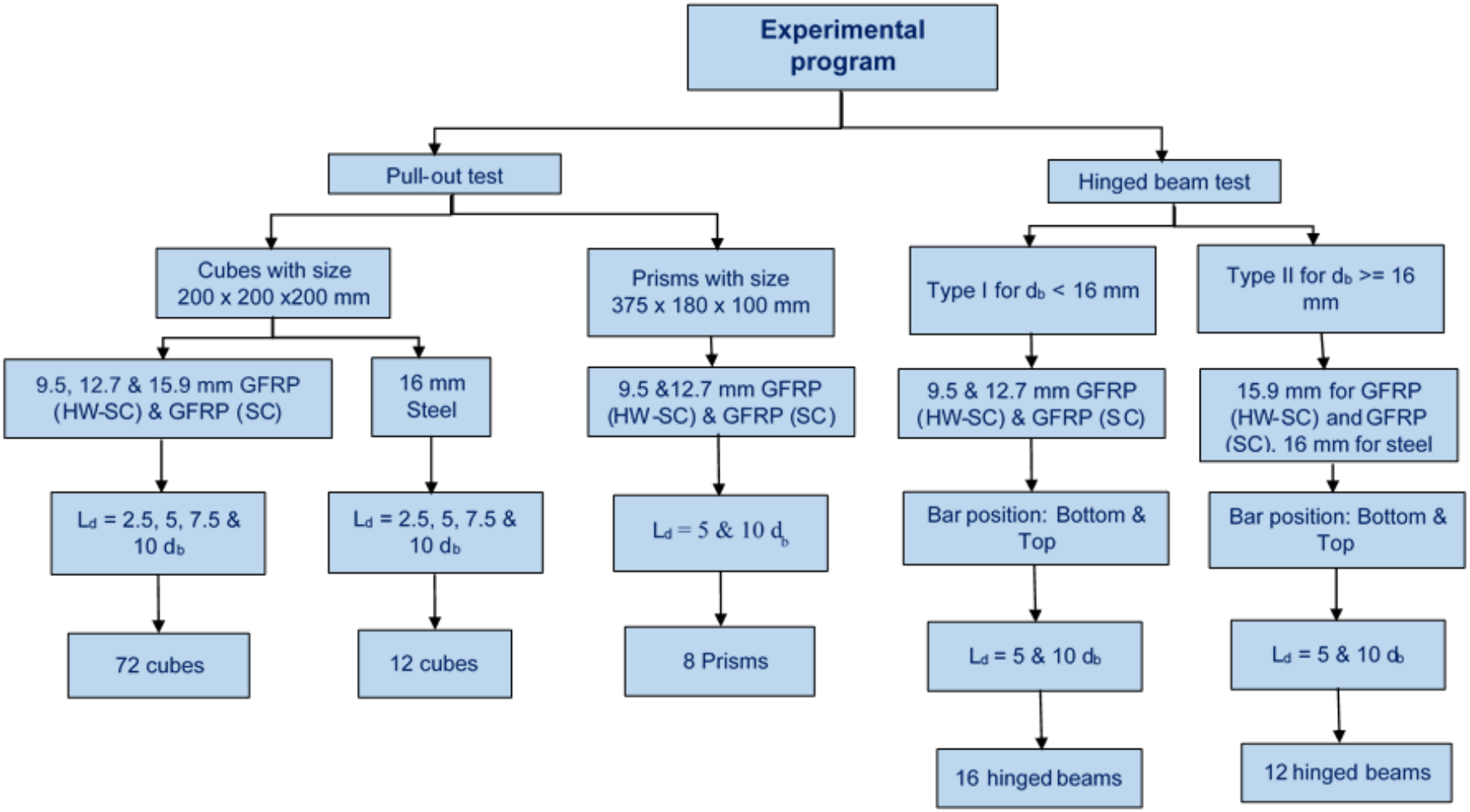

Figure 3.3 - General overview of the experimental work

3.4 Material properties

3.4.1 Concrete

All specimens were constructed using ready – mixed concrete with the maximum aggregate size of 10 mm. The specimens reinforced with GFRP (HW-SC) bars were cast using the first batch (C1), whereas those reinforced with GFRP (SC) bars were cast using the second batch (C2). Cylinder (150 x 300 mm) and cube (100 x 100 x 100 mm) specimens were cast and cured under the same condition as the test specimens. Cylinders and cubes were tested immediately after testing specimens to provide the splitting tensile strength and cube compressive strengths of concrete, as illustrated in Figure 3.4. This study aimed to cast all tested specimens reinforced with both GFRP types using concrete having the same mixture proportion, however, the second Ready-mix had different material proportions compared to the first concrete mixture. As a result, the variation in the average cube compressive strength of concrete between C1 and C2 is around 20%. The average cube compressive strength of concrete C1 and C2 obtained from testing four cubes were in the range of 97.38 MPa to 102.36 MPa with an average of 100.17 MPa and a coefficient of variation (COV) of 2.4% and 77.47 MPa to 83.07 MPa with an average of 79.24 MPa and a COV of 2.9%, respectively. The average splitting tensile strength of concrete C1 and C2 obtained from testing three cylinders varied from 4.13 MPa to 4.71 MPa with an average of 4.34 MPa and a COV of 7.3% and changed from 3.24 MPa to 3.67 MPa with an average of 3.46 MPa and a COV of 6.2%, respectively. Cylinders and cubes were tested on the same day as the specimen test.

Figure 3.4 - Concrete cubes and cylinders for compressive and tensile strength test

3.4.2 FRP and steel reinforcement

Two types of glass fibre reinforced polymer (GFRP) bars and conventional steel bars were used in this study. GFRP bars - Aslan 100 having a helically wrapped with slightly sand coated surface were manufactured by Hughes brothers, Inc. USA and acquired from Fortius, Belgium. GFRP bars having a sand coated surface were manufactured by V-RODS Pultrall Inc., Canada. The surface configuration of both GFRP types are shown in Figure 3.5. GFRP bars were made of continuous longitudinal fibres impregnated in vinylester resin: the minimum content of continuous ECR-glass fibres was 75% (per unit weight) and the maximum content of vinylester resin was 25% for GFRP (type A), and the content of continuous E-glass fibres 80% (per unit weight) and vinylester resin 20% for GFRP (type B). Both GFRP bars treated their surfaces to improve their bond with the surrounding concrete. The outer diameters were measured in the laboratory

according to ACI 440.3R. The nominal and measured diameters are presented in Table 3.1. The tensile strength and elastic of modulus of GFRP and steel bars were determined in the laboratory according to specifications ASTM D7205/D7205M and ASTM A706/A706M, respectively. Three samples were prepared for each bar diameter with the total length of 1240 mm as indicated in Figure 3.6 (a). Before testing GFRP bar samples, the two ends of each GFRP bar were anchored by a steel tube to prevent the premature failure of the GFRP bar at the steel jaws due to the lower transverse strength of the GFRP bar. The outside diameter of the steel tube was 25 mm for 9.5 mm bar diameter and 35 mm for 12.7 and 15.9 mm bar diameters. The thickness and length of steel tube was 3 mm and 300 mm for all bar diameters. The gap between GFRP bar and steel tube was filled by expansive grout named Dynacem, as illustrated in Figure 3.6 (b). An extensometer was installed at the centre of each bar sample to measure the corresponding longitudinal strain. The samples were tested using a 500 kN – capacity testing machine as shown in Figure 3.6 (c). The rupture failure of GFRP (type A) and GFRP (type B) are described in Figure 3.7. The mechanical properties of GFRP and steel bars are summarized in Table 3.2. In addition, the stress – strain characteristics of both GFRP types and steel bars are shown in Figure 3.8.

Table 3.1 - Nominal and Actual Diameters of GFRP Bars

	V-Rods Pultrall			Aslan 100		
Bar size	3#	4#	5#	3#	4#	5#
Nominal diameter (mm) [a]	9.5	12.7	15.9	10	13	16
Measured diameter (mm) [b]	10.4	13.33	16.74	10.76	13.44	16.76

[a]Reported by the manufacturer.
[b]Measured in the laboratory (The values are the average of five samples).

Table 3.2 - Mechanical properties of GFRP and steel bars

	V-Rods Pultrall			Aslan 100			steel
Bar size	3#	4#	5#	3#	4#	5#	5#
Tensile strength (MPa)	1227.3 (1224.6)	1375 (1175.4)	1373.7 (1210.3)	827 (940.2)	758 (797)	724 (867.9)	672 (666)
Ultimate strain (%)	2.4	2.7	2.7	1.79	1.64	1.57	-
Elastic of modulus (GPa)	50 (50.98)	51 (51.57)	51 (52.15)	46 (51.7)	46 (49.7)	46 (46.9)	200 (199)
Yielding strength (MPa)	-	-	-	-	-	-	582 (569)
Resin type	vinylester			vinylester			-

The values between brackets measured in the laboratory are the average of three samples, whereas other values are provided by the manufacturer. (-): Not applicable.

(a) GFRP (type A) **(b) GFRP (type B)**

Figure 3.5 - Surface configuration of (a) helically wrapped with slightly sand coated GFRP bars and (b) sand – coated GFRP bars

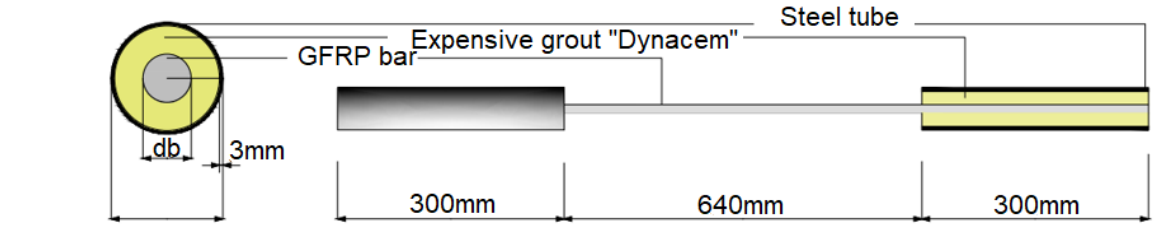

25mm for db=9.5mm
35mm for db=12.7mm and 15.9mm

(a)

(b) **(c)**

Figure 3.6 - (a) Details of the test specimens (b) Specimens after filling with expansive grout and (c) Tensile test set-up

(a) **(b)**

Figure 3.7 - Rupture failure of (a) GFRP (HW-SC) bar and (b) GFRP (SC) bar

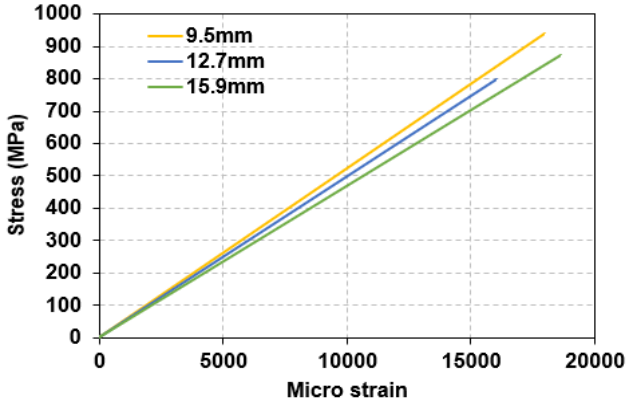

(a) GFRP (HW-SC) bars

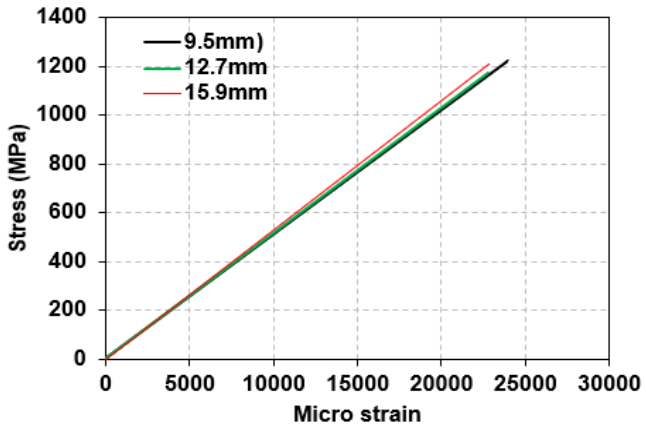

(b) FRP (SC) bars

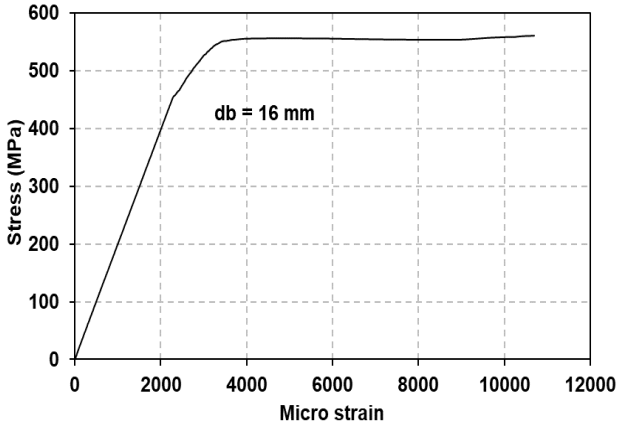

(c) Steel bar

Figure 3.8 - Stress – strain curves for GFRP and steel bars

3.5 Preparation and test set-up of pull-out specimens

3.5.1 Bar preparation

The bars were cut to 650 mm for pull-out cubes and 1500 mm for pull-out prisms and marked so that the different embedment lengths were 2.5, 5, 7.5 and 10 times the bar diameter for cube specimens and 5 and 10 times the bar diameter for prism specimens. The remaining parts of the embedment length were sheathed

with a PVC tube in order to prevent bonding between the FRP bar and the concrete, also to prevent the effect of compressive stresses produced from the loading plate on the bond behaviour of the bar as shown in Figure 3.9. The un-bonded length located at the upper zone of cube is illustrated in Figure 3.9 (a), whereas in Figure 3.9 (b), two un-bonded lengths were at the two ends of the prism as the same as hinged beam. The transverse strength of FRP bars is very low, therefore the tensile load cannot be applied directly to FRP bars as the steel bars. As a result, the loaded end of FRP bar should be anchored using a steel tube as detailed in specification ASTM D7205M to avoid the damage of bar at the gripping zone and the other end of bar acts as the unloaded end.

3.5.2 Mould preparation, casting and curing procedure

The wooden moulds with sizes of (200x200x200mm) and (375x180x100mm) were made to cast concrete cubes and prisms, respectively. The FRP bars were positioned vertically and centrally in the moulds and passed through a circle hole at the bottom and top of the moulds to hold the bars as shown in Figure 3.9 (a). The bar was placed in a horizontal and eccentric position in pull-out prisms as demonstrated in Figure 3.9 (b). The concrete was placed in three layers and each layer was vibrated using the means of hammer vibrators as shown in Figure 3.10 (a and b). The casting direction was parallel to the bar in cubes, while in prisms, the casting direction was perpendicular to the bar. Compacting and smoothing were performed to eliminate voids and minimize geometric irregularities as shown in Figure 3.10 (c). Before casting, the inner sides of moulds were covered by a thin film of oil to ease demoulding of the specimens. After casting, all specimens

were covered with a polythene sheet to prevent evaporation of water from unhardened concrete until demoulding. After one week of casting, the specimens were demoulded, marked, covered with a polythene sheet and stored in a temperature-controlled laboratory until testing as illustrated in Figure 3.10 (d and e).

(a) Cube mould **(b) Prism mould**

Figure 3.9 - Position of FRP bar in the mould

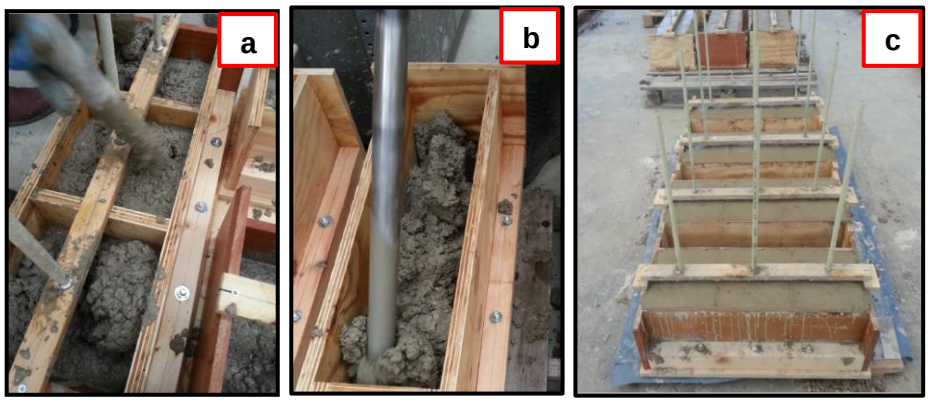

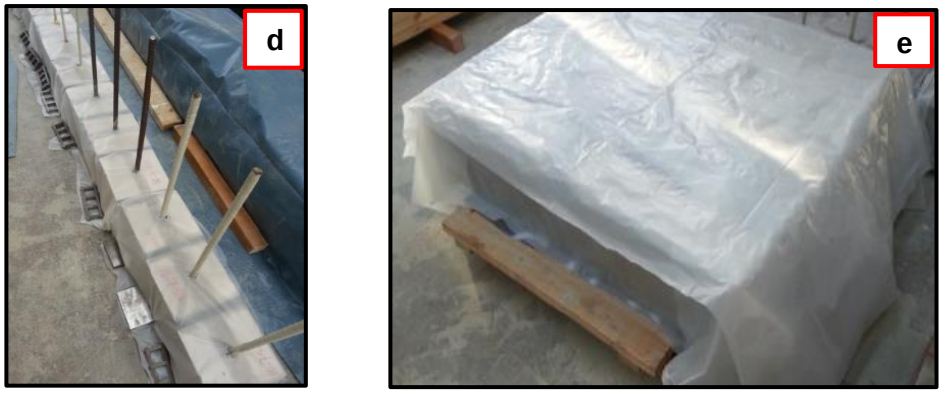

Figure 3.10 - Casting, levelling and covering cubes and prisms

3.5.3 Experimental set-up and testing procedure

The pullout test arrangement is shown in Figure 3.11. The specimen was placed in a specially made steel frame that was positioned in the testing machine. The loading steel frame consisted of three steel plates 10 mm in thickness. The bottom and the middle steel plates were connected to each other by four 20 mm rods at the corner. The top and middle steel plates were also connected with six 16 mm rods. All connection rods were from grade 8.8 steel. The top plate had a 40 mm diameter hole at its center allowing the FRP bar to pass through it. Also, three additional holes in a triangular arrangement were around the centric hole for linear variable displacement transducers (LVDTs). LVDTs were connected to the bar by a plastic rigid rig and touched the top surface of the specimen to measure the loaded end slip (accurate to ± 0.025 mm). Only one LVDT was attached to a small steel frame which was fixed to the bottom surface of the concrete specimen to measure the free end slip (accurate to ± 0.025 mm), where the unloaded end of the bar protruded by 20 mm to attached the LVDT. Small irregularities at the top surface of the specimen might result in accidental bending of the bar during

loading or movements caused by local crushing. Therefore, a 5-mm-thick rubber plate was introduced to secure the contact between the top surface of the concrete block and the steel bearing plate. The loading rate was changed for each 15 mm of head movement of the machine to be 0.02, 0.05 and 0.1 mm/sec, respectively. The reason for increasing the loading rate was to accelerate the test after the occurrence of pull-out failure. The displacement-control mode was selected to record the post-peak curve. The load capacity of the testing machine was beyond 500 kN which was more than adequate for the test purposes. Applied load and LVDT readings were automatically recorded using the data logging system.

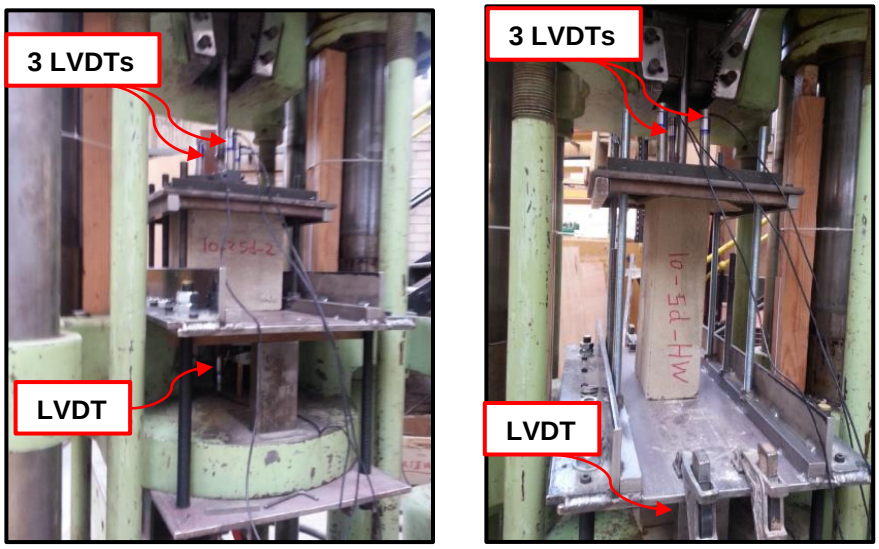

(a) Cube **(b) Prism**

Figure 3.11 - Pull-out test set-up

3.6 Preparation and test set-up of hinged beam specimens

3.6.1 Bar preparation

GFRP and steel bars were cut to 1500 mm lengths and marked so that the embedment lengths were five and ten times the bar diameter. The un-bonded length was covered by a PVC tube to prevent contact between the FRP bar and concrete. The extra length of the bar extended outside of concrete block to fix the linear variable displacement transducer (LVDT) during hinged beam testing to measure the free end slip on both sides.

3.6.2 Moulding, casting and curing procedure

The wooden moulds used to cast the hinged beams are shown in Figure 3.12 (a). The interior dimensions of the moulds were 100 x 180 x 800 mm for hinged beam (type I) and 150 x 240 x1260 mm for hinged beams (type II). Each mould was sectioned off into two sections for pouring concrete. Only one bar was placed horizontally and eccentrically in the mould with consideration of bar position (bottom and top). The concrete mix C1 was used to cast twelve specimens reinforced with GFRP (type A) and two steel reinforced concrete hinged beams having embedment length $5d_b$. Specimens reinforced with GFRP (type B) and those reinforced with steel bars having embedment length $10d_b$ were cast using the second batch C2. Before casting, the inner sides of the wooden moulds were covered by a thin film of oil to ease demoulding of the specimens. The concrete was placed in two layers and each layer was vibrated by using a poker vibrator as illustrated in Figure 3.12 (b). In Figure 3.12 (c), compacting and levelling were

required to reduce the voids and make the surface regular. After casting, all specimens were covered with a polythene sheet to prevent evaporation of water from unhardened concrete until demoulding. After two weeks, the specimens were demoulded, marked, covered with a polythene sheet and stored in the temperature-controlled lab until testing, as presented in Figure 3.12 (d). The space between two concrete blocks should be compatible with the measurement of the steel hinge that was placed at testing. In addition, this space was kept with a special piece of wood after demoulding the specimens to avoid any damage in the FRP bar until a test day.

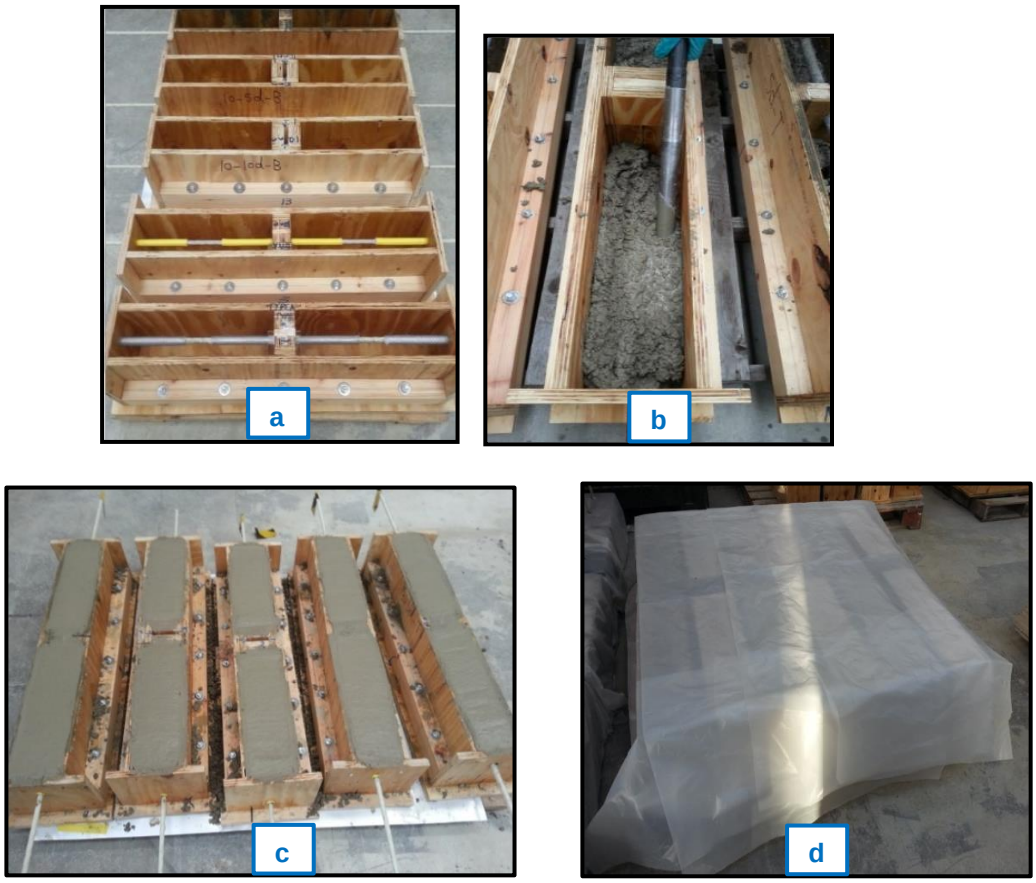

Figure 3.12 - (a) Wooden formwork, (b) casting, (c) levelling and (d) covering

3.6.3 Experimental set – up and testing procedure

The beam tests were conducted in accordance with the requirements of the RILEM specification. Specimens consisted of two rectangular concrete blocks joined at the top by a steel hinge as indicated in Figure 3.13 (c) and at the bottom by a reinforcing bar to investigate its bond with concrete. The hinged beam was resting on two roller bearings and subjected to two equal forces symmetrically on either side of a ball joint using a testing machine of 500 kN capacity as shown in Figure 3.13 (a). Linear variable displacement transducers (LVDTs) were attached to the extended part of the reinforcing bar and held against the concrete end surface to measure the unloaded end slips (the LVDT accuracy of ± 0.025 mm) as shown in Figure 3.13 (b). Applied load and LVDT readings were automatically recorded using a data logger. All specimens were tested under displacement control mode so that the post-peak behaviour recorded. The loading rate was 0.02 mm/sec and it was kept constant and continuous until complete failure. The hinged beam tests were carried out each day in order to avoid problems of variability in concrete strength. Each four (type I) hinged beams having the same embedment length were tested at the same day, while only two (type II) hinged beams with the same embedment length were tested at the same day because of long duration of large-scale testing.

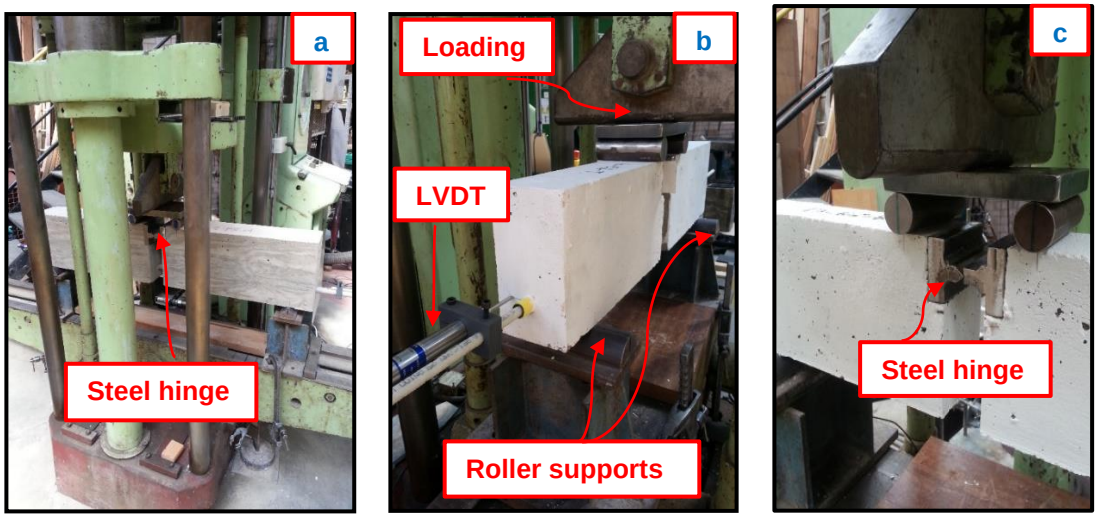

Figure 3.13 - Beam test set-up: (a) front view, (b) side view and (c) steel hinge

3.7 Bond strength measurement

3.7.1 Measuring bond strength in pull-out specimens

Experimental data obtained from pull-out tests were used to produce the bond stress – slip relationships. At each increment of loading rate, the load and slip were recorded by data logger. As known, the shear stress distribution along the bonded length is not constant, however, for simple behaviour, it is usually assumed to be uniformly distributed. Subsequently, the bond stress was calculated by dividing the applied load by the surface area of embedment length as shown in equation 3.1:

$$\tau = \frac{F}{\pi . d_b . l_e} \tag{3.1}$$

where τ is the bond stress (MPa), d_b is the nominal bar diameter (mm), l_e is the embedment length (mm) and F is the applied tensile load (N). The maximum bond

strength with the corresponding loaded and unloaded slips are shown in Tables 4.1 to 4.3.

Three LVDTs at the loaded end of bar were measured the loaded end slip including the elastic elongation of bar. The net loaded end slip (s_{le}) was calculated by subtracting the measured loaded end slip (s_{total}) from the bar extension (s_e) as illustrated in equations 3.2 and 3.3:

$$s_{le} = s_{total} - s_e \tag{3.2}$$

$$s_e = \frac{F.L_a}{A_b.E_{frp}} \tag{3.3}$$

where A_b is the cross-sectional area of bar (mm^2), L_a is the length from the LVDTs support point to the top surface of the bonded bar (mm) (see Figure 3.1) and E_{frp} is the elastic modulus of bar (MPa). The displacement at the unloaded end of bar was directly obtained from the slip measurement of the bottom LVDT.

3.7.2 Measuring bond strength in hinged beam specimens

The measurements obtained from the experimental investigation were used to develop the bond stress – slip response. The tensile force and the correlated tensile stress acting on the reinforcing bar can be determined by equilibrium between the applied loads and the corresponding reactions to the specimens as follows:

For type I specimens

$$T = \frac{\frac{F}{2}.a}{j} = 1.25\,.(F) \tag{3.4}$$

For type II specimens

$$T = \frac{\frac{F}{2}.a}{j} = 1.50\,.(F) \tag{3.5}$$

$$f_f = \frac{T}{A_b} \tag{3.6}$$

where T is the tensile load (N); $\frac{F}{2}$ is the applied load (N); a is the shear span (mm); j is the lever arm (mm); f_f is the tensile stress in the bar (MPa) and A_b is the cross-sectional area of bar (mm^2).

The average bond stress at each increment of the applied load was calculated by dividing the tensile load on the nominal surface area of the embedment length as presented in equation 3.7:

$$\tau = \frac{T}{\pi.d_b.l_e} \tag{3.7}$$

where τ is the bond stress (MPa), d_b is the nominal bar diameter (mm) and l_e is the embedment length (mm). The maximum bond stress (τ_{max}) with the corresponding free end slip (s_{ul}) are presented in Tables 5.1 and 5.2.

3.8 Conclusions

In this chapter, an experimental program is presented in comprehensive detail, including test pull-out specimens and hinged beams, material property tests of GFRP bar, steel bar and concrete, specimen preparation, test setup and testing procedure of pull-out specimens, as well as hinged beams, and finally measurement bond strength.

Chapter 4

Experimental results and discussions of pull-out specimens

4.1 Introduction

The preparation and test set-up of pull-out cubes and prisms were characterized in chapter 3. A detailed description of the observations and results of the pull-out specimens is presented in this chapter. These include the bond behaviour of GFRP (type A) and GFRP (type B) bars embedded in high strength concrete and failure modes. The influence of bar diameter, embedment length and surface configuration on bond behaviour is also demonstrated. Furthermore, the comparative analysis of experimental results was performed.

4.2 Experimental results

Test specimens, material properties, specimen preparation, test setup and testing procedure were described in chapter 3. The estimation of bond stress and the corresponding loaded and unloaded end slips were also detailed in chapter 3. Three identical cubes for each configuration were tested, whilst only one prism was cast for each configuration to investigate the bond behaviour. The bond stress - slip relationships were developed and plotted using measured data. The maximum bond strength (τ_{max}) with the corresponding loaded end slip (S_{le}) and unloaded end slip (S_{ul}), failure mode, the average compressive strength of four concrete cubes (f_{cu}) and average splitting tensile strength of three concrete cylinders (f_t) are presented for each specimen in Tables 4.1 to 4.3. The mean

values of bond strength (τ_{avg}) and the corresponding loaded end and free end slips ($s_{le,m}$ and $s_{ul,m}$) (obtained as an average of the results of three identical specimens) are also reported. The cube compressive strength of concrete C1 was in the range of 97.38 to 102.36 MPa with an average of 100.17 MPa and a coefficient of variation (COV) of 2.4%. As for concrete C2, it changed from 77.47 to 83.07 MPa with an average of 79.24 MPa and a COV of 2.9%. The average splitting tensile strength of concrete C1 and C2 obtained from testing three cylinders varied from 4.13 MPa to 4.71 MPa with an average of 4.34 MPa and a COV of 7.3% and changed from 3.24 MPa to 3.67 MPa with an average of 3.46 MPa and a COV of 6.2%, respectively. A small difference was observed among the bond strengths of the three identical cubes because of the non-homogenous nature of conventional concrete. The definition of specimen notation is described in Figure 4.1.

Table 4.1 - Experimental results of pull-out cubes reinforced with GFRP (HW-SC) bars in concrete C1

Specimen label	f_{cu} (MPa)	f_t (MPa)	F_{max} (kN)	τ_{max} (MPa)	S_{ul} (mm)	S_{le} (mm)	τ_{avg} (MPa)	$S_{ul,m}$ (mm)	$S_{le,m}$ (mm)	Failure Mode
A-9.5-2.5d-1	97.38	4.13	14.95	21.09	0.434	0.531				PO
A-9.5-2.5d-2	97.38	4.13	14.11	19.9	0.193	0.228	20.55	0.306	0.416	PO
A-9.5-2.5d-3	97.38	4.13	14.64	20.66	0.291	0.490				PO
A-9.5-5d-1	97.38	4.13	28.47	20.08	0.124	0.378				PO
A-9.5-5d-2	97.38	4.13	27.83	19.63	0.391	0.659	20.08	0.211	0.448	PO
A-9.5-5d-3	97.38	4.13	29.11	20.53	0.118	0.309				PO
A-9.5-7.5d-1	97.38	4.13	The testing machine suddenly stopped before debonding failure							
A-9.5-7.5d-2	97.38	4.13	41.98	19.73	0.104	1.127	19.76	0.106	0.898	PO
A-9.5-7.5d-3	97.38	4.13	42.1	19.79	0.108	0.67				PO
A-9.5-10d-1	97.38	4.13	55.7	19.65	0.411	1.486	19.27	0.621	1.620	PO

A-9.5-10d-2	97.38	4.13	55.3	19.49	0.659	1.477				PO
A-9.5-10d-3	97.38	4.13	53	18.68	0.793	1.897				PO
A-12.7-2.5d-1	97.72	4.19	28.26	22.3	0.407	0.436				PO
A-12.7-2.5d-2	97.72	4.19	23.01	18.16	0.75	0.80	19.79	0.486	0.547	PO
A-12.7-2.5d-3	97.72	4.19	23.95	18.90	0.301	0.405				PO
A-12.7-5d-1	97.72	4.19	41.15	16.24	6.94	7.03				PO
A-12.7-5d-2	97.72	4.19	40.61	16.02	5.99	6.151	16.13	6.439	6.542	PO
A-12.7-5d-3	97.72	4.19	40.86	16.13	6.387	6.446				PO
A-12.7-7.5d-1	97.72	4.19	61.60	16.20	0.506	1.338				PO
A-12.7-7.5d-2	97.72	4.19	59.04	15.53	0.736	1.139				PO
A-12.7-7.5d-3	97.72	4.19	69.90	18.39	0.797	1.169	16.71	0.679	1.215	PO
A-12.7-10d-1	97.72	4.19	77.47	15.28	0.468	1.545				PO
A-12.7-10d-2	97.72	4.19	79.94	15.77	0.744	1.798	16.05	0.728	1.612	PO
A-12.7-10d-3	97.72	4.19	86.70	17.10	0.974	1.493				PO
A-15.9-2.5d-1	101.68	4.71	42.13	21.21	0.458	0.634				PO
A-15.9-2.5d-2	101.68	4.71	38.55	19.42	0.330	0.414	19.42	0.363	0.496	PO
A-15.9-2.5d-3	101.68	4.71	35	17.62	0.302	0.440				PO
A-15.9-5d-1	101.68	4.71	70.65	17.78	0.388	1.049				PO
A-15.9-5d-2	101.68	4.71	79.04	19.90	0.826	1.111	18.70	0.60	1.097	PO
A-15.9-5d-3	101.68	4.71	73.20	18.42	0.586	1.131				PO
A-15.9-7.5d-1	102.36	4.71	97.21	16.32	0.439	1.170				PO
A-15.9-7.5d-2	102.36	4.71	98.51	16.53	0.858	1.234	16.32	0.533	1.208	PO
A-15.9-7.5d-3	102.36	4.71	96.02	16.11	0.304	1.220				PO
A-15.9-10d-1	102.36	4.71	115.5	14.55	0.410	1.561				PO
A-15.9-10d-2	102.36	4.71	116.9	14.72	0.656	1.619	14.82	0.660	1.628	PO
A-15.9-10d-3	102.36	4.71	120.7	15.20	0.915	1.706				PO
C-16-2.5d-1	97.38	4.13	76.2	37.88	0.939	1.481				PO
C-16-2.5d-2	97.38	4.13	76.85	38.21	0.593	1.408	38	0.766	1.444	PO

C-16-5d-1	101.7	4.71	120.5	29.94	-	1.924				PO
C-16-5d-2	101.7	4.71	101.4	25.20	1.534	1.804	27.56	1.534	1.864	PO
C-16-5d-3	101.7	4.71	110.8	27.55	-	1.864				PO

Table 4.2 - Experimental results of pull-out cubes reinforced with GFRP (SC) bars in concrete C2

Specimen label	f_{cu} (MPa)	f_t (MPa)	F_{max} (kN)	τ_{max} (MPa)	S_{ul} (mm)	S_{le} (mm)	τ_{avg} (MPa)	$S_{ul,m}$ (mm)	$S_{le,m}$ (mm)	Failure Mode
B-9.5-2.5d-1	83.07	3.67	20.49	28.91	0.203	0.272				PO
B-9.5-2.5d-2	83.07	3.67	21.55	30.38	0.193	0.225	28.91	0.237	0.287	PO
B-9.5-2.5d-3	83.07	3.67	19.45	27.44	0.315	0.365				PO
B-9.5-5d-1	77.68	3.24	37.20	26.23	0.138	0.581				PO
B-9.5-5d-2	77.68	3.24	37.57	26.49	0.200	0.776	25.51	0.139	0..57	PO
B-9.5-5d-3	77.68	3.24	33.78	23.82	0.081	0.377				PO
B-9.5-7.5d-1	77.68	3.24	49.96	23.48	0.203	0.695				PO
B-9.5-7.5d-2	77.68	3.24	45.94	21.59	0.213	0.726	22.15	0.187	0.716	PO
B-9.5-7.5d-3	77.68	3.24	45.50	21.39	0.145	0.729				PO
B-9.5-10d-1	77.68	3.24	54	19.05	0.191	0.971				PO
B-9.5-10d-2	77.68	3.24	54.79	19.31	0.219	1.106	19.05	0.191	1.079	PO
B-9.5-10d-3	77.68	3.24	53.30	18.79	0.165	1.160				PO
B-12.7-2.5d-1	79.72	3.48	37.34	29.48	0.124	0.213				PO
B-12.7-2.5d-2	79.72	3.48	34.27	27.04	0.170	0.286	28.26	0.145	0.230	PO
B-12.7-2.5d-3	79.72	3.48	35.81	28.26	0.142	0.193				PO
B-12.7-5d-1	79.72	3.48	57.36	22.63	0.216	0.504				PO
B-12.7-5d-2	79.72	3.48	60.96	24.05	0.232	0.548	23.21	0.261	0.523	PO
B-12.7-5d-3	79.72	3.48	58.14	22.94	0.336	0.518				PO
B-12.7-7.5d-1	77.47	3.24	75.36	19.83	0.218	0.827				PO
B-12.7-7.5d-2	77.47	3.24	77.44	20.37	0.206	0.879	19.83	0.232	0.858	PO
B-12.7-7.5d-3	77.47	3.24	73.35	19.29	0.273	0.869				PO

B-12.7-10d-1	77.47	3.24	92.53	18.25	0.223	1.418				PO
B-12.7-10d-2	77.47	3.24	92.12	18.18	0.092	1.297	18.18	0.166	1.345	PO
B-12.7-10d-3	77.47	3.24	91.77	18.10	0.185	1.322				PO
B-15.9-2.5d-1	77.47	3.24	55.15	27.77	0.250	0.406				PO
B-15.9-2.5d-2	77.47	3.24	57.69	29.04	0.210	0.320	27.77	0.250	0.369	PO
B-15.9-2.5d-3	77.47	3.24	52.61	26.5	0.291	0.381				PO
B-15.9-5d-1	77.47	3.24	90.23	22.71	0.199	0.596				PO
B-15.9-5d-2	77.47	3.24	84.63	21.30	0.161	0.583	21.52	0.179	0.595	PO
B-15.9-5d-3	77.47	3.24	81.60	20.54	0.178	0.607				PO
B-15.9-7.5d-1	77.47	3.24	125.6	21.08	0.063	1.025				PO
B-15.9-7.5d-2	77.47	3.24	103.5	17.38	0.763	1.212	19.23	0.332	1.027	PO
B-15.9-7.5d-3	77.47	3.24	114.5	19.23	0.170	0.845				PO
B-15.9-10d-1	77.47	3.24	150.4	18.93	0.441	1.766				PO
B-15.9-10d-2	77.47	3.24	156.2	19.67	-	1.832	19.41	0.441	1.763	PO
B-15.9-10d-3	77.47	3.24	155.9	19.63	-	1.693				PO
C-16-7.5d-1	78.28	3.48	142	>23.54	0.281	0.646				Y
C-16-7.5d-2	78.28	3.48	142.7	>23.65	0.252	0.615	>23.1	0.199	0.587	Y
C-16-7.5d-3	78.28	3.48	134	>22.21	0.066	0.502				Y
C-16-10d-1	78.28	3.48	133.9	>16.64	0.495	0.758				Y
C-16-10d-2	78.28	3.48	131.3	>16.33	0.541	0.607	>16.60	0.446	0.740	Y
C-16-10d-3	78.28	3.48	135.4	>16.84	0.304	0.857				Y

Table 4.3 - Experimental results of pull-out prisms reinforced with GFRP (HW-SC) and GFRP (SC) bars in concrete (C2)

Specimen label	f_{cu} (MPa)	f_t (MPa)	F_{max} (kN)	τ_{max} (MPa)	S_{ul} (mm)	S_{le} (mm)	Failure Mode
A-9.5-5d	79.97	3.48	27.66	19.51	0.408	0.862	PO
A-9.5-10d	79.97	3.48	46.72	16.47	0.593	1.703	PO
A-12.7-5d	79.97	3.48	38.97	15.38	8.734	9.211	PO
A-12.7-10d	79.97	3.48	65.31	12.88	0.263	1.155	SP

B-9.5-5d	79.40	3.48	32.32	22.79	0.317	0.757	PO
B-9.5-10d	79.40	3.48	58.12	20.49	0.384	1.299	PO
B-12.7-5d	79.40	3.48	51.09	20.16	0.503	0.938	PO
B-12.7-10d	79.40	3.48	85.16	16.80	0.757	1.548	PO

Note: PO = Pull-out failure; SP = Splitting failure and Y = Bar yielding
(-) = Not measured (stopped LVDT)

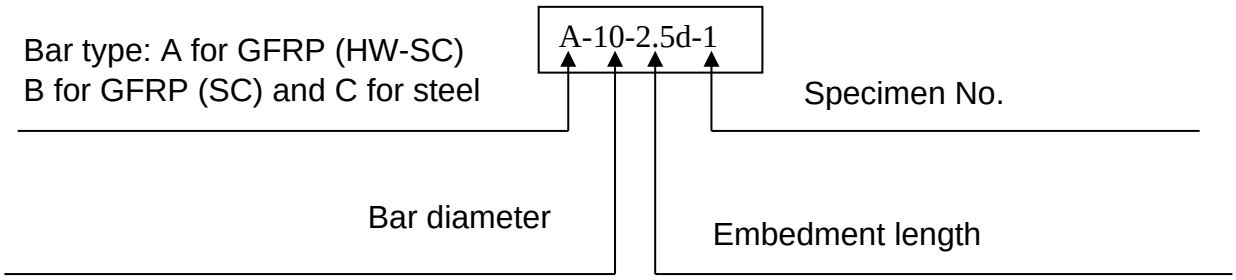

Figure 4.1 - Pull-out specimen nomenclature

4.2.1 Bond stress - slip relationship

The response of bond stress – loaded and unloaded end slips for each specimen is illustrated in Figures 4.2 to 4.4 for cubes reinforced with GFRP (type A) bars and Figures 4.5 to 4.7 for GFRP (type B) reinforced cubes. Figures 4.8 and 4.9 present the bond stress – slip responses for GFRP (type A) and GFRP (type B) reinforced prisms, respectively. The bond stress – slip curves for cubes reinforced with steel bars are also plotted in Figure 4.10. The bond stress – slip relationships are presented according to bar diameter, embedment length, surface characteristics, bar type and specimen size to observe the influence of these main parameters on the bond behavior in case of high strength concrete.

The general trend of bond stress – slip curve for GFRP (HW-SC) bars is similar to that obtained by Lee et al. (2012), Baena et al. (2009), Davalos et al. (2008),

Okelo and Yuan (2005) and Vint and Sheikh (2015) from testing GFRP (HW-SC) reinforced specimens. In addition, the bond stress – slip behaviour for GFRP (SC) bars is similar to that reported by Vint and Sheikh (2015), Baena et al. (2009), Davalos et al. (2008), Hossain et al. (2014), El Refai et al. (2014), Lee et al. (2012), Antonietta Aiello et al. (2007) and Arias et al. (2012) from testing GFRP (SC) reinforced specimens.

The general behaviour of the bond stress – slip relationship is described by a high initial increase in bond stress without a significant slip in both GFRP types and steel bars due to good chemical adhesion between the bar surface and the concrete. This stage describes the initial stiffness. After the chemical adhesion resistance is lost, bond stress continues to increase with increasing the applied load until the peak point, but the amount of the slip increase is small. At this stage, bearing (undulations) and friction resistances control to prevent de-bonding in GFRP (HW-SC) reinforced specimens. However, friction resistance is dominant only in specimens reinforced with GFRP (SC) bars and the mechanical interlock only controls to resist the pull-out force in steel reinforced specimens. In the descending stage (after bond failure), the bond stress reduces with increasing the slip in both GFRP types, but the shape of the softening curve changes with differing surface configuration. In specimens reinforced with helically wrapped and slightly sand coated GFRP bars, bond stress degraded gradually with increasing the loaded and unloaded end slips. It was noted that the reduction rate in bond stresses increases with decreasing bar diameter because of increasing the rib spacing of smaller diameter bars, indicating that residual bond stresses depend on bar size. As for GFRP (type B) reinforced specimens, the bond stress reduced

suddenly to be almost zero with a strong slip accompanied with a loud bang (relative brittle failure and significant energy release) due to detaching of the sand coated layer. No data was recorded during that short moment. Then, bond stress started to increase again up to a certain level, followed by an increase in the slip owing to the remaining frictional resistance. The residual bond stresses produced in GFRP (SC) reinforced specimens are lower than those produced in GFRP (HW-SC) reinforced specimens due to loss of frictional resistance, when sand coating layer was entirely stripped, leading to a smooth surface. For steel reinforced cubes failed in a pull-out mode, the post-peak bond stresses reduced gradually similar to GFRP (HW-SC) bars, however, the reduction was faster than the reduction in GFRP (HW-SC) reinforced specimens owing to lower frictional resistance. From the bond stress – slip curves, it can be noted that the loaded end slip is higher than the unloaded end slip at the same pull-out load, indicating that the high bond stress at the loaded end reduces gradually towards the unloaded end (non-linear distribution).

The bond strength of GFRP (SC) bars is higher than that of GFRP (HW-SC) bars, but the corresponding slip for GFRP (SC) bars is smaller than that for GFRP (HW-SC) bars, indicating that bond properties of sand coated surface are better than those of the helically wrapped surface, and the amount of slip is influenced by the bar surface. The effect of surface configuration on the slip was confirmed by Lee et al. (2012) and Pepe et al. (2013). In addition, it is noticed that the loaded end slip corresponding to the maximum bond stress increases with increasing embedment length for the same bar diameter in both GFRP types and this was also reported by Pepe et al. (2013) and Tekle et al. (2016). Steel reinforced cubes

having embedment lengths of 7.5 and 10 times bar diameter were failed by yielding as shown in Figure 4.10, because the pullout force exceeded the force causing the bar fracture.

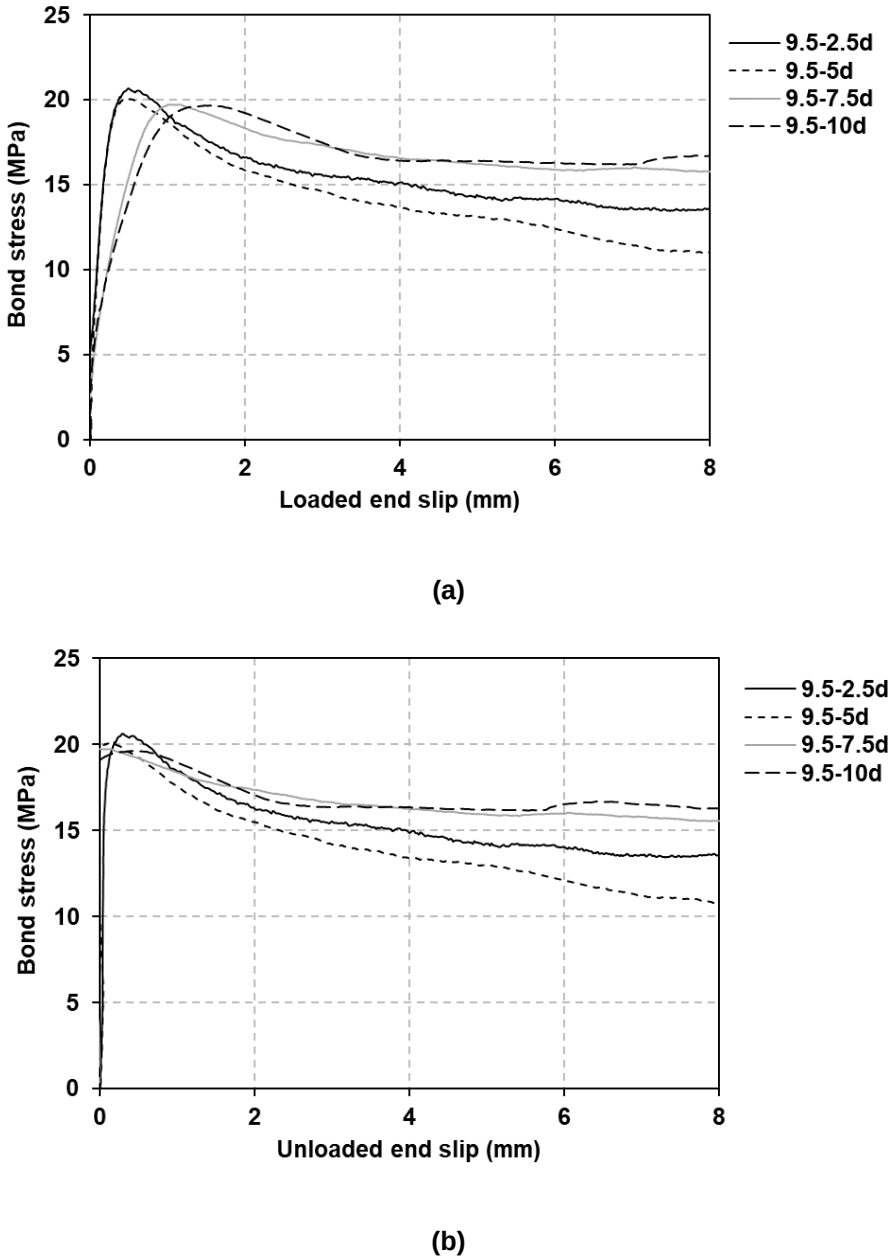

Figure 4.2 - Bond stress - slip relationship for 9.5 mm GFRP (type A) reinforced cubes: (a) loaded and (b) unloaded end slip

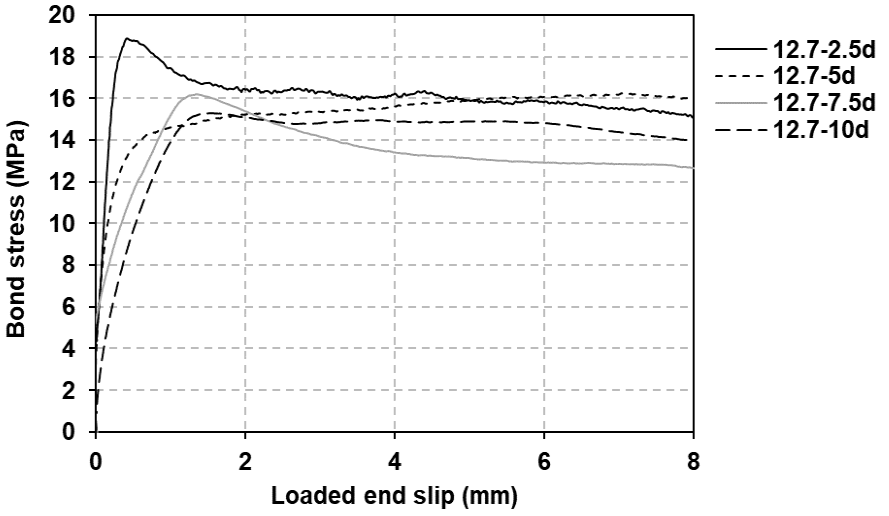

(a)

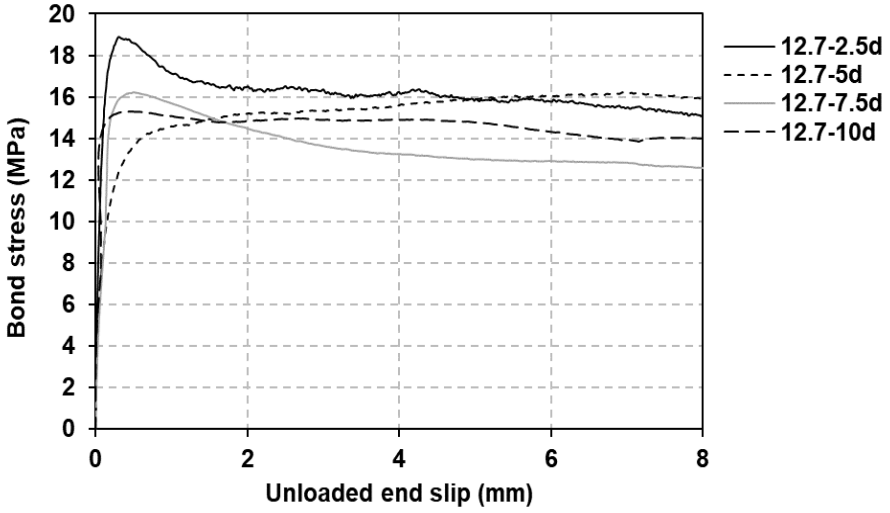

(b)

Figure 4.3 - Bond stress - slip relationship for 12.7 mm GFRP (type A) reinforced cubes: (a) loaded and (b) unloaded end slip

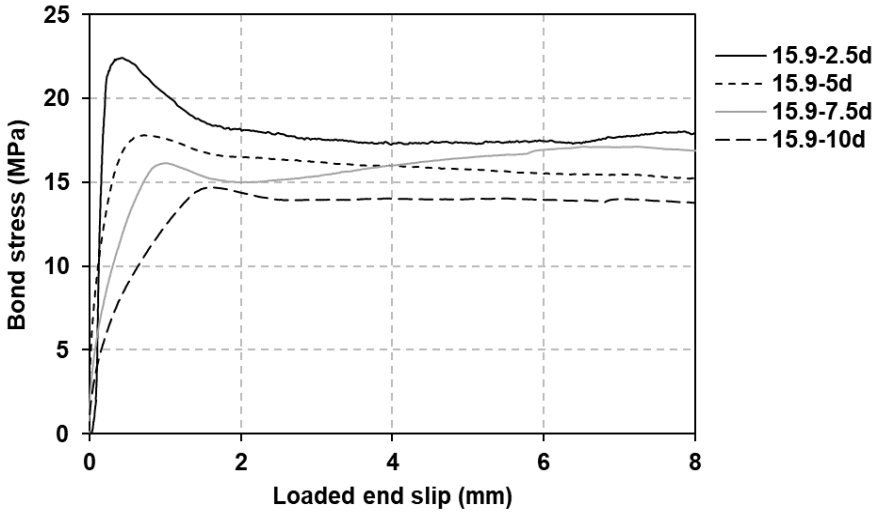

(a)

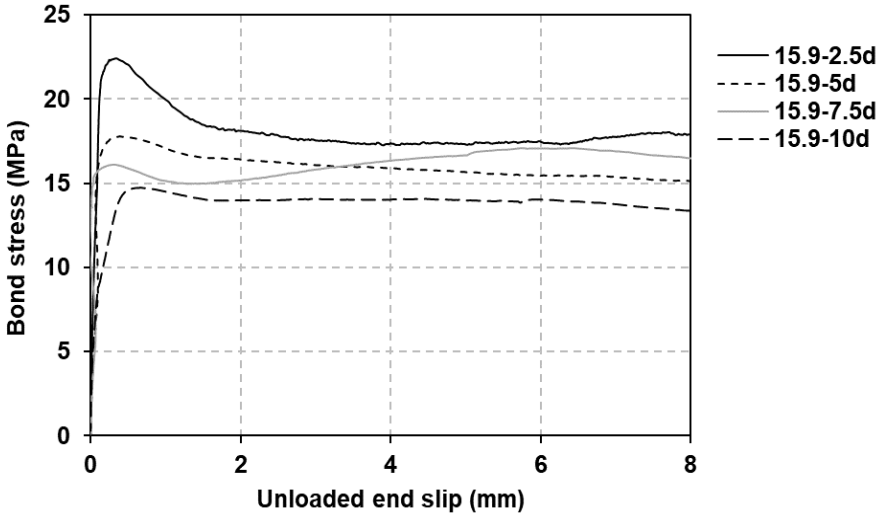

(b)

Figure 4.4 - Bond stress - slip relationship for 15.9 mm GFRP (type A) reinforced cubes: (a) loaded and (b) unloaded end slip

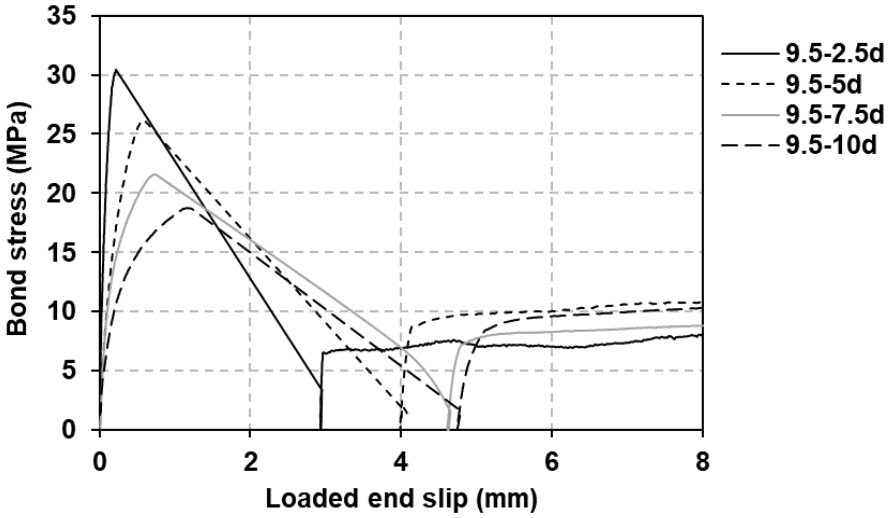

(a)

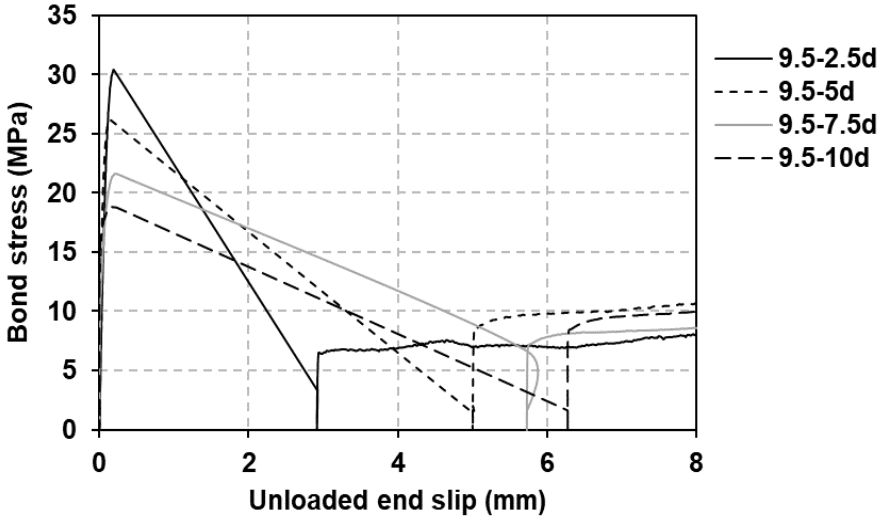

(b)

Figure 4.5 - Bond stress - slip relationship for 9.5 mm GFRP (type B) reinforced cubes: (a) loaded and (b) unloaded end slip

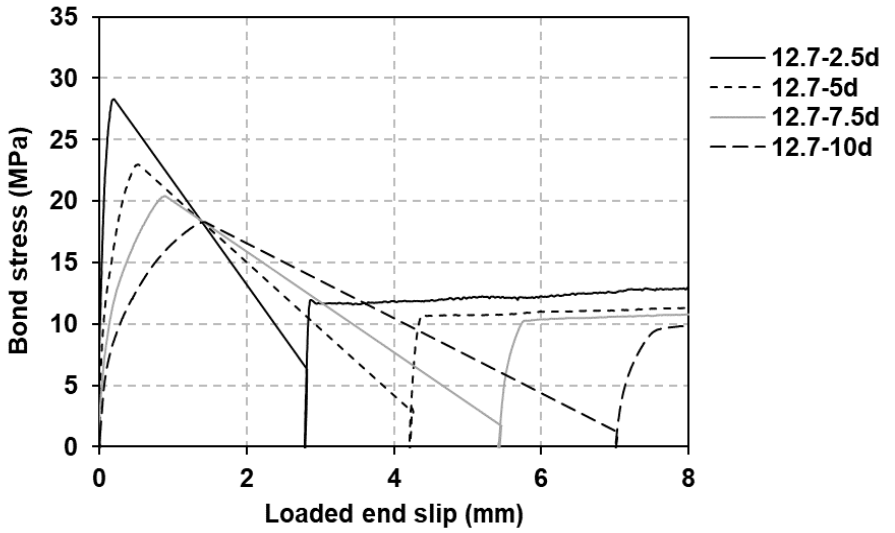

(a)

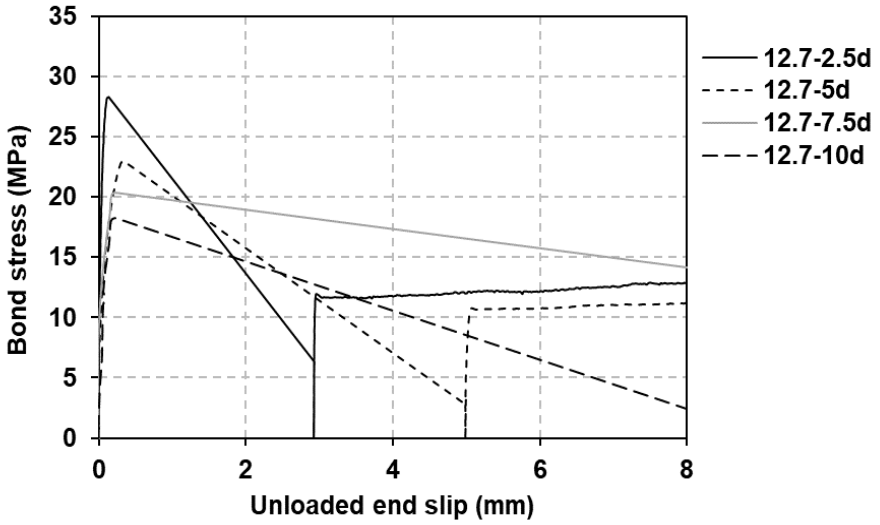

(b)

Figure 4.6 - Bond stress - slip relationship for 12.7 mm GFRP (type B) reinforced cubes: (a) loaded and (b) unloaded end slip

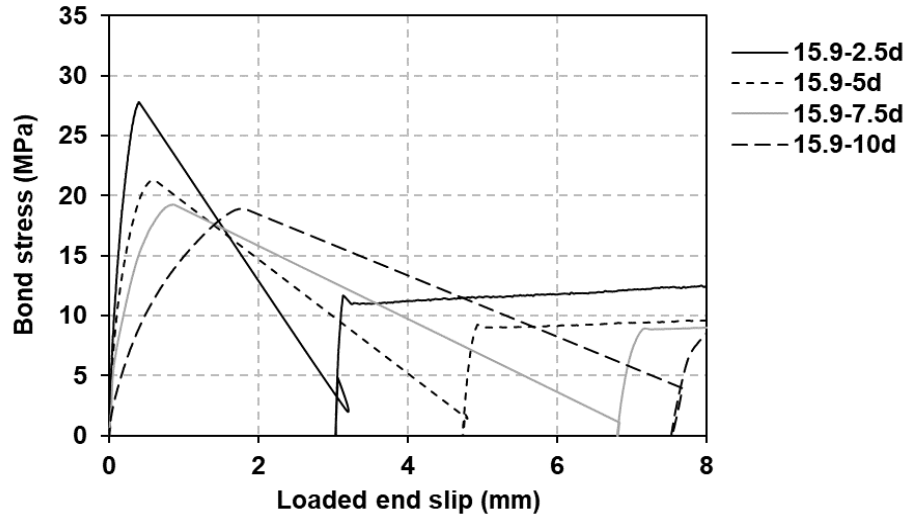

(a)

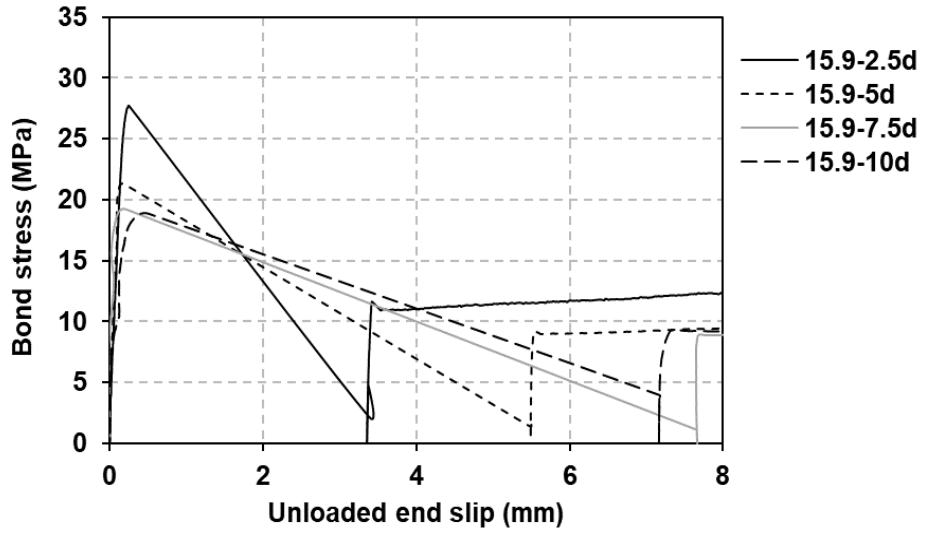

(b)

Figure 4.7 - Bond stress - slip relationship for 15.9 mm GFRP (type B) reinforced cubes: (a) loaded and (b) unloaded end slip

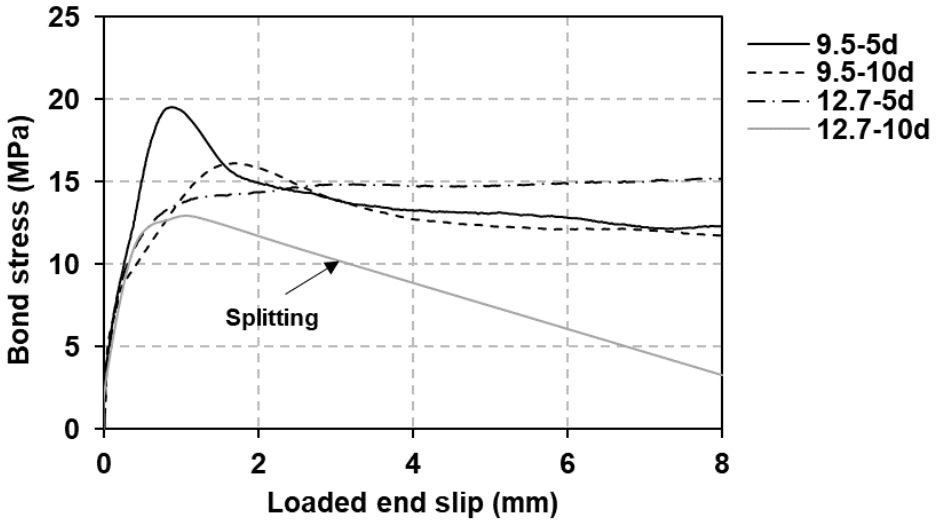

(a)

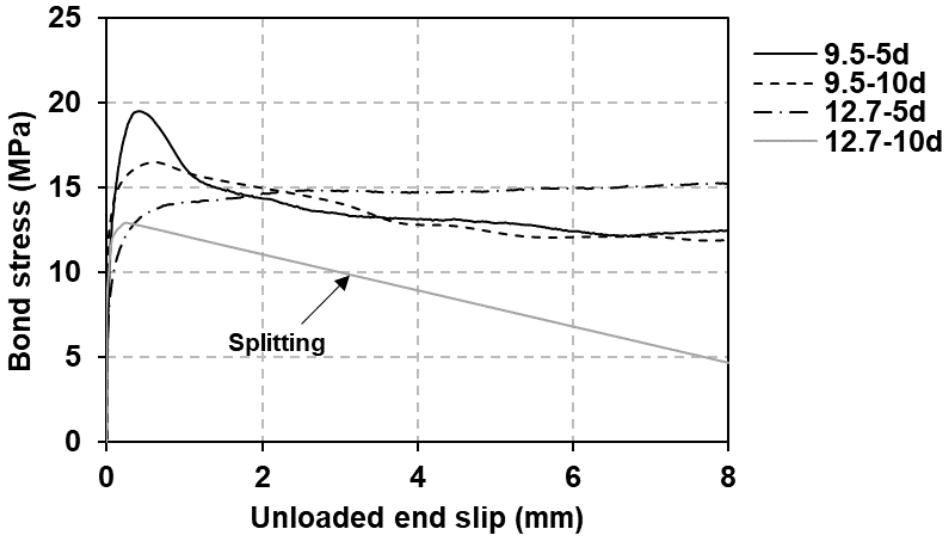

(b)

Figure 4.8 - Bond stress - slip relationship for 9.5 and 12.7 mm GFRP (type A) reinforced prisms: (a) loaded and (b) unloaded end slip

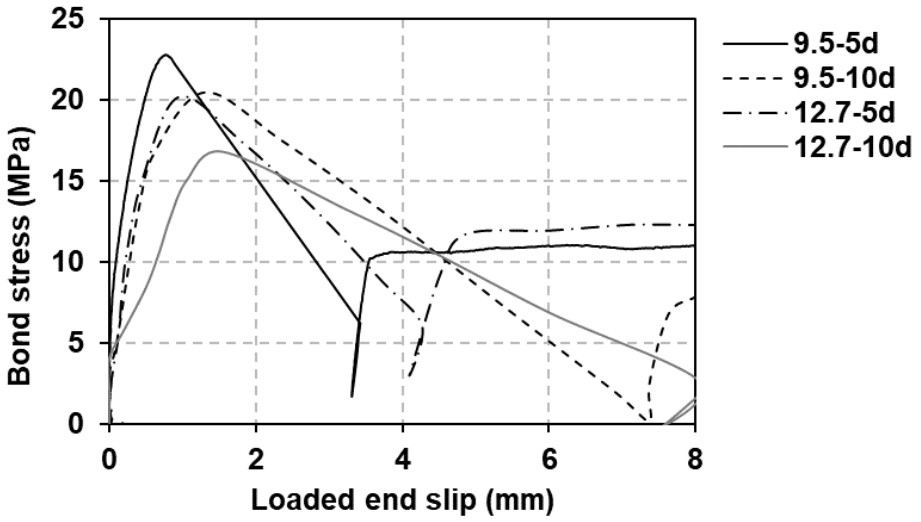

(a)

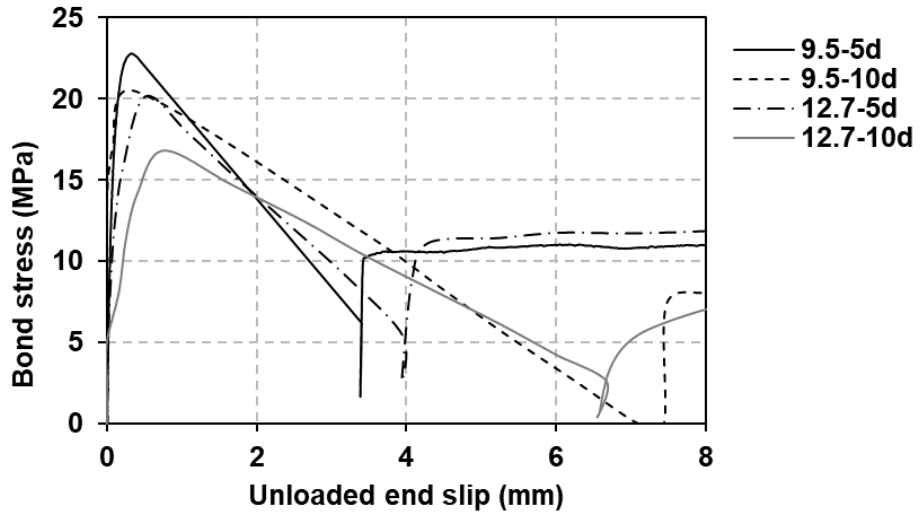

(b)

Figure 4.9 - Bond stress - slip relationship for 9.5 and 12.7 mm GFRP (type B) reinforced prisms: (a) loaded and (b) unloaded end slip

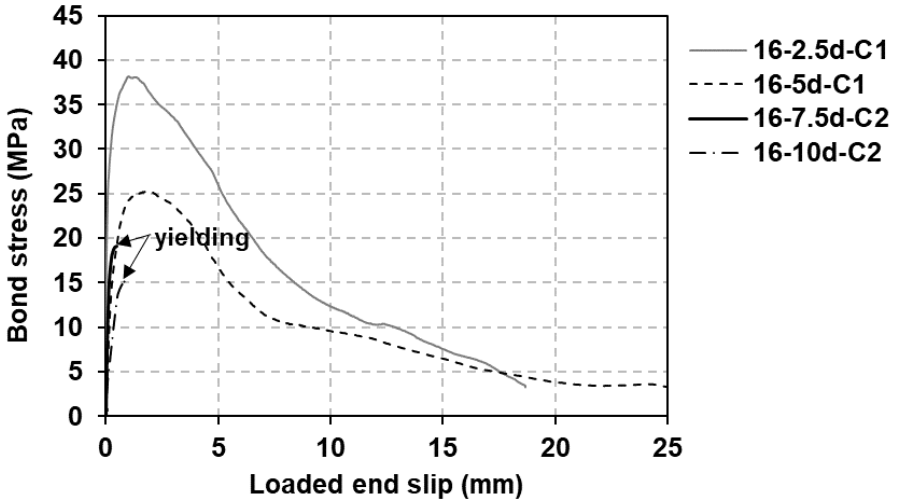

(a)

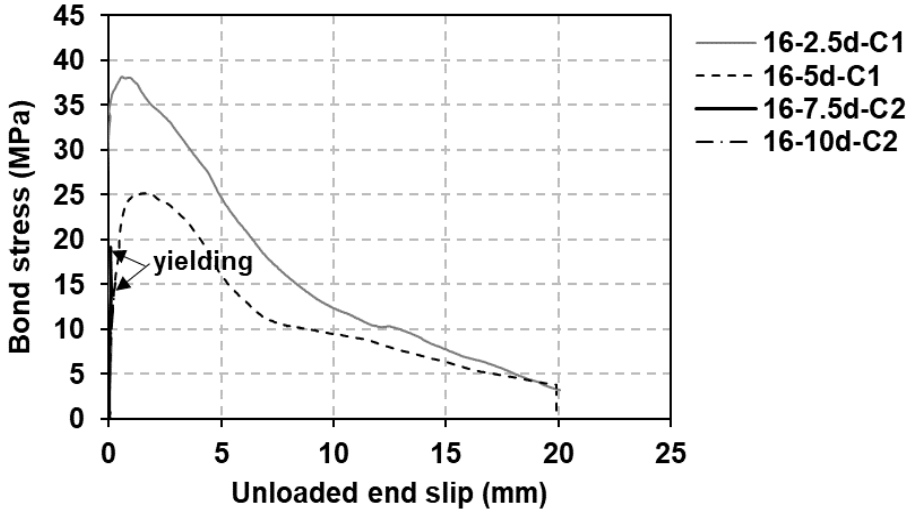

(b)

Figure 4.10 - Bond stress - slip relationship for 16 mm steel reinforced cubes: (a) loaded and (b) unloaded end slip

4.2.2 Initial stiffness

Figure 4.11 (a and b) shows that the initial stiffness reduces with increasing the embedment length as reported by Pepe et al. (2013) and Achillides and Pilakoutas (2004). This might be attributed to non-uniformly distribution of bond stresses

along the bonded length. Also, it is found that the initial stiffness for steel bars is higher than that for GFRP (HW-SC) bars as shown in Figure 4.11 (a). This may be because of differing surface properties and elastic modulus. This result was also confirmed by Baena et al. (2009) from testing the pull-out cubes.

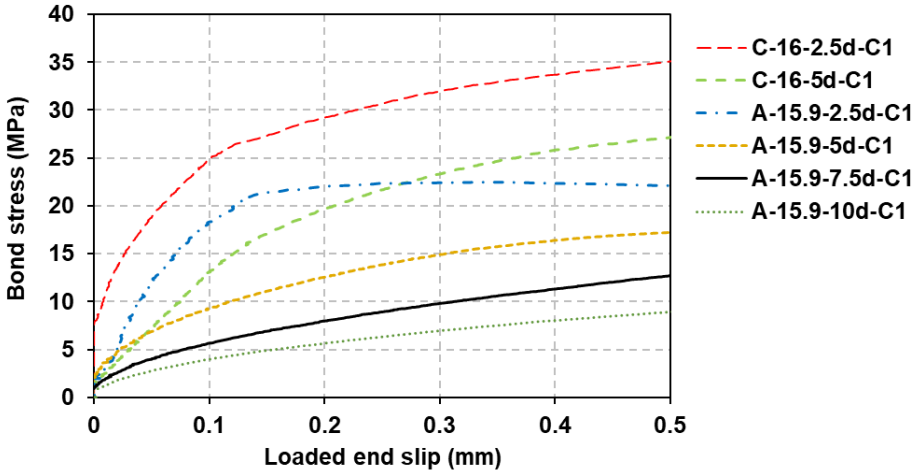

(a)

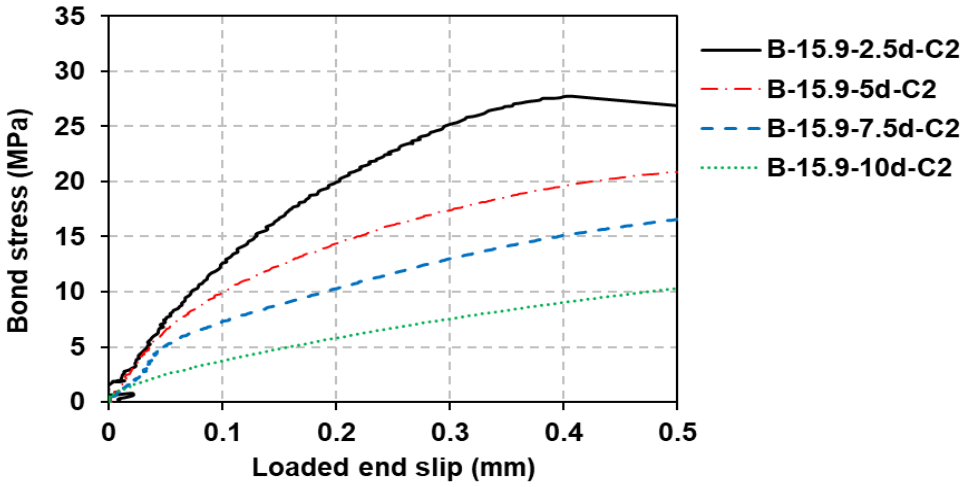

(b)

Figure 4.11 - Influence of elastic modulus and embedment length of bar on initial stiffness

4.2.3 Bond failure mechanism

The failure mode observed for each pull-out test is listed in Tables 4.1 to 4.3. As anticipated, most specimens were failed by a pull-out mode as shown in Figure 4.12 (a), because the cube compressive strength of concrete was designed to be higher than 80 MPa to ensure the occurrence of failure at the bar – concrete interface, rather than in concrete. However, only one specimen was failed by splitting cracks as illustrated in Figure 4.12 (b). Splitting failure observed in prism (A-12.7-10d) occurred before reaching the maximum pull-out load. The splitting failure was unexpected and attributed to test imperfections during the test set-up. In addition, the specimens reinforced with steel bars, having the embedment lengths of $7.5d_b$ and $10d_b$, failed by bar fracture before attaining the bond strength as presented in Figure 4.14 (b). It can be concluded that the required development length to avoid bond failure between the high-strength concrete and steel bars could be equal to or more than $7.5d_b$.

The specimens were split after testing to visually assess the bar and surrounding concrete conditions. As for the specimens reinforced with GFRP (HW-SC) bars, some abrasions were noted on the outer surface with stripping of sand coating as shown in Figure 4.13 (b and c). White residue was seen on the trace of the whole embedment length, which indicated crushing of the resin. As noted the specimens with longer embedment lengths failed by damage of the fibres as illustrated in Figure 4.13 (a). No apparent crushing of the surrounding concrete was monitored in any of the GFRP reinforced specimens. The de-bonding failure in the GFRP-SC reinforced specimens occurred by the entire detachment of the sand coated

layer accompanied with a loud bang, when bond stress reached the peak value as demonstrated in Figure 4.13 (d and e). The concrete also remained uncrushed. This indicated that the bond strength between the outer layer and bar core was lower than that between the high-strength concrete and sand coating. Therefore, failure was controlled by the shear strength at the resin – bar core interface rather than the shear strength between the bar and the concrete. This mode of failure was expected in the case of high-strength concrete. Similarity, Marta Baena et. al (2009) found that the sand coated layer was totally stripped from the GFRP-SC rebar, when the compressive strength of concrete was around 50 MPa. The specimens with concrete strength of 30 MPa were failed by a pull-out mode due to damage in the concrete surface. Concerning steel reinforced cubes failed by pull-out, Figure 4.14 (a) shows the remaining of concrete still attached to the outer surface of steel rebar. This is an indicator that bond failure occurred by shearing off of the concrete between ribs.

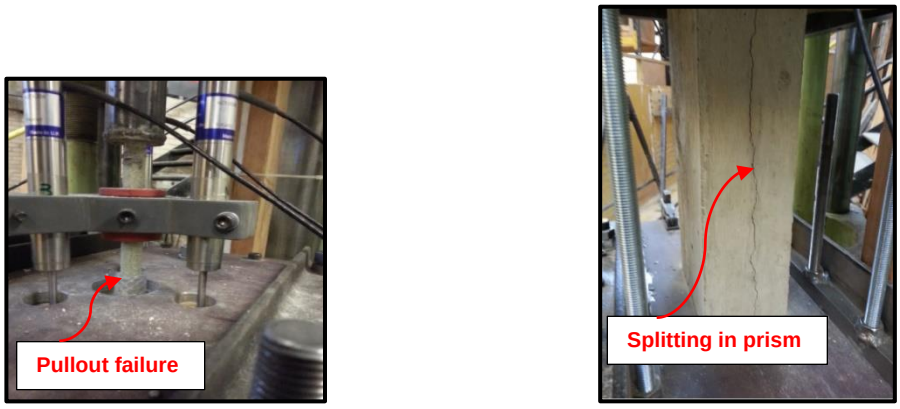

(a) **(b)**

Figure 4.12 - Bond failure modes

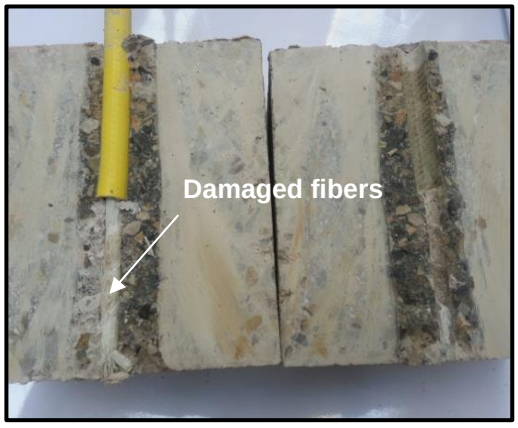

(a) Cube (A-9.5-10d-3)

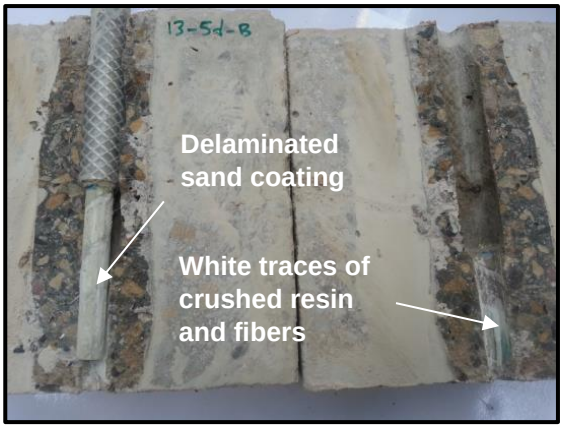

(b) Cube (A-12.7-5d-2)

(c) Prism (A-9.5-10d)

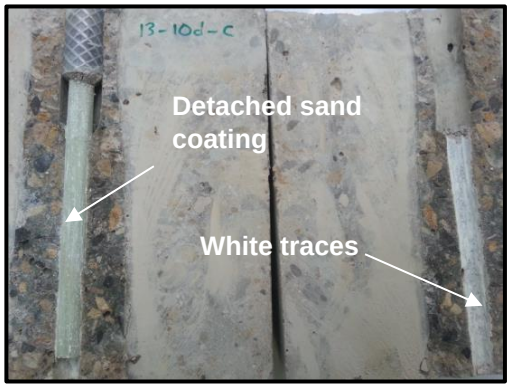

(d) Cube (B-12.7-10d-2)

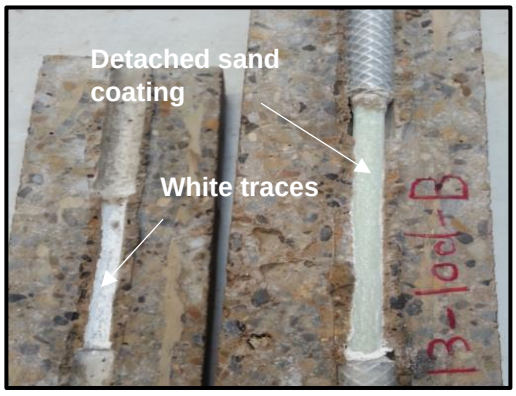

(e) Prism (B-12.7-10d)

Figure 4.13 - Visual inspection for the specimens failed by pull-out

(a) Shear off concrete in cube (C-16-2.5d-1) **(b) Bar Fracture**

Figure 4.14 - Visual inspection of specimens reinforced with steel bars

4.3 Factors influencing bond strength

4.3.1 Effect of the embedment length on bond strength

Generally, the trend of the test results points out that the longer the embedment length, the smaller the value of the average bond strength. This observation is obtained for each bar diameter in both GFRP types as well as steel bars. The failure load increases with increasing the embedment length. The relationships between the bond strength and embedment length are shown in Figures 4.15 to 4.18 for GFRP (type A) and GFRP (type B) reinforced cubes and prisms with different bar diameters. Based on the experimental results, it can be reported that the bond strength increases with reducing the bonded length and this observation was also confirmed by some previous authors (Achillides and Pilakoutas, 2004, Okelo and Yuan, 2005, El Refai et al., 2014, Hossain et al., 2014, Tekle et al., 2016). This is attributed to two main factors: 1) non-linear distribution of bond stress along the embedment length, and 2) the reduction in the bar size due to poisson's ratio effect, leading to reduce the frictional and mechanical interlock resistances along the embedment length. In Figure 4.15, it is noted that no significant change occurred in the bond strength with the increase of embedment

length for smaller bar diameters. For example, the bond strength of a 9.5 mm GFRP (HW-SC) bar having an embedment length of $10d_b$ is reduced by approximately 6% compared to that having an embedment length of $2.5d_b$. However, for larger bar diameters, the reduction rates in the bond strength of $10d_b$ specimens were 19% and 24% compared to $2.5d_b$ specimens, for 12.7 and 15.9 mm bar diameters, respectively. In Figure 4.16, the bond strength of $10d_b$ specimens having 9.5, 12.7 and 15.9 mm diameters is decreased by almost 34%, 36% and 32% in comparison with $2.5d_b$ specimens, respectively. In general, the reduction rate in bond strength of GFRP (type B) is higher than the reduction rate in bond strength of GFRP (type A). As the embedment length increases from $5d_b$ to $10d_b$ in 9.5 mm GFRP (type A) reinforced prisms, the bond strength reduces by 15.6%. With increasing the embedment length in GFRP (type B) reinforced prisms, the reduction rates are 10% and 16.66% for 9.5 and 12.7 mm bar diameters, respectively. For comparison purposes, steel reinforced specimens also were tested to compare their bond strength with those reinforced with GFRP re-bars. It was found that the bond strength of GFRP (type A) bars was lower (50 to 65%) than that of steel bars, depending on embedment length. This is because of different mechanical properties and surface configurations. Regarding $7.5d_b$ and $10d_b$ steel reinforced cubes, the failure observed was a bar rupture instead of a pull-out bar. Subsequently, these specimens did not compare with counterparts reinforced with GFRP (type B) bars. It was noticed that the loaded end slip increased with increasing the embedment length for the same bar diameter in both GFRP types. The same observation was reported by Pepe et al.

(2013) from testing hinged beams and Tekle et al. (2016) from testing pullout specimens.

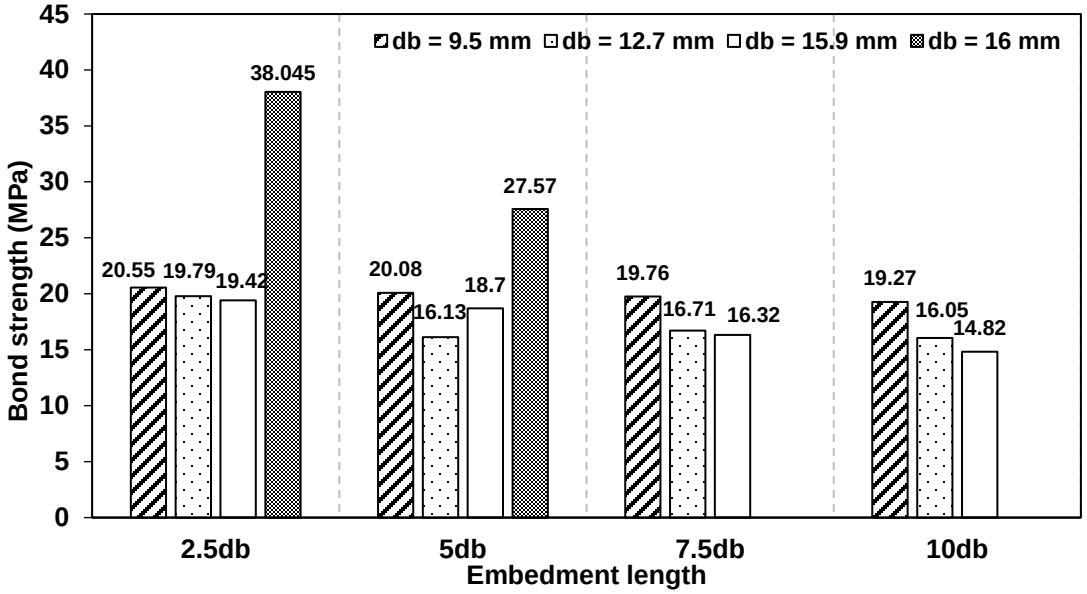

Figure 4.15 - Effect of the embedment length and bar diameter on the average bond strength of GFRP (HW-SC) bars embedded in HSC cubes

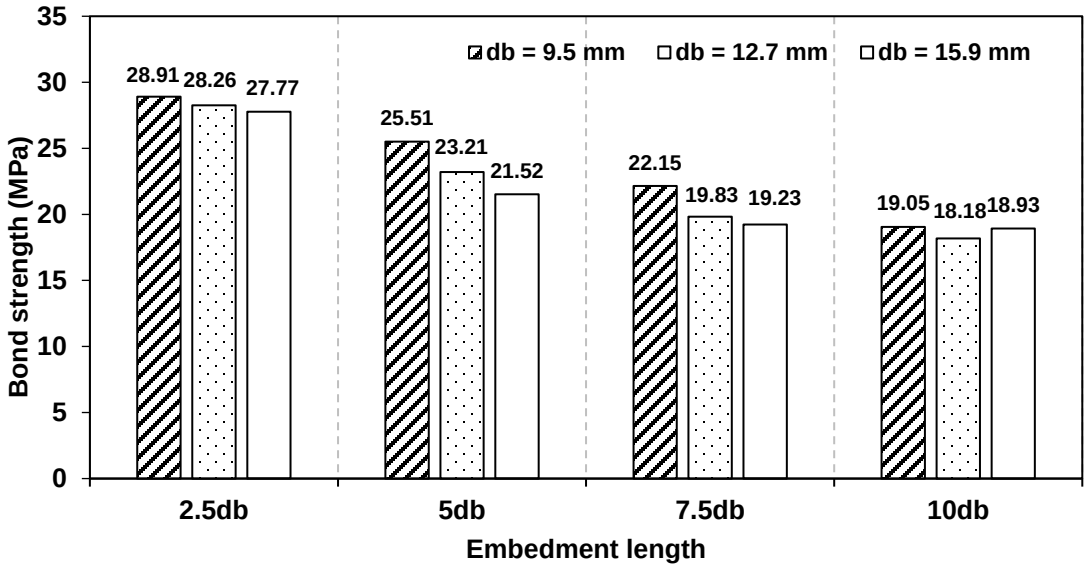

Figure 4.16 - Effect of the embedment length and bar diameter on the average bond strength of GFRP (SC) bars embedded in HSC cubes

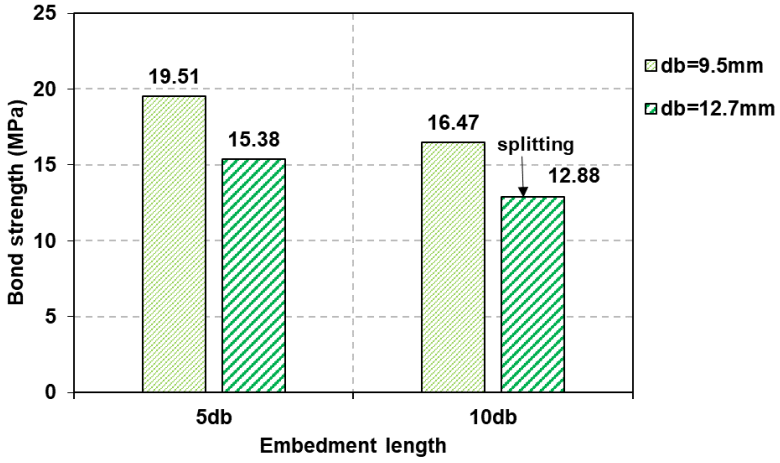

Figure 4.17 - Effect of the embedment length and bar diameter on the average bond strength of GFRP (HW-SC) bars embedded in HSC prisms

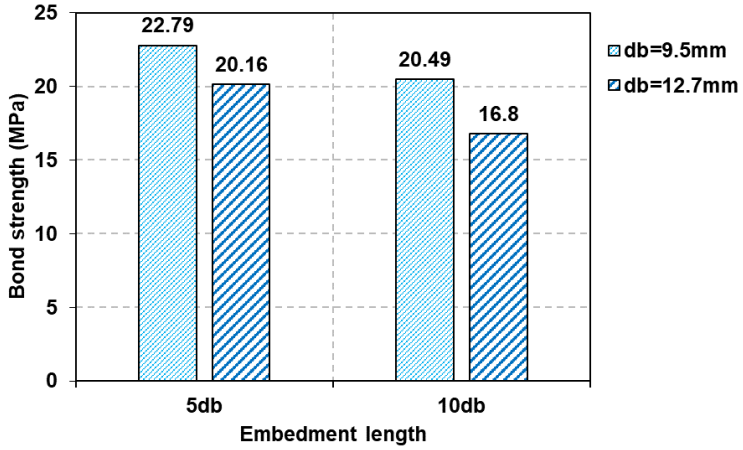

Figure 4.18 - Effect of the embedment length and bar diameter on the average bond strength of GFRP (SC) bars embedded in HSC prisms

4.3.2 Effect of the bar diameter on bond strength

As shown in Figures 4.15 to 4.18, the average bond strength of GFRP bars reduces with increasing the bar diameter similar to steel bars. This observation is valid for all test specimens regardless of the embedment length. This trend was also reported by Nanni et al. (1995), Benmokrane et al. (1996), Cosenza et al. (1997), Tighiouart et al. (1998), Achillides (1998), Achillides and Pilakoutas

(2004), Okelo and Yuan (2005), Tepfers (2006), Xue et al. (2008), Baena et al. (2009), Hossain et al. (2014), El Refai et al. (2014) and Lee et al. (2017). This is attributed to the nonlinear distribution of bond stresses along the embedment length (Benmokrane et al., 1996, Achillides and Pilakoutas, 2004, Baena et al., 2009), which is more pronounced in larger bar diameters as longer embedment lengths are required. In addition, Achillides and Pilakoutas (2004) reported that the Poisson effect may have an effect on this behavior by reducing the bar diameter subjected to the pull-out load, this reduction in bar diameter increases with the bar size. Subsequently, the frictional and mechanical interlock stresses decrease along the embedment length. Shear lag was also considered as a factor in explaining this phenomenon. The difference in non-linear distribution of normal stresses through the cross-section of the bar increases with increasing bar diameter, leading to diminish the average bond strength (Achillides and Pilakoutas, 2004). From Figure 4.15, GFRP (type A) bars with 9.5 mm diameters showed bond strengths 5.5%, 6.9%, 17.4% and 23.1% higher than the bond strengths developed by the 15.9 mm diameters for the embedment lengths of 2.5, 5, 7.5 and 10 times the bar diameter, respectively, with an average increase of 13.2%. It can be stated that the decrease of bar diameter led to a slight increase in the bond strength for the shorter embedment lengths. These percentages were 3.7%, 19.6%, 15.4% and 16.7% more than the bond strengths developed by the 12.7 mm bar diameters for the same embedment lengths, with an average increase of 13.8%. As can be seen in Figure 4.16, GFRP (type B) bars with 12.7 mm bar diameters showed bond strengths that were 2.3%, 9%, 10.4% and 4.5% lower than those developed by 9.5 mm bar diameters for the embedment lengths

of 2.5, 5, 7.5 and 10 times bar diameter, respectively, with an average reduction of 6.5%. As for 15.9 mm diameters, these percentages were 4.1%, 18.5%, 15.2% and 0.6% less than those developed by 9.5 mm diameters for the same embedment lengths, with an average reduction of 9.6%. The increase rate in bond strength with reducing bar diameter was also investigated in GFRP (type A) reinforced prisms, where the bond strength of 9.5 mm diameter was higher 21% than that of 12.7 mm diameter for the embedment length of $5d_b$. This percentage was not showed for the embedment length of $10d_b$ due to splitting failure in the 12.7 mm specimen. From Figure 4.18, the test results of GFRP (type B) bars revealed that bond strengths obtained from 9.5 mm diameters were11.5% and 18% more than those obtained from 12.7 mm diameters for the embedment lengths of $5d_b$ and $10d_b$, respectively, with an average increase of 14.7%. For high strength concrete pull-out cubes, it was noticed that a reduction rate in bond strength reduced with increasing the bar diameter for all embedment lengths. A similar observation was confirmed by Lee et al. (2017) and they also reported that the influence of bar diameter on bond strength was affected by concrete compressive strength.

4.3.3 Effect of the bar surface on bond strength

As mentioned in the literature, the surface deformations play an important role in improving the bond at the bar to concrete interface. Due to the importance of the surface properties on bond behaviour, it is worth comparing the bond performance of different surface treatments. This research focused on investigating the bond behaviour and failure mechanism of two common bar surfaces. GFRP bars used

in this study had helical wrapped with slight sand coated and sand coated surfaces. The GFRP (HW-SC) surface was manufactured by wrapping glass fibers around smooth surface with spraying a little sand on the outer surface to improve the bond characteristics. The GFRP (SC) surface was only made of sand coating. Bond failure in both GFRP types occurred at the interface between the outer layer of the surface and the bar core, which indicated that the bond strength was controlled by surface configuration in the case of high strength concrete. From Figures 4.19 and 4.20, it can be seen that the bond strength of GFRP (SC) bars is higher than that of GFRP (HW-SC) bars due to their sand coated surface, which is similar to the results obtained from testing pull-out specimens for cylinder compressive strengths of concrete in the range of 57 to 63 MPa (Davalos et al., 2008). The bond strength of GFRP (SC) bars strongly depends on friction resistance provided by surface treatment. While, little bearing resistance was provided by GFRP (HW-SC) bars, unlike steel bars. However, according to the findings of Baena et al. (2009), the bond strength of GFRP (HW-SC) bars was higher than that of GFRP (SC) bars for a concrete strength of 53 MPa, despite the fact that the GFRP bars used were similar to the GFRP bars used in the current study. Moreover, Baena et al. (2009) reported that the influence of bar surface configurations on bond strength depended on the concrete strength, where the effect was less important in low - strength concrete compared to high - strength concrete. In addition, Lee et al. (2012) found that bond strengths achieved by GFRP (HW-SC) re-bars were more than those achieved by GFRP (SC) re-bars for different concrete strengths 25, 40 and 70 MPa. As illustrated in Figure 4.19, the ratio of GFRP (type B) bond strength to GFRP (type A) bond

strength varied from 0.99 to 1.44 with an average of 1.25, depending on bar diameter and embedment length. With regard to prisms, these ratios were in the range of 1.17 to 1.31 with an average of 1.24, depending on bar diameter and embedment length. It was also noted that the corresponding loaded end slip in GFRP (SC) bars is smaller than that in GFRP (HW-SC) bars as shown in Tables 4.1 to 4.3. The same observation was reported by Lee et al. (2012).

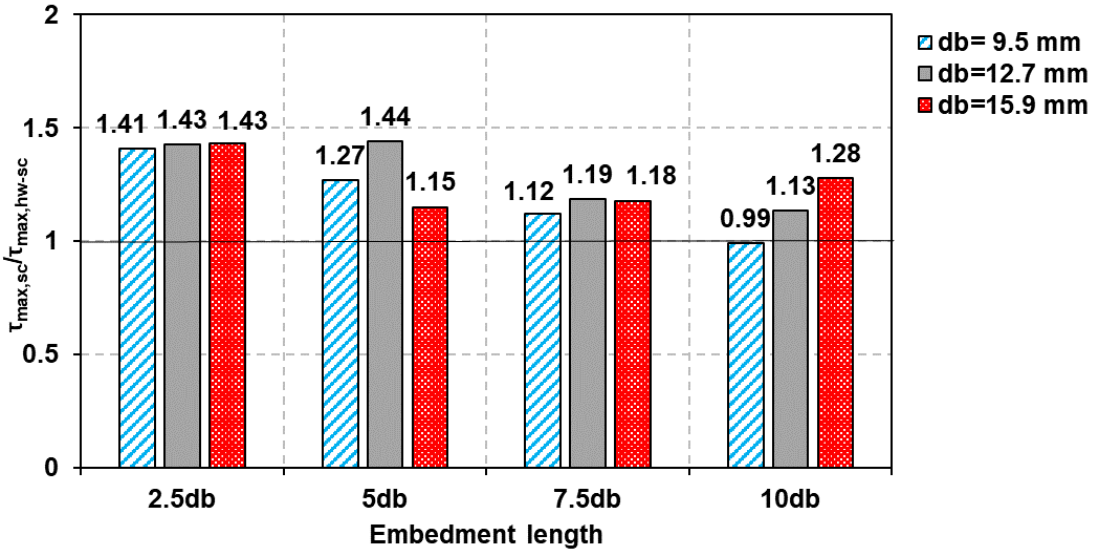

Figure 4.19 - Comparison between bond strength of GFRP (SC) bars and bond strength of GFRP (HW-SC) bars for HSC cubes

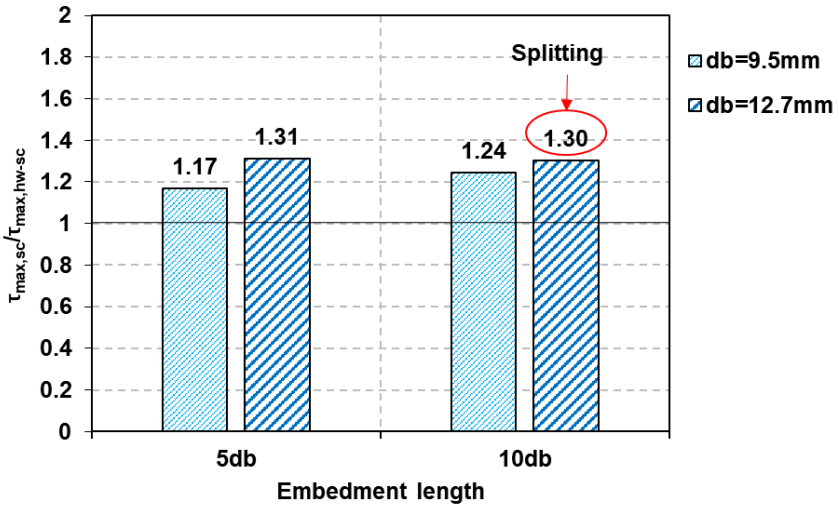

Figure 4.20 - Comparison between bond strength of GFRP (SC) bars and bond strength of GFRP (HW-SC) bars for HSC prisms

4.4 Investigating the effect of concrete strength on bond strength using the current and previous experimental data

Data concerning the relationship between bond strengths of GFRP (HW-SC) bars and concrete strength were collected from the literature (Baena et al., 2009, Okelo and Yuan, 2005, Davalos et al., 2008, Lee et al., 2012, Lee et al., 2017, M. Baena et al., 2016, Sooriyaarachchi, 2006, Mesbah et al., 2017), as well as the tested results of this study as shown in Figure 4.21 (a). These data are based on GFRP bars having helical wrapping with a slight sand coating, pull-out failure, diameters of 6 to 25.4 mm and an embedment length of $5d_b$. To omit the effect of embedment length on bond strength, only one embedment length was selected for investigating the trend. Most specimens in the previous investigations had an embedment length of $5d_b$, therefore the current observation was conducted for this length. From Figure 4.21 (a), it is obvious that the bond strength increases with increasing concrete compressive strength up to almost 40 MPa and then a slight increase in bond strength with increasing concrete compressive strength

(more than 40 MPa) is noted. In addition, Lee et al. (2017) found that the increase rate in bond strength of sand coated GFRP and helical wrapped GFRP bars was small, as the concrete strength increased from 40 to 60 MPa for both bar diameters of 13 and 19 mm. Therefore, it can be reported that the concrete strength influences the bond strength up to a certain limit beyond which there is no further enhancement of bond strength with the increase of concrete strength and this was also confirmed by Karlsson (1997), Achillides (1998) and Davalos et al. (2008) from testing different surface properties of FRP bars. They explained this change in the trend because of changing the failure mode, where a splitting failure took place, when concrete strength was less than 30 MPa, otherwise a pullout failure occurred. However, all specimens in Figure 4.21 (a) were failed by a pull-out failure, this means that the failure mode isn't related to the concrete strength. Subsequently, it may be attributed to improvements in the chemical adhesion and bearing resistances with increasing concrete strength. On the contrary, the results obtained by Lee et al. (2008) and Lee et al. (2012) presented the failure at the interface between the concrete and the bar, and showed that the bond strength of GFRP (HW-SC) bars steadily increased with increasing the concrete strength (from 25 to 92 MPa) owing to improvement in the chemical adhesion.

To investigate the effect of concrete strength on bond strength of GFRP (SC) bars, the experimental results were also collected from previous studies (Baena et al., 2009, Lee et al., 2012, Arias et al., 2012, Davalos et al., 2008, El Refai et al., 2014, Lee et al., 2017), as well as the tested results of the current investigation as illustrated in Figure 4.21 (b). Very limited data are available in the literature

regarding bond strength of GFRP (SC) bars. The points plotted in Figure 4.21 (b) are for an embedment length of $5d_b$ due to the majority of the tested specimens having the $5d_b$ embedment length, bar diameters of 9.5 – 25.4 mm, sand coated surface and pull-out failure. From Figure 4.21 (b), the bond strength is directly proportional to the concrete compressive strength, when the concrete strength is less than 40 MPa. However, there are large variations in the values of bond strengths, when the concrete strength is greater than 40 MPa. Thus, there is no clear conclusion.

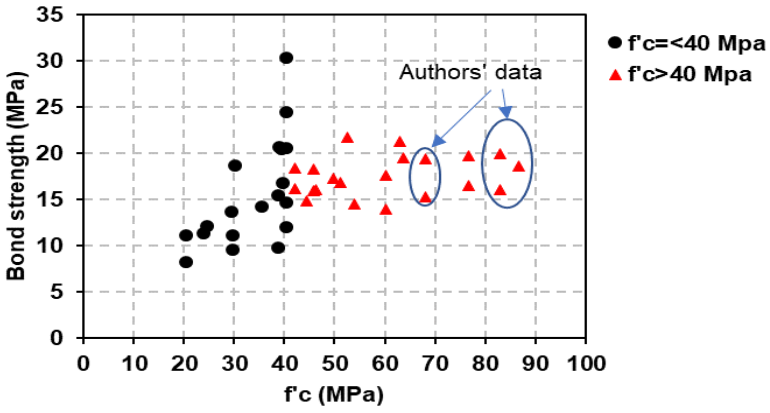

(a) $5d_b$ specimens reinforced with GFRP (HW-SC) bars

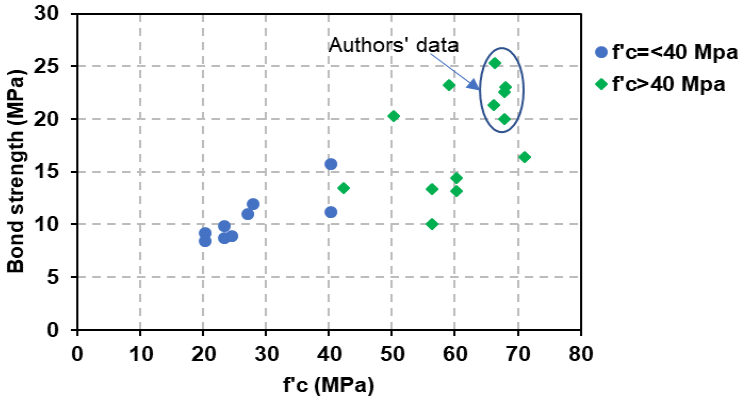

(b) $5d_b$ specimens reinforced with GFRP (SC) bars

Figure 4.21 - Bond strength versus concrete strength

4.5 Comparison between bond strengths in cubes and prisms

As mentioned earlier, all prisms were cast using the second batch C2 as the same as GFRP (SC) reinforced concrete cubes, while cubes reinforced with GFRP (HW-SC) bars were cast using the first batch C1. The comparison between bond strengths in cubes and prisms reinforced with GFRP (type A) was carried out because the difference in their concrete strength is about 17%. For comparison purposes, all other parameters were the same, except the specimen size, which was investigated to analyze its effect on bond strength. The dimensions of the cube and prism were 200 x 200 x 200 mm and 100 x 180 x 375 mm, respectively. In addition, all specimens failed by a pull-out mode, except one prism (A-12.7-10d). Figure 4.22 presents the bond strengths in cubes compared to those in prisms for both GFRP types. Generally, it can be seen that the maximum bond stress in cubes is higher than that in prisms, this could be due to the difference in concrete cover. The ratio of bond strength for GFRP (type B) reinforced cubes to that for GFRP (type B) reinforced prisms changed from 0.93 to 1.15, depending on bar diameter, and embedment length. As for GFRP (HW-SC) reinforced specimens, the ratio of bond strength in cubes to that in prisms is in the range of 1.03 to 1.17, depending on bar diameter and embedment length. The bond strength variations between cubes and prisms are small. Similar observations were made by Hossain et al. (2014). They reported that the change in concrete cover from 40 to 60 mm for both bar diameters 15.9 and 19.1 mm led to increase in the bond strength by 10% and 20%, respectively. This is also confirmed by Kotynia et al. (2017) from testing a hinged beam. It can be stated that the concrete

cover has a less important influence on the bond strength of both GFRP types in the case of high strength concrete. However, the bond strength slightly decreased for cubic concrete compressive strengths of 23.3, 38.9 and 56.3 MPa, and increased for cubic concrete compressive strength of 62.3 MPa, when the concrete cover increased from 10 to 20 mm (Veljkovic et al., 2017). In addition, Veljkovic et al. (2017) reported that the eccentric pull-out specimens reinforced with ribbed GFRP bars exhibited higher bond strength and lower slip values, comparing to the centric pull-out specimens.

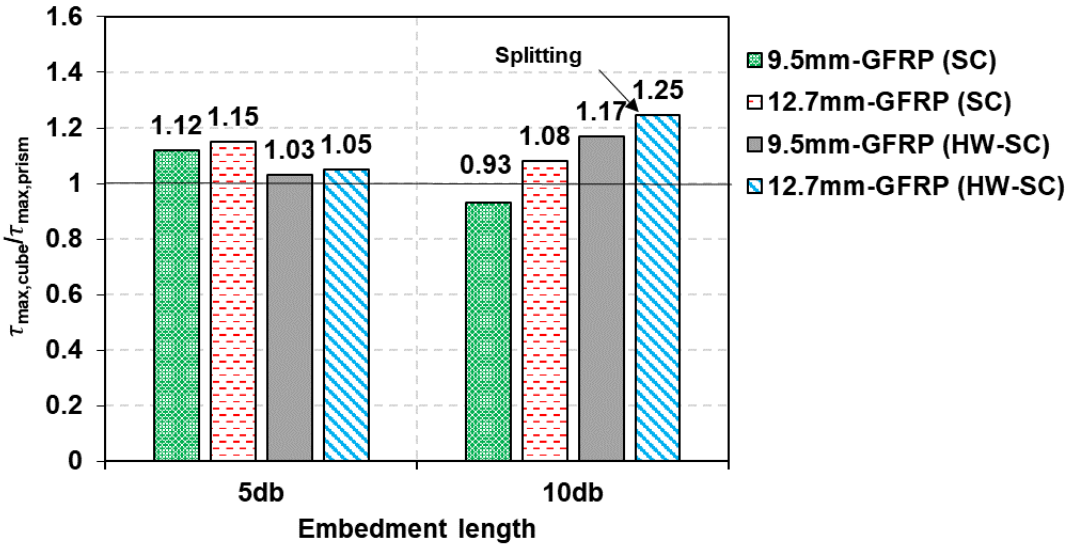

Figure 4.22 - Comparison between bond strength of GFRP bars in cube and bond strength of GFRP bars in prism

4.6 Conclusions

In this chapter, test results of 92 HSC pull-out specimens reinforced with GFRP and steel bars have been presented and discussed. The main parameters investigated were diameter, embedment length and surface configuration of

reinforcing bars, as well as concrete cover. According to this experimental work, the following conclusions are drawn:

- The majority of specimens failed by a pull-out mode. In general, the bond failure usually occurred within the interfaces of resin-rich layer and fibers for GFRP (HW-SC) bars. As for GFRP (SC) bars, the bond failure usually occurred within the interfaces between the sand coated layer (sand embedded in resin-rich layer) and the bar core, whereas the failure in control specimens was governed by shearing off of concrete between steel ribs.
- GFRP bars with helical wrapping and a slight sand coating showed interfacial bond behaviour differing from that of sand coated GFRP bars. GFRP (HW-SC) bars produced a more ductile post peak response with high residual stresses owing to high friction forces between remaining undulations and concrete similar to the behaviour observed in other investigations for normal strength concrete pull-out specimens reinforced with GFRP (HW-SC) bars. GFRP bars with a sand coated surface produced a brittle failure because of the complete stripping of sand grains from the bar core, unlike the behaviour observed in the literature in the case of normal strength concrete, where the softening curve was smoother (less ductile).
- Overall, the bond strength investigated using a pull-out cube and prism increased with reducing the embedment length for both GFRP types. The decrease of bar diameter resulted in increasing bond strength.

- For high strength concrete, in general, a reduction rate in bond strength reduced with increasing the bar diameter and embedment length for pull-out cubes reinforced with both GFRP types.
- The sand coated surface offered the bond strength higher than that offered by the helically wrapped with slightly sand coated surface for a given concrete strength, but the corresponding slip for GFRP (SC) bars was less than that for GFRP (HW-SC) bars.
- The increase of high concrete strength does not lead to a significant increase in bond strength. Therefore, it can be reported that concrete strength influences the bond strength up to a certain limit (almost 40 MPa) beyond which there is no further improvement of bond strength with the increase of concrete strength. This may be attributed to change the failure mode.
- For high strength concrete, a little increase occurred in bond strength with increasing the concrete cover thickness in both GFRP types.

Chapter 5

Experimental results and discussions of hinged beams

5.1 Introduction

Very limited data are available in the literature regarding bond properties of FRP bars measured using a hinged beam test due to the complication of specimen preparation and test. No study has been conducted on high-strength concrete hinged beams to investigate bond behaviour of FRP bars. Therefore, this chapter aims to investigate bond behaviour of GFRP bars in high strength concrete using hinged beams. The preparation and test set-up of hinged beams were characterized in chapter 3. This chapter presents the experimental results of 24 HSC hinged beams reinforced with GFRP bars, including bond behaviour, failure mode and analysis of the effect of the following parameters: bar diameter (9.5, 12.7 and 15.9 mm), embedment length (5 and 10 times bar diameter), surface configuration (helical wrapping with slight sand coating (HW-SC) and sand coating (SC)) and bar location (top and bottom) on bond strength. Four hinged beams reinforced with 16 mm steel bars were also presented for comparison purposes.

5.2 Experimental results

Test specimens, material properties, specimen preparation, test setup and testing procedure were described in chapter 3. The estimation of bond stress and the corresponding unloaded end slip were also detailed in chapter 3. The bond stress

- slip relationships were developed and plotted using measured data. The maximum applied load (F_{max}), the maximum bond stress (τ_{max}) with the corresponding free end slip (s_{ul}) and failure mode are presented in Tables 5.1 (for type A specimens) and 5.2 (for type B specimens). The average cube compressive strength of concrete C1 and C2 obtained from testing ten cubes were 97.38 MPa and 81.74 MPa respectively at the testing day of hinged beams, while the splitting tensile strength of concrete C1 and C2 obtained from testing five cylinders were 4.13 MPa and 3.24 MPa respectively at the testing day of hinged beams. The definition of beam notation is as follows: the first letter denotes the bar type (A for GFRP (HW-SC), B for GFRP (SC) and C for steel); the first number indicates the bar diameter; the third one denotes the embedment length and the last letter refers to the bar position (B for bottom and T for top bar location).

Table 5.1 - Bond test results of GFRP (type A) and steel bars in concrete C1

Beam label.	F_{max} (kN)	τ_{max} (MPa)	s_{ul} (mm)	Failure mode
A-9.5-5d-B	30.56	26.94	0.536	Pull-out
A-9.5-5d-T	29.43	25.94	0.609	Pull-out
A-12.7-5d-B	45.39	22.39	4.426	Pull-out
A-12.7-5d-T	39.95	19.70	11.91	Pull-out
A-15.9-5d-B	55.09	20.80	0.213	Pull-out
A-15.9-5d-T	48.02	18.13	1.176	Pull-out
A-9.5-10d-B	65.49	28.86	0.642	Pull-out
A-9.5-10d-T	59.43	26.19	0.418	Pull-out
A-12.7-10d-B	68.91	16.99	2.33	Pull-out
A-12.7-10d-T	68.18	16.81	1.80	Pull-out
A-15.9-10d-B	82.35	15.55	0.119	Pull-out /Splitting
A-15.9-10d-T	81.41	15.37	0.263	Pull-out /Splitting
C-16-5d-B	69.92	>26.07	0.31	Shear
C-16-5d-T	64.54	>24.06	0.21	Shear

Table 5.2 - Bond test results of GFRP (type B) and steel bars in concrete C2

Beam label.	F_{max} (kN)	τ_{max} (MPa)	s_{ul} (mm)	Failure mode
B-9.5-5d-B	33.72	29.72	0.141	Pull-out
B-9.5-5d-T	33.20	29.26	0.11	Pull-out
B-12.7-5d-B	59.78	29.48	0.115	Pull-out
B-12.7-5d-T	49.30	24.31	0.316	Pull-out
B-15.9-5d-B	73.21	27.64	0.104	Pull-out
B-15.9-5d-T	52.22	19.72	0.12	Pull-out
B-9.5-10d-B	64.33	28.34	0.096	Pull-out
B-9.5-10d-T	58.46	25.76	0.1	Pull-out
B-12.7-10d-B	91.11	22.47	0.231	Pull-out
B-12.7-10d-T	83.94	20.70	0.073	Pull-out
B-15.9-10d-B	112.1	>21.16	0.053	Shear
B-15.9-10d-T	83.27	15.72	0.07	Pull-out
C-16-10d-B	109.2	>20.37	0.173	Yielding
C-16-10d-T	105.4	>19.65	0.088	Yielding

5.2.1 Bond stress – slip relationship

Bond stress – unloaded end slip curves for GFRP (type A) and GFRP (type B) reinforced hinged beams were plotted in Figures 5.1 and 5.2, respectively. Figure 5.3 presents the bond stress – unloaded end slip responses for steel reinforced hinged beams. In general, the bond stress – slip curves of identical specimens with differing bar position only are similar. The bond stress – slip relationships are presented according to bar diameter, embedment length, surface characteristics, bar position and bar type to observe the influence of these main parameters on the bond behaviour in the case of high strength concrete.

The general bond stress – slip behaviour is described by a high increase of initial bond stress without a significant slip in both GFRP types because of good

chemical adhesion between the bar surface and surrounding concrete. After the chemical adhesion is exhausted, bond stress continues to increase with a small slip increase until the peak point. At this stage, bearing and friction dominate to resist the pull-out load in the case of specimens reinforced with GFRP (HW-SC) bars, whereas for the GFRP (SC) reinforced hinged beams, only friction resistance controls the response. The post – peak bond stress of the GFRP (type A) reinforced specimens that failed by pull-out only decayed gradually with increasing free end slip in a controlled ductile way. For hinged beams having 12.7 mm bar diameter with embedment length of $10d_b$, their bond stress dropped suddenly with a sharp slip due to shear cracks subsequent to the pull-out failure. Also, the same softening trend occurred in specimens (A-15.9-10d-B/T), as a result of splitting cracks. The ascending curve was similar for all specimens having the same surface configuration. However, the descending curve varied with changing the failure mode. In addition, it was noted that the shape of bond stress – slip curve of GFRP (type A) bar changes with differing bar diameter. It may be attributed to the difference in the rib spacing with the bar diameter. For the sand coated GFRP reinforced specimens, the bond failure was relatively brittle and bond stress decayed abruptly to be almost zero accompanied with a loud bang owing to stripping of sand coated layer. The post – peak bond stress starts again to increase up to a certain value with an increase in the slip due to remaining frictional resistance. This trend was observed for all hinged beams reinforced with GFRP (type B), except two specimens (B-9.5-5d-B and B-12.7-5d-T), where their softening branches reduced smoothly because of the partial detaching of sand coating. Also, the sudden decrease in bond stress was noticed in hinged beam

(B-15.9-10d-B) due to shear failure. The residual stresses in GFRP (SC) reinforced hinged beams are lower than those in GFRP (HW-SC) reinforced hinged beams because of the full detachment of the sand coated layer, leading to a smooth surface that was not able to provide with much frictional resistance. The slip corresponding to the maximum bond stress obtained from GFRP (type A) reinforced specimens is higher than that obtained from GFRP (type B) reinforced specimens, indicating that the amount of slip is influenced by the surface treatment. The effect of surface properties on the slip was also confirmed by Lee et al. (2012) and Pepe et al. (2013). All specimens reinforced with steel bars exhibited high initial stiffness without a slip when chemical adhesion was dominant. Then, bond stress continued to increase with very little slip until failure. At this stage, mechanical interlock and friction controlled to resist the pull-out force. Unexpected failures occurred, such as shear failure prior to the bond failure in specimens having an embedment length of $5d_b$ and yielding happened before de-bonding, following by shear crack in steel reinforced hinged beams having an embedment length of $10d_b$, which in turn resulted in abruptly dropping the value of the bond stress as shown in Figure 5.3.

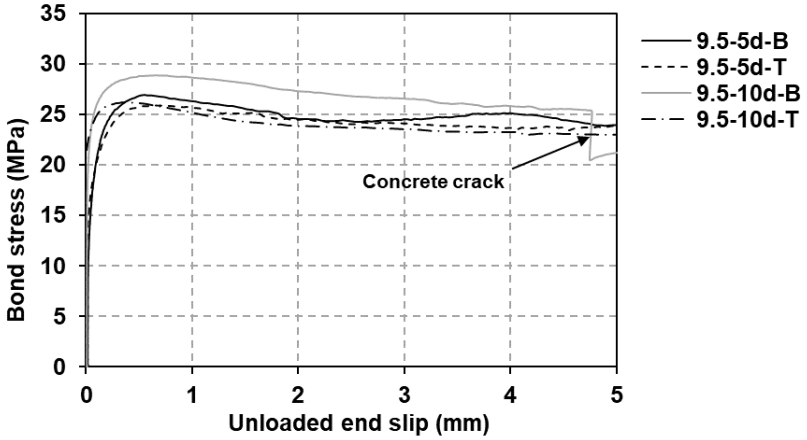

(a)

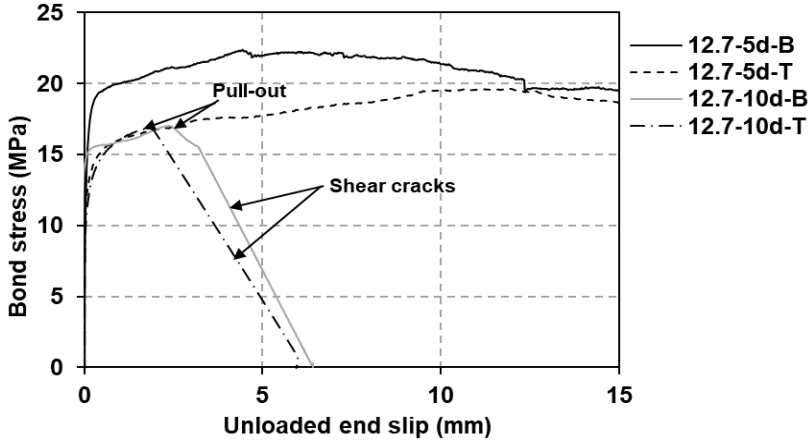

(b)

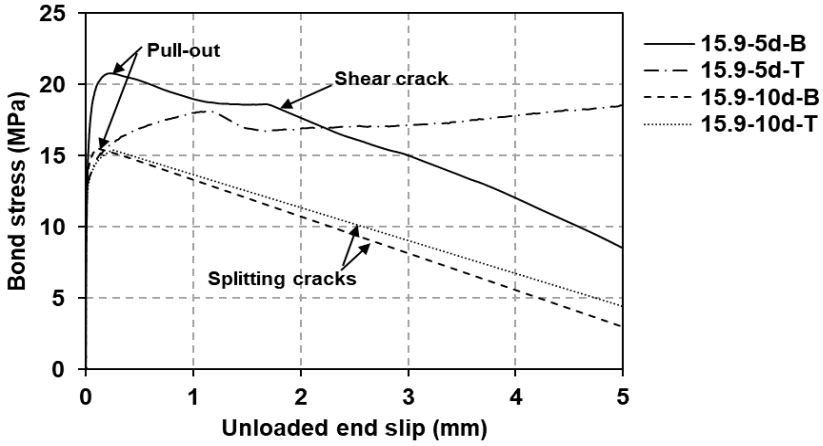

(c)

Figure 5.1 - Bond stress versus free end slip for GFRP (HW-SC) bars

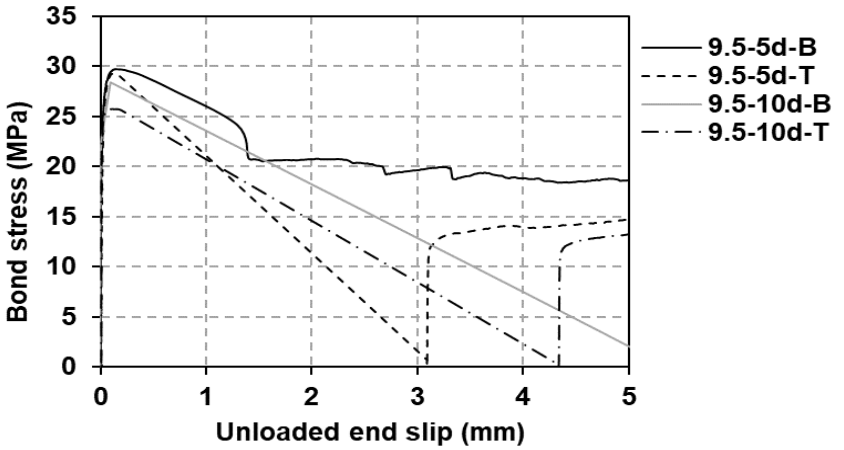

(a)

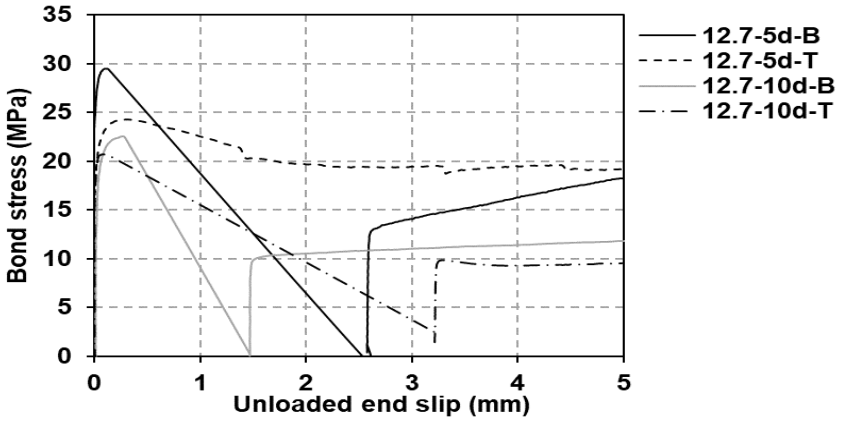

(b)

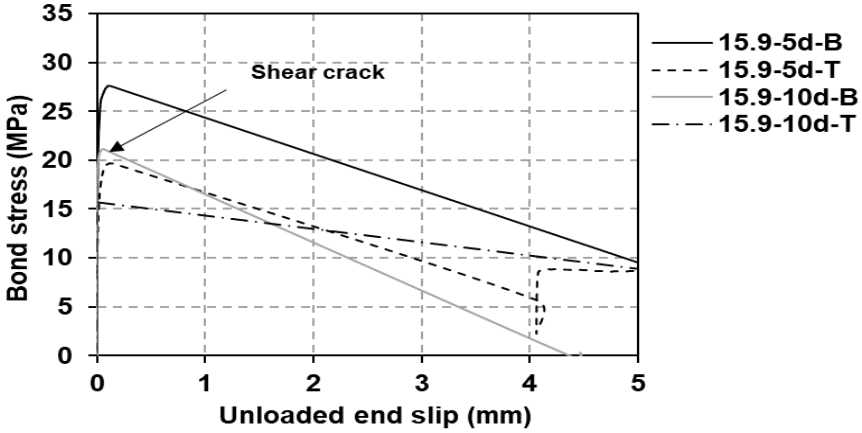

(c)

Figure 5.2 - Bond stress versus free end slip for GFRP (SC) bars

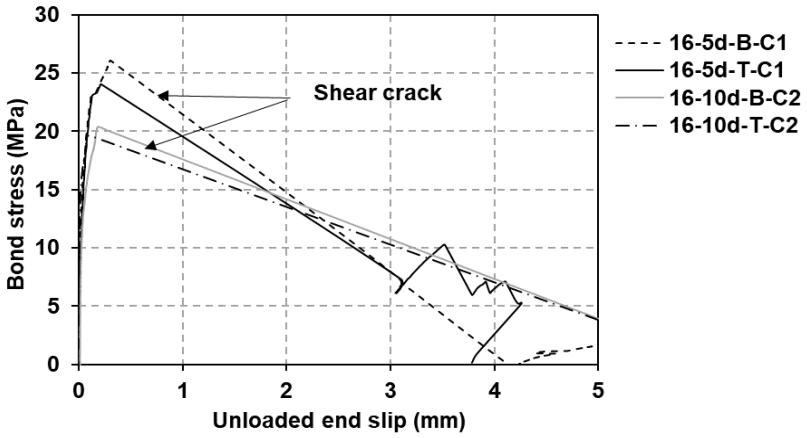

Figure 5.3 - Bond stress versus free end slip for steel bars

5.2.2 Bond failure mechanism

The failure mode observed for each hinged beam is listed in Tables 5.1 and 5.2. Most specimens failed by a pull-out mode as shown in Figures 5.4 (a) and 5.5 (a), except for the specimens reinforced with steel bars (C-16-5d-B/T) and specimen (B-15.9-10d-B) that failed by shear cracks as illustrated in Figure 5.5 (b and c). For specimens (A-15.9-10d-B/T), pull-out failure accompanied with splitting cracks was observed as indicated in Figure 5.4 (c). While the specimens (A-12.7-10d-B/T) and (A-15.9-5d-B) failed by a pull-out mode followed by narrow diagonal cracks as shown in Figure 5.4 (b). Steel reinforced hinged beams having an embedment length of $10d_b$ failed by yielding, followed by shear cracks.

To understand failure mechanism, some hinged beams were split into two parts after testing. The outer surface of the GFRP reinforcing bar and the surrounding concrete within the embedded portion were inspected for providing useful information about the interaction phenomena. For helically wrapped with slightly sand coating GFRP reinforced specimens, some abrasions were noted on the

outer layer with stripping of sand coated layer as described in Figure 5.6 (b). In addition, there was white residue on the trace of the whole embedment length, indicating crushing of resin. However, the specimens with longer embedment lengths failed by a damage of fibres as shown in Figure 5.6 (a). No apparent crushing of the surrounding concrete was monitored. As for specimens reinforced with sand coated GFRP bars, it was found that the concrete also remained uncrushed and sand grains detached completely as shown in Figure 5.6 (c), indicating that the bond strength between the outer layer and bar core is lower than that between the high-strength concrete and sand coating.

(a)

(b)

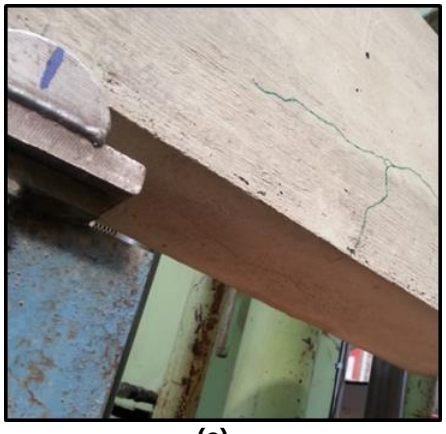

(c)

Figure 5.4 - (a) Pull-out failure of GFRP (HW-SC) reinforced specimen, (b) Narrow shear cracks in specimen (A-12.7-10d-T/B) and (c) Splitting failure in specimen (A-15.9-10d-T/B)

(a)

(b)

(c)

Figure 5.5 - (a) Pull-out failure of GFRP (SC) reinforced specimen, (b) Shear crack in specimen (B-15.9-10d-B) and (c) Shear failure in steel reinforced specimen

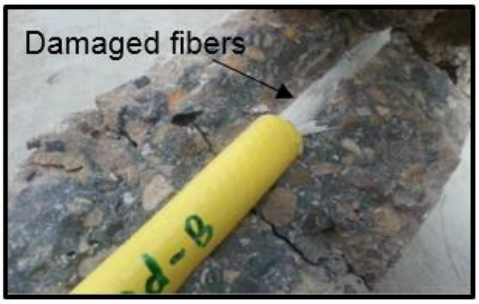

(a) Specimen (A-9.5-10d-B)

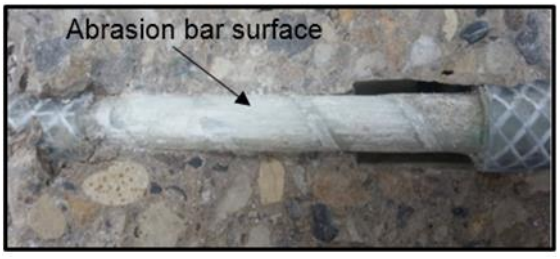

(b) Specimen (A-12.7-5d-B)

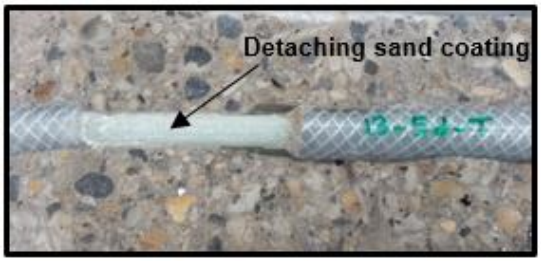

(c) Specimen (B-12.7-5d-T)

Figure 5.6 - Visual inspection for the specimens failed by pull-out

5.3 Factors influencing bond strength

5.3.1 Effect of embedment length on bond strength

In general, bond strength reduces with increasing bonded length as shown in Figures 5.7 and 5.8 because of non-linear distribution of bond stresses along the embedment length. This finding was confirmed by the results of Tighiouart et al. (1998). As the load increases, the bond stress at the vicinity of the unloaded end increases owing to the redistribution of shear stresses along the embedment length (Benmokrane et al., 1996). It is noticed that the reduction rate of bond strength of GFRP (HW-SC) reinforced specimens is approximately constant for all bar sizes, except for the 9.5 mm bar diameter. It is 24% and 15% for bottom and top bar positions, respectively. However, for GFRP (SC) reinforced specimens, the reduction rate of bond strength in smaller bar diameters is lower than that in larger bar diameters. It is in the range of 5% to 24% and 12% to 20% for the bottom and top bar positions, respectively. The bond strengths of sand coated and helically wrapped with slightly sand coated GFRP bars measured in the current investigation are much higher than those observed in the literature

(Benmokrane et al., 1996, Tighiouart et al., 1998) due to the high strength concrete of the current investigation and different surface configuration.

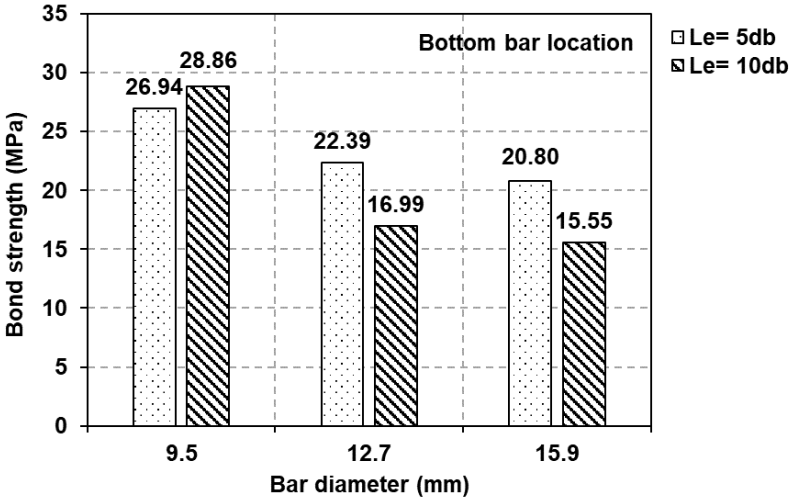

(a)

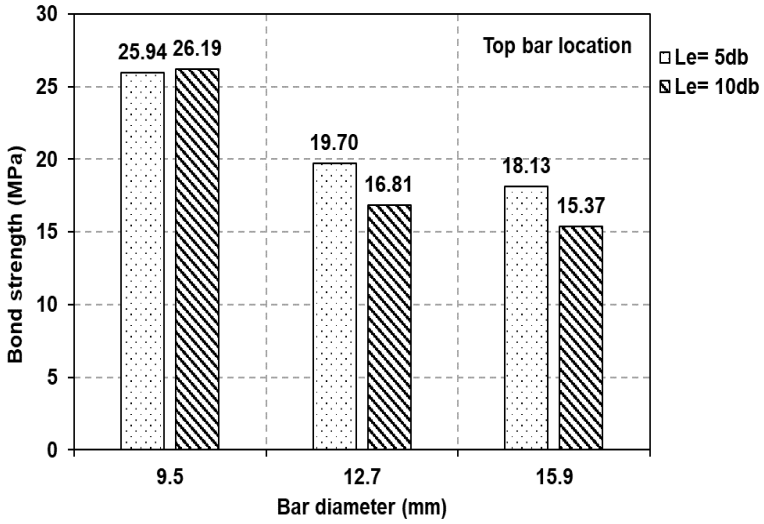

(b)

Figure 5.7 - Effect of the embedment length and bar diameter on the average bond strength of GFRP (HW-SC) bars (a) Bottom bar position and (b) Top bar position

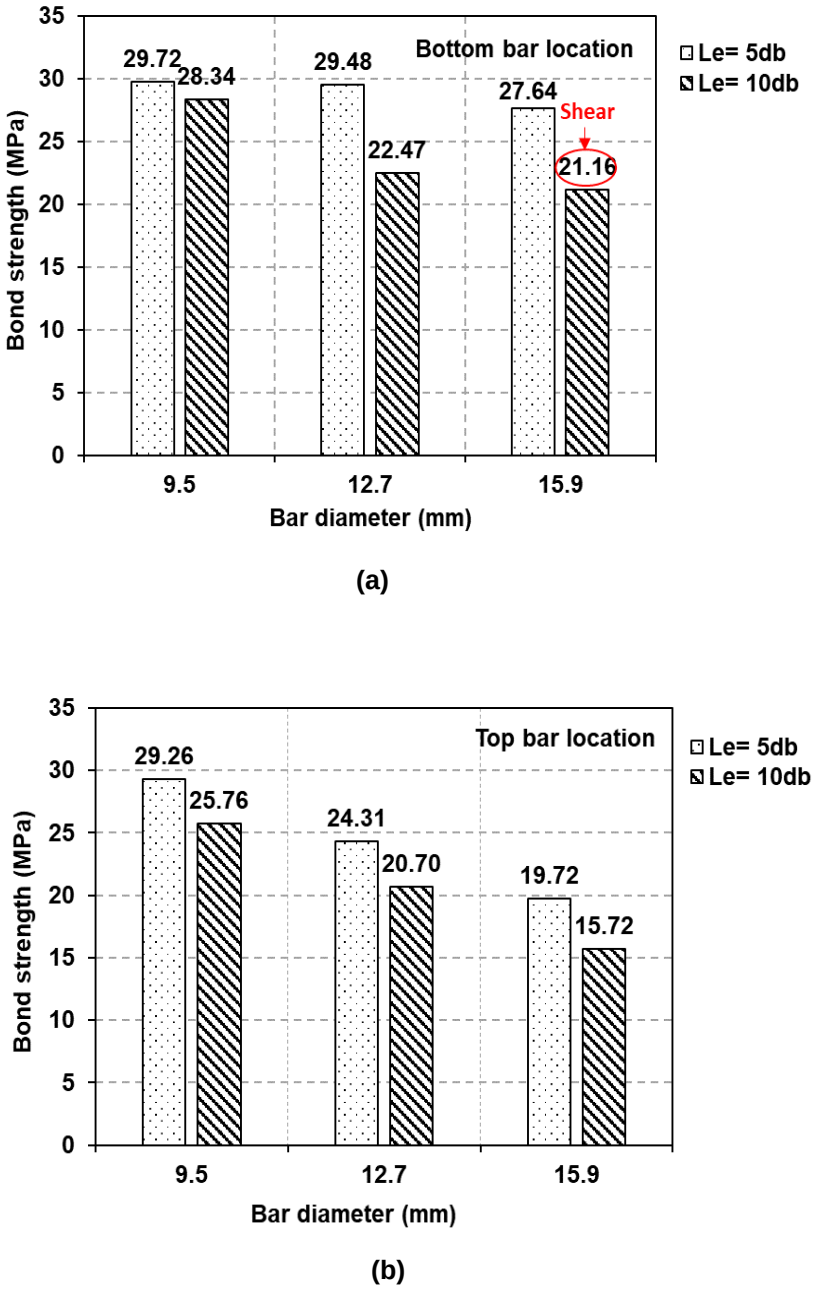

Figure 5.8 - Effect of the embedment length and bar diameter on the average bond strength of GFRP (SC) bars (a) Bottom bar position and (b) Top bar position

5.3.2 Effect of bar diameter on bond strength

It can be seen from Figures 5.7 and 5.8 that the maximum bond stress increases for smaller bar diameters, agreeing with previous investigations on FRP and steel

bars (Achillides, 1998, Tighiouart et al., 1998, Benmokrane et al., 1996, Baena et al., 2009, Okelo and Yuan, 2005). This phenomenon occurs due to bleeding of water underneath the bar, creating voids which in turn result in reducing the contact area between the bar and the concrete (Tighiouart et al., 1998). The quantity of bleeding water trapped beneath larger bar diameters is greater than smaller ones. Therefore, the bond strength in larger bar diameters is lower than that in smaller bar diameters. For high strength concrete, the reduction rate in bond strength decreased with increasing bar diameter in GFRP (type A) reinforced specimens and bottom casting specimens reinforced with GFRP (type B) bars. The same conclusion was also reported by Lee et al. (2017) for pull-out specimens, whereas, a constant reduction rate in bond strength was observed in specimens having GFRP (type B) top bars.

5.3.3 Effect of bar position on bond strength

Figures 5.9 and 5.10 show the distribution of ratios of the maximum bond stress of the bottom bars to that of the top bars for both GFRP types. Top - cast bar specimens have bond strengths slightly lower than those of bottom - cast bar specimens because the concrete slump was not as high as other investigations (Pay et al., 2014, Ferguson and Thompson, 1962, Jirsa et al., 1982), therefore, bleeding water was not a major effect. It was observed that an average reduction in bond strength is 7% and 15% for GFRP (Type A) and GFRP (Type B), respectively. The most significant reduction (14%) was measured in GFRP (HW-SC) reinforced specimens having 12.7 mm and 15.9 mm bar diameters and $5d_b$ embedment length. As the bonded length increased to $10d_b$, the ratio decreased

leading to only a 1% strength reduction, while, it is 17% and 28% for GFRP (SC) reinforced specimens with 12.7 mm and 15.9 mm bar diameters, respectively, and $5d_b$ bonded length. This reduction in bond strength is owing to bleeding water and segregation close to the top layers of concrete. Therefore, the concrete surrounding the top bars is less consolidated compared to that surrounding the bottom bars, a similar conclusion was obtained by Chaallal and Benmokrane (1993), Ehsani et al. (1996b), and Tighiouart et al. (1998) from conducting the pull-out tests, and by Pay et al. (2014) from testing lap-splice beams.

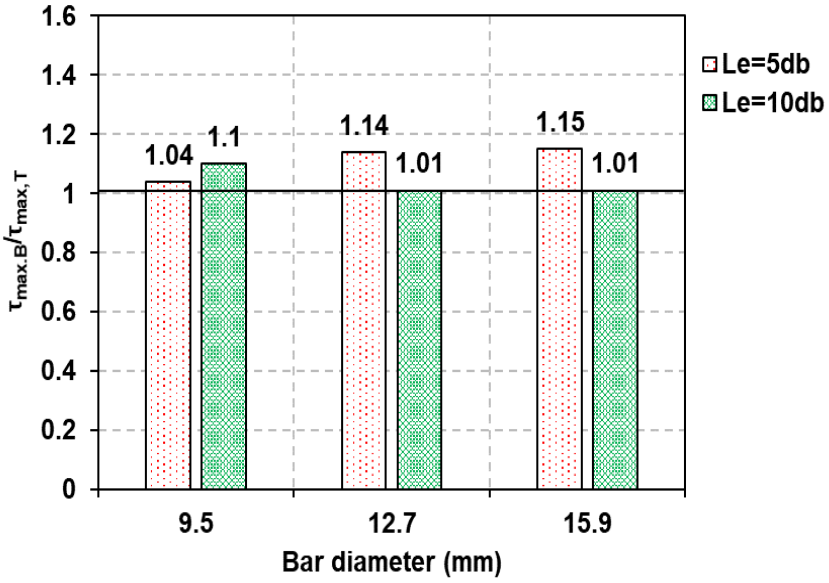

Figure 5.9 - Comparison between bond strengths of GFRP (HW-SC) bottom bars and top bars

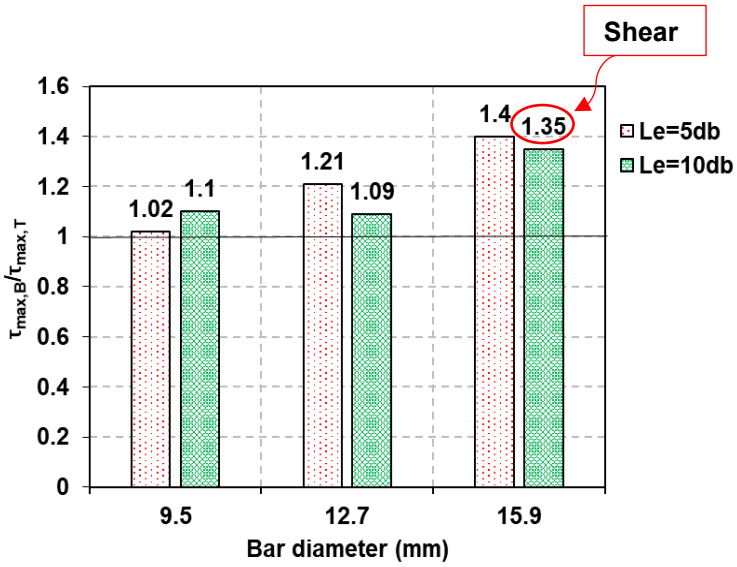

Figure 5.10 - Comparison between bond strengths of GFRP (SC) bottom bars and top bars

5.3.4 Effect of bar surface on bond strength

From Figures 5.11 and 5.12, it can be seen that the bond strength of GFRP (SC) bars is higher than that of GFRP (HW-SC) bars owing to their sand coating surface. The ratio varied from 1.1 to 1.36 and from 1.02 to 1.23 based on bar diameter and embedment length for the bottom and top bars, respectively. However, the corresponding slip for GFRP (SC) surface is smaller than that for GFRP (HW-SC) surface as demonstrated in Tables 5.1 and 5.2. It can be reported that sand coating improves the bond performance better than helical wrapping as also reported by Cosenza et al. (1997) and Davalos et al. (2008). However, Lee et al. (2012) found that the bond strength of GFRP (HW-SC) bars is higher than that of GFRP (SC) bars for concrete strengths (25, 40 and 70 MPa) from testing pull-out specimens.

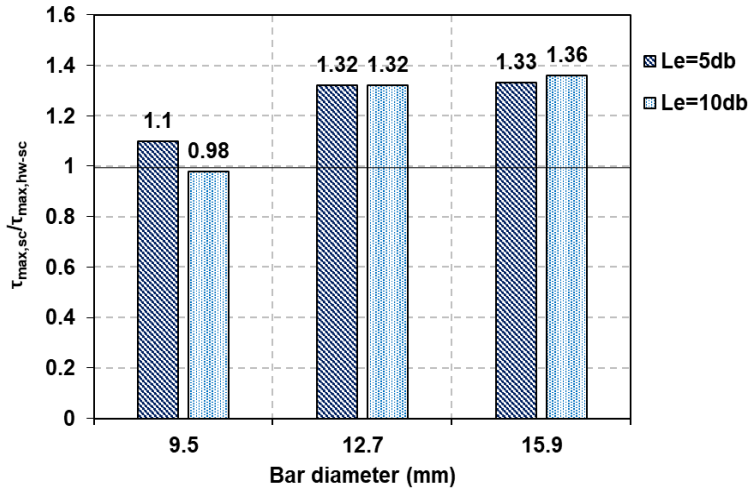

Figure 5.11 - Comparison between bond strengths of GFRP (SC) and GFRP (HW-SC) surfaces for bottom bars

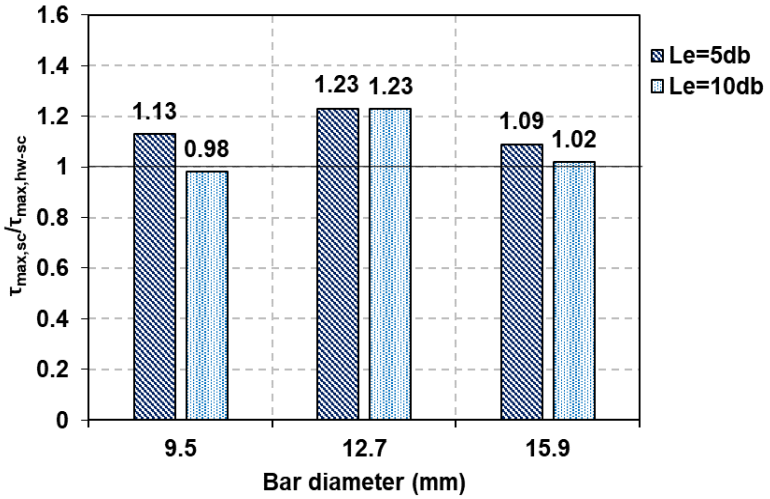

Figure 5.12 - Comparison between bond strengths of GFRP (SC) and GFRP (HW-SC) surfaces for top bars

5.4 Conclusions

Test results of 28 HSC hinged beams reinforced with GFRP and steel bars have been presented and discussed in this chapter. The parameters investigated were diameter, embedment length, surface configuration and position of reinforcing bars. The following conclusions are drawn:

1. Pull-out failure was observed in most specimens. Bond failure was governed by damage of the outer layer of GFRP (HW-SC) bars, while it was due to detachment of sand grains on the GFRP (SC) surface.
2. Both GFRP types showed different interfacial bond behaviours. After the peak bond stress, the GFRP (HW-SC) bars showed a gradual reduction in bond stresses due to friction resistance, whereas the GFRP (SC) bars showed a sudden bond failure with the complete loss of bond resistance because of stripping of the sand grains.
3. The bond strength of GFRP (SC) bars is higher than that of GFRP (HW-SC) bars. However, the corresponding slip for GFRP (SC) bars is less than that for GFRP (HW-SC) bars.
4. Bond strength reduces with increasing embedment length and bar diameter. For high strength concrete, the reduction rate in bond strength decreased with increasing bar size in all specimens, except top-cast specimens reinforced with GFRP (SC) bars having a constant reduction rate.
5. Top-cast specimens exhibited slightly lower bond strengths (average 7% and 15% reduction for GFRP (HW-SC) and GFRP (SC), respectively) than bottom-cast specimens.

Chapter 6

Correlation between pull-out test and hinged beam test

6.1 Introduction

The experimental results obtained from the pull-out and hinged beam tests are fully described in chapters 4 and 5, respectively. This chapter aims to compare the bond strengths measured by a hinged beam test with those measured by a pull-out test. A comparison among the bond stress - slip curves obtained from testing a pull-out cube, pull-out prism and bottom – cast hinged beam is also presented with keeping the critical parameters (bar diameter, embedment length and surface configuration) constant in order to analyze the effect of test method and specimen size on the bond behaviour. Finite element analysis is also presented to predict the pull-out force acting on the bar in the hinged beam and to examine the tensile and bond stress distributions along the embedment length in the pull-out cube, pull-out prism and hinged beam.

6.2 Comparison between test methods

For comparative purposes, tested hinged beams were not provided with transverse reinforcement as recommended by the RILEM specification. Thus, the contribution of transverse reinforcement in increasing the bond strength was omitted to make the parameters that influence bond strength in hinged beam specimens the same as those in pull-out specimens. The pull-out prisms had the same geometrical dimensions as hinged beams (type I), however, the dimensions

of pull-out cubes were different. The same machine was used to test the pull-out and hinged beam specimens. In the pull-out test, the tensile load was applied directly to the bar as shown in Figure 3.11 (a and b), refer to chapter 3. The reaction of the tensile load was transferred to the concrete block by a steel plate. As a result of this, the concrete surrounding the bar was under compressive stress. In the hinged beam test, two equal forces were applied symmetrically on either side of a steel hinge as illustrated in Figure 3.13, see chapter 3. Subsequently, the tensile force acting on the bar was produced from bending moment and the concrete surrounding the bar was under tensile stress. In the pull-out specimen, three LVDTs were attached to the bar at the top of the specimen to measure the loaded end slip and only one LVDT was placed at the bottom of the specimen to measure the unloaded end slip. One LVDT at each side of hinged beam was attached to the bar to measure the unloaded end slip. The displacement - control mode was selected for both test methods to obtain the post - peak behaviour. The loading rate for a pull-out test was kept at 0.02 mm/sec until the head movement of the machine reached to 15 mm. As pull-out failure occurred, the loading rate was changed to accelerate the test to be 0.05 mm/sec and 0.1 mm/sec for the head movement 30 mm and 45 mm, respectively, while the loading rate for a hinged beam test was 0.02 mm/sec and it was kept constant until complete failure occurred.

6.3 Comparison of bond stress – slip responses

Figures 6.1 to 6.7 show the bond stress versus free end slip relationships for pull-out specimens and bottom - cast hinged beams reinforced with GFRP (type A),

GFRP (type B) and steel bars in high strength concrete. According to the experimental results, it can be seen that all cubes, prisms and hinged beams reinforced with both GFRP types display similar behaviour consisting of high initial stiffness and nonlinear behaviour prior to the peak point, regardless of bar diameter, embedment length and surface characteristics. In general, a higher bond strength is observed in hinged beams, followed by cubes and then prisms. The corresponding slip value in prisms is higher than that in cubes and hinged beams. The softening curves are similar for all specimens having the same parameters and failed by a pull-out mode, whereas they are different with a differing failure mode. From Figures 6.1 to 6.6, it can be observed that the post – peak bond stress for all GFRP (type A) reinforced specimens failed by a pull-out mode deteriorated gradually with increasing the unloaded end slip. However, it dropped suddenly in GFRP (type A) reinforced specimens that failed by a pull-out mode accompanied by concrete cracks. All GFRP (type B) reinforced specimens failed by pull-out, the descending bond stress dropped suddenly with a strong unloaded end slip owing to stripping the sand coating abruptly. Generally, the residual stresses in hinged beams are higher than those in pull-out specimens for both GFRP types. The comparison of the bond stress – free end slip curves for specimens reinforced with steel bars is not performed because of different failure modes as shown in Figure 6.7, where hinged beams were failed by shear cracks and pull-out cubes having the bonded length of $10d_b$ were failed by yielding. Whilst a pull-out failure occurred only in the concrete cubes having the embedment length of $5d_b$.

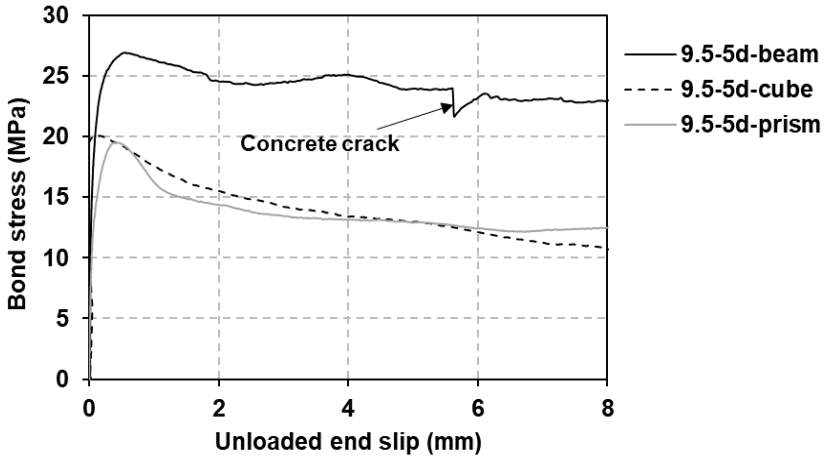

(a)

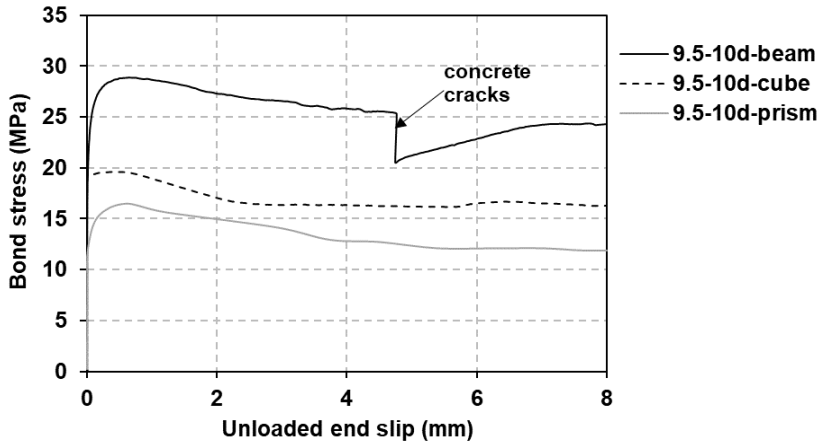

(b)

Figure 6.1 - Bond stress versus slip curves for specimens reinforced with 9.5 mm GFRP (type A) bars with different embedment lengths

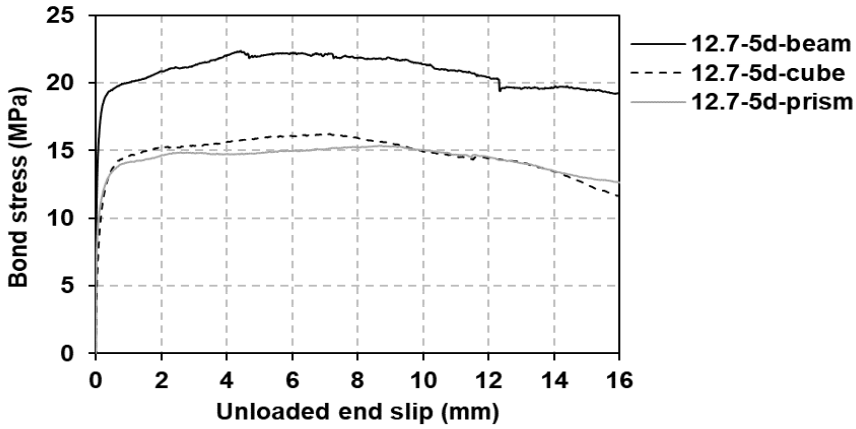

(a)

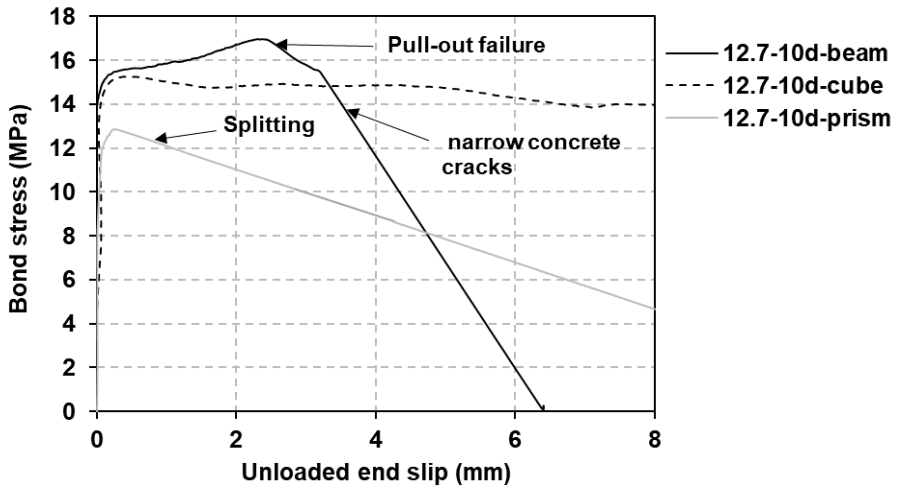

(b)

Figure 6.2 - Bond stress versus slip curves for specimens reinforced with 12.7 mm GFRP (type A) bars with different embedment lengths

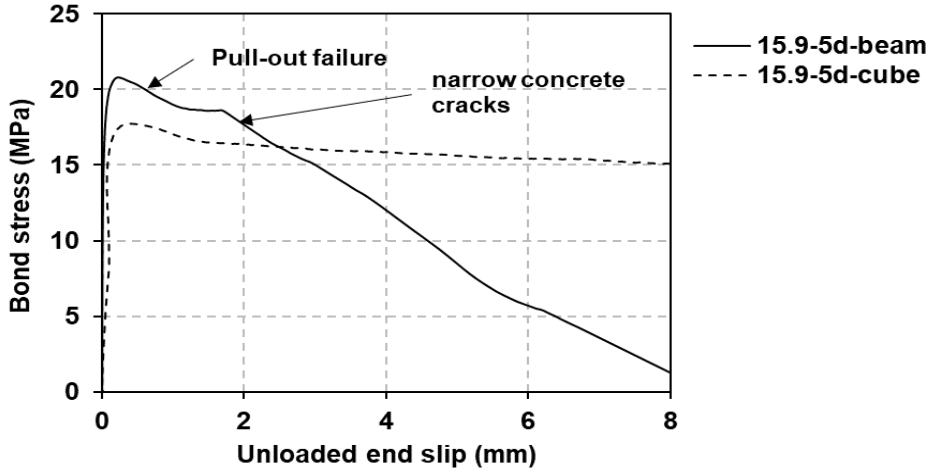

(a)

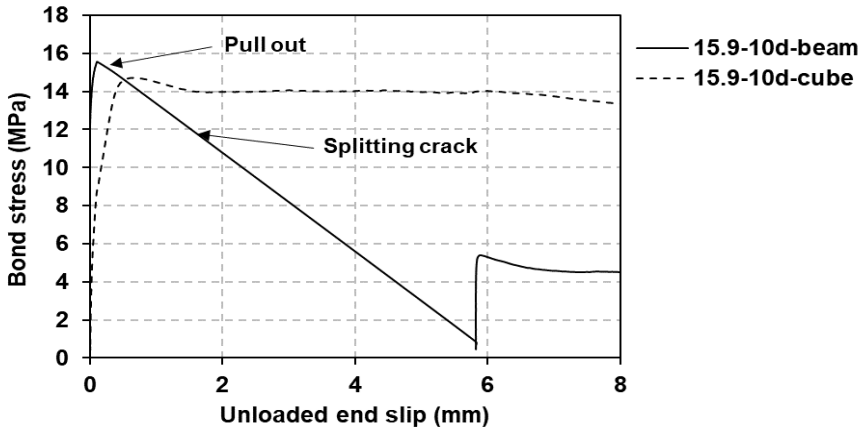

(b)

Figure 6.3 - Bond stress versus slip curves for specimens reinforced with 15.9 mm GFRP (type A) bars with different embedment lengths

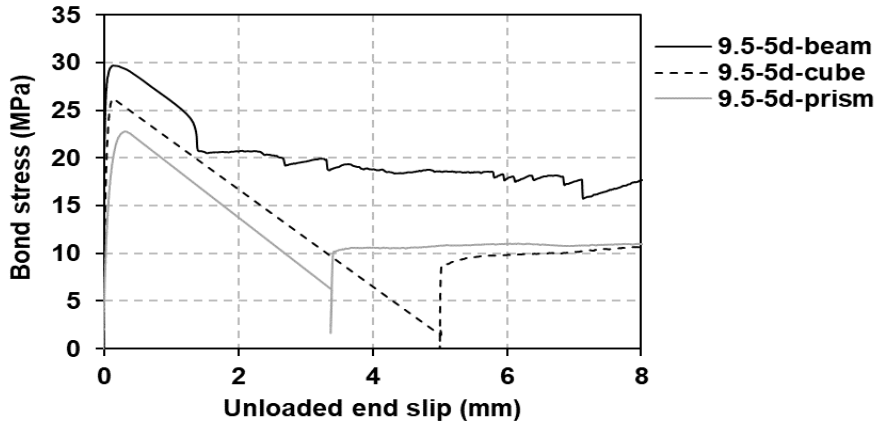

(a)

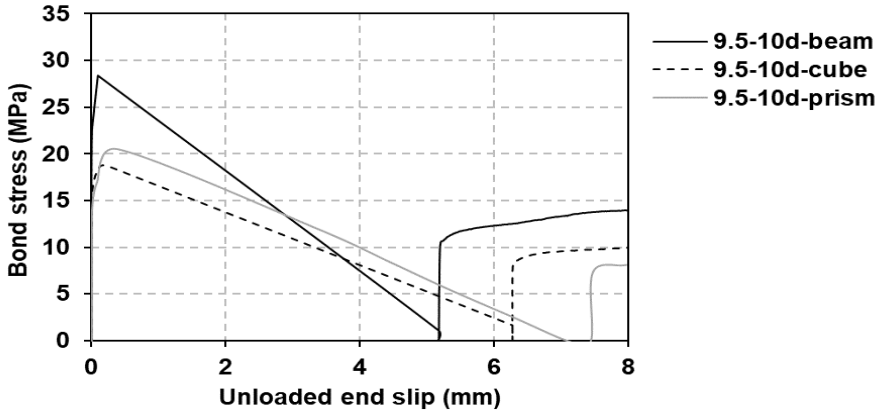

(b)

Figure 6.4 - Bond stress versus slip curves for specimens reinforced with 9.5 mm GFRP (type B) bars with different embedment lengths

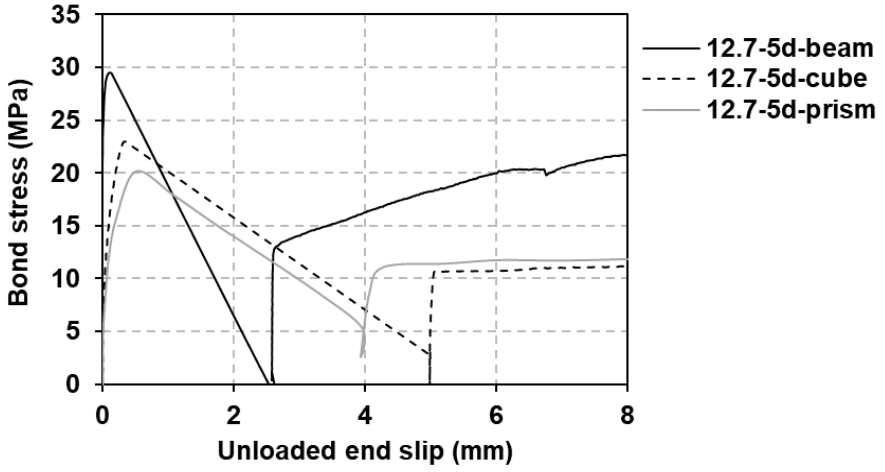

(a)

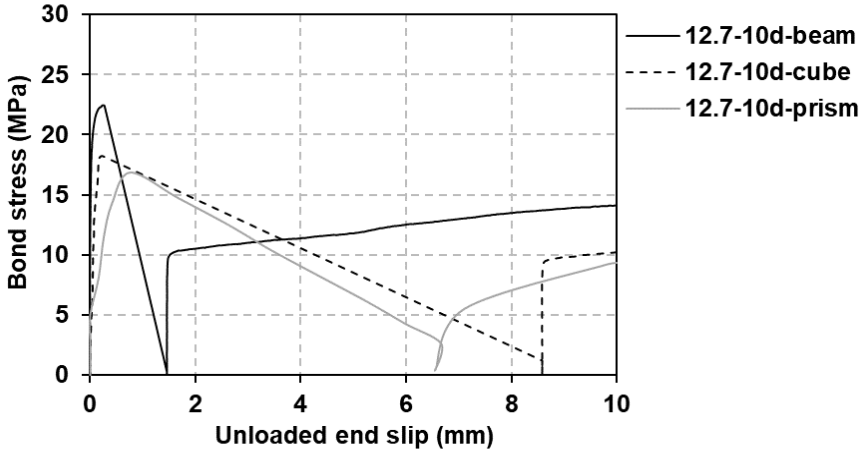

(b)

Figure 6.5 - Bond stress versus slip curves for specimens reinforced with 12.7 mm GFRP (type B) bars with different embedment lengths

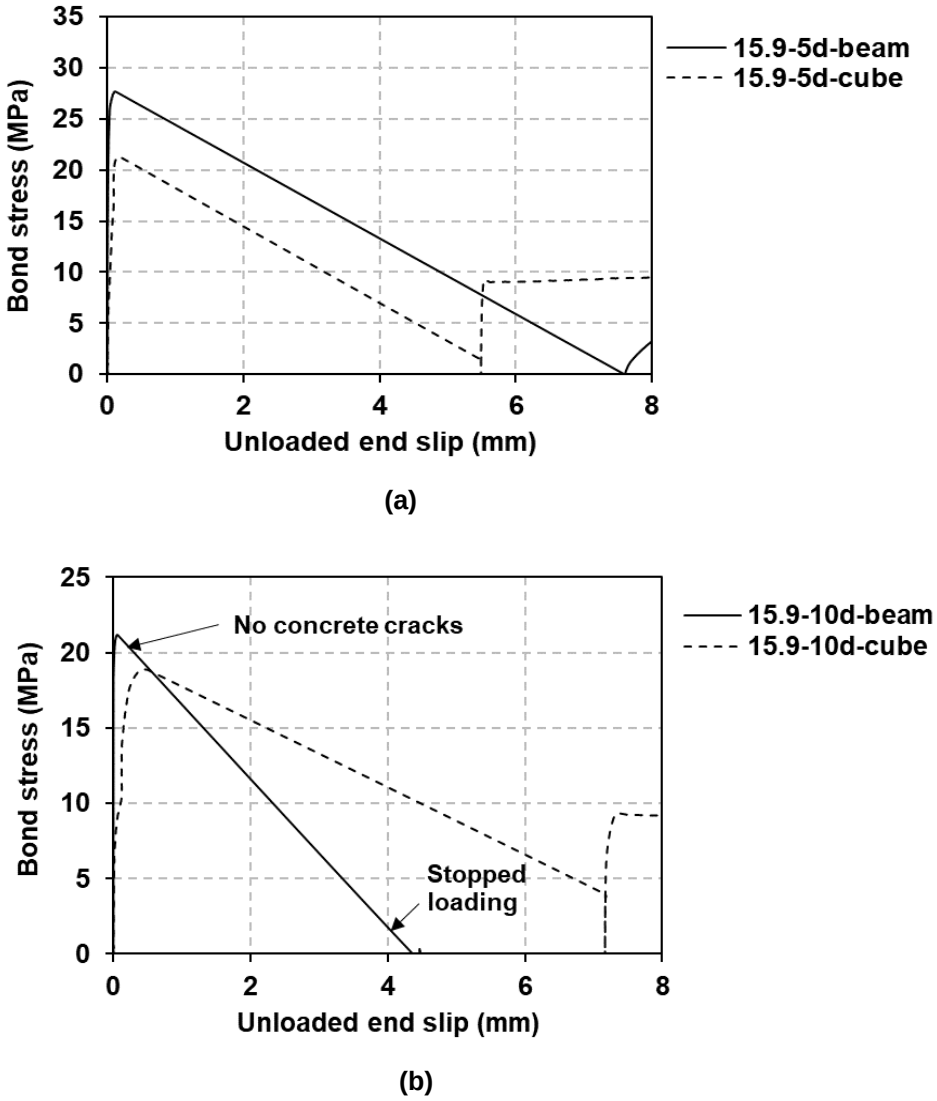

Figure 6.6 - Bond stress versus slip curves for specimens reinforced with 15.9 mm GFRP (type B) bars with different embedment lengths

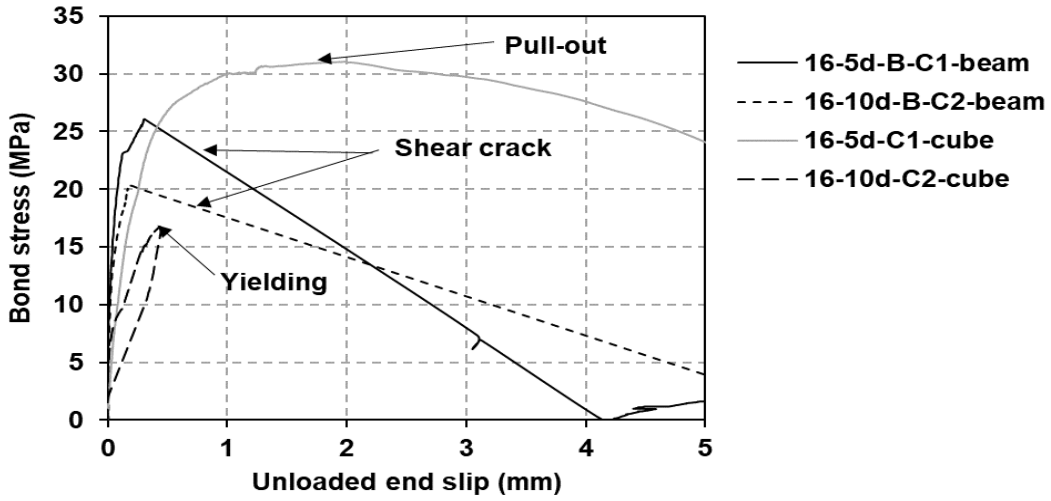

Figure 6.7 - Bond stress versus slip curves for specimens reinforced with 16 mm steel bars with different embedment lengths

6.4 Comparison of bond failure mechanisms

As previously mentioned in chapters 4 and 5, most of the pull-out specimens and hinged beams reinforced with GFRP bars failed by a pull-out mode as illustrated in Figure 6.8, except for B-15.9-10d hinged beam that failed by a shear crack because of reaching its concrete shear capacity before the maximum pull-out load. In addition, a splitting failure was observed in the A-12.7-10d prism. The A-15.9-10d hinged beam failed by a pull-out accompanied by concrete splitting. Overall, it can be stated that both pull-out and hinged beam specimens had the same failure mode. The bond failure in GFRP (type A) reinforced pull-out and beam specimens occurred due to damage of the outer surface of the GFRP (type A) bar as indicated in Figure 6.9 (a, b and e). In the pull-out specimens and hinged beams reinforced with the GFRP (type B) bars, the detachment of sand coating was observed. Thus, this resulted in breaking the interface between the concrete

and the bar as shown in Figure 6.9 (c, d and f). Generally, it can be concluded that both pull-out and hinged beam specimens have similar bond failure.

(a)

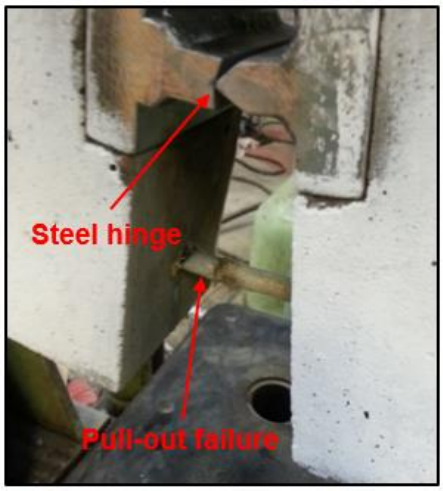

(b)

Figure 6.8 - Pull-out failure in (a) Pull-out specimen and (b) Hinged beam

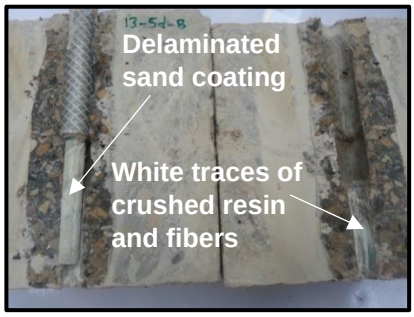

(a) Cube (A-12.7-5d)

(b) Hinged beam (A-12.7-5d-B)

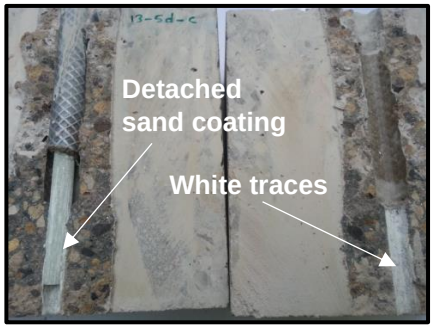

(c) Cube (B-12.7-5d)

(d) Hinged beam (B-12.7-5d)

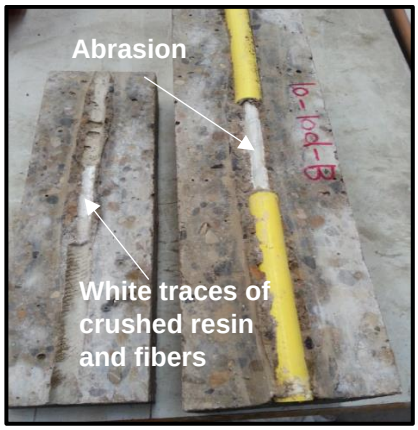

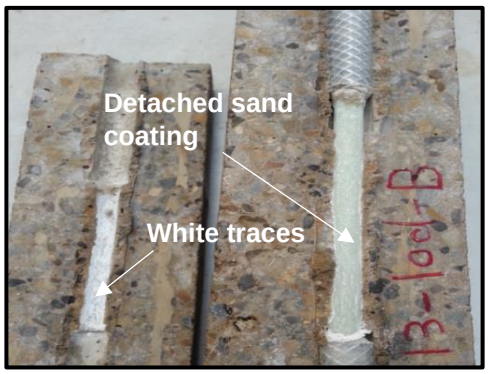

(e) Prism (A-9.5-10d) **(f) Prism (B-12.7-10d)**

Figure 6.9 - Visual inspection for specimens failed by pull-out

6.5 Comparison of bond strengths

Tables 6.1 and 6.2 summarize the experimental results of GFRP (type A) and GFRP (type B) bars embedded in high strength concrete, which were obtained from pull-out and hinged beam tests. The definition of specimen notation is described in Figure 6.10. From Table 6.1, it is noted that the concrete strength for prism specimens is lower than the concrete strength for cubes and hinged beams due to different concrete batches. Bottom-cast hinged beams were selected instead of top-cast hinged beams to compare their bond strengths with those for the pull-out specimens. This is because of no water bleeding in the bottom-cast hinged beams, like the pull-out specimens. Tensile forces acting on the bar in hinged beams shown in Tables 6.1 and 6.2 were calculated using equilibrium forces as recommended by the RILEM specification. It can be seen that the bond strength performed by a hinged beam is higher than that performed by a pull-out cube and a pull-out prism in both GFRP types as illustrated in Figures 6.11 and

6.12. The ratio of the bond strength in the hinged beam to the bond strength in the cube is in the range of 1.05 to 1.50 for GFRP (type A) bars and 1.16 to 1.49 for GFRP (type B) bars. The ratio of 1.12 shown in Figure 6.11 (b) is not considered because of different failures (shear failure observed in the hinged beam and pull-out failure observed in the cube). The ratio of the bond strength obtained from a hinged beam to that obtained from a pull-out prism is varied from 1.38 to 1.75 and 1.30 to 1.46 for GFRP (type A) and GFRP (type B) bars, respectively. The ratio of 1.32 shown in Figure 6.12 (a) also is not considered because of different failures (splitting observed in the prism and pull-out observed in the hinged beam). The variation of these ratios depends on bar diameter, embedment length, bar surface and specimen size. In addition, these ratios are influenced by the rate of variation in bond strengths with changing bar diameter and embedment length in both pull-out specimens and hinged beams. Therefore, no significant trend is monitored. The results obtained by Chan (2012) found that the bond strength of the hinged beam is higher than the bond strength of the pull-out cube reinforced with steel bars in high strength concrete (around 50 MPa). Furthermore, it was reported that the bond strength of the pull-out tests was lower than the bond strength achieved by the hinged beam tests during investigating glass fibre reinforced polymer bars embedded in high performance and ultra-high-performance concrete (Ametrano et al., 2011). This was attributed to performing the pull-out test in unconfined concrete, while the hinged beam tests had a large amount of internal reinforcement which in turn provided confinement, thus increasing the bond strength (Ametrano et al., 2011). However, Tighiouart et al. (1998) found that the ratio of the bond strength of the pull-out specimen to the

bond strength of the hinged beam reinforced with GFRP bars in normal concrete strength of 31 MPa changed from 1.05 to 1.84, depending on bar diameter. This was because of concrete surrounding the bar subjected to compressive stresses in the pull-out test, thus reducing the cracking and increasing the bond strength. It was subjected to tensile stresses in the hinged beam test and this led to cracking, which in turn decreased the bond strength (Tighiouart et al., 1998). A different conclusion was obtained by de Almeida Filho et al. (2008), the pull-out tests gave approximately the same results as the hinged beam tests when investigating the bond properties at the interface between steel bars and normal strength concrete.

Table 6.1 - Summary of bond strengths in pull-out cubes, pull-out prisms and hinged beams reinforced with GFRP (type A) bars

Specimen label	Concrete cover (mm)	f_{cu} (MPa)	F_{max} (kN)	T_{max} (kN)	τ_{max} (MPa)	Failure mode
A-9.5-5d-C1-cube	95.25	97.38	28.47	28.47	20.08	PO
A-9.5-5d-C2-prism	45.25	79.97	27.66	27.66	19.51	PO
A-9.5-5d-C1-beam	45.25	97.38	30.56	38.2	26.94	PO
A-9.5-10d-C1cube	95.25	97.38	54.67	54.67	19.27	PO
A-9.5-10d-C2-prism	45.25	79.97	46.72	46.72	16.47	PO
A-9.5-10d-C1-beam	45.25	97.38	65.49	81.86	28.86	PO
A-12.7-5d-C1-cube	93.65	97.72	40.88	40.88	16.13	PO
A-12.7-5d-C2-prism	43.65	79.97	38.97	38.97	15.38	PO
A-12.7-5d-C1-beam	43.65	97.38	45.39	56.74	22.39	PO
A-12.7-10d-C1-cube	93.65	97.72	81.37	81.37	16.05	PO
A-12.7-10d-C2-prism	43.65	79.97	65.31	65.31	12.88	SP
A-12.7-10d-C1-beam	43.65	97.38	68.91	86.14	16.99	PO
A-15.9-5d-C1-cube	92.05	101.68	74.30	74.30	18.70	PO
A-15.9-5d-C1-beam	42.05	97.38	55.09	82.64	20.80	PO
A-15.9-10d-C1-cube	92.05	102.36	117.77	117.77	14.82	PO
A-15.9-10d-C1-beam	42.05	97.38	82.35	123.53	15.55	PO/SP

Note: f_{cu} is the cube compressive strength of concrete (MPa); F_{max} is failure load (kN); T_{max} is the ultimate tensile force acting on the bar (kN) and τ_{max} is the bond strength (MPa).

Table 6.2 - Summary of bond strengths in pull-out cubes, pull-out prisms and hinged beams reinforced with GFRP (type B) bars

Specimen label	Concrete cover (mm)	f_{cu} (MPa)	F_{max} (kN)	T_{max} (kN)	τ_{max} (MPa)	Failure mode
B-9.5-5d-C2-cube	95.25	77.68	36.18	36.18	25.51	PO
B-9.5-5d-C2-prism	45.25	79.40	32.32	32.32	22.79	PO
B-9.5-5d-C2-beam	45.25	81.74	33.72	42.15	29.72	PO
B-9.5-10d-C2-cube	95.25	77.68	54.05	54.05	19.05	PO
B-9.5-10d-C2-prism	45.25	79.40	58.12	58.12	20.49	PO
B-9.5-10d-C2-beam	45.25	81.74	64.30	80.38	28.34	PO
B-12.7-5d-C2-cube	93.65	79.72	58.82	58.82	23.21	PO
B-12.7-5d-C2-prism	43.65	79.40	51.09	51.09	20.16	PO
B-12.7-5d-C2-beam	43.65	81.74	59.78	74.73	29.48	PO
B-12.7-10d-C2-cube	93.65	77.47	92.15	92.15	18.18	PO
B-12.7-10d-C2-prism	43.65	79.40	85.16	85.16	16.80	PO
B-12.7-10d-C2-beam	43.65	81.74	91.11	113.89	22.47	PO
B-15.9-5d-C2-cube	92.05	77.47	85.49	85.49	21.52	PO
B-15.9-5d-C2-beam	42.05	81.74	73.21	109.82	27.64	PO
B-15.9-10d-C2-cube	92.05	77.47	150.44	150.44	18.93	PO
B-15.9-10d-C2-beam	42.05	81.74	112.10	168.15	>21.16	Shear

Note: f_{cu} is the cube compressive strength of concrete (MPa); F_{max} is failure load (kN); T_{max} is the ultimate tensile force acting on the bar (kN) and τ_{max} is the bond strength (MPa).

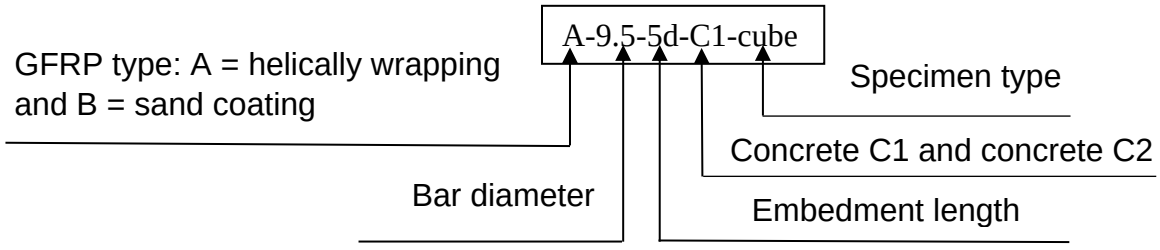

Figure 6.10 - Specimen nomenclature

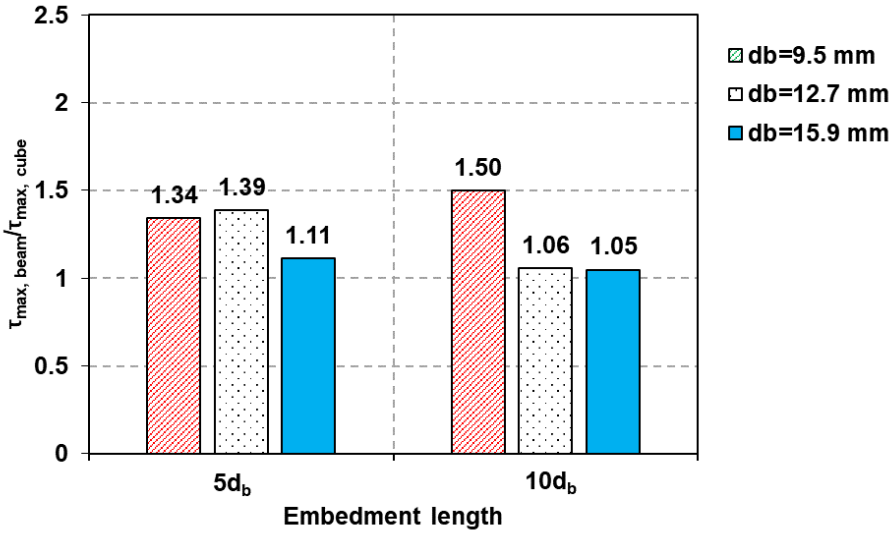

(a)

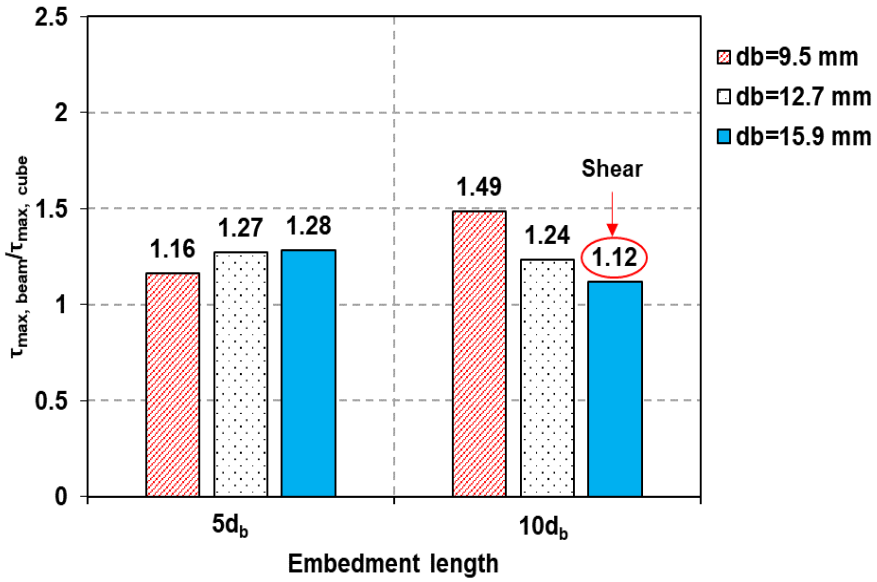

(b)

Figure 6.11 - The ratio of bond strength in hinged beam to bond strength in pull-out cube reinforced with (a) GFRP (type A) and (b) GFRP (type B)

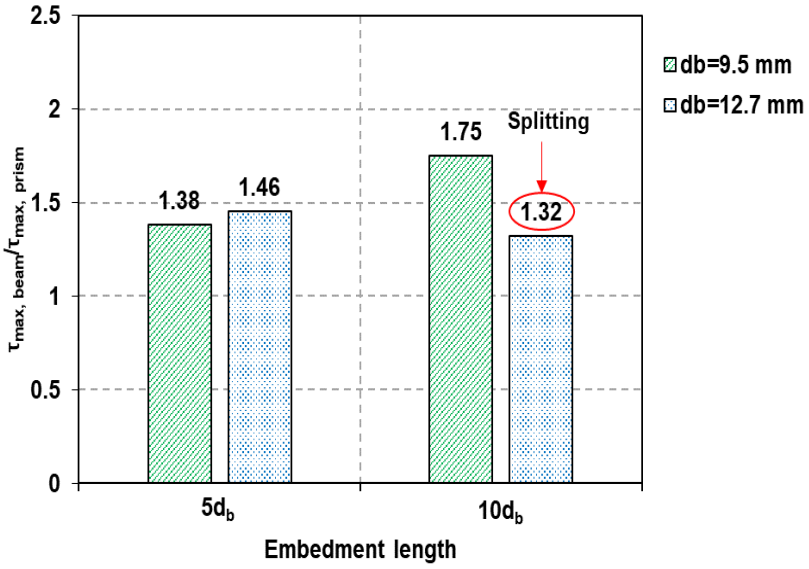

(a)

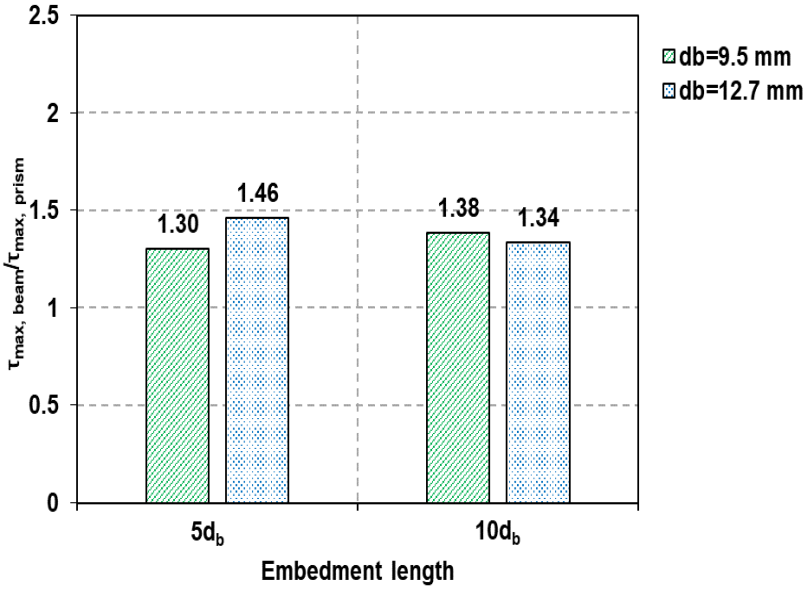

(b)

Figure 6.12 - The ratio of bond strength in hinged beam to bond strength in pull-out prism reinforced with (a) GFRP (type A) and (b) GFRP (type B)

6.6 Finite element model

To investigate the pull-out force acting on the bar in a hinged beam, the nonlinear finite element analysis was introduced to conduct this study. All beams reinforced

with GFRP bars detailed in chapter 5 were used to develop the finite element model (FEM) and then the estimation of the pull-out force. In addition, in the current experimental work, strain gauges were not installed within the bonded length for preventing the disturbance of bond between an embedded part of a bar and surrounding concrete. Therefore, the distribution of tensile and bond stresses was not experimentally investigated. As a result of this, a nonlinear finite element analysis was performed to analyze experimentally tested pull-out and hinged beam specimens to understand the distribution of tensile and bond stresses along the embedment length in GFRP reinforced concrete.

A three – dimensional finite element model (FEM) was developed using ABAQUS/standard package 6.14, which has good performance in simulating the complex non-linear structural behaviour. The accuracy of the finite element model was determined by ensuring that the load – slip curves were reasonably close to the experimental results and failure modes were in a good agreement with the experimental failures.

6.6.1 Model geometry, element type, mesh and boundary conditions

As illustrated in Figure 6.13 (a), only one half of hinged beam was considered in the FE model to reduce the size of finite element model and to fulfill computational efficiency. Subsequently, the structural symmetry of loading, boundary and material properties was applied. The complete pull-out cube and prism were modelled as shown in Figure 6.13 (b and c), because of their small specimen sizes. Thus, the analysis of the model did not take too much time. Three-dimensional hexahedral element including C3D8 (8-node linear brick) was

adopted to model the concrete, bar and steel hinge. This element is suitable for complex non-linear analysis in regards to extensive contacts and large deformations. Reduced integration was used to reduce computational cost and the hexahedral element (C3D8R) provided a solution of comparable accuracy with fewer convergence difficulties and less cost time than other elements.

The mesh size was investigated through a sensitivity analysis to obtain the most accurate results compared with the experimental results and to reduce the computational time. The analysis showed that a suitable mesh size was 10 mm for concrete and 5 mm for the reinforcing bar and steel hinge. For the boundary conditions in the pull-out specimen, a fixed support was used at the top of concrete block representing the steel plate to prevent the specimen from movement and rotation in all directions. As for the hinged beam, symmetry around the z-axis was applied at the middle of hinged beam. The support was defined by constraining the freedoms in all directions with allowing only movement in the z-direction and rotation in the x-direction. The load was applied as a displacement in both the pull-out and the hinged beam specimens. The load was applied directly to the bar in the pull-out specimen, whereas, hinged beam was loaded by a concentrated force applied on the side of the steel hinge. The total load applied to the specimen was calculated by summing up the reactions of the support. The static general method was used to run the model as it led to more accurate predictions with no convergence problems.

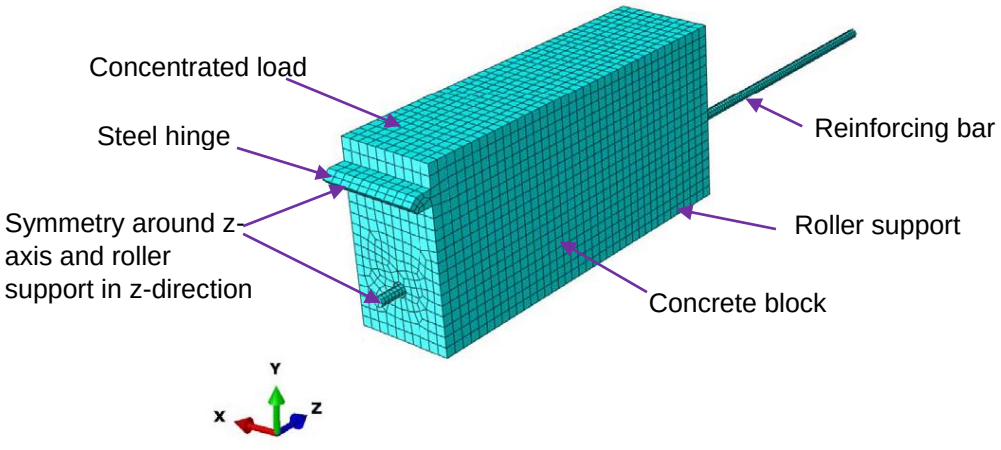

(a) Half of hinged beam

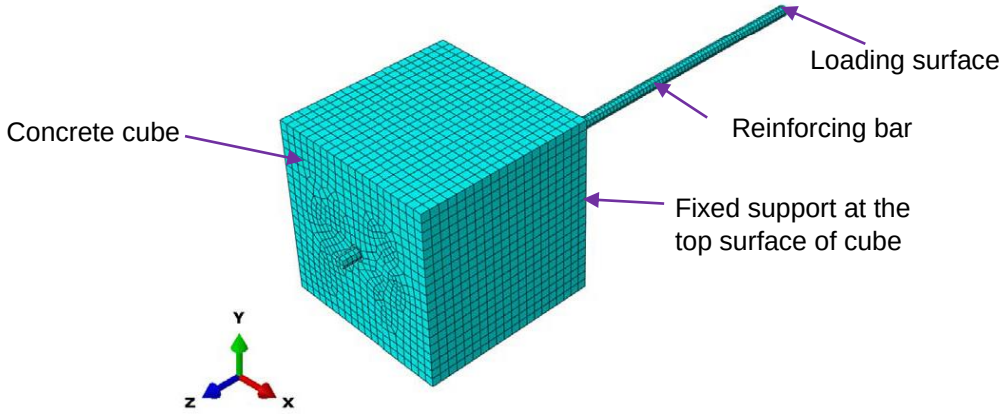

(b) Pull-out cube

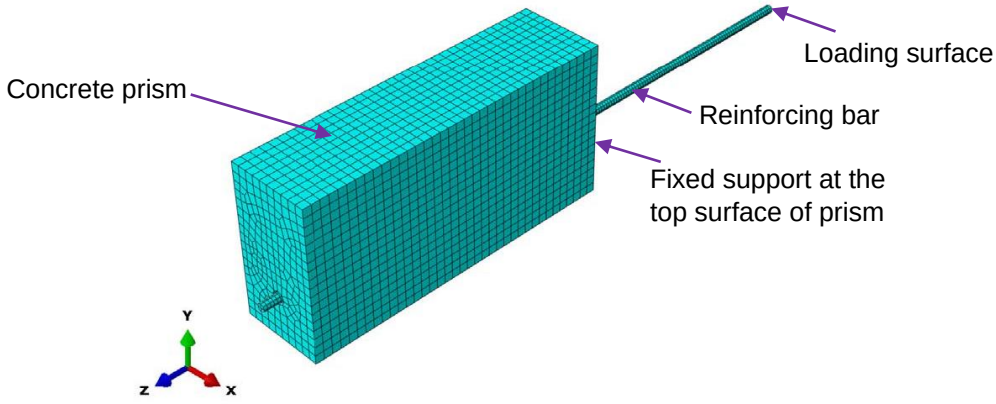

(c) Pull-out prism

Figure 6.13 - Meshing and modelling

6.6.2 Material models

There are three types of constitutive laws for modelling the concrete behaviour at low confining pressures in ABAQUS: Concrete Smeared Cracking, Concrete Damage Plasticity and Drucker–Prager. For characterizing the mechanical behaviour of concrete, concrete damage plasticity model (CDPM) was chosen among all the three models available in ABAQUS. This model assumes an isotropic damaged elasticity in tension and compression to present the inelastic behaviour of concrete. It is designed for applications in which the concrete is subjected to arbitrary loading conditions, including monotonic, cyclic and/or dynamic loading under low confining pressures. The model takes into consideration the degradation of the elastic stiffness induced by plastic straining both in tension and compression (ABAQUS, 2014).

The concrete damage plasticity constitutive model is defined by the elastic modulus and the Poisson's ratio of concrete, a uniaxial compression and tension response, and also five parameters which are required to identify the shape of the flow potential surface and the yield surface. The entire stress – strain curve for concrete is not available from the experimental tests, and only the usual parameters were reported (cube compressive strength and tensile strength of concrete).

In this study, Eurocode (EN-1992-1-1, 2004) is used to represent the nonlinear stress –strain relationship for concrete under uniaxial compression as shown in Figure 6.14 by applying the following equations:

$$\sigma_c = f_c' \frac{K\eta - \eta^2}{1 + (K-2)\eta} \tag{6.1}$$

$$K = 1.05E_c\,\varepsilon_{c1}/f_c' \tag{6.2}$$

$$E_c = 22000\left[\frac{f_c' + 8}{10}\right]^{0.3} \tag{6.3}$$

$$\eta = \varepsilon_c/\varepsilon_{c1} \tag{6.4}$$

where σ_c is the compressive stress of concrete (MPa), f_c' is the mean value of concrete cylinder compressive strength (MPa), E_c is the elastic modulus of concrete (MPa), ε_c is the compressive strain of concrete at any stress σ_c and ε_{c1} is the strain at peak stress. Equation 6.1 is valid for the strain value from zero up to the ultimate strain ε_{cu1}.

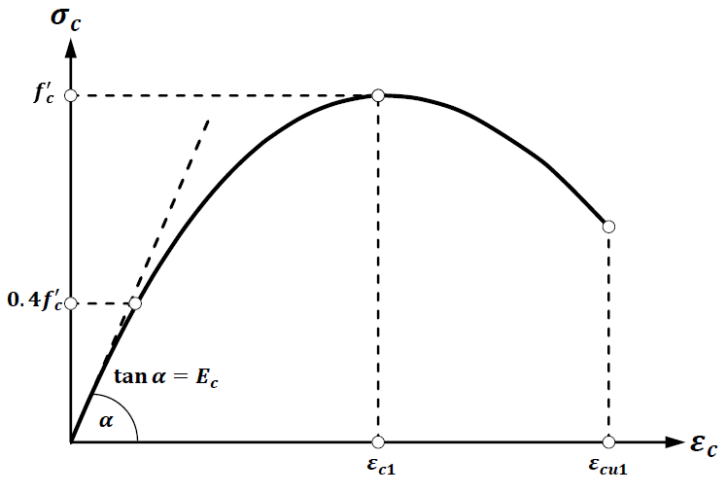

Figure 6.14 - Stress – strain curve for concrete under compression (BS EN 1992-1-1:2004)

In tension, the behaviour is assumed to be elastic up to the onset of cracking and then followed by the tension softening curve. Tension softening can be defined by a stress – cracking strain curve, stress – displacement or considering fracture energy. The stress-cracking strain method was used in the current study to model the softening branch due to its accuracy of prediction and no convergence

problems. The hardening and softening branches shown in Figure 6.15 are obtained by applying equations 6.5 and 6.6 (Abdeldjelil and Thomas, 1994):

$$\sigma_1 = E_c \varepsilon_1 \qquad \varepsilon_1 \leq \varepsilon_{cr} \tag{6.5}$$

$$\sigma_1 = f_{cr} \left(\frac{\varepsilon_{cr}}{\varepsilon_1} \right)^{0.4} \qquad \varepsilon_1 > \varepsilon_{cr} \tag{6.6}$$

where E_c is modulus of elasticity of concrete (MPa); f_{cr} is cracking stress of concrete (MPa); ε_{cr} is cracking strain of concrete; σ_1 is tensile stress of concrete (MPa) and ε_1 is tensile strain at any stress. On the contrary, the GFRP bar is modelled as a linear elastic material as illustrated in Figure 6.16 and also the steel hinge is defined as a linear elastic material.

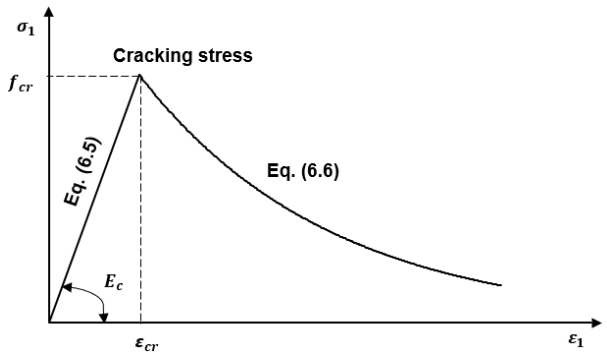

Figure 6.15 - Stress – strain curve for concrete under tension

Five constitutive parameters needed to complete the definition of the CDPM are dilation angle (ψ), flow potential eccentricity (ϵ), the ratio of the second stress invariant in tension to that in compression (K_c), the ratio of initial equibiaxial compressive yield stress to initial uniaxial compressive yield stress (f_b/f_c) and viscosity. Default values in ABAQUS were used to define all parameters, except a dilation angle and a viscosity parameter. Flow potential eccentricity ϵ = 0.1 was selected to simulate the tri-axial behaviour of the concrete material. The tri-

dimensional yield surface is controlled by a shape parameter K_c = 0.667 and the ratio between the biaxial and uniaxial compressive strength f_b/f_c = 1.16. The viscosity value of 0.0005 was chosen for the analysis. The non-associative plastic volumetric deformations of the material are not directly proportional to the changes in stresses and these are represented by a dilation angle. The dilation angle is in the range of 30° to 45°, the value of 38° was adopted in this study since it offered a good agreement with the experimental results.

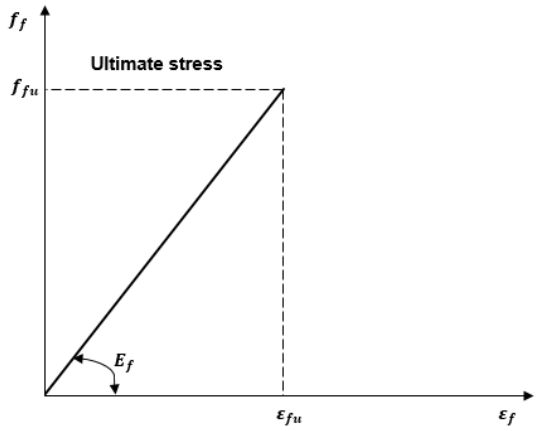

Figure 6.16 - Tensile stress – strain curve of FRP reinforcing bar

6.6.3 Bond model

Two strategies may be considered to model the bond interaction between the reinforcing bar and the concrete: 1) cohesive behaviour and 2) cohesive element. In this study, cohesive behaviour is chosen to model the bond behaviour because the interface thickness is negligibly small. The surface based cohesive behaviour is defined in ABAQUS using the traction-separation law as described in Figure 6.17. The traction-separation model assumes initially linear elastic behaviour before damage and also assumes failure of the cohesive bond to be characterized by progressive degradation of the cohesive stiffness, which is driven by a damage

process (the initiation and evolution of damage). The elastic behaviour is written in terms of an elastic constitutive matrix that relates the normal and shear stresses to the normal and shear separations across the interface. The traction-separation behaviour can be coupled or uncoupled as expressed in equations (6.7) and (6.8), respectively. However, there is not enough information on how to calculate the stiffness coefficients (k_{ij}). Therefore, uncoupled normal and tangential components of the stiffness is selected:

$$T = \begin{bmatrix} t_n \\ t_s \\ t_t \end{bmatrix} = \begin{bmatrix} k_{nn} & k_{ns} & k_{nt} \\ k_{sn} & k_{ss} & k_{st} \\ k_{tn} & k_{ts} & k_{tt} \end{bmatrix} \begin{bmatrix} \delta_n \\ \delta_s \\ \delta_t \end{bmatrix} = K\delta \tag{6.7}$$

$$T = \begin{bmatrix} t_n \\ t_s \\ t_t \end{bmatrix} = \begin{bmatrix} k_{nn} & 0 & 0 \\ 0 & k_{ss} & 0 \\ 0 & 0 & k_{tt} \end{bmatrix} \begin{bmatrix} \delta_n \\ \delta_s \\ \delta_t \end{bmatrix} = K\delta \tag{6.8}$$

where t_n= nominal traction in the normal direction; t_s and t_t are nominal stresses in the two local shear directions; δ_n, δ_s and δ_t are the corresponding displacements.

According to Henriques et al. (2013), k_{nn}, k_{ss} and k_{tt} are given as follows:

$$k_{ss} = k_{tt} = \tau_{max}/s_1 \tag{6.9}$$

$$k_{nn} = 100k_{ss} = 100k_{tt} \tag{6.10}$$

where k_{nn} is the stiffness in normal direction; k_{tt} and k_{ss} are the stiffness in tangential directions; τ_{max} is the maximum bond stress (MPa) and s_1 is the corresponding slip (mm), both are obtained from the experimental results.

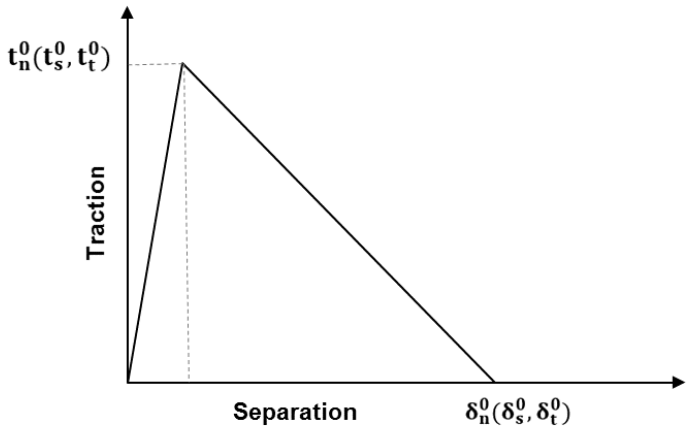

Figure 6.17 - Typical traction – separation response available in ABAQUS (2014)

6.6.4 Results and discussion

6.6.4.1 Verification of the numerical models

The accuracy of the hinged beam, the pull-out cube and the pull-out prism models is validating by comparing the FEM results with the experimental results. The first validation is to compare the load – slip curves obtained from experimental test with those obtained from FE model. The FEA results showed a good agreement for both load - free end slip and load - loaded end slip curves in B-12.7-5d-B hinged beam, B-12.7-5d cube and B-9.5-5d prism as shown in Figures 6.18, 6.20 and 6.21. The models simulated both the ascending and descending branches of the load-slip curves. Moreover, the models are validated by comparing the predicted failure mode with the experimental one. As can be reminded from the experiments, the pull-out failure was observed in most specimens. The B-12.7-5d-B hinged beam, B-12.7-5d cube and B-9.5-5d prism were experimentally failed by a pull-out. As can be seen in Figures 6.19 and 6.22, a similar failure was predicted by the FM models. In the hinged beam, the concrete was crushed at the

top of the bar because of the un-bonded bar remaining in the horizontal position (no rotation). The embedded portion of the bar rotated with the same slope as the concrete block. Thus, this led to impact the concrete with the horizontal portion of the un-bonded bar as illustrated in Figure 6.19 (b). The validated models are used to examine the tensile and bond stress distribution along the bonded length as detailed in section 6.6.4.3. As can be noted, the distribution of the tensile and bond stresses was developed for only one cube, prism and hinged beam in this chapter because the same trend was observed in all specimens.

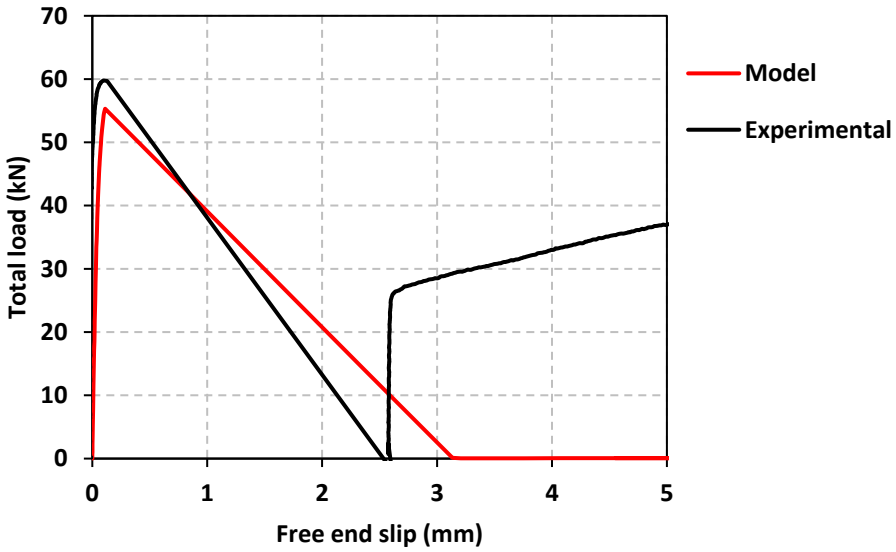

Figure 6.18 - Comparison of load - free end slip responses for hinged beam 12.7-5d-GFRP (type B)

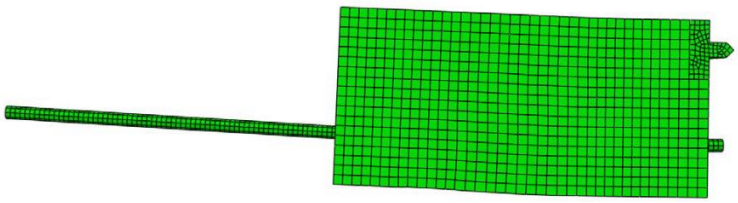

(a) Deformation (vertical deflection)

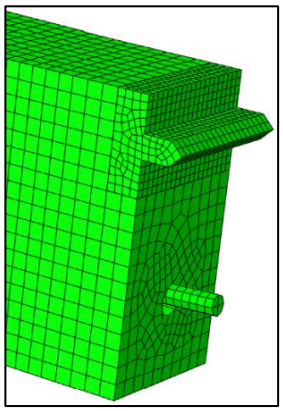

(b) Concrete crushing at the top of the bar

Figure 6.19 - Comparison of failures in hinged beam 12.7-5d-GFRP (type B)

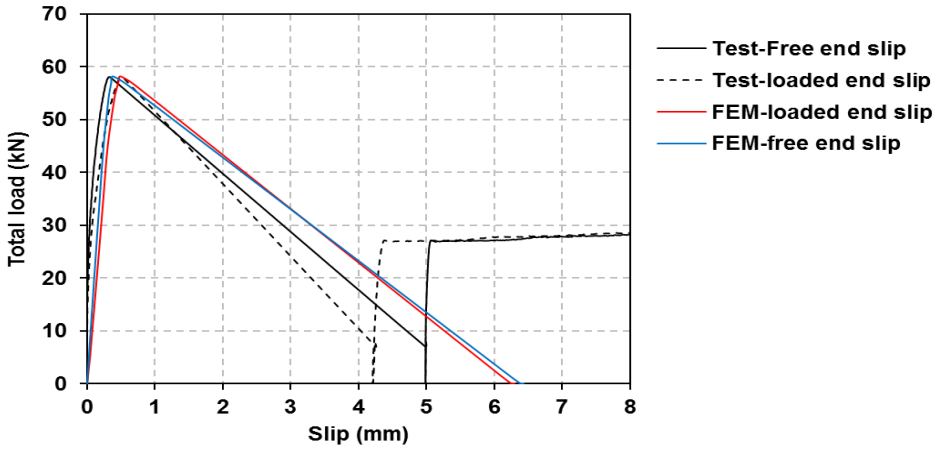

Figure 6.20 - Comparison of load - slip responses for pull-out cube 12.7-5d-GFRP (type B)

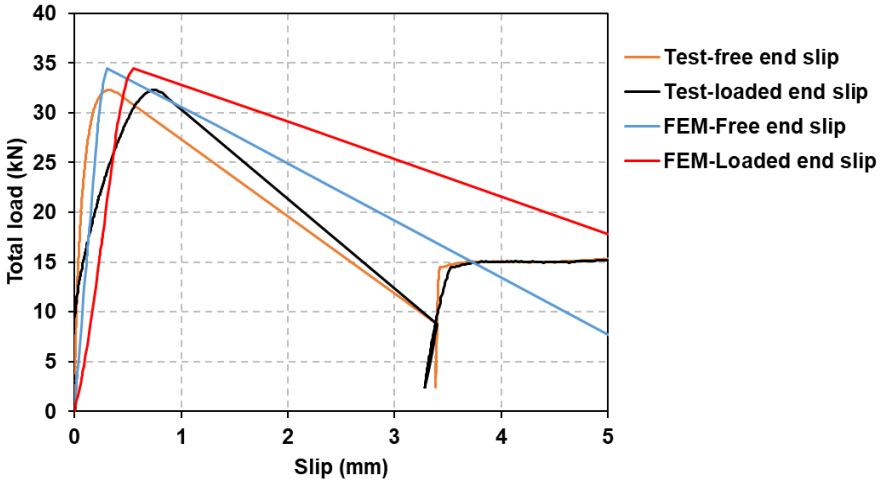

Figure 6.21 - Comparison of load - slip responses for pull-out prism 9.5-5d-GFRP (type B)

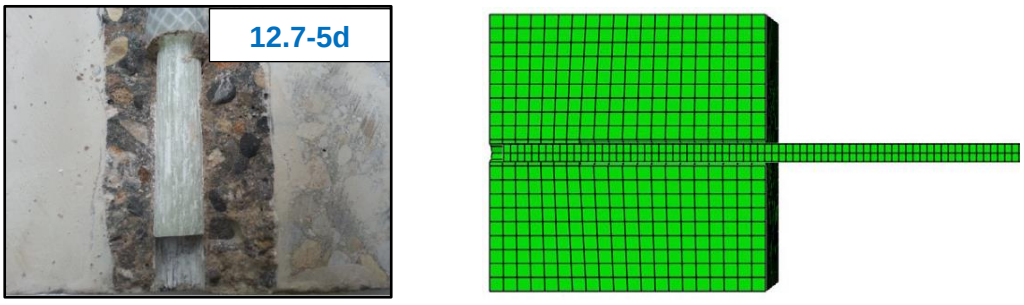

(a) Pull-out failure in cube

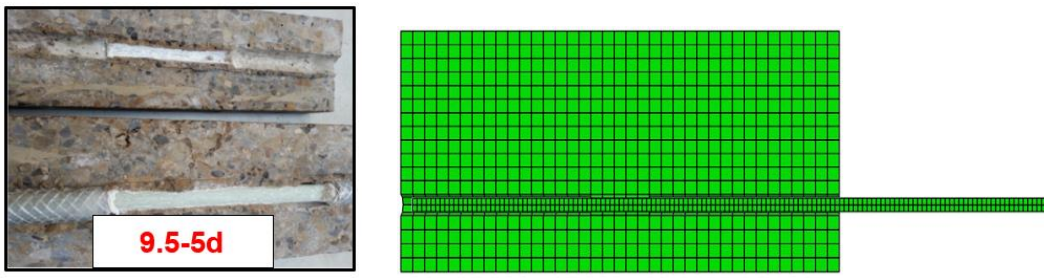

(b) Pull-out failure in prism

Figure 6.22 - Comparison of failures in cube and prism reinforced with GFRP (type B)

6.6.4.2 Comparison between experimental and predicted results

All hinged beams having the bottom bar position were modelled by finite elements to determine the actual tensile force acting on the bar. All hinged beams were failed by the same pull-out mode as that which occurred in the experiments. Comparisons between the experimental failure load and predicted failure load are presented in Tables 6.3 and 6.4. The statistical analysis (mean, standard deviation and coefficient of variation) are calculated to assess the accuracy of the FE Models as shown in Tables 6.3 and 6.4. The mean, standard deviation and coefficient of variation are 1.12, 11% and 10% for hinged beams reinforced with GFRP (type A) bars, and 1.09, 9% and 8% for hinged beams reinforced with GFRP (type B) bars, respectively. It can be reported that the predictions produced from the current computational analysis show a reasonable agreement compared to the experimental results.

Based on these satisfactory results, the tensile forces acting on the bar at the failure load was calculated by multiplying the numerical value of normal tensile stress parallel to the bar by the cross-sectional area of the bar as demonstrated

in Tables 6.5 to 6.8. The hinged beam tensile forces estimated by equilibrium forces and finite element model are compared to the prism tensile force and cube tensile force as shown in Tables 6.5 to 6.8.

For GFRP (type A) reinforced specimens, the ratio of the tested tensile force obtained from the hinged beam to that obtained from the pull-out prism is in the range of 1.38 to 1.75 as shown in Table 6.5, depending on bar diameter and embedment length. While the ratio of the predicted tensile force for the hinged beam to the experimental tensile force for the prism changed from 1.16 to 1.19. From Table 6.6, it can be seen that the ratio of the tested tensile force in the hinged beam to the cube tensile force ranged from 1.04 to 1.49 with changing bar diameter, embedment length and specimen size, whilst the ratio of the predicted tensile force for the hinged beam to the cube tensile force varied from 0.81 to 1.13. As for GFRP (type B) reinforced specimens, the ratio of the hinged beam tensile force to the prism tensile force changed from 1.30 to 1.46, depending on bar diameter and embedment length as illustrated in Table 6.7. However, the ratio of the tensile force predicted by a hinged beam model to that measured by a prism test is in the range of 0.98 to 1.18. From Table 6.8, it is obvious that the ratio of the hinged beam tensile force to the cube tensile force ranged from 1.16 to 1.48, whereas the ratio of the predicted tensile force to the cube tensile force is in the range of 1.01 to 1.12, depending on bar diameter, embedment length and specimen size. The difference between the experimental and predicted tensile forces for hinged beams indicates that the equation derived by equilibrium of forces to calculate the tested tensile force needs to be modified, because the RILEM specification ignores the geometrical deformations (vertical deflection) and

considers that the arm (distance between the steel hinge connection point and the centre of the bar) is constant. However, this distance actually changes due to geometrical deformation. This is also confirmed by Mazaheripour et al. (2013), when the arm change was measured by installing two vertical LVDTs. It can be reported that the tensile force calculated by RILEM recommendations is overestimated.

The rotation angle of the concrete block which is only measured using the developed FE model is very small. Therefore, no significant change occurred in the value of tested tensile force acting on the bar in a hinged beam with considering the rotation angle.

Table 6.9 presents the factors to calculate the hinged beam bond strength by knowing the pull-out bond strength for GFRP (type A) and GFRP (type B) bars embedded in high strength concrete. In case of specimens reinforced with GFRP (type A) bars, the average ratios of the predicted tensile force in the hinged beam to the tested tensile force in the cube are 1.01 and 1.05 and the maximum ratios are 1.13 and 1.12 for specimens reinforced with GFRP (type A) and GFRP (type B) bars, respectively. Therefore, the ratios of 1.13 and 1.12 can be used as a factor to estimate the bond strength of the hinged beam by multiplying the bond strength obtained from the cube by a factor of 1.13 and 1.12. The average ratios of the predicted tensile force in the hinged beam to the tested tensile force in the prism are 1.17 and 1.10 and the maximum ratios are 1.19 and 1.18 for specimens reinforced with GFRP (type A) and GFRP (type B) bars, respectively. Thus, the ratios of 1.19 and 1.18 can be used as factors to calculate the bond strength of the hinged beam by knowing the bond strength of the prism. Based on these

comparisons, there is no significant difference between bond strengths measured by a pull-out test and those predicted by a hinged beam model. Subsequently, it can be recommended to use the pull-out test to estimate the bond strength rather than the hinged beam test which needs much time to prepare and test. A similar conclusion was obtained by de Almeida Filho et al. (2008) from investigating the bond strength of steel bars embedded in normal and self-compacting concrete using a pull-out test and a hinged beam test.

Factors of 1.25 and 1.5 derived from the method of equilibrium forces were modified based on numerical analysis as indicated in Tables 6.10 and 6.11. It was noted that the modified factors for 9.5 and 12.7 mm bar diameters are similar regardless of embedment length and surface configuration, as well as the15.9 mm bar diameter. Thus, it can be reported that the average modified factors are 1.1 and 1.43 for hinged beam (type I) and hinged beam (type II), respectively. The modified factor for the hinged beam (type II) does not significantly change, and this confirms that these factors primarily depend on the specimen size and the amount of geometrical deformation.

Table 6.3 - Comparisons between the predicted and experimental failure load for hinged beams reinforced with GFRP (type A)

Hinged beam label.	$F_{exp,beam}$ (kN)	$F_{pred,beam}$ (kN)	$\frac{F_{exp}}{F_{pred}}$
A-9.5-5d-B	30.56	29.44	1.03
A-9.5-10d-B	65.49	50.90	1.28
A-12.7-5d-B	45.39	42.53	1.06
A-12.7-10d-B	68.91	54.72	1.26
A-15.9-5d-B	55.09	50.311	1.09
A-15.9-10d-B	82.35	81.47	1.01
Mean			1.12
Standard deviation (%)			11
Coefficient of variation (%)			10

Table 6.4 - Comparisons between the predicted and experimental failure load for hinged beams reinforced with GFRP (type B)

Hinged beam label.	$F_{exp,beam}$ (kN)	$F_{pred,beam}$ (kN)	$\frac{F_{exp}}{F_{pred}}$
B-9.5-5d-B	33.72	32.80	1.03
B-9.5-10d-B	64.33	51.22	1.25
B-12.7-5d-B	59.78	55.30	1.08
B-12.7-10d-B	91.11	88.31	1.03
B-15.9-5d-B	73.21	66.03	1.10
B-15.9-10d-B	Shear failure		
Mean			1.09
Standard deviation (%)			9
Coefficient of variation (%)			8

Note: $F_{exp,beam}$ is the experimental failure load (kN) and $F_{pred,beam}$ is the predicted failure load (kN) obtained from the proposed ABAQUS model.

Table 6.5 - Comparison between pull-out prisms and hinged beams reinforced with GFRP (HW-SC) bars

Specimen label.	$T_{exp,prism}$ (kN)	$T_{exp,beam}$ (kN)	$T_{pred,beam}$ (kN)	$\frac{T_{exp,beam}}{T_{exp,prism}}$	$\frac{T_{pred,beam}}{T_{exp,prism}}$
A-9.5-5d	27.66	38.20	32.28	1.38	1.16
A-9.5-10d	46.72	81.86	56	1.75	1.19
A-12.7-5d	38.97	56.73	45.67	1.45	1.17
A-12.7-10d	65.31	86.13	63.85	Splitting in prism	
Average				1.52	1.17

Table 6.6 - Comparison between pull-out cubes and hinged beams reinforced with GFRP (HW-SC) bars

Specimen label.	$T_{exp,cube}$ (kN)	$T_{exp,beam}$ (kN)	$T_{pred,beam}$ (kN)	$\frac{T_{exp,beam}}{T_{exp,cube}}$	$\frac{T_{pred,beam}}{T_{exp,cube}}$
A-9.5-5d	28.47	38.20	32.28	1.34	1.13
A-9.5-10d	54.66	81.86	56	1.49	1.02
A-12.7-5d	40.88	56.73	45.67	1.38	1.11
A-12.7-10d	78.70	86.13	63.85	1.09	0.81
A-15.9-5d	71.92	82.64	72.66	1.15	1.01
A-15.9-10d	117.76	123.52	116.66	1.04	0.99
Average				1.29	1.01

Table 6.7 - Comparison between pull-out prisms and hinged beams reinforced with GFRP (SC) bars

Specimen label.	$T_{exp,prism}$ (kN)	$T_{exp,beam}$ (kN)	$T_{pred,beam}$ (kN)	$\frac{T_{exp,beam}}{T_{exp,prism}}$	$\frac{T_{pred,beam}}{T_{exp,prism}}$
B-9.5-5d	32.32	42.15	36.39	1.30	1.12
B-9.5-10d	58.12	80.41	57	1.38	0.98
B-12.7-5d	51.09	74.72	60.76	1.46	1.18
B-12.7-10d	85.16	113.88	98.47	1.33	1.15
Average				1.37	1.10

Table 6.8 - Comparison between pull-out cubes and hinged beams reinforced with GFRP (SC) bars

Specimen label.	$T_{exp,cube}$ (kN)	$T_{exp,beam}$ (kN)	$T_{pred,beam}$ (kN)	$\frac{T_{exp,beam}}{T_{exp,cube}}$	$\frac{T_{pred,beam}}{T_{exp,cube}}$
B-9.5-5d	36.18	42.15	36.39	1.16	1.01
B-9.5-10d	54.04	80.41	57	1.48	1.05
B-12.7-5d	58.82	74.72	60.76	1.27	1.03
B-12.7-10d	92.15	113.88	98.47	1.23	1.06
B-15.9-5d	85.48	109.81	96.14	1.28	1.12
B-15.9-10d	153.36	Shear failure			
Average				1.28	1.05

Note: $T_{exp,beam}$ is the ultimate tensile force of hinged beam at the experimental failure load (kN); $T_{pred,beam}$ is the predicted ultimate tensile force of hinged beam at the predicted failure load (kN); $T_{exp,prism}$ is the ultimate tensile load of pull-out prism (kN) and $T_{exp,cube}$ is the ultimate tensile load of pull-out cube (kN).

Table 6.9 - Factors to calculate the bond strengths in hinged beam

GFRP surface	$\mathbf{factor_{cube}}$	$\mathbf{factor_{prism}}$
Helical wrapping with slightly sand coating	1.13	1.19
Sand coating	1.12	1.18

Table 6.10 - Modified factors for hinged beams reinforced with GFRP (type A) bars

Specimen label.	$F_{pred,beam}$ (kN)	$\mathbf{T_{pred,beam}}$ (kN)	$\mathbf{Factor} = \frac{\mathbf{T_{pred,beam}}}{\mathbf{F_{pred,beam}}}$	Average factor
A-9.5-5d	29.44	32.28	1.09	1.10 < 1.25
A-9.5-10d	50.90	56	1.10	
A-12.7-5d	42.53	45.67	1.07	
A-12.7-10d	54.72	63.85	1.16	
A-15.9-5d	50.311	72.66	1.44	1.43 < 1.5
A-15.9-10d	81.47	116.66	1.43	

Table 6.11 - Modified factors for hinged beams reinforced with GFRP (type B) bars

Specimen label.	$F_{pred,beam}$ (kN)	$\mathbf{T_{pred,beam}}$ (kN)	$\mathbf{Factor} = \frac{\mathbf{T_{pred,beam}}}{\mathbf{F_{pred,beam}}}$	Average factor
B-9.5-5d	32.80	36.39	1.10	1.10 < 1.25
B-9.5-10d	51.22	57	1.11	
B-12.7-5d	55.30	60.76	1.09	
B-12.7-10d	88.31	98.47	1.11	
B-15.9-5d	66.03	96.14	1.45	1.45 < 1.5
B-15.9-10d	Shear failure			

6.6.4.3 Distribution of tensile and bond stresses

Tensile and bond stress distribution along the embedment length are important properties as they can provide information on the state of stress along the embedment length. Figure 6.23 displays these stresses in a differential segment of a bar embedded in concrete. The change in the tensile stress along differential bonded length of the bar is accompanied by the bond stress around the embedment length. The bond stress is calculated according to Equation 6.11,

which is derived from the equilibrium of forces along the differential embedment length of the bar. The bond stress is directly proportional to the rate of change of the tensile stress along the reinforcing bar:

$$\tau = \frac{d_b \mathrm{d}\sigma}{4dx} \tag{6.11}$$

where d_b is the bar diameter (mm), $\mathrm{d}\sigma$ is the rate of change in tensile stress along dx (MPa), dx is the differential embedment length of the bar (mm) and τ is the bond stress along dx (MPa).

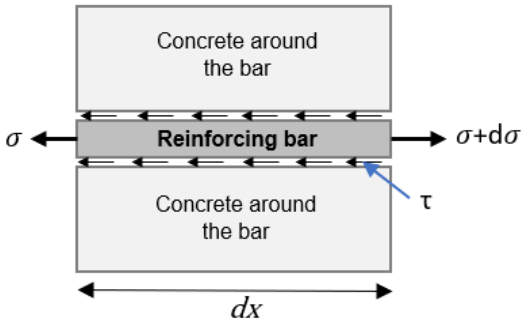

Figure 6.23 - Derivation of bond stress

The tensile stress values are obtained from the numerical bar stress values at each node along the bonded length. Also, the bond stress values are obtained from the numerical contact shear stress values at each node along the bonded length. The bond stress can also be calculated by the rate of change of tensile stress between two successive nodes using equation 6.11. The bond stress values derived from two previous methods showed negligible differences, so the one based on obtaining the bond stress values directly from the numerical contact shear stress values was adopted for all specimens. All hinged beams modelled using FEM showed a similar trend in distribution of tensile and bond stresses, also the same observation was noted for all pull-out cubes and pull-out prisms

modelled. Consequently, it was decided to select only one hinged beam, pull-out cube and pull-out prism to view distribution of stresses at the interface between the bar and the concrete.

Tensile and bond stresses are plotted at different load levels, ranging from 20% to 100% of the failure load, to observe the stress distribution with increasing the load. From Figures 6.24 (a), 6.25 (a) and 6.26 (a), a nonlinear tensile stress distribution was observed and it is obvious at lower load values. The experimental results obtained by Benmokrane et al. (1996) from testing the hinged beam confirmed that the distribution of tensile strain was non-linear along the embedment length and also the tensile strain in the bar increases rapidly from the unloaded end to the loaded end. This observation is also remarked in this study as can be seen in Figures 6.24 (a), 6.25 (a) and 6.26 (a). Although the tensile stress distribution is nonlinear at lower load levels, it becomes nearly linear when the applied load approaches the failure load and this leads to a constant value of bond stress.

At low load levels, the bond stress values are low at the free end. However, as the load increases, the bond stress values at the vicinity of the free end increase, and the difference between bond stress values becomes less evident along the bonded length as illustrated in Figures 6.24 (b), 6.25 (b) and 6.26 (b). This may be attributed to the redistribution of the bond stresses along the bonded length when the load increases. It is also interesting to monitor that bond stress becomes constant at the loaded end, when the bond stress reached the value of bond strength used in the modelling. With continuing the increase of the applied load, bond stress stayed constant at this end and increased at the free end. A similar

distribution of tensile and bond stresses was obtained by Achillides and Pilakoutas (2006) and Tekle et al. (2016) from FE modelling of the pull-out specimen. Furthermore, the same observation was confirmed by Tekle et al. (2017a) from modelling the beam-end specimen. The hinged beam (B-12.7-5d-B), cube (B-12.7-5d) and prism (B-9.5-5d) showed almost similar trend of distribution of tensile and bond stresses along the embedment length.

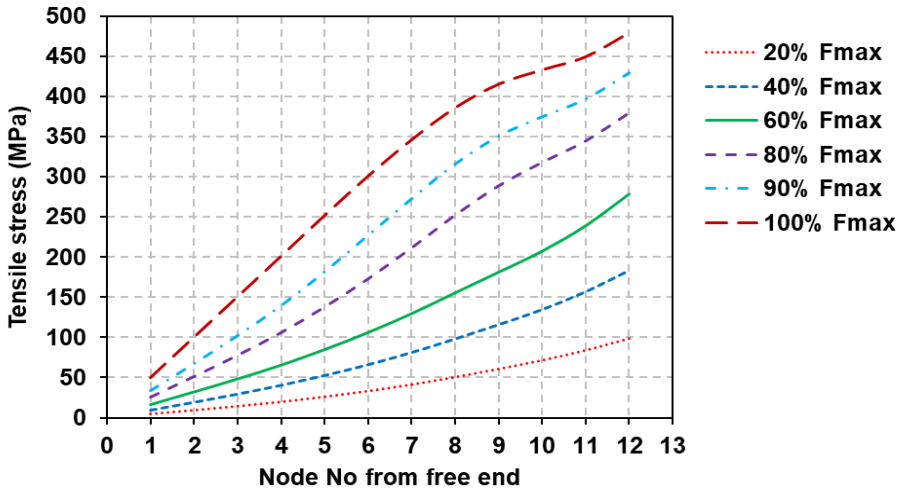

(a)

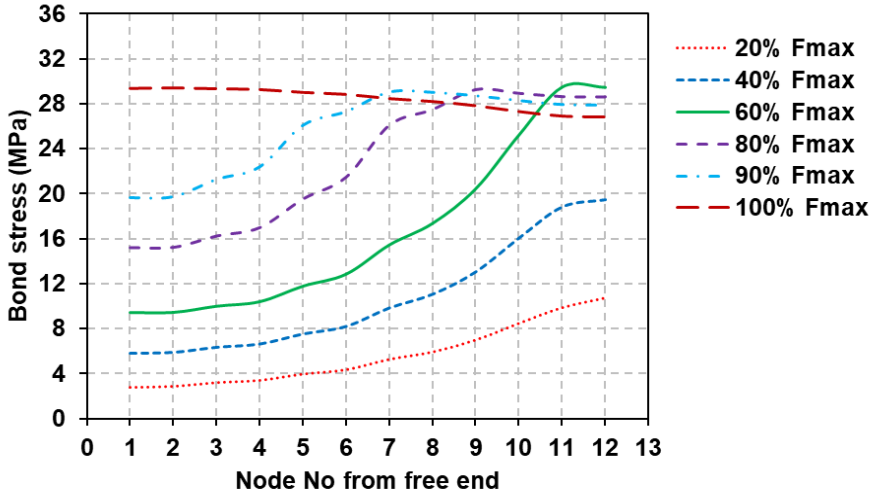

(b)

Figure 6.24 - Distribution of (a) normal tensile stress and (b) bond stress along the embedment length at different loading levels in hinged beam (B-12.7-5d-B)

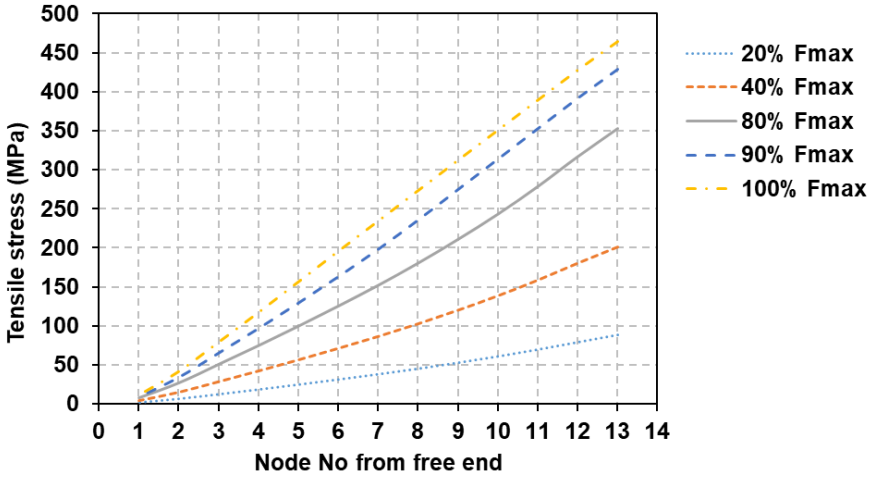

(a)

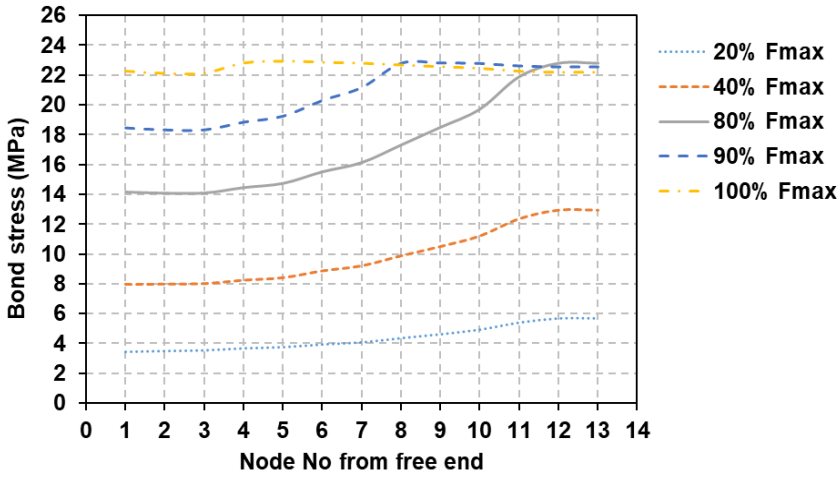

(b)

Figure 6.25 - Distribution of (a) normal tensile stress and (b) bond stress along the embedment length at different loading levels in cube (B-12.7-5d)

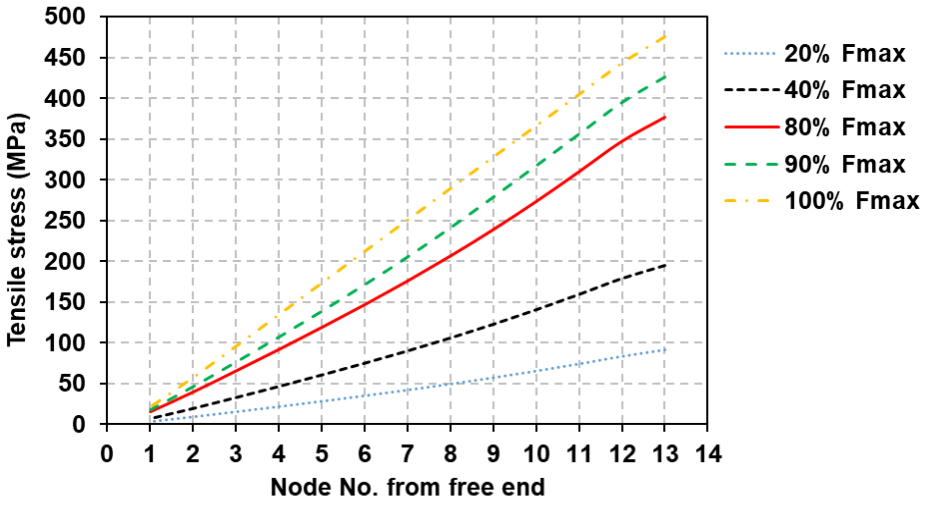

(a)

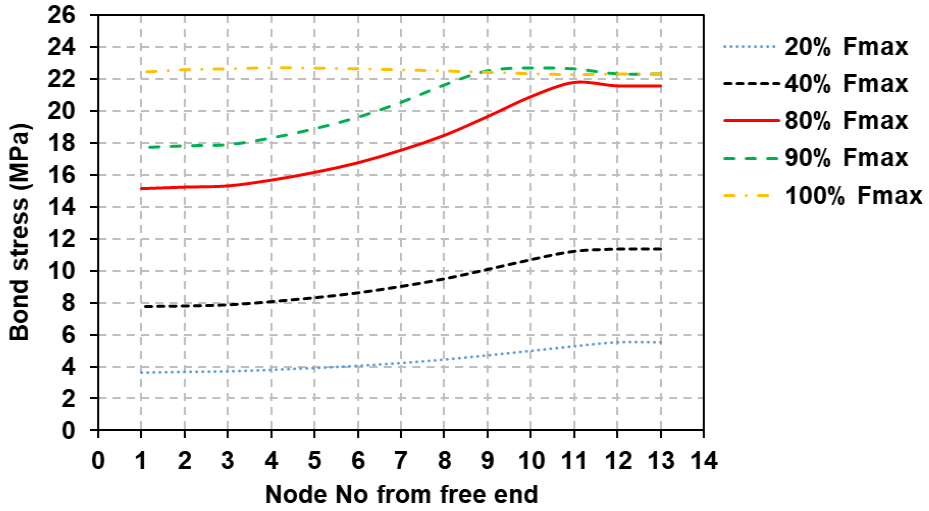

(b)

Figure 6.26 - Distribution of (a) normal tensile stress and (b) bond stress along the embedment length at different loading levels in prism (B-9.5-5d)

6.7 Conclusions

In this chapter, comparisons were conducted between the bond properties of both GFRP types measured by the hinged beam and those measured by the pull-out specimen. Parameters examined were bar diameter, embedment length, bar surface and specimen size. In addition, the finite element analysis was used to

predict the tensile force acting on the bar in the hinged beam and to investigate the distribution of tensile and bond stresses along the embedment length. The following conclusions are drawn:

1. All test methods show similar bond stress – slip curves, which consist of high initial stiffness and a nonlinear ascending branch for both GFRP types. Also, the softening curves with differing test methods only are similar, except specimens having a pull-out failure accompanied with concrete cracks, giving a different trend.
2. Both pull out and hinged beam specimens reinforced with GFRP (type A) bars failed by outer surface damage of the bar. For those reinforced with GFRP (type B) bars, pull-out failure occurred by the debonding of the whole sand coated layer from the bar.
3. Experimental bond strength of hinged beam is higher than both bond strengths measured by the pull-out cube and pull-out prism. The ratio of the experimental tensile force of the hinged beam to the experimental tensile force of the pull-out prism is in the range of 1.38 to 1.75 and 1.30 to 1.46 for GFRP (type A) and GFRP (type B), respectively. The ratio of the experimental tensile force obtained from the hinged beam to that obtained from the pull-out cube varied from 1.04 to 1.49 and 1.16 to 1.48 for GFRP (type A) and GFRP (type B), respectively. The variation of ratios depends on bar diameter and embedment length.
4. The FEM results showed that the models reasonably reproduced the experimental behaviour of the pull-out cube, pull-out prism and hinged beam in terms of load – slip curve and failure mode.

5. It was found that the tensile force value estimated by the FE model of the hinged beam is very close to that measured by the pull-out cube and prism. The ratio of the predicted tensile force in the hinged beam to the experimental tensile force in the prism changed from 1.16 to 1.19 and 0.98 to 1.18 for GFRP (type A) and GFRP (type B), respectively. The ratio of the predicted tensile force in the hinged beam to the experimental tensile force in the cube ranged from 0.81 to 1.13 and 1.01 to 1.12 for GFRP (type A) and GFRP (type B), respectively. These ratios are affected by bar diameter, embedment length, specimen size and the amount of geometrical deformation. Consequently, the pull-out test can be used to determine the bond strength rather than the hinged beam test which requires far much more time to prepare and test.
6. According to the FEM results, it can be reported that the tensile force in the reinforcing bar in hinged beams calculated from equilibrium condition is overestimated, because of ignoring the large deformation at failure.
7. The numerical method is useful in investigating the distribution of tensile and bond stresses. It is found that both stresses are nonlinear along the embedment length and bond stress at the vicinity of the free end increases with increasing the load due to redistribution of bond stresses along the embedment length.

Chapter 7

Design codes evaluation against experimental results of pull-out specimens and hinged beams

7.1 Introduction

Experimental investigation of pull-out and hinged beam specimens reinforced with GFRP bars has been described in chapter 3. The test results and discussions for pull-out specimens and hinged beams have been presented in chapters 4 and 5, respectively. Bond strength of GFRP bar to concrete has been specified in the design codes and is summarized to ensure that engineers better understand their applicability. The main aim of this chapter is to validate the design code equations ACI-440.1R (2015), CAN/CSA-S6 (2014), CAN/CSA-S806 (2012) and JSCE (1997) in predicting the bond strength. This evaluation was conducted by comparing bond strengths obtained from design code equations with those obtained from experimental tests.

7.2 Design code predictions

The ACI-440.1R (2015) code has derived an equation for GFRP bars based on the work conducted by Wambeke and Shield (2006) as shown below:

$$\frac{\tau_{max}}{0.083\sqrt{f'_c}} = 4 + 0.3\frac{c}{d_b} + 100\frac{d_b}{l_e} \qquad (7.1)$$

where τ_{max} is the bond strength (MPa), f_c' is the cylinder compressive strength of concrete (MPa) and c is the lesser of the cover to the bar centre or one-half of the centre-to-centre spacing of the bars being developed (mm). The ratio of c/d_b is limited to be less than 3.5 so that the same equation can be used for either splitting or pull-out failure. The CAN/CSA-S806 (2012) and CAN/CSA-S6 (2014) Canadian codes have also proposed the expressions for estimating the development length of FRP bars in conventional concrete in order to avoid bond failure. These equations were substituted in equation 7.2 to produce the expressions 7.3 and 7.4 for CAN/CSA-S806 and CAN/CSA-S6, respectively, which are used to calculate bond strength:

$$\tau = \frac{T}{\pi . d_b . l_e} \tag{7.2}$$

$$\tau_{max} = \frac{d_{cs}\sqrt{f_c'}}{1.15 k_1 k_2 k_3 k_4 k_5 \pi d_b} \tag{7.3}$$

$$\tau_{max} = \frac{\left(d_{cs} + k_{tr}\frac{E_{frp}}{E_s}\right) f_{cr}}{0.45 k_1 k_6 \pi d_b} \tag{7.4}$$

where:

$$k_{tr} = \frac{A_{tr} f_y}{10.5 s N} \qquad and \qquad \left(d_{cs} + k_{tr}\frac{E_{frp}}{E_s}\right) \leq 2.5 d_b$$

where T is the tensile load in reinforcing bar (N), k_1 is a bar location factor (1.3 for horizontal reinforcement placed so that more than 300 mm of fresh concrete is cast below the development length or splice, 1.0 for other cases), k_2 is a concrete density factor (1.3 for structural low-density concrete, 1.2 for structural semi-low-

density concrete, 1.0 for normal density concrete), k_3 is a bar size factor (0.8 for $A_b \leq 300$ mm^2, 1.0 for $A_b > 300$ mm^2), $\mathrm{A_b}$ is the cross-sectional area of FRP bar (mm^2), k_4 is a bar fibre factor (1.0 for GFRP), k_5 is a bar surface factor (1.0 for surface-roughened or sand-coated surfaces and 1.05 for spiral pattern surface), k_6 is a bar surface factor, being the ratio of the bond strength of the FRP bar to that of a steel deformed bar with the same cross-sectional area as the FRP bar, but not greater than 1.0. In the absence of experimental data, k_6 shall be taken as 0.8, $\mathrm{d_{cs}}$ is the smaller of the cover to the bar centre or two-thirds of the centre-to-centre spacing of the bars being developed (mm) (not greater than 2.5 $\mathrm{d_b}$), k_{tr} is a transverse reinforcement index, A_{tr} is the cross-sectional area of transverse reinforcement (mm^2), s is maximum spacing centre to centre of transverse bars within l_{db} (mm), f_{yt} is yield stress in transverse reinforcement (MPa), N is the number of bars being developed along the potential plane of bond splitting, f_{cr} is the cracking strength of concrete (MPa) ($0.4\sqrt{f_c'}$ for normal-density concrete, $0.34\sqrt{f_c'}$ for semi-low-density concrete, $0.3\sqrt{f_c'}$ for low-density concrete), $\mathrm{E_{frp}}$ and $\mathrm{E_s}$ are the modulus of elasticity of FRP and steel bars, respectively. The square root of concrete strength should be less than 5 and 8 MPa for CSA-S806 and CSA-S6, respectively.

The Japanese Design Code (JSCE-1997) derived the equation 7.5 to evaluate the bond strength of FRP bars to concrete:

$$\tau_{max} = \frac{f_{bod}}{\alpha_1} \tag{7.5}$$

where:

$$f_{bod} = 0.28\alpha_2 f_c'^{2/3}/1.3 \quad \leq 3.2\ N/mm^2$$

where f_{bod} is the design bond strength of concrete (MPa), α_2 is the modification factor for bond strength of CFRM (= 1 when bond strength of CFRM is equal to or greater than that of deformed steel bars); otherwise α_2 shall be decreased according to test results, α_1 is a confinement modification factor (= 1 when $k_c \leq 1$; 0.9 when $1 < k_c \leq 1.5$; 0.8 when $1.5 < k_c \leq 2$; 0.7 when $2 < k_c \leq 2.5$ and 0.6 when $k_c > 2.5$), k_c is specified as $\left(= \frac{c}{d_b} + \frac{15A_t}{sd_b} + \frac{E_t}{E_s}\right)$, c is the smaller of the bottom clear cover of main reinforcement or half of the clear space between the reinforcement being developed (mm), A_t is the cross-sectional area of transverse reinforcement (mm^2), s is maximum spacing centre to centre of transverse bars within l_{db} (mm), E_t is Young's modulus of elasticity for the transverse reinforcement (MPa) and E_s is the Young's modulus for steel (MPa). Critical analysis and discussions of the design guidelines are presented in section 2.10.

7.3 Comparison of test results of pullout cubes with current codes

For comparison purposes, the bond strengths provided by code equations were determined based on the geometrical and mechanical properties of the pull-out cubes. Tables 7.1 and 7.2 summarize the comparative results of the experimental bond strengths of various specimens with the predicted bond strengths calculated from the methods provided in ACI 440.1R-15, CSA-S806-12, CSA-S6-14 and JSCE 1997. In Figure 7.1 (a to d), the predictions provided by the ACI 440.1R, CSA-S806, CSA-S6 and JSCE equations were plotted using the geometrical and

mechanical properties of the pull-out cube in the present research. It can be seen that the ACI 440 code overestimates the bond strength of both GFRP bars having an embedment length of $2.5d_b$, while it is conservative for larger embedment lengths. The average ratio of experimental to predicted bond strengths obtained from the ACI 440 code is 1.06 with a COV of 34.3% and 1.45 with a COV of 25.6 for GFRP (type A) and GFRP (type B) reinforced cubes, respectively. CSA-S806, CSA-S6 and JSCE codes are too conservative, where the average ratios of experimental to predicted bond strengths for GFRP (type A) reinforced cubes are 4.41, 2.56 and 3.4 with a COV of 10.9%, respectively. They are 5.26, 3.21 and 4.26 with a COV of 17.4% for GFRP (type B) reinforced cubes. Tables 7.1 and 7.2 show that the bond strength obtained from Canadian and Japanese codes is not influenced by bar diameter and embedment length because of the limitations of d_{cs} and k_c in the Canadian and Japanese codes, respectively, as well as ignoring the effect of the embedment length on bond strength in both codes. This conclusion was also confirmed by Hossain et al. (2014), from comparing the tested results with the Canadian code predictions. In contrast to the Canadian codes, the bond strength reduces with increasing embedment length as per the ACI 440.1R code. No change was noted in the ACI predictions for identical specimens with the only one variable being bar diameter, and this is due to the limitation of the ratio of c/d_b and the value of the embedment length, that was taken as the ratio of the bar diameter, and this led to cancel the effect of bar diameter in the term of d_b/l_e. However, from Tables 7.1 and 7.2, there is a slight change in bond strength with the increase of bar diameter for the cubes with the same embedment length, because of a small variation of concrete strength. The

ACI code does not acknowledge the influence of surface properties on bond strength. However, experimental results of GFRP (type A) and GFRP (type B) reinforced specimens plotted in Figure 7.1 (a) revealed that bond strength of GFRP (type B) bars is slightly higher than that of GFRP (type A) bars owing to the difference of surface configuration. It was noticed that the tested results for helical wrapped with slightly sand coated GFRP bars were closer to the ACI predicted curve than the tested results for sand coated GFRP (SC) bars. This may be attributed to the fact that the ACI 440 equation was developed based on existing database containing limited surface types of only two (spiral wrapping and helical lugs). The Japanese design code also neglects the effect of surface configuration on bond strength. On the contrary, the Canadian codes acknowledge the effect of bar surface on bond strength by suggesting a bar surface factor of k_5 in the CSA-S806 equation and k_6 in the CSA-S6 equation. The ACI 440.1R equation was developed based on concrete strength in the range of 28 to 45 MPa (Wambeke and Shield, 2006). Therefore, it cannot be assumed to be accurate for predicting the bond strength of GFRP bar in HSC. The Canadian code limitations regarding concrete strength ($\sqrt{f_c'}$ should not be more than 5 and 8 MPa for CSA-S806 and CSA-S6, respectively) and concrete cover (d_{cs} is not greater than $2.5d_b$) lead to a constant value of the predicted bond strength for all specimens as illustrated in Figure 7.1 (b and c). The modification factor, α_2, in the Japanese equation was taken as 1. According to the Japanese code limitation regarding the design bond strength of concrete, the predicted bond strength is constant when the concrete strength exceeds 57 MPa as shown in Figure 7.1 (d). Because of the absence of

transverse reinforcement in the pull-out cubes, the effect of confinement considered by the transverse reinforcement index, k_{tr}, in the CSA S6 equation and the transverse reinforcement in the JSCE equation was neglected. The minimum value of the bond strength in experimental results is higher than the bond strengths obtained from Canadian and Japanese design codes, thus, the development length provided by these codes will be over satisfactory.

Table 7.1 - Comparison of test results of GFRP (type A) reinforced cubes with different code's predictions

Specimen label	τ_{exp} (MPa)	ACI 440.1R τ_{pred} (MPa)	$\frac{\tau_{exp}}{\tau_{pred}}$	CSA-S806 τ_{pred} (MPa)	$\frac{\tau_{exp}}{\tau_{pred}}$	CSA-S6 τ_{pred} (MPa)	$\frac{\tau_{exp}}{\tau_{pred}}$	JSCE 1997 τ_{pred} (MPa)	$\frac{\tau_{exp}}{\tau_{pred}}$
A-9.5-2.5d	20.55	34	0.60	4.11	5	7.07	2.91	5.33	3.85
A-9.5-5d	20.08	18.91	1.06	4.11	4.89	7.07	2.84	5.33	3.77
A-9.5-7.5d	19.76	13.88	1.42	4.11	4.81	7.07	2.79	5.33	3.71
A-9.5-10d	19.27	11.36	1.70	4.11	4.69	7.07	2.73	5.33	3.61
A-12.7-2.5d	19.79	34.07	0.58	4.11	4.82	7.07	2.80	5.33	3.71
A-12.7-5d	16.13	18.95	0.85	4.11	3.92	7.07	2.28	5.33	3.02
A-12.7-7.5d	16.71	13.90	1.20	4.11	4.07	7.07	2.36	5.33	3.13
A-12.7-10d	16.05	11.38	1.41	4.11	3.91	7.07	2.27	5.33	3.01
A-15.9-2.5d	19.42	34.76	0.56	4.11	4.73	7.07	2.75	5.33	3.64
A-15.9-5d	18.70	19.33	0.97	4.11	4.55	7.07	2.64	5.33	3.51
A-15.9-7.5d	16.32	14.23	1.15	4.11	3.97	7.07	2.31	5.33	3.06
A-15.9-10d	14.82	11.65	1.27	4.11	3.61	7.07	2.10	5.33	2.78
Average			1.06		4.41		2.56		3.40
COV %			34.3		10.9		10.9		10.9

Note: τ_{exp} is the experimental bond strength; τ_{pred} is the predicted bond strength and COV is a Coefficient of variation.

Table 7.2 - Comparison of test results of GFRP (type B) reinforced cubes with different code's predictions

Specimen label	τ_{exp} (MPa)	ACI 440.1R τ_{pred} (MPa)	$\frac{\tau_{exp}}{\tau_{pred}}$	CSA-S806 τ_{pred} (MPa)	$\frac{\tau_{exp}}{\tau_{pred}}$	CSA-S6 τ_{pred} (MPa)	$\frac{\tau_{exp}}{\tau_{pred}}$	JSCE 1997 τ_{pred} (MPa)	$\frac{\tau_{exp}}{\tau_{pred}}$
B-9.5-2.5d	28.91	31.42	0.92	4.32	6.69	7.07	4.09	5.33	5.42
B-9.5-5d	25.51	16.89	1.51	4.32	5.91	7.07	3.61	5.33	4.78
B-9.5-7.5d	22.15	12.40	1.79	4.32	5.13	7.07	3.13	5.33	4.15
B-9.5-10d	19.05	10.15	1.88	4.32	4.41	7.07	2.69	5.33	3.57
B-12.7-2.5d	28.26	30.78	0.92	4.32	6.54	7.07	4.00	5.33	5.30
B-12.7-5d	23.21	17.12	1.36	4.32	5.37	7.07	3.28	5.33	4.35
B-12.7-7.5d	19.83	12.38	1.60	4.32	4.59	7.07	2.80	5.33	3.72
B-12.7-10d	18.18	10.14	1.79	4.32	4.21	7.07	2.57	5.33	3.41
B-15.9-2.5d	27.77	30.34	0.92	4.32	6.43	7.07	3.93	5.33	5.21
B-15.9-5d	21.52	16.87	1.28	4.32	4.98	7.07	3.04	5.33	4.04
B-15.9-7.5d	19.23	12.38	1.55	4.32	4.45	7.07	2.72	5.33	3.61
B-15.9-10d	18.93	10.14	1.87	4.32	4.38	7.07	2.68	5.33	3.55
Average			1.45		5.26		3.21		4.26
COV %			25.6		17.4		17.4		17.4

Note: τ_{exp} is the experimental bond strength; τ_{pred} is the predicted bond strength and COV is a Coefficient of variation.

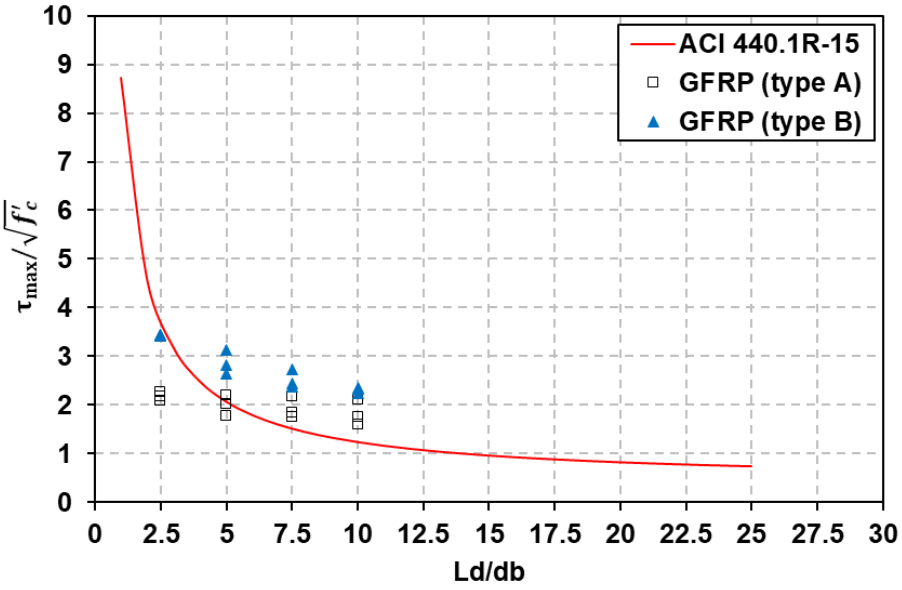

(a) Variation of maximum bond stress with embedment length

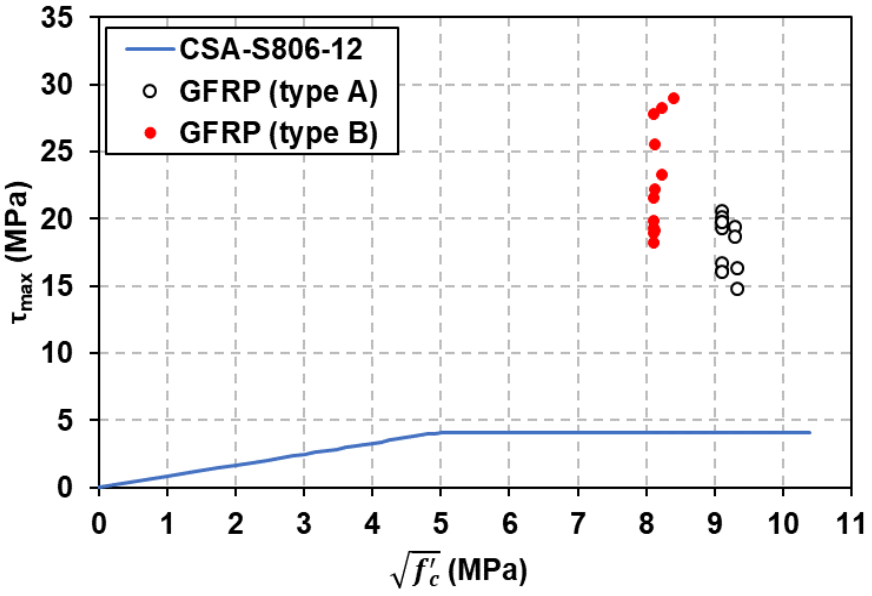

(b) Bond strength vs. square root of concrete strength

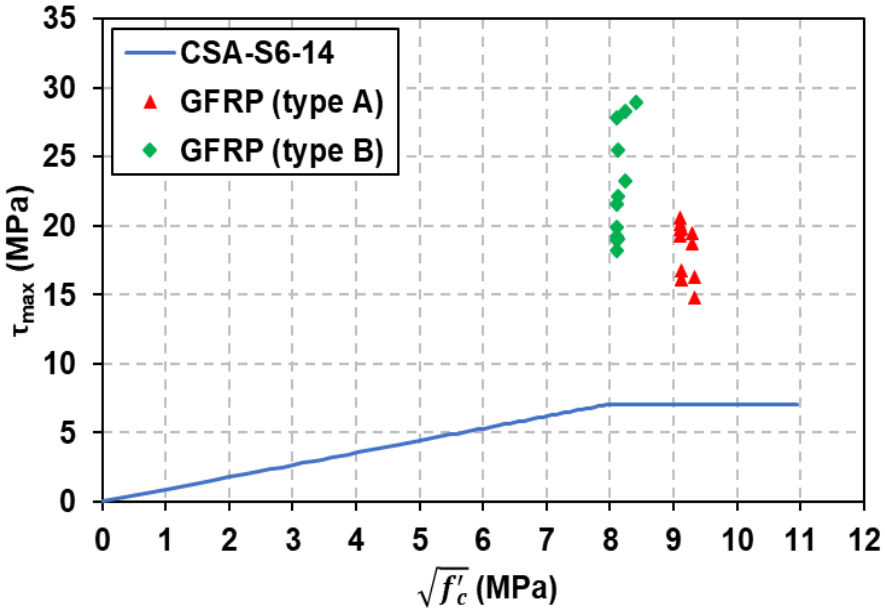

(c) Bond strength vs. square root of concrete strength

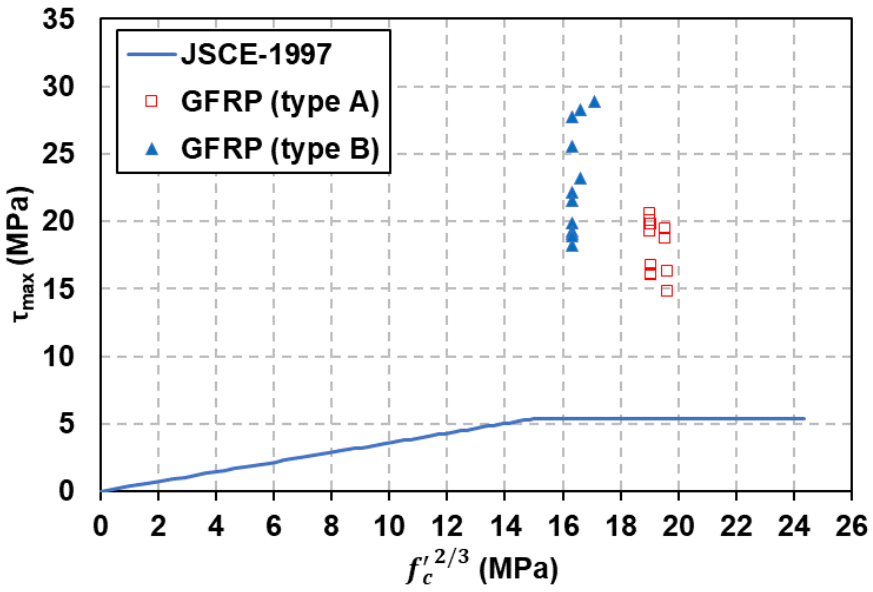

(d) Bond strength vs. concrete strength

Figure 7.1 - Comparison between experimental and different design code predicted bond strengths for cubes

7.4 Comparison of test results of pull-out prisms with current codes

As clearly shown in Figures 7.2 and 7.3, bond strengths obtained from the tests are higher than those predicted by the four design standards, indicating that the codes are conservative. The bond strengths predicted by the ACI 440.1R -15 are closer to the test results as opposed to the other codes, where the mean ratios of experimental to predicted bond strengths are 1.22 with a COV of 23.9% and 1.54 with a COV of 23.4% for GFRP (type A) and GFRP (type B) reinforced prisms as illustrated in Tables 7.3 and 7.4, respectively. A similar observation was detailed in the literature (Veljkovic et al., 2017, Yan et al., 2016), where Veljkovic et al. (2017) used eccentric pull-out specimens reinforced with ribbed GFRP bars, with cubic concrete compressive strengths of 23.3 and 62.3 MPa, and Yan et al. (2016) used the experimental results of sand-coated GFRP reinforced hinged beams

tested by Ametrano et al. (2011), with concrete compressive strengths of 71.2, 115, 147.8 and 174.5 MPa. Furthermore, some small variation among the bond strengths obtained from CSA S806 -12, CSA S6 -14 and JSCE 1997 was noted for each prism. For the GFRP (type A) reinforced prisms, the mean ratios of experimental to predicted bond strengths obtained from CSA S806 -12, CSA S6 -14 and JSCE 1997 are 3.39, 2.27 and 3.01 with a COV of 17.11% as demonstrated in Tables 7.3 and 7.4, respectively. As for the GFRP (type B) reinforced prisms, they are 4.64, 2.84 and 3.76 with a COV of 12.3% as shown in Tables 7.3 and 7.4, respectively. The influence of the main factors considered by design codes on bond strength, which was analyzed and discussed in section 7.3, was also observed in the predictions for pull-out prisms.

Table 7.3 - Comparison of test results of GFRP (type A) reinforced prisms with predictions from different codes

Specimen label	τ_{exp} **(MPa)**	**ACI 440.1R** τ_{pred} **(MPa)**	$\frac{\tau_{exp}}{\tau_{pred}}$	**CSA-S806** τ_{pred} **(MPa)**	$\frac{\tau_{exp}}{\tau_{pred}}$	**CSA-S6** τ_{pred} **(MPa)**	$\frac{\tau_{exp}}{\tau_{pred}}$	**JSCE 1997** τ_{pred} **(MPa)**	$\frac{\tau_{exp}}{\tau_{pred}}$
A-9.5-5d	19.51	17.14	1.14	4.11	4.75	7.07	2.76	5.33	3.66
A-9.5-10d	16.47	10.30	1.60	4.11	4.01	7.07	2.33	5.33	3.09
A-12.7-5d	15.38	17.14	0.90	4.11	3.74	7.07	2.18	5.33	2.88
A-12.7-10d	12.88	10.30	1.25	4.11	3.13	7.07	1.82	5.33	2.42
Average			1.22		3.91		2.27		3.01
COV %			23.90		17.11		17.11		17.11

Note: τ_{exp} is the experimental bond strength; τ_{pred} is the predicted bond strength and COV is a Coefficient of variation.

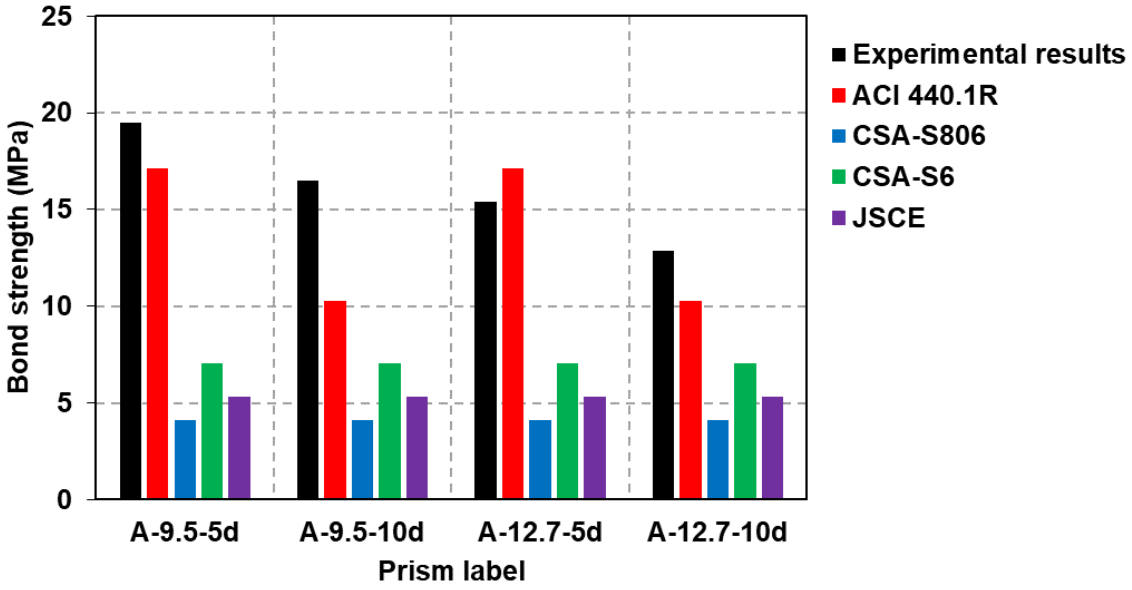

Figure 7.2 - Comparison between experimental and predicted bond strengths for GFRP (type A) reinforced prisms

Table 7.4 - Comparison of test results of GFRP (type B) reinforced prisms with predictions from different codes

Specimen label	τ_{exp} (MPa)	ACI 440.1R τ_{pred} (MPa)	$\frac{\tau_{exp}}{\tau_{pred}}$	CSA-S806 τ_{pred} (MPa)	$\frac{\tau_{exp}}{\tau_{pred}}$	CSA-S6 τ_{pred} (MPa)	$\frac{\tau_{exp}}{\tau_{pred}}$	JSCE 1997 τ_{pred} (MPa)	$\frac{\tau_{exp}}{\tau_{pred}}$
B-9.5-5d	22.79	17.08	1.33	4.32	5.28	7.07	3.22	5.33	4.27
B-9.5-10d	20.49	10.26	2.00	4.32	4.74	7.07	2.90	5.33	3.84
B-12.7-5d	20.16	17.08	1.18	4.32	4.67	7.07	2.85	5.33	3.78
B-12.7-10d	16.8	10.26	1.64	4.32	3.89	7.07	2.38	5.33	3.15
Average			1.54		4.64		2.84		3.76
COV %			23.4		12.3		12.3		12.3

Note: τ_{exp} is the experimental bond strength; τ_{pred} is the predicted bond strength and COV is a Coefficient of variation.

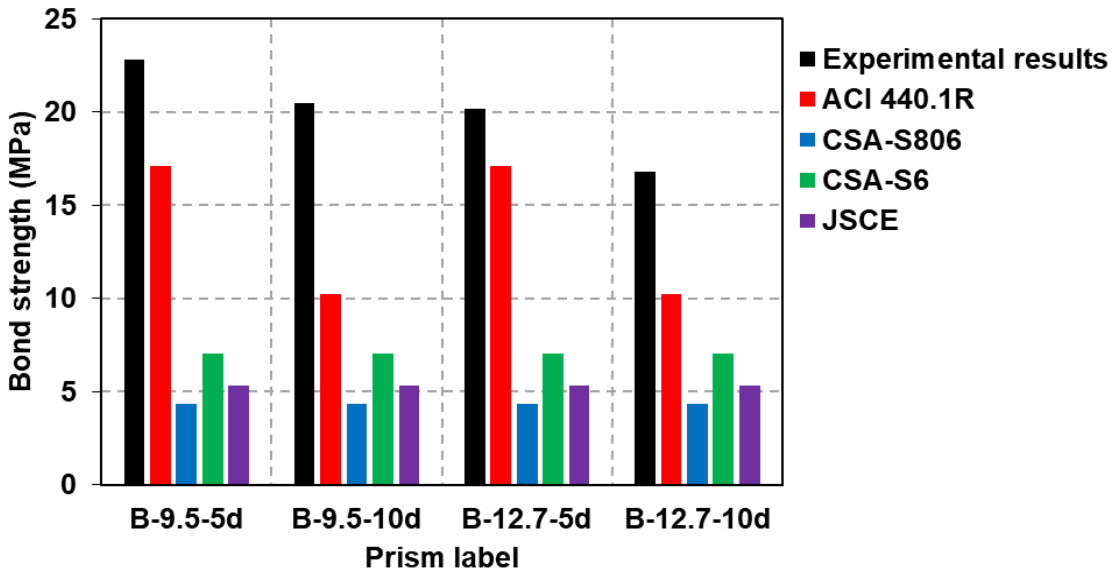

Figure 7.3 - Comparison between experimental and predicted bond strengths for GFRP (type B) reinforced prisms

7.5 Comparison of test results of hinged beams with current codes

The bond strengths provided by code equations were determined based on the geometrical and mechanical properties of the tested hinged beams. Tables 7.5 and 7.6 summarize the comparison of the experimental bond strengths of various specimens and predictions using the methods provided in ACI 440.1R-15, CSA S806-12, CSA S6-14 and JSCE 1997. In addition, the code predictions shown in Figure 7.4 (a to d) were plotted using the geometrical and mechanical properties of the hinged beam in the current research. It can be seen that the ACI 440.1R code was more conservative for top-cast GFRP reinforced specimens than bottom-cast GFRP reinforced ones. The CSA S806, CSA S6 and JSCE codes are too conservative, where the average ratios of experimental to predicted bond strengths are 5.33, 3.1 and 4.11 with a COV of 24% for GFRP (type A) bottom bars, respectively, whereas, they are 4.95, 2.88 and 3.82 with a COV of 23% for

GFRP (type A) top bars, respectively. As for the GFRP (type B) reinforced specimens, the average ratios of experimental to predicted bond strengths are 6.37, 3.89 and 5.17 with a COV of 11% for the bottom bars and 5.23, 3.19 and 4.24 with a COV of 21% for the top bars. However, the average ratio of experimental to predicted bond strengths obtained from the ACI 440 code is 1.52 and 2.13 with a COV of 34% for the bottom and top GFRP (type A) bars, respectively. It is 1.98 with a COV of 24% for the bottom GFRP (type B) bars and 2.55 with a COV of 28% for the top GFRP (type B) bars. Tables 7.5 and 7.6 showed that the bond strength obtained by Canadian and Japanese codes is not influenced by bar diameter and embedment length, and this is attributed to the same reason that was mentioned in section 7.3. The CSA-S806 code considers that the bond strength of a helically wrapped surface is less (5%) than that of a sand coated surface, while the CSA-S6 code recommended to use 0.8 for all surfaces, in absence the experimental data. Moreover, both Canadian and Japanese codes neglect the effect of bar position on bond strength, as the depth of concrete underneath the bars is less than 300mm. Therefore, there is no change in bond strength with changing bar position as illustrated in Tables 7.5 and 7.6. The same observation was also confirmed by Hossain et al. (2014). In contrast to the Canadian and Japanese codes, the bond strength reduces with increasing embedment length as per the ACI 440.1R code as shown in Figure 7.4 (a). The effect of bar diameter on the ACI predictions has been omitted owing to the limitation of the ratio of c/d_b and the value of the embedment length, which was taken as the ratio of the bar diameter, and this resulted in cancelling the effect of bar diameter in the term of d_b/l_e. In addition, the ACI 440. 1R code ignores the

influence of surface configuration on bond strength. However, from Tables 7.5 and 7.6, there is a slight increase in bond strength of GFRP (HW-SC) reinforced specimens compared to those reinforced with GFRP (SC) bars, because of a small variation of concrete strength. It is also noted from Figure 7.4 (a) that the predicted bond strength of the top bars is lower than that of the bottom bars, because the ACI 440. 1R code acknowledges the effect of bar position by a modification factor of 1.5. The ACI 440.1R equation was developed based on concrete strength in the range of 28 to 45 MPa (Wambeke and Shield, 2006). Therefore, it cannot be assumed to be accurate for predicting the bond strength of GFRP bar in HSC. The Canadian code limitations regarding concrete strength and concrete cover lead to a constant value of predicted bond strength for all test specimens as indicated in Figure 7.4 (b and c). In addition, the Japanese code limitation regarding the design bond strength of concrete ($f_{bod} \leq 3.2\ MPa$) results in a constant value of the predicted bond strength as shown in Figure 7.4 (d). Because of the absence of transverse reinforcement in hinged beam specimens, the effect of confinement provided by transverse reinforcement on bond strength was neglected in the CSA-S6 and JSCE equations. The minimum value of the bond strength in experimental results is higher than the bond strengths obtained from Canadian and Japanese design codes, thus, the development length provided by these codes is expected to be over satisfactory.

Table 7.5 - Comparison of test results of GFRP (type A) with predictions from different codes

Specimen label	τ_{exp} (MPa)	ACI 440.1R τ_{pred} (MPa)	$\frac{\tau_{exp}}{\tau_{pred}}$	CSA-S806 τ_{pred} (MPa)	$\frac{\tau_{exp}}{\tau_{pred}}$	CSA-S6 τ_{pred} (MPa)	$\frac{\tau_{exp}}{\tau_{pred}}$	JSCE 1997 τ_{pred} (MPa)	$\frac{\tau_{exp}}{\tau_{pred}}$
A-9.5-5d-B	26.94	18.23	1.42	4.11	6.55	7.07	3.81	5.33	5.05
A-9.5-10d-B	28.86	10.95	2.54	4.11	7.02	7.07	4.08	5.33	5.41
A-12.7-5d-B	22.39	18.23	1.18	4.11	5.45	7.07	3.17	5.33	4.20
A-12.7-10d-B	16.99	10.95	1.49	4.11	4.13	7.07	2.40	5.33	3.19
A-15.9-5d-B	20.80	18.16	1.10	4.11	5.06	7.07	2.94	5.33	3.90
A-15.9-10d-B	15.55	10.88	1.38	4.11	3.78	7.07	2.20	5.33	2.92
Average			1.52		5.33		3.10		4.11
COV%			34		24		24		24
A-9.5-5d-T	25.94	12.16	2.06	4.11	6.31	7.07	3.67	5.33	4.87
A-9.5-10d-T	26.19	7.30	3.46	4.11	6.37	7.07	3.70	5.33	4.91
A-12.7-5d-T	19.70	12.16	1.56	4.11	4.79	7.07	2.79	5.33	3.70
A-12.7-10d-T	16.81	7.30	2.22	4.11	4.09	7.07	2.38	5.33	3.15
A-15.9-5d-T	18.13	12.10	1.44	4.11	4.41	7.07	2.56	5.33	3.40
A-15.9-10d-T	15.37	7.25	2.04	4.11	3.74	7.07	2.17	5.33	2.88
Average			2.13		4.95		2.88		3.82
COV%			34		23		23		23

Note: τ_{exp} is the experimental bond strength; τ_{pred} is the predicted bond strength and COV is a Coefficient of variation.

Table 7.6 - Comparison of test results of GFRP (type B) with predictions from different codes

Specimen label	τ_{exp} (MPa)	ACI 440.1R τ_{pred} (MPa)	$\frac{\tau_{exp}}{\tau_{pred}}$	CSA-S806 τ_{pred} (MPa)	$\frac{\tau_{exp}}{\tau_{pred}}$	CSA-S6 τ_{pred} (MPa)	$\frac{\tau_{exp}}{\tau_{pred}}$	JSCE 1997 τ_{pred} (MPa)	$\frac{\tau_{exp}}{\tau_{pred}}$
B-9.5-5d-B	29.72	17.33	1.71	4.32	6.88	7.07	4.20	5.33	5.58
B-9.5-10d-B	28.34	10.41	2.72	4.32	6.56	7.07	4.01	5.33	5.32
B-12.7-5d-B	29.48	17.33	1.70	4.32	6.82	7.07	4.17	5.33	5.53
B-12.7-10d-B	22.47	10.41	2.16	4.32	5.20	7.07	3.18	5.33	4.22
B-15.9-5d-B	27.64	17.26	1.60	4.32	6.40	7.07	3.91	5.33	5.19
B-15.9-10d-B	>21.16	10.34	N/A	4.32	N/A	7.07	N/A	5.33	N/A
Average			1.98		6.37		3.89		5.17
COV%			24		11		11		11
B-9.5-5d-T	29.26	11.55	2.53	4.32	6.77	7.07	4.14	5.33	5.49
B-9.5-10d-T	25.76	6.94	3.71	4.32	5.96	7.07	3.64	5.33	4.83
B-12.7-5d-T	24.31	11.55	2.10	4.32	5.63	7.07	3.44	5.33	4.56
B-12.7-10d-T	20.70	6.94	2.98	4.32	4.79	7.07	2.93	5.33	3.88

B-15.9-5d-T	19.72	11.50	1.71	4.32	4.56	7.07	2.79	5.33	3.70
B-15.9-10d-T	15.72	6.89	2.28	4.32	3.64	7.07	2.22	5.33	2.95
Average			2.55		5.23		3.19		4.24
COV%			28		21		21		21

Note: τ_{exp} is the experimental bond strength; τ_{pred} is the predicted bond strength and COV is a Coefficient of variation.

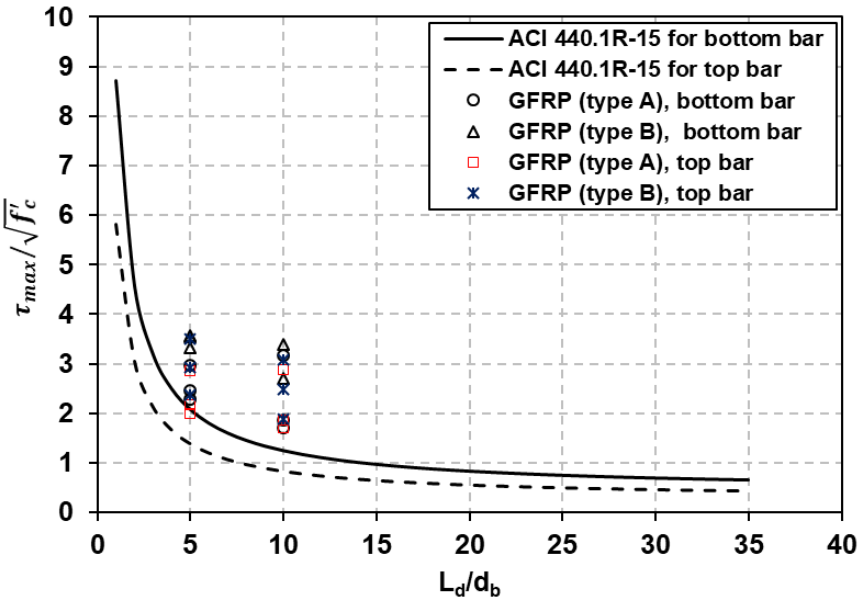

(a) Variation of maximum bond stress with embedment length

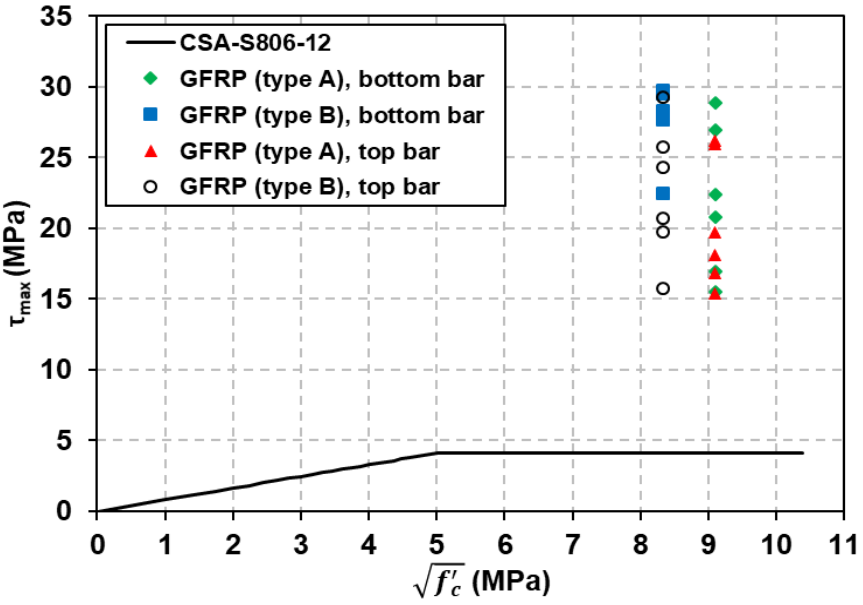

(b) Bond strength vs. square root of concrete strength

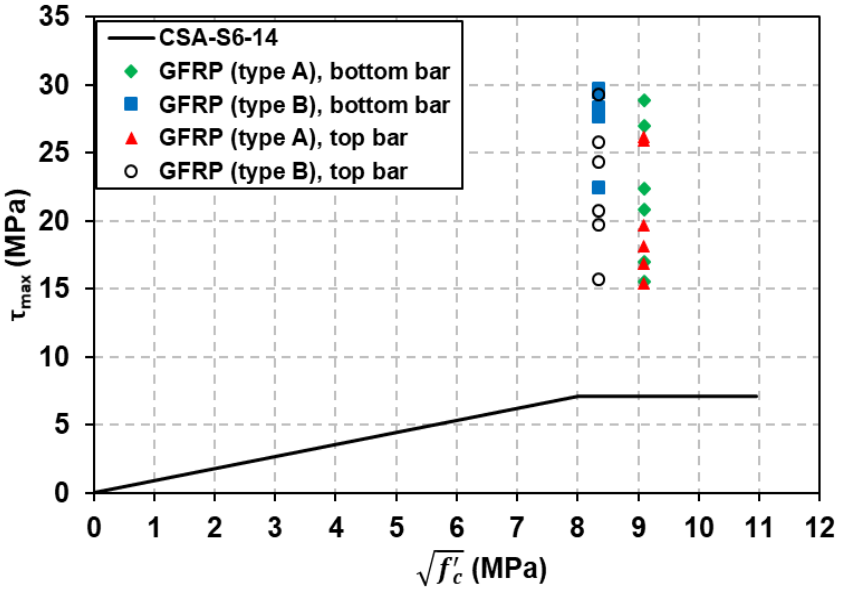

(c) Bond strength vs. square root of concrete strength

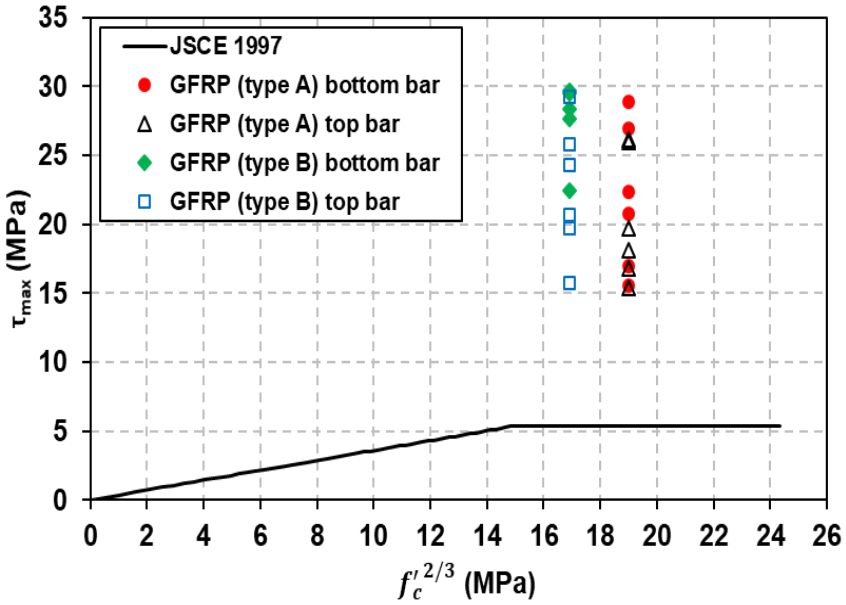

(d) Bond strength vs. concrete strength

Figure 7.4 - Comparison between experimental and different design code predicted bond strengths for hinged beams

7.6 Conclusions

The applicability of existing bond strength models available in the codes on HSC specimens reinforced with GFRP bars is checked by comparing the experimental bond strengths with code predictions. Based on the comparative results and discussions, the following conclusions are drawn:

1. Comparisons between different design codes regarding bond strength prediction show that four key parameters, including concrete strength, bar diameter, concrete cover and bar location, are taken into consideration in all these codes.
2. Embedment length is considered only in the ACI 440 code for bond strength calculation. In contrast, bar surface is considered only in the Canadian codes. The confinement provided by transverse reinforcement is taken into account in CSA-S6-14 and JSCE 1997 codes, which is ignored in ACI 440.1R and CSA-S806 codes. Moreover, fibre type is considered only in both Canadian codes.
3. The ACI 440 equation regarding bond strength is mainly developed for splitting failure. Also, JSCE equation has been developed for a splitting controlled failure. Hence, formula for pull-out failure needs to be developed in both codes.
4. In general, all design codes showed conservative results for all specimens tested, but ACI predictions were unconservative for pull-out cubes having embedment length of $2.5d_b$. ACI predictions give a good agreement with experimental data compared to other codes.

5. Both Canadian and Japanese codes are overly safe. Therefore, modifications to these codes are necessary for more accurate prediction of bond strength of GFRP bars embedded in HSC.
6. Due to the limitations suggested by Canadian and Japanese codes, bond strength predictions were constant for all high-strength concrete specimens.
7. The effect of transverse reinforcement on bond strength considered by CSA-S6 and JSCE was neglected in all pull-out and hinged beam specimens owing to the fact that no transverse reinforcement was provided in the current research specimens.

Chapter 8

Prediction of bond strength of GFRP re-bars in concrete using artificial neural networks

8.1 Introduction

There are several parameters affecting bond strength of GFRP bars embedded in concrete as described in section 2.6. The effect of these parameters is complex and non-linear; thus, it is difficult to develop a model using rational approaches with a sufficient degree of accuracy. Therefore, an artificial neural network (ANN) is introduced in this chapter to model the bond strength of GFRP bars in concrete using pull-out test data. This chapter will describe a database used to train the NN and construction of the ANN model. The main parameters considered to develop the ANN model are bar diameter, embedment length, concrete compressive strength and concrete cover. In addition, a parametric study will be conducted using the proposed model to investigate the generalization ability of the ANN model and the effect of main parameters on the bond strength of GFRP bars.

8.2 Applications of artificial neural networks in concrete structures

Artificial neural networks (ANNs) are applied to several civil engineering problems which are complicated to be solved using conventional engineering methods. The ANN is an efficient tool for engineering applications and it can provide reasonable accuracy for civil engineering problems (Jeng et al., 2003). Neural network modelling is inspired by the biological functioning of the human brain (Dahou et

al., 2009) and the applications and principles of ANN in civil engineering were summarized in the work by Flood and Kartam (1994) and Adeli (2001). The neural network toolbox used to develop the models is available in MATLAB. Several previous studies have created the ANN models to deal with complex civil engineering problems. For example, the ANN - based model was developed by Dahou et al. (2009) for predicting the bond strength of steel re-bars embedded in concrete, and the results showed that the created model provides good predictions. In addition, Sakla and Ashour (2005) predicted the tensile capacity of single adhesive anchors using ANN, and a good predictive performance was achieved. Ashour and Alqedra (2005) also employed ANN for predicting concrete breakout strength of single anchors in tension, and the predictions are in a good agreement with the experimental results. Furthermore, the applications of artificial neural networks have been developed for structural members reinforced with fibre reinforced polymer (FRP) re-bars, such as the prediction of the shear strength of FRP reinforced concrete members (Bashir and Ashour, 2012), the prediction of performance evaluation of RC rectangular beams with externally bonded glass fibre reinforced polymer reinforcement (Pannirselvam et al., 2010) and the prediction of the behaviour of FRP-strengthened RC structural members (Naderpour et al., 2011), as well as the prediction of FRP - concrete ultimate bond strength (Abdalla et al., 2011). It was reported that ANNs provided with results close to real-life results. In spite of these successful applications, the ANN experiences from the drawback of the searching strategy. During the training process, the values of initial weights and biases are randomly chosen; thus, it takes a long time to reach the accurate solution and the convergence. In addition,

iterations lead to additional cost because of the longer operational time. Another disadvantage is an overfitting, in this case, the ANN is not able to generalize new data within the range of inputs, although it has a good performance.

8.3 Artificial neural network background

This section will describe the basic concepts of ANN and in particularly, the structure and training process of the ANN model.

8.3.1 Neural network structure and the concept of neuron

Artificial neural network models are composed of input, hidden and output layers that are linked to each other by arrows to construct a dense network. These arrows that represent the strength of connection between the neurons have weights. Each signal travelling across the connection is multiplied by a weight (numerical value) and each layer consists of a large number of processing units known as nodes or neurons. A neural network accepts certain inputs and yields certain outputs (Ashour and Alqedra, 2005). No rules are specified to determine the number of hidden layers and the number of neurons in the hidden layer, therefore a trial and error method will be conducted to select the optimum number of hidden layers and hidden neurons (Ashour and Alqedra, 2005). In ANN, each neuron can have a number of input signals, coming from the previous layer, but it produces only one output signal as shown in Figure 8.1, a neuron consists of two parts: the net function and the activiation function. The net function clarifies how input signals coming from the previous layer neurons combine together to produce net input signal (s). The net input signal is defined by equation (8.1).

$$s = \sum_{i=1}^{n} w_i x_i + b \tag{8.1}$$

where w_i is the weight of input x_i, b is the bias and is used to model the threshold, n is the number of neurons in a previous layer and s is net input signal of neuron. The output signal of the neuron (y_i) is connected to the net input signal (s_i) by the activation function $f(s)$. No calculations are fulfilled in the input neurons.

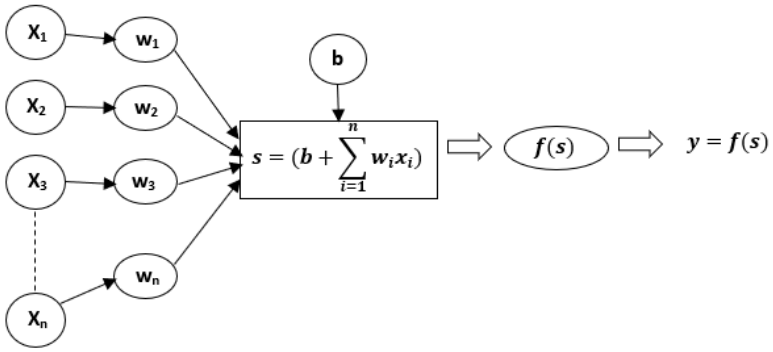

Figure 8.1 - Schematic diagram of the Neuron (Dahou et al., 2009)

Several activation functions have been proposed in the various ANN models, but the sigmoid function is the most commonly used function (Sakla and Ashour, 2005). It is a non-linear and continuously differential function. This function achieves a smooth mapping $(-\infty, +\infty)$ to $(-1, 1)$ for tan sigmoid function and $(-\infty, +\infty)$ to $(0, 1)$ for log sigmoid function as shown in Figure 8.2 (a and b). They are formulated as follows:

For Tan sigmoid function

$$y_i = f(s_i) = \frac{2}{1 + e^{-2s_i}} - 1 \tag{8.2}$$

For Log sigmoid function

$$y_i = f(s_i) = \frac{1}{1 + e^{-s_i}} \tag{8.3}$$

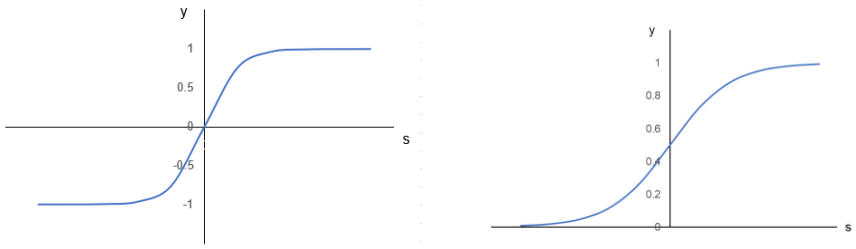

(a)Tan Sigmoid **(b) Log sigmoid**

Figure 8.2 - Activation Functions

8.3.2 Neural network training

During the training process of ANN model, at the beginning, the weights and biases are randomly chosen and then they are updated using an iterative back-propagation process until the difference between the actual output, t_k, and the predicted output, x_k, is diminished. The iterations are named as epochs and the algorithm stops when the error reaches to a minimal value, the error stops improving or epochs reach to the specified number. The performance function is selected to be the mean absolute percentage of error (MAPE).

$$\mathrm{MAPE}(\%) = \frac{1}{\mathrm{M}}\sum_{\mathrm{k=1}}^{\mathrm{M}} \mathrm{ABS}\left(1 - \frac{x_k}{t_k}\right) 100 \qquad (8.4)$$

where M is the number of data. After achieving the successful training, the weights and biases are fixed and employed for predictive purposes. The common problem that encounters the network training is over-fitting, so the network is not able to generalize new cases. This phenomenon can be monitored, if the error starts increasing during the training process. There are three ways to avoid the occurrence of over-fitting. The first way is to reduce the number of hidden neurons, the second one is to use early stopping which requests a validation

dataset and the third way is to utilize weight-decay regularization which involves modifying the performance function by adding the term involving the sum of squares of weights and biases to improve the generalization ability of the trained neural network. This modification will lead to obtaining the smaller weights and biases, thus a smoother network is produced without the probability of overfitting (Sakla and Ashour, 2005). Early stopping is an effective and widely used method. Therefore, it will be used to improve the generalization of neural network and the training algorithm used is Levenberg-Marquardt (trainlm). This algorithm is allowed to run until the convergence (the error is close to zero). Database will be divided into three subsets: training, testing and validation subsets. The training data is used to calculate the gradient and to adjust the weights and biases to minimize the training error. When the validation error that is observed during the training process increases after a number of iterations, the training will stop, and the weights and biases at the lowest validation error will return. The testing data is not used to train the network, but it is used to verify the created network (Bashir and Ashour, 2012).

8.4 Experimental data

Previous research works have been conducted to understand the bond behaviour of FRP bars embedded in concrete using a pull-out test. It was reported that the bond strength is influenced by several parameters as mentioned in section 2.6. The ones that will be only considered in this study are bar diameter (d_b), embedment length (l_e), concrete compressive strength (f_c') and concrete cover (c). The current experimental study only focused on investigating the bond

strength of two common GFRP types (helical wrapping with slightly sand coating and sand coating). Therefore, database related to bond strength of GFRP (HW-SC) and GFRP (SC) bars was only taken into account in this study to develop the ANN models. Two databases were collected from the literature regarding a pull-out test only, including authors' results. The first database contains the experimental bond strength results of 52 GFRP (HW-SC) reinforced concrete specimens. The second database consists of the experimental bond strength results of 65 GFRP (SC) reinforced concrete specimens. All specimens were failed by a pull-out mode. Some pull-out specimens have the cube shape and others have the prism shape. The material and geometrical properties of the 117 test specimens as well as their original sources are given in Appendix A (Tables A.1 and A.2 for GFRP (HW-SC) and GFRP (SC) reinforced specimens, respectively). The statistical properties of experimental database of both GFRP types are summarized in Tables 8.1 and 8.2. The range of different input parameters in the GFRP (HW-SC) and GFRP (SC) database used for training, testing and validating the ANN model is presented in Figures 8.3 and 8.4, respectively.

Table 8.1 - Statistical properties of pull-out specimens reinforced with GFRP (HW-SC) bars

Neural network input parameters	Minimum	Maximum	Mean	SD	COV%
Cylinder compressive strength of concrete, f_c' (MPa)	20	92.40	52.50	20.90	39.81
Embedment Length, L_e (mm)	23.75	190	82.92	36.52	44.04
Diameter of GFRP re-bar, d_b(mm)	6	25.4	14.67	4.21	28.72
Concrete cover, c (mm)	43.65	137.3	89.62	17	18.97
Bond strength, τ_{max} (MPa)	8.41	30.59	16.96	4.21	24.79

Note: SD is a standard deviation and COV is a coefficient of variation.

Table 8.2 - Statistical properties of pull-out specimens reinforced with GFRP (SC) bars

Neural network input parameters	Minimum	Maximum	Mean	SD	COV%
Cylinder compressive strength of concrete, f_c' (MPa)	20	92.40	57.94	18.27	31.52
Embedment Length, L_e (mm)	23.75	191	83.80	40.66	48.52
Diameter of GFRP re-bar, d_b (mm)	8	25.4	14.48	4.20	28.99
Concrete cover, c (mm)	40	137.3	71.52	27.39	38.29
Bond strength, τ_{max} (MPa)	3.66	28.91	15.54	6.55	42.13

Note: SD is the standard deviation and COV is the coefficient of variation.

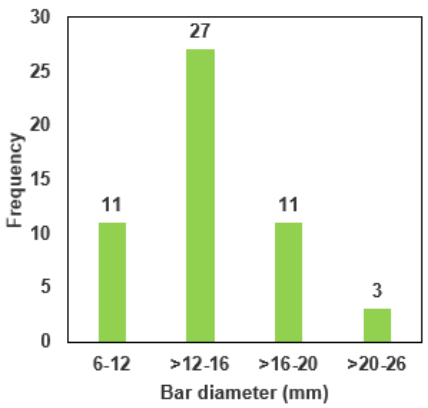

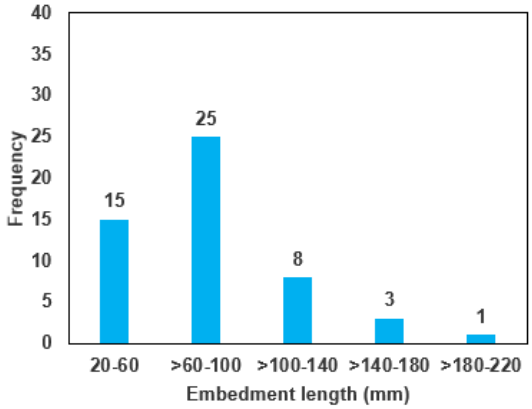

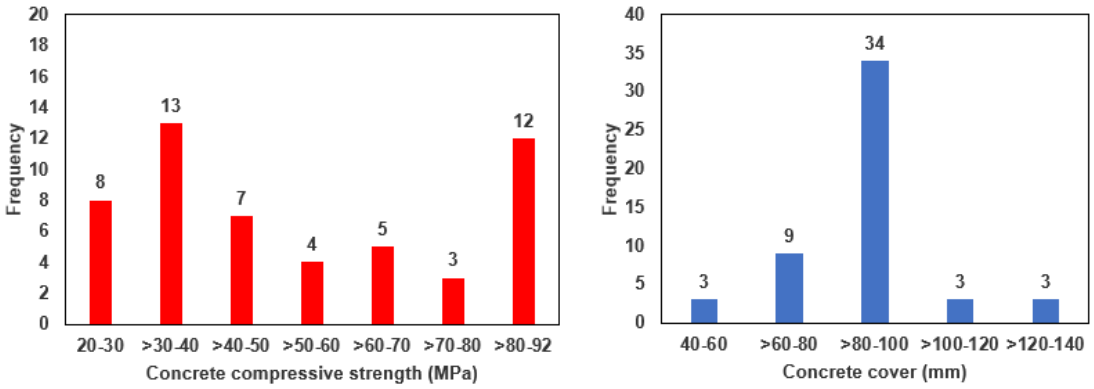

Figure 8.3 - Distribution of different parameters in the GFRP (HW-SC) database

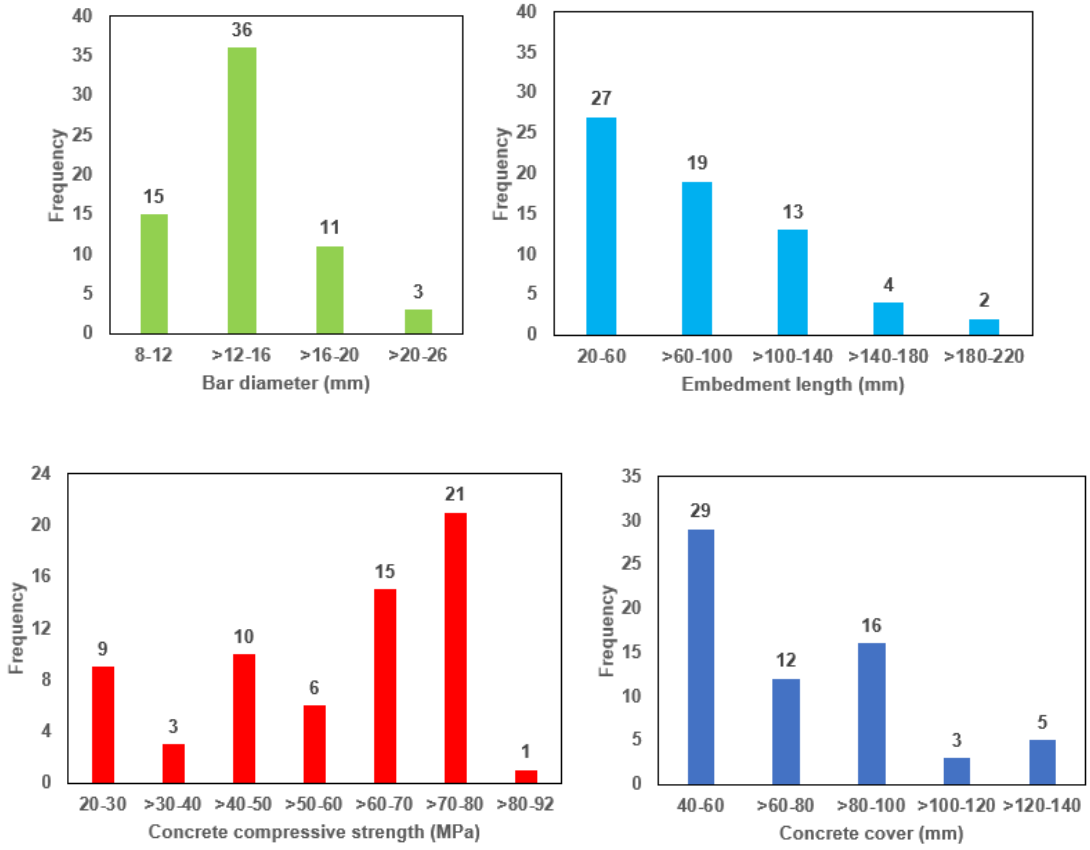

Figure 8.4 - Distribution of different parameters in the GFRP (SC) database

8.5 Data normalization

Tan sigmoid transfer function is employed in the hidden layer rather than log sigmoid function because it is more suitable for multi-layer networks developed

for non-linear applications (Bashir and Ashour, 2012). Tan sigmoid produces the outputs in the range (-1, +1). The input is sensitive in the range not much larger than (-1, +1), therefore, all input data are scaled to be in the range from -1 to +1 before being presented to the network using the below equation.

$$I_n = 2\left(\frac{I - I_{min}}{I_{max} - I_{min}}\right) - 1 \tag{8.5}$$

where I_n and I are the normalized and unnormalized values of the training set, I_{min} and I_{max} are the minimum and maximum values of the data set, respectively. The benefit of normalization of the input data is to improve the learning speed and to reduce the trained network error. A linear transfer function is used in the output layer and this function produces the outputs in the range of $(-\infty, +\infty)$. Therefore, the target values are not scaled and the outputs do not need to be rescaled.

8.6 Construction of the ANN model

8.6.1 Neural network toolbox

The neural network toolbox available in MATLAB version 9.1 (R2016b) is used to build the current network model. The ANN toolbox is able to model the problem using back propagation NN with a wide range of transfer functions, learning techniques, network architectures, training functions and performance functions (Ashour and Alqedra, 2005).

8.6.2 Development of the ANN model

The multi-layered feed-forward neural network with a back-propagation algorithm is used in this study. It is the most widely used to train the input data in order to

obtain the output data and it is used extensively for its efficient generalization abilities (Dahou et al., 2009). The ANN model consists of one input layer, one hidden layer and one output layer as shown in Figure 8.5. The input layer contains four parameters (diameter of GFRP bar, embedment length of GFRP bar, compressive strength of concrete and concrete cover). Each of the four parameters is represented by a single neuron in the input layer. A hidden layer consists of nodes, whose number is not estimated by a rule, but for avoiding the overfitting, the smallest number of neurons was assigned for the hidden layer as mentioned in section 8.3.2. The hidden neurons were increased from one to five. In addition, empirical criteria for the number of the hidden neurons are summarized by Miličević and Šipoš (2017). The one which is suitable for the current problem is that the hidden neuron number is equal to or smaller than the sum of input and output parameters. The only one neuron in the output layer is the predicted bond strength. The number of database that is fed to the ANN is 52 and 65 for GFRP (HW-SC) and GFRP (SC), respectively. The database was randomly divided into 75% (39 GFRP (HW-SC) specimens and 49 GFRP (SC) specimens) for training subset, 20% (10 GFRP (HW-SC) specimens and 13 GFRP (SC) specimens) for testing subset and 5% (3 specimens for both GFRP types) for validation subset. The range of each parameter in the training subset was examined to ensure that it covers the considered range. As noted, the highest percentage is 75% to train the ANN in order to create a more accurate model. Figures 8.6 and 8.7 show the frequency distribution of each variable for each group in the database of GFRP (HW-SC) and GFRP (SC) specimens, respectively. The data flows in one direction from the input layer to the output

layer, no feedback loop presents. A trial and error approach was used during the training process until reaching the acceptable results. The frequency distribution of database changes at each training trial, where the testing subset that gives a high error will move into the training subset and be replaced with another random data to perform better results and learning. Two criteria were utilized to evaluate the network performance: a regression value, R, which measures the correlation between outputs and targets, and error value, MAPE. The best performance should have regression and error values equal to or close to one and zero, respectively. A total of 5 different NNs with a different number of hidden neurons are created and tested for both GFRP types, as listed in Tables 8.3 and 8.4. The model which gives the lowest prediction error is the selected one. At first, weights and biases are randomly chosen by the NN toolbox of MATLAB. Then during the training process of the network, all weights and biases are adjusted using an iterative back-propagation procedure until the difference between the target and output is minimized. The developed model will be used to conduct a parametric study as described in section 8.7

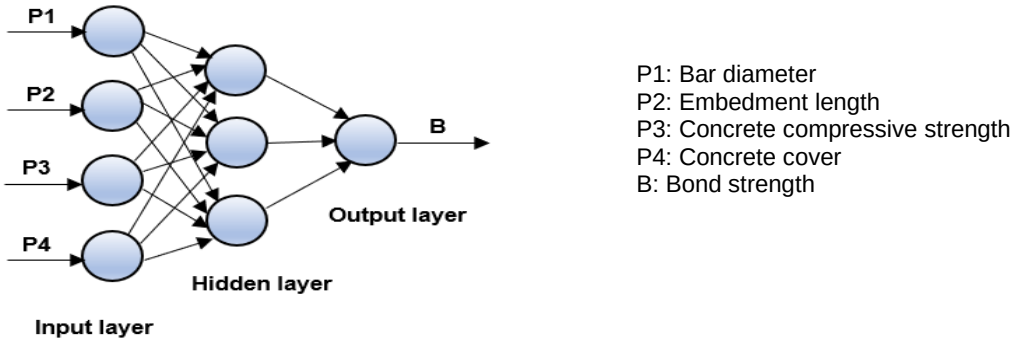

Figure 8.5 - A schematic diagram of typical neural network architecture

8.6.3 Performance of the developed ANN model

Statistical observations (mean, standard deviation, coefficient of variation and mean absolute percentage error of τ_{exp}/τ_{pred}) are used to monitor the network performance. Tables 8.3 and 8.4 summarize the statistical results for all helical wrapped GFRP and sand coated GFRP specimens, respectively. The influence of changing of the number of the hidden neurons on the mean absolute percentage error is shown in Tables 8.3 and 8.4. As can be seen that the number of hidden neurons has a little effect on the performance of the ANNs. In Table 8.3, although the mean, standard deviation and coefficient of variation of the ratio of the experimental to predicted bond strengths for different NNs are similar, the model with three neurons is selected due to having the prediction error less than others. Moreover, the 4x3x1 model is able to correctly predict the trend of different influencing variables on the bond strength of GFRP (HW-SC) bars in concrete. The mean absolute percentage of error of this network is 9.57%. In Table 8.4, the developed models with three or five neurons give the lowest prediction error. However, the 4X3X1 NN is chosen, because of less possibility of overfitting and it also gives a reasonable trend of the effect of the main parameters on the bond strength of GFRP (SC) bars as detailed later. The MAPE% of this network is 11.82%, which is not far from that (11.45%) of the network having five hidden neurons. Comparisons between the experimental and predicted bond strengths for GFRP (HW-SC) and GFRP (SC) bars are shown in Figure 8.8 (a) to (c) and Figure 8.9 (a) to (c) for training, testing and all data sets, respectively. There is a good agreement between the predicted values and the experimental results. For

GFRP (HW-SC) reinforced specimens, the regression value, R, is 0.84 and 0.78 for training and testing subsets, respectively. The mean ratio of measured to predicted bond strengths for training and testing subsets is 1.01 and 1.00, respectively. The mean absolute percentage of error is 10.24% and 8.86% for training and testing data, respectively. As for GFRP (SC) reinforced specimens, the regression value, R, is 0.95 and 0.96 for training and testing subsets, respectively. The mean ratio of measured to predicted bond strengths for training and testing subsets is 1.00 and 1.02, respectively. The mean absolute percentages of error are 12.65% and 10.30% for training and testing data, respectively. It can be concluded that the ANN is successful in learning the relationship between the input and output data.

Table 8.3 - Statistical results of the 5 models created for GFRP (HW-SC) reinforced specimens

NN architecture	Mean	SD	COV%	MAPE%
4x1x1	1.04	0.17	15.91	11.69
4x2x1	1.02	0.16	15.95	10.87
4x3x1	1.01	0.13	13.20	9.57
4x4x1	1.05	0.16	15.07	9.94
4x5x1	1.02	0.15	14.31	10.95

Table 8.4 - Statistical results of the 5 models created for GFRP (SC) reinforced specimens

NN architecture	Mean	SD	COV%	MAPE%
4x1x1	1.10	0.35	32.09	38.60
4x2x1	1.01	0.17	16.41	12.91
4x3x1	1	0.14	14.06	11.82
4x4x1	0.98	0.15	15.38	12.82
4x5x1	1.02	0.16	15.47	11.45

Note: The first and last numbers refer to the number of neurons in the input and output layers, respectively. The second number refers to the number of hidden neurons. SD is a standard deviation; COV is a coefficient of variation and MAPE is a mean absolute percentage error.

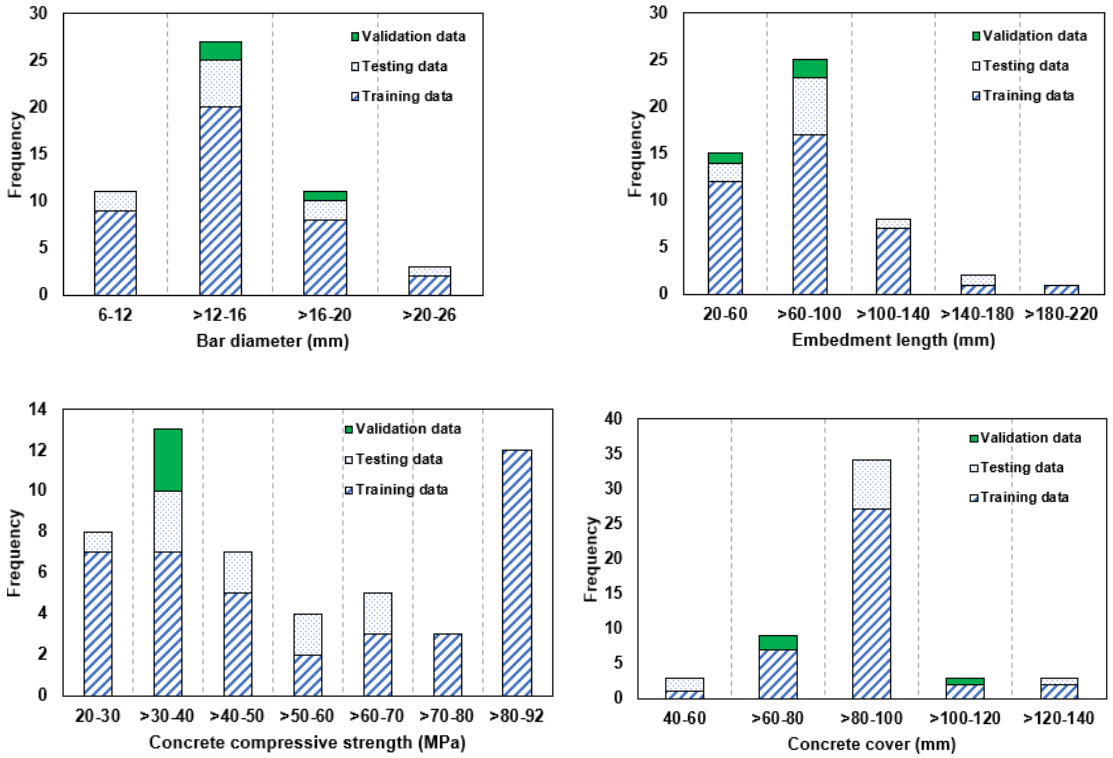

Figure 8.6 - Distribution of different main variables in the database of GFRP (HW-SC) reinforced specimens

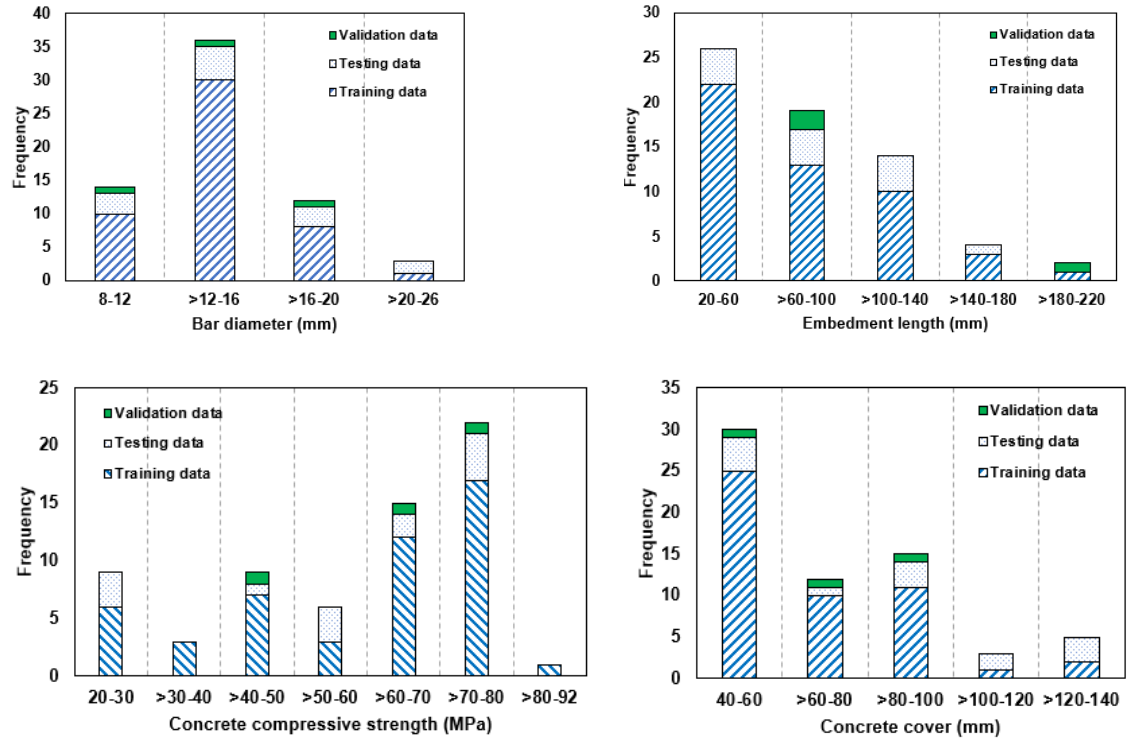

Figure 8.7 - Distribution of different main variables in the database of GFRP (SC) reinforced specimens

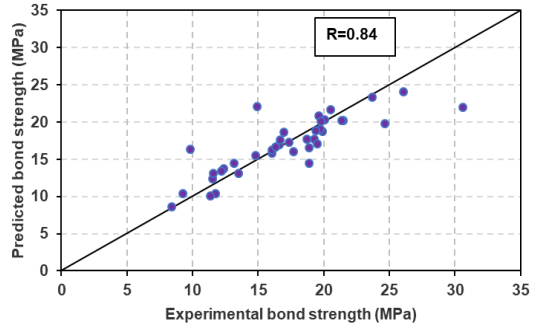

(a) 39-training subset

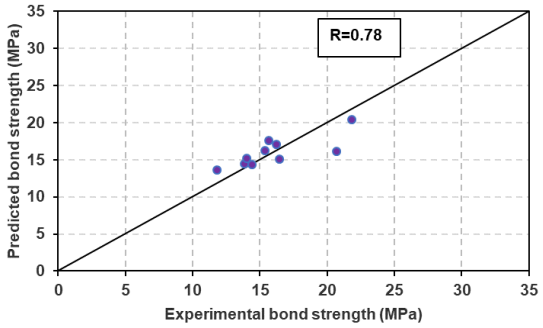

(b) 10-testing subset

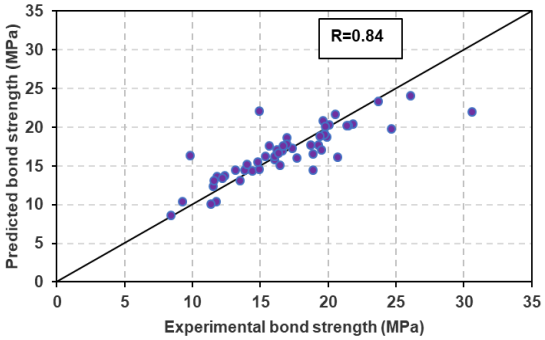

(c) 52-training, testing and validation data set

Figure 8.8 - Comparison of experimental and predicted bond strengths for the ANN training, testing and all data sets of GFRP (HW-SC) reinforced specimens

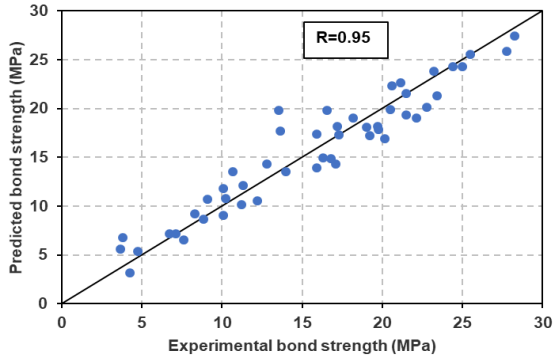

(a) 49-training subset

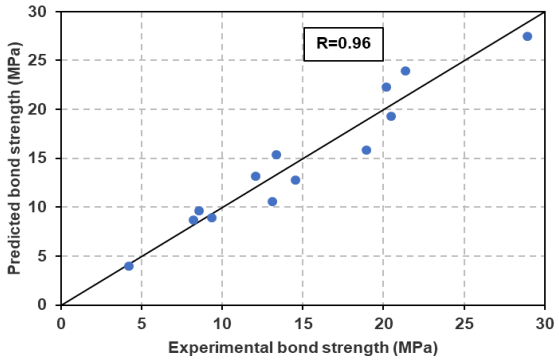

(b) 13-testing subset

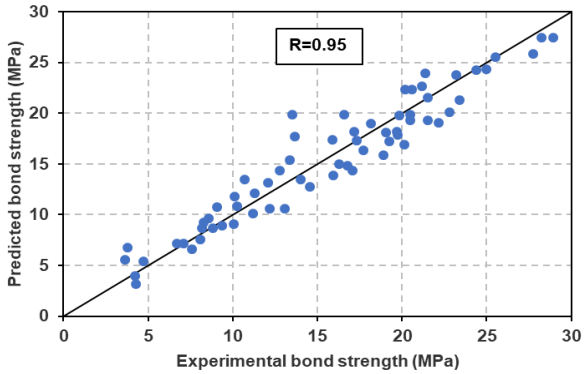

(c) 65-training, testing and validation data set

Figure 8.9 - Comparison of experimental and predicted bond strengths for the ANN training, testing and all data sets of GFRP (SC) reinforced specimens

8.7 Parametric study

To investigate the generalization ability of the ANNs and the effect of the main input parameters (embedment length, bar diameter, concrete compressive strength and concrete cover) on the bond strength, a parametric study is conducted using the developed networks. The ranges that are covered in the database are only considered in this parametric study to obtain reliable trends. The below relationships between the main parameters and the bond strength are represented by selecting the values of parameters within a range having a high frequency. These values are determined for both GFRP types as shown in Table 8.5. For each relationship, only one parameter is changed for the sake of investigating its effect on the bond strength. and other parameters are kept constant.

Table 8.5 - The constant values of parameters used in a parametric study

GFRP type	d_b (mm)	L_e (mm)	f'_c (MPa)	c (mm)
Helical wrapping with slightly sand coating	12.7	$5d_b$	40	92.05
Sand coating	12.7	$5d_b$	74.2	40

8.7.1 Influence of embedment length on bond strength

Figure 8.10 shows the variation in bond strength versus the embedment length. The bond strength reduces gradually with increasing the embedment length because of the nonlinear distribution of the bond stresses along the embedment length (Achillides and Pilakoutas, 2004). This trend agrees with the results obtained from the previous studies by Tastani and Pantazopoulou (2006), Okelo and Yuan (2005), Achillides and Pilakoutas (2004) and Tighiouart et al. (1998). In

addition, it is similar to the result achieved using steel re-bars. This effect is also acknowledged by the ACI-440.1R (2015) code. However, the Canadian and Japanese codes ignore the embedment length in their bond strength equations. Experimental results having concrete compressive strength, bar diameter and concrete cover similar to those used to represent the below trend of GFRP (HW-SC) bars (Sooriyaarachchi, 2006) were plotted in Figure 8.10 (a) to compare with the predicted results. The only available experimental data having bar diameter and concrete cover similar to those used to represent the below curve of GFRP (SC) bars with differing concrete compressive strength of 67.49 MPa were presented in chapter 4 and plotted in Figure 8.10 (b) to compare with the predicted results. In general, the predicted NN bond strengths have a good agreement with the experimental results.

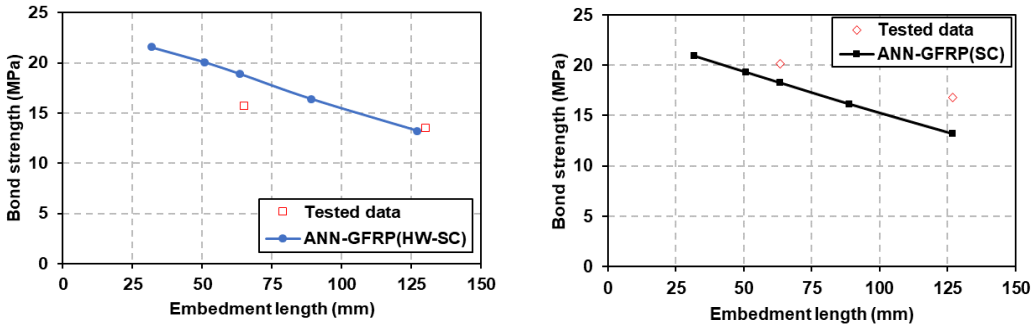

(a) **(b)**

Figure 8.10 - Effect of embedment length on the predicted bond strength

8.7.2 Influence of bar diameter on bond strength

Larger diameters develop less bond strength than smaller ones as predicted by the trained ANN and shown in Figure 8.11. This result was also reported by Hao et al. (2007), Baena et al. (2009), Okelo and Yuan (2005) and Achillides and

Pilakoutas (2004). This tendency is due to the bleeding of water underneath the big diameters, generating big voids, which in turn reduce the contact area between the rebar and the concrete, leading to decrease the bond strength (Hao et al., 2007, Tighiouart et al., 1998), whereas, Achillides and Pilakoutas (2004) explained that this phenomenon is owing to three factors: embedment length, Poisson effect and shear lag, which are described in more detail in section 2.6.2. In addition, the bar diameter is included in all design code equations developed to predict the bond strength. Limited experimental data available in the previous study (Okelo and Yuan, 2005) for GFRP (HW-SC) pull-out specimens and the current study for GFRP (SC) pull-out specimens are also plotted in Figure 8.11 (a) and (b), respectively. The concrete compressive strength of 67.49 MPa for the GFRP (SC) tested data is slightly different from that used to represent the predicted trend. The tested data presented in Figure 8.11 (b) gives a better agreement with the predicted bond strengths than that presented in Figure 8.11 (a) because the ANN model developed for GFRP (SC) has higher regression values than the ANN model developed for GFRP (HW-SC).

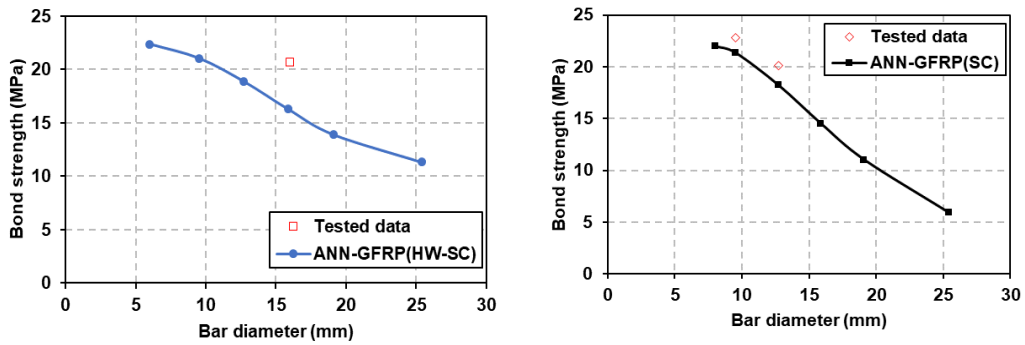

(a) **(b)**

Figure 8.11 - Effect of bar diameter on the predicted bond strength

8.7.3 Influence of concrete compressive strength on bond strength

Figure 8.12 illustrates the effect of changing the concrete compressive strength on the bond strength for both GFRP types. The increase in concrete compressive strength leads to the increase of bond strength of both GFRP bars, which is similar to the results obtained by Xue et al. (2008), Lee et al. (2008) and Xue et al. (2014). However, this effect disappears, when the value of concrete compressive strength reaches 60 MPa for both GFRP types. Subsequently, it can be stated that concrete strength influences the bond strength up to a certain limit beyond which no further enhancement of bond strength with the increase of concrete strength as reported by Karlsson (1997), Achillides (1998) and Davalos et al. (2008). The improvement in bond strength due to increasing the concrete compressive strength is more significant in steel re-bars than GFRP re-bars (Lee et al., 2008). All design codes acknowledge the effect of concrete strength on the bond strength by including the concrete strength in their bond strength equations. Limited experimental data available in the literature (Baena et al., 2009, Sooriyaarachchi, 2006) for pull-out specimens reinforced with GFRP (HW-SC) bars and presented in chapter 4 for pull-out specimens reinforced with GFRP (SC) bars are plotted in Figure 8.12 (a) and (b), respectively. It is found that the predicted bond strengths are close to the experimental results.

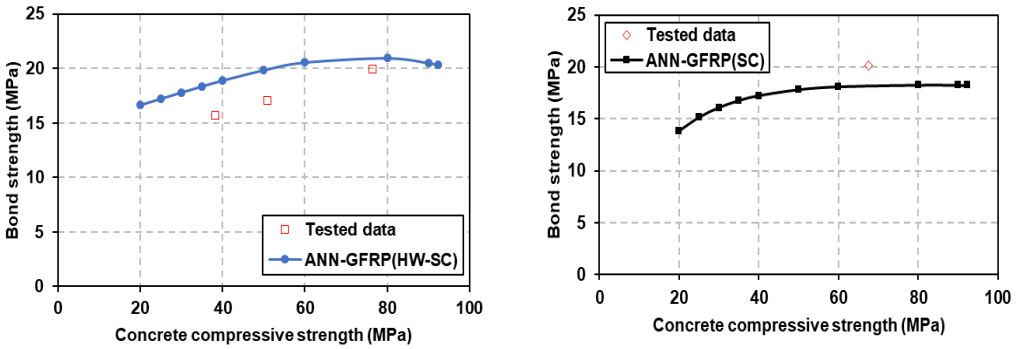

(a) (b)

Figure 8.12 - Effect of concrete compressive strength on the predicted bond strength

8.7.4 Influence of concrete cover on bond strength

Figure 8.13 shows the effect of increasing the concrete cover on the predicted bond strength for both GFRP types. The bond strength of GFRP bars increases, as the concrete cover increases, agreeing with the result obtained by Veljkovic et al. (2017) and Hossain et al. (2014). However, it can be noted that this effect disappears, when the value of concrete cover reaches 110 mm and 120 mm for GFRP (HW-SC) and GFRP (SC) bars, respectively. The concrete cover is considered as one of the main parameters affecting bond strength in all design code equations proposed to predict the bond strength. No more data having parametric values similar to those used to represent the below trends is available in the literature for comparing with the predicted NN bond strengths. The tested data obtained by Lee et al. (2012) and Sooriyaarachchi (2006), and presented in chapter 4 are plotted in Figure 8.13 (a) and (b) for GFRP (HW-SC) and GFRP (SC), respectively. The concrete compressive strength for the experimental results plotted in Figure 8.13 (b) is slightly less (67.49 MPa) than that for the predicted trend of GFRP (SC) pull-out specimens. The predicted bond strengths

of GFRP (SC) bars show a better agreement with the tested data than the predicted bond strengths of GFRP (HW-SC) bars due to the accuracy of its developed NN model.

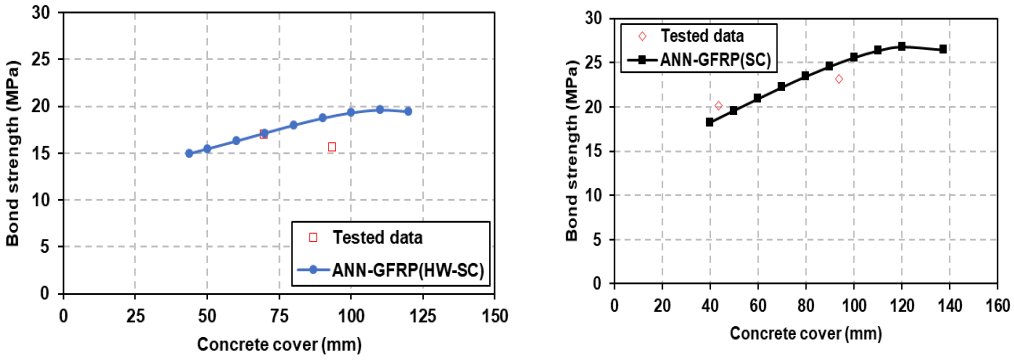

(a) **(b)**

Figure 8.13 - Effect of concrete cover on the predicted bond strength

8.8 The effect of bar surface on bond strength

The effect of surface configuration on the bond strength of GFRP bars in concrete is presented in Figure 8.14. The curves are represented based on the values of various parameters similar to those used in the current study for the comparative purposes. The values of these parameters (concrete compressive strength of 74.2 MPa, concrete cover of 92 mm and embedment length of $5d_b$, $7.5d_b$ and $10d_b$ for each figure) were kept constant with changing the value of bar diameter only (9.5 mm, 12.7 mm and 15.9 mm). From Figure 8.14, the predicted bond strength of sand-coated GFRP bars is higher than that of helical wrapped with slight sand coated GFRP bars due to their sand coating surface, which is similar to the results obtained from testing pull-out specimens in this research and obtained by Davalos et al. (2008). The predicted NN bond strengths show a good agreement with the

experimental results presented in chapter 4 as clarified in Figure 8.14 (a to c). This indicates that the proposed NN models have modelled the problem of the bond strength adequately. The Canadian codes also acknowledge the effect of surface configuration on the bond strength by suggesting a bar surface factor in their equations, but American and Japanese codes do not consider this effect in their bond strength equations.

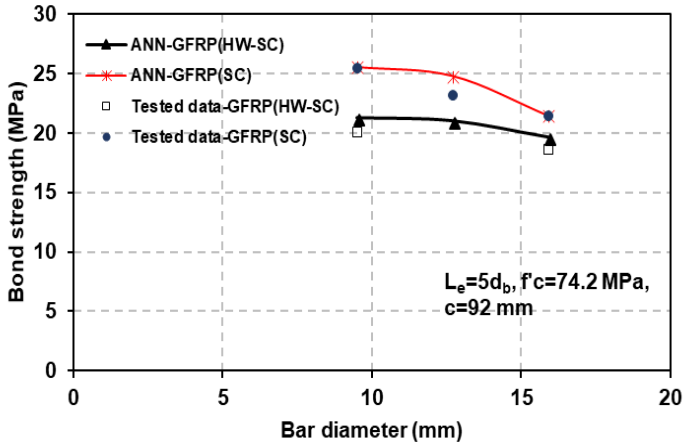

(a)

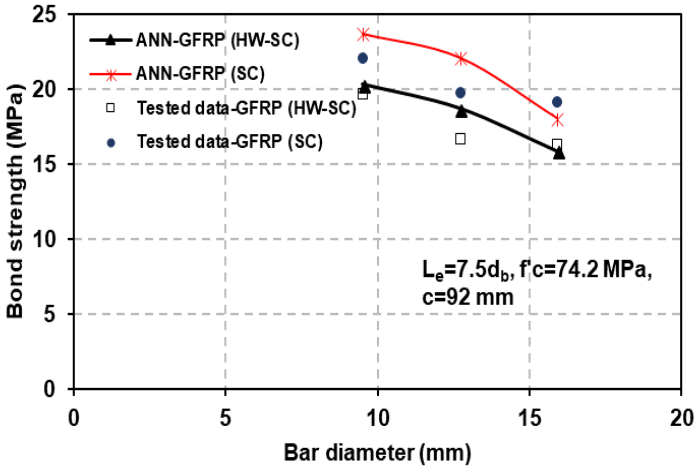

(b)

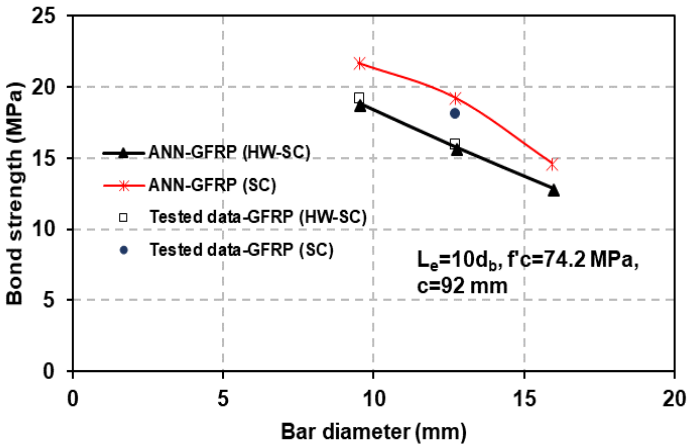

(c)

Figure 8.14 - Effect of bar surface on the predicted bond strength

8.9 Conclusions

A back-propagation neural network with Levenberg – Marquardt training algorithm was successfully trained to predict the bond strength of GFRP bars in concrete. The training of the NN was fulfilled using the experimental database collected from the literature. The following conclusions can be drawn from this study:

- The NN models were successfully developed using a limited data of 52 and 65 specimens reinforced with helical wrapped with slight sand coated and sand coated GFRP bars, respectively.
- High regression values and low mean absolute percentage of errors were obtained for both training and testing subsets, indicating that the NN model has learned well to map the relationship between the bond strength and the influencing parameters.
- The ANN is a good tool to model the bond strength, also to save time and reduce the design costs.

- The bond strength of both GFRP types is inversely proportional to the bar diameter and the embedment length.
- The bond strength of both GFRP types increases with increasing concrete compressive strength up to 60 MPa, after that the increase in concrete compressive strength has no significant effect on the bond strength.
- The bond strength of both GFRP types is directly proportional to the concrete cover, but beyond a concrete cover of 110 mm and 120 mm for GFRP (HW-SC) and GFRP (SC) bars, respectively, the effect of increasing the concrete cover on the bond strength is negligible.
- The bond strength of sand coated GFRP bars is higher than that of helical wrapped with slight sand coated GFRP bars.
- The accuracy of the developed ANN model primarily depends on the reliability of collected database and the volume of database.
- The developed NN model is only valid within the range of inputs considered in this study, in other words, it can't give accurate predictions beyond this range. As soon as more data are available, the NN needs to be retrained and the range of inputs will be extended.

Chapter 9

Conclusions and future work

9.1 Summary

The bond behaviour of GFRP bars in high strength concrete was investigated in this thesis. The research work consists of four stages. Firstly, the experimental investigation was conducted using pull-out and hinged beam specimens as presented in chapters 3, 4 and 5. Secondly, the finite element analysis was presented in chapter 6 to predict the tensile force acting on the reinforcing bar in a hinged beam and to better understand the bond behaviour. Thirdly, design code equations were evaluated against the experimental results of this research as described in chapter 7. Finally, an artificial neural network was also carried out to predict the bond strength of helically wrapped with slight sand coated and sand coated GFRP bars in concrete as presented in chapter 8.

The experimental part includes the construction and testing of 72 pull-out cubes, eight pull-out prisms and 24 hinged beams reinforced with GFRP bars. In addition, twelve pull-out cubes and four hinged beams reinforced with steel bars were also tested for comparison purposes. The main parameters investigated were bar diameter, embedment length and surface configuration. Moreover, bar position was only studied in hinged beams. The experimental observation focused on the failure modes, slips and failure loads.

A numerical simulation was carried out in this research to predict the tensile force acting on the bar in hinged beams, and also to investigate the distribution of

tensile and bond stresses along the embedment length in pull-out specimens and hinged beams. Three-dimensional nonlinear finite element models were developed using ABAQUS 6.14 package. The proposed models were validated against the experimental results of the pull-out cubes, pull-out prisms and hinged beams tested in the current research.

The final part of this research included a numerical study which was conducted using the neural network toolbox available in MATLAB version 9.1 (R2016b). The ANN models were developed to predict the bond strength of GFRP bars in concrete, and also to investigate the effect of different main parameters such as bar diameter, embedment length, concrete compressive strength and concrete cover on bond strength of GFRP bars.

Assessment of design code equations for bond strength against the current experimental results has been also conducted to evaluate the applicability of these equations in predicting the bond strength of GFRP bars in the case of high strength concrete.

The main aim of this chapter is to summarize the principal findings of the research carried out in this study and provide a number of recommendations and suggestions for future work.

9.2 Conclusions

At the end of each chapter, conclusions drawn from each phase of the work have been given in more detail. The principal findings drawn from this research work can be summarized as follows:

1. The majority of pull-out specimens and hinged beams were failed by a pull-out mode. Bond failure was governed by damage of the outer layer of helically wrapped with slight sand coated GFRP bars, while the detachment of sand grains on the sand coated GFRP surface was observed in specimens failed by a pull-out mode. The bond failure occurred by shearing off of concrete between steel ribs in the specimens reinforced with steel bars.
2. In both HSC pull-out and hinged beam specimens, the descending branch of GFRP (HW-SC) bars gradually reduced due to friction resistance, whilst GFRP (SC) bars showed a sudden drop in the descending branch with the complete loss of bond resistance because of stripping of the sand grains.
3. In general, bond strength of both GFRP types increased with reducing the bar diameter and the embedment length for both pull-out and hinged beam specimens. For high strength concrete, it was also observed that a reduction rate in bond strength decreased with increasing the bar size. In addition, a little increase in bond strength was noted with increasing the concrete cover thickness in pull-out specimens reinforced with both GFRP types.
4. In both pull-out specimens and hinged beams, the bond strength of GFRP (SC) bars is higher than that of GFRP (HW-SC) bars owing to their sand coated surface. However, the corresponding slip for GFRP (SC) bars is less than that for GFRP (HW-SC) bars.
5. Bond strengths obtained from top-cast hinged beams were slightly lower (average 7% and 15% reduction for GFRP (HW-SC) and GFRP (SC), respectively) than those obtained from bottom-cast hinged beams due to a lower concrete slump.

6. All pull-out specimens and hinged beams demonstrated almost similar bond stress – slip behaviours, which consisted of high initial stiffness and nonlinear ascending branch for both GFRP types. In addition, the softening branches with differing test methods only were also similar, except specimens failed by a pull-out mode accompanied with concrete cracks, giving a different trend.
7. The predicted tensile force in the reinforcing bar obtained from the three-dimensional nonlinear finite element model for a hinged beam was very close to the tensile force measured by pull-out cube and prism. The ratio of the predicted tensile force in a hinged beam to the experimental tensile force in a prism changed from 1.16 to 1.19 and 0.98 to 1.18 for GFRP (HW-SC) and GFRP (SC) bars, respectively. The ratio of the predicted tensile force in a hinged beam to the experimental tensile force in a cube ranged from 0.81 to 1.13 and 1.01 to 1.12 for GFRP (HW-SC) and GFRP (SC) bars, respectively. These ratios were influenced by bar diameter, embedment length and the amount of geometrical deformation. As a result, the pull-out test can be used to measure the bond characteristics of reinforcing bar in concrete rather than the hinged beam test that spends much time to prepare and test.
8. The tensile force acting on the reinforcing bar in hinged beams, which was calculated from equilibrium conditions, is overestimated because of ignoring the large deformation at failure.
9. The developed FE models for the hinged beam, pull-out cube and prism were used to investigate the distribution of tensile and bond stresses. It was found that both stresses were nonlinear along the embedment length and bond

stress at the vicinity of the free end increased with increasing the load due to redistribution of bond stresses along the embedment length.

10. Overall, all design guidelines (ACI-440.1R, 2015, CAN/CSA-S6, 2014, CAN/CSA-S806, 2012, JSCE, 1997) showed conservative bond strengths for all specimens tested, but ACI predictions were unconservative for pull-out cubes having an embedment length of 2.5 d_b. In general, ACI predictions were closer to the experimental results than other codes.
11. The developed neural network models to predict the bond strength of GFRP (HW-SC) and GFRP (SC) bars in concrete had good predictions and generalization ability with acceptable errors.
12. The parametric study conducted using the proposed ANN models for both GFRP types revealed that both concrete compressive strength and concrete cover influence bond strength up to a certain limit beyond which there is no significant change in bond strength with increasing concrete compressive strength and concrete cover.
13. In general, predictions obtained from both numerical methods (Finite element analysis and artificial neural network) have good agreements and accuracy in comparison with the experimental results. However, because of assuming the homogenous concrete, the linear behaviour of the pre-peak bond stress-slip curve, the isotropic GFRP bar and the uniform distributed load in the proposed FE models, and not enough database available in the literature trained to develop the ANN models, these assumptions inevitably ignored some imperfections existing in the tested specimens and caused difference between the numerical prediction and experimental observation.

9.3 Recommendations for future work

The following important areas are proposed for future study:

1. It is well known that a wide range of FRP bars are available in the market. Thus, the bond performance of high strength concrete with different FRP bars such as CFRP, BFRP and AFRP as well as GFRP bars with different surface deformations from those considered here should be studied to further understand the bond performance of these materials in the case of HSC, and subsequently increase the flexibility in material selection.
2. Very limited data is available in the literature regarding the bond properties of FRP bars measured by a hinged beam test. Therefore, more hinged beam investigations will be needed.
3. The investigation of bond strength of GFRP bars with a wide range of concrete compressive strengths and concrete covers has not been covered in the literature to establish full relationships between bond strength and the main parameters (concrete compressive strength and concrete cover). Therefore, further research needs to be conducted.
4. In the present study, the tensile force acting on the bar in a hinged beam was only estimated using a finite element method. Thus, it is recommended to install strain gauges at the middle of the hinged beam span as another method for calculating the tensile force acting on the bar.
5. Comparisons between bond strengths of GFRP bars obtained from pull-out specimens and those obtained from hinged beams in the case of HSC were carried out in this research considering only the influence of three parameters

(bar diameter, embedment length and bar surface). More experiments on pull-out specimens and hinged beams with different values of concrete compressive strengths and various types of FRP bars are required to find the correlation between pull-out specimens and hinged beams.

6. In the current research work, a three-dimensional finite element model was proposed and the bond interaction between the GFRP bar and the concrete was defined using the maximum bond stress value and an elastic bond stiffness for the initiation of the bond damage. However, the bond stress – slip relationship changes along the embedment length of reinforcing bar and the pre-peak bond stress-slip curve is not perfectly linear. Therefore, it is recommended to take into account these behaviours to define the bond action because they might provide better understanding the bond behaviour of GFRP reinforced concrete structures.
7. It is recommended to retrain the developed neural networks as more experimental data become available, making it applicable to more range of inputs.
8. Other artificial intelligence techniques, namely fuzzy logic, support vector regression, M5P model tree and genetic algorithm, as well as hybrid modelling strategy are recommended to predict the bond strength of GFRP bars embedded in concrete.

References

ABAQUS 2014. A finite Element Computer Program. Version 6.14. User's and Theory Manuals, ed. Vélizy-Villacoublay, Inc.

ABDALLA, J. A., HAWILEH, R. & AL-TAMIMI, A. Prediction of FRP-concrete ultimate bond strength using Artificial Neural Network. Modeling, Simulation and Applied Optimization (ICMSAO), 2011 4th International Conference on, 2011. IEEE, 1-4.

ABDELDJELIL, B. & THOMAS, T. C. H. 1994. Constitutive Laws of Concrete in Tension and Reinforcing Bars Stiffened By Concrete. Structural Journal, 91, 465-474.

ACHILLIDES, Z. 1998. Bond behaviour of FRP bars in concrete. PhD thesis, University of Sheffield.

ACHILLIDES, Z. & PILAKOUTAS, K. 2004. Bond behavior of fiber reinforced polymer bars under direct pullout conditions. Journal of Composites for Construction, 8, 173-181.

ACHILLIDES, Z. & PILAKOUTAS, K. 2006. FE modelling of bond interaction of FRP bars to concrete. Structural Concrete, 7, 7-16.

ACI-318 2005. building code requirements for structural concrete. Farmington Hills MI: : ACI Committee 318.

ACI-408R 2003. Bond and Development of Straight Reinforcing Bars in Tension. Farmington Hills, Michigan, USA: ACI Committee 408.

ACI-440.1R 2003. Guide for the Design and Construction of Structural Concrete Reinforced with FRP Bars. Farmington Hills, M1.: ACI Committee 440.

ACI-440.1R 2006. Guide for the Design and Construction of Structural Concrete Reinforced with FRP Bars. Farmington Hills, M1.: ACI Committee 440.

ACI-440.1R 2015. Guide for the design and construction of concrete reinforced with FRP bars. Farmington Hills, M1: ACI Committee 440.

ACI-440.3R 2012. Guide Test Methods for Fiber-Reinforced Polymers (FRPs) for Reinforcing or Strengthening Concrete Structures. Farmington Hills, M1.: ACI Committee 440.

ACI-440R 1996. State of the art report on fiber reinforced plastic reinforcement for concrete structures, American Concrete Institute. Detroit.

ADELI, H. 2001. Neural networks in civil engineering: 1989–2000. Computer-Aided Civil and Infrastructure Engineering, 16, 126-142.

ALY, R., BENMOKRANE, B. & EBEAD, U. 2006. Tensile lap splicing of fiber-reinforced polymer reinforcing bars in concrete. ACI structural journal, 103, 857-864.

ALY, R. S. M. 2005. Experimental and analytical studies on bond behaviour of tensile lap spliced FRP reinforcing bars in concrete. Ph.D. Thesis, University of Sherbrooke, Sherbrooke, Quebec, QC.

AMETRANO, D., HOSSAIN, K. & LACHEMI, M. 2011. Bond characteristics of glass fibre reinforced polymer bars embedded in high performance and ultra-high performance concrete.

ANTONIETTA AIELLO, M., LEONE, M. & PECCE, M. 2007. Bond performances of FRP rebars-reinforced concrete. Journal of materials in civil engineering, 19, 205-213.

ARIAS, J. P. M., VAZQUEZ, A. & ESCOBAR, M. M. 2012. Use of sand coating to improve bonding between GFRP bars and concrete. Journal of composite materials, 46, 2271-2278.

ASHOUR, A. & ALQEDRA, M. 2005. Concrete breakout strength of single anchors in tension using neural networks. Advances in Engineering Software, 36, 87-97.

ASTM-A706/A706M-09B 2009. Standard Specification for Low-Alloy Steel Deformed and Plain Bars for Concrete Reinforcement. West Conshohocken, United States: ASTM International.

ASTM-C234 2000. Standard Test Method for Comparing Concretes on the Basis of the Bond Developed with Reinforcing Steel. American Society for Testing and Materials, 1957.

ASTM-D7205/D7205M-06 2006. Standard test method for tensile properties of fibre reinforced polymer matrix composite bars. West Conshohocken, United States: ASTM International.

BAENA, M., TORRES, L., TURON, A. & BARRIS, C. 2009. Experimental study of bond behaviour between concrete and FRP bars using a pull-out test. Composites Part B: Engineering, 40, 784-797.

BASHIR, R. & ASHOUR, A. 2012. Neural network modelling for shear strength of concrete members reinforced with FRP bars. Composites Part B: Engineering, 43, 3198-3207.

BENMOKRANE, B. & MASMOUDI, R. FRP C-bar as reinforcing rod for concrete structures. PROCEEDINGS OF THE 2ND INTERNATIONAL CONFERENCE ON ADVANCED COMPOSITE MATERIALS IN BRIDGES AND STRUCTURES, ACMBS-II, MONTREAL, 1996. 11-14.

BENMOKRANE, B., TIGHIOUART, B. & CHAALLAL, O. 1996. Bond strength and load distribution of composite GFRP reinforcing bars in concrete. ACI Materials Journal, 93, 246-252.

BG50152 1992. Ministry of Construction of the P. R. China, Chinese Standard Methods for Testing of Concrete Structures China Architecture & Building Press, Beijing, 65pp.

BROWN, V. L. & BARTHOLOMEW, C. L. 1993. FRP Reinforcing Bars in Reinforced Concrete Members. ACI Materials Journal, 90, 34-39.

BS/ISO-10406-1 2013. Fibre-reinforced polymer (FRP) reinforcement of concrete - Test methods. British Standards Institution.

CAN/CSA-S6 2014. Canadian Highway Bridge Design Code. Canadian Standard Association.

CAN/CSA-S806 2012. Design and construction of building structures with fibre-reinforced polymers. Mississauga, Ontario, Canada: Canadian Standards Association.

CEB-BULLETIN-151 1982. Bond action and bond behaviour of reinforcement. State of the art report.

CEB-FIP 2010. fib model Code for concrete structures. Germany: Wilhelm Ernst & Sohn, Verlag für Architektur.

CHAALLAL, O. & BENMOKRANE, B. 1993. Pullout and bond of glass-fibre rods embedded in concrete and cement grout. Materials and structures, 26, 167-175.

CHAALLAL, O., BENMOKRANE, B. & MASMOUDI, R. 1992. An Innovative Glass Fibre Composite Rebar for Concrete Structures. Advanced composite materials in bridges and structures: 1st International conference. Mountreal: Canadian Society of Civil Engineers.

CHAN, S. H. C. 2012. Bond and cracking of reinforced concrete. Cardiff University.

COSENZA, E., MANFREDI, G. & REALFONZO, R. Analytical modelling of bond between FRP reinforcing bars and concrete. In: TAERWE L, ed. Nonmetallic (FRP) reinforcement for concrete structure 1995. London: E & FN Spon;, 164-171.

COSENZA, E., MANFREDI, G. & REALFONZO, R. 1997. Behavior and modeling of bond of FRP rebars to concrete. Journal of composites for construction, 1, 40-51.

DAHOU, Z., MEHDI SBARTAÏ, Z., CASTEL, A. & GHOMARI, F. 2009. Artificial neural network model for steel–concrete bond prediction. Engineering Structures, 31, 1724-1733.

DARWIN, D., ZUO, J., THOLEN, M. L. & IDUN, E. K. 1996. Development length criteria for conventional and high relative rib area reinforcing bars. ACI Structural Journal, 93, 347-359.

DAVALOS, J. F., CHEN, Y. & RAY, I. 2008. Effect of FRP bar degradation on interface bond with high strength concrete. Cement and Concrete Composites, 30, 722-730.

DE ALMEIDA FILHO, F. M., MOUNIR, K. & EL DEBS, A. L. H. 2008. Bond-slip behavior of self-compacting concrete and vibrated concrete using pull-out and beam tests. Materials and Structures, 41, 1073-1089.

DE LARRARD, F., SHALLER, I. & FUCHS, J. 1993. Effect of the bar diameter on the bond strength of passive reinforcement in high-performance concrete. ACI Materials Journal, 90, 333-339.

DEFREESE, J. M. & ROBERTS-WOLLMANN, C. L. 2002. Glass fiber reinforced polymer bars as top mat reinforcement for bridge decks. VIRGINIA TRANSPORTATION RESEARCH COUNCIL

EHSANI, M., SAADATMANESH, H. & TAO, S. 1993. Bond of GFRP rebars to ordinary-strength concrete. ACI Special Publication, 138, 333-345.

EHSANI, M., SAADATMANESH, H. & TAO, S. 1995. Bond of hooked glass fiber reinforced plastic (GFRP) reinforcing bars to concrete. ACI Materials Journal, 92, 391-400.

EHSANI, M. R., SAADATMANESH, H. & TAO, S. 1996a. Design Recommendation for Bond of GFRP Rebars to Concrete. Journal of Structural Engineering, 122, 247-257.

EHSANI, M. R., SAADATMANESH, H. & TAO, S. Bond Behaviour and Design Recommendations for Fiberglass Reinforcing Bars. Proceeding of the first International Conference on Composites in Infrastructure (ICCI-96), 1996b Tucson, Ariz. 466-477.

EL REFAI, A., AMMAR, M.-A. & MASMOUDI, R. 2014. Bond performance of basalt fiber-reinforced polymer bars to concrete. Journal of Composites for Construction, 19, 04014050.

ELIGEHAUSEN, R., POPOV, E. P. & BERTERO, V. V. 1983. Local bond stress-slip relationships of deformed bars under generalized excitations. Earthquake Engineering Research Center, University of California; Berkeley, USA., 69-80.

EN-1992-1-1 2004. Eurocode 2 design of concrete structures – Part 1–1: General rules and rules for buildings. CEN, Brussels.

ESFAHANI, M. R., RAKHSHANIMEHR, M. & MOUSAVI, S. R. 2013. Bond Strength of Lap-Spliced GFRP Bars in Concrete Beams. Journal of Composites for Construction, 17, 314-323.

FAZA, S. & GANGARAO, H. 1993. Glass FRP reinforcing bars for concrete. Fiber reinforced (FRP) reinforcement for concrete structures: properties and applications. In: Developments in civil engineering, 42, 167-188.

FAZA, S. S. & GANGARAO, H. V. S. 1990. Bending and Bond Behavior of Concrete Beams Reinforced with Plastic Rebars. Bridge engineering: 3rd conference. Transportation Research Board.

FERGUSON, P. M. & THOMPSON, J. N. 1962. Development Length of High Strength Reinforcing Bars in Bond. ACI Journal, 59, 887-922.

FLOOD, I. & KARTAM, N. 1994. Neural networks in civil engineering. I: Principles and understanding. Journal of Computing in Civil Engineering, 8, 131-148.

FOCACCI, F., NANNI, A. & BAKIS, C. E. 2000. Local bond-slip relationship for FRP reinforcement in concrete. Journal of composites for construction, 4, 24-31.

GAO, D., BENMOKRANE, B. & TIGHIOUART, B. 1998. Bond Properties of FRP Rebars to Concrete, Technical Report. Department of Civil Engineering, University of Sherbrooke, Sherbrooke, Quebec, Canada, pp 27.

GOLAFSHANI, E., RAHAI, A. & SEBT, M. 2015. Artificial neural network and genetic programming for predicting the bond strength of GFRP bars in concrete. Materials and structures, 48, 1581-1602.

GOLAFSHANI, E. M., RAHAI, A. & SEBT, M. H. 2014. Bond behavior of steel and GFRP bars in self-compacting concrete. Construction and Building Materials, 61, 230-240.

GOORANORIMI, O., SUARIS, W. & NANNI, A. 2017. A model for the bond-slip of a GFRP bar in concrete. Engineering Structures, 146, 34-42.

GRAVINA, R. J. & SMITH, S. T. 2008. Flexural behaviour of indeterminate concrete beams reinforced with FRP bars. Engineering Structures, 30, 2370-2380.

HAO, Q.-D., WANG, Y.-L., ZHANG, Z.-C. & OU, J.-P. 2007. Bond strength improvement of GFRP rebars with different rib geometries. Journal of Zhejiang University SCIENCE A, 8, 1356-1365.

HARAJLI, M. & ABOUNIAJ, M. 2010. Bond performance of GFRP bars in tension: Experimental evaluation and assessment of ACI 440 guidelines. Journal of Composites for Construction, 14, 659-668.

HENRIQUES, J., DA SILVA, L. S. & VALENTE, I. B. 2013. Numerical modeling of composite beam to reinforced concrete wall joints: Part I: Calibration of joint components. Engineering Structures, 52, 747-761.

HOSSAIN, K. M. A., AMETRANO, D. & LACHEMI, M. 2014. Bond Strength of Standard and High-Modulus GFRP Bars in High-Strength Concrete. Journal of Materials in Civil Engineering, 26, 449-456.

JENG, D. S., CHA, D. & BLUMENSTEIN, M. Application of Neural Network in Civil Engineering Problems. Proceedings of the International Conference on Advances in the Internet, Processing, Systems and Interdisciplinary Research (IPSI-2003), 2003.

JIRSA, J. O., BREEN, J. E., LUKE, J. J. & HAMAD, B. S. Effect of casting position on bond. International Conference on Bond in Concrete, 1982 Paisley College of Technology, Paisley, Scotland. 300-307.

JSCE-E539 1995. Test Method for Bond Strength of Continuous Fiber Reinforcing Materials by pull out Testing.

JSCE 1997. Recommendation for Design and Construction of Concrete Structures using Continuous Fiber Reinforcing Materials. Tokyo, Japan: Research Committee Fibre-Reinforcing Materials.

KANAKUBU, T., YONEMARU, K., FUKUYAMA, H., FUJISAWA, M. & SONOBE, Y. 1993. Bond performance of concrete members reinforced with FRP bars. ACI Special Publication, 138, 767-788.

KARLSSON, M. 1997. Bond Between C-BAR FRP Reinforcement and Concrete. the degree of Doctor of Philosophy, Chalmers University of Technology, Goteborg, Sweden.

KOTYNIA, R., SZCZECH, D. & KASZUBSKA, M. 2017. Bond Behavior of GRFP Bars to Concrete in Beam Test. Procedia Engineering, 193, 401-408.

LARRALDE, J. & SILVA-RODRIGUEZ, R. 1993. Bond and slip of FRP rebars in concrete. Journal of Materials in Civil Engineering, 5, 30-40.

LEE, J.-Y., KIM, T.-Y., KIM, T.-J., YI, C.-K., PARK, J.-S., YOU, Y.-C. & PARK, Y.-H. 2008. Interfacial bond strength of glass fiber reinforced polymer bars in high-strength concrete. Composites Part B: Engineering, 39, 258-270.

LEE, J.-Y., LIM, A.-R., KIM, J. & KIM, J. 2017. Bond behaviour of GFRP bars in high-strength concrete: bar diameter effect. Magazine of Concrete Research, 69, 541-554.

LEE, J. Y., YI, C. K., CHEONG, Y. G. & KIM, B. I. 2012. Bond stress–slip behaviour of two common GFRP rebar types with pullout failure. Magazine of Concrete Research, 64, 575-591.

LIN, X. & ZHANG, Y. 2014. Evaluation of bond stress-slip models for FRP reinforcing bars in concrete. Composite Structures, 107, 131-141.

LIU, H. 2003. Experimental of theory analytical study on concrete flexural members reinforced with fiber reinforced polymer bars. MS Thesis, University of Tongji.

LOSBERG, A. 1963. Force transfer and stress distribution at anchorage and curtailment of reinforcement. Goteborg, Sweden, 49.: Chalmers Univ. of Technology, .

LUNDGREN, K., KETTIL, P., HANJARI, K. Z., SCHLUNE, H. & ROMAN, A. S. S. 2012. Analytical model for the bond-slip behaviour of corroded ribbed reinforcement. Structure and Infrastructure Engineering, 8, 157-169.

M. BAENA, L., TORRES, A., TURON, M., LLORENS, C. & BARRIS 2016. Bond behaviour between recycled aggregate concrete and glass fibre reinforced polymer bars. Construction and Building Materials, 106, 449-460.

MAKITANI, E., IRISAWA, I. & NISHIURA, N. 1993. Investigation of bond in concrete member with fiber reinforced plastic bars. ACI Special Publication, 138, 315-331.

MALVAR, L. J. 1994. Bond stress-slip characteristics of FRP rebars. DTIC Document; Naval Facilities Engineering Service Center; California.

MASHREI, M. A., SERACINO, R. & RAHMAN, M. 2013. Application of artificial neural networks to predict the bond strength of FRP-to-concrete joints. Construction and Building Materials, 40, 812-821.

MAZAHERIPOUR, H., BARROS, J. A., SENA-CRUZ, J., PEPE, M. & MARTINELLI, E. 2013. Experimental study on bond performance of GFRP bars in self-compacting steel fiber reinforced concrete. Composite Structures, 95, 202-212.

MESBAH, H.-A., BENZAID, R. & BENMOKRANE, B. 2017. Evaluation of Bond Strength of FRP Reinforcing Rods in Concrete and FE Modelling. International Journal of Civil Engineering and Construction Science, 4, 21-41.

MILIČEVIĆ, I. & ŠIPOŠ, T. K. 2017. Prediction of properties of recycled aggregate concrete. Građevinar, 69, 347-357.

MONTI, G. & SPACONE, E. 2000. Reinforced concrete fiber beam element with bond-slip. Journal of Structural Engineering, 126, 654-661.

MOSLEY, C. P., TUREYEN, A. K. & FROSCH, R. J. 2008. Bond strength of nonmetallic reinforcing bars. ACI Structural Journal, 105, 634-642.

NADERPOUR, H., KHEYRODDIN, A., AMIRI, G. G. & VAEZ, S. 2011. Estimating the behavior of FRP-strengthened RC structural members using artificial neural networks. Procedia Engineering, 14, 3183-3190.

NANNI, A., AL-ZAHARANI, M., AL-DULAIJAN, S., BAKIS, C. & BOOTHBY, I. bond of FRP reinforcement to concrete-experimental results. Non-Metallic (FRP) Reinforcement for Concrete Structures: Proceedings of the Second International RILEM Symposium, 1995. CRC Press, 135-145.

OKELO, R. 2007. Realistic bond strength of FRP rebars in NSC from beam specimens. Journal of Aerospace Engineering, 20, 133-140.

OKELO, R. & YUAN, R. L. 2005. Bond strength of fiber reinforced polymer rebars in normal strength concrete. Journal of composites for construction, 9, 203-213.

OLIVEIRA, R., RAMALHO, M. & CORRÊA, M. 2008. A layered finite element for reinforced concrete beams with bond–slip effects. Cement and Concrete Composites, 30, 245-252.

ORANGUN, C., JIRSA, J. & BREEN, J. A reevaulation of test data on development length and splices. ACI Journal Proceedings, 1977. ACI, 114-122.

OVITIGALA, T. & ISSA, M. 2013. Mechanical and Bond Strength of Basalt Fiber Reinforced Polymer (BFRP) Bars for Concrete Structures. Proceedings of the 11th International Symposium on FRP for Reinforced Concrete Structures. Guimaraes, Portugal.

PANNIRSELVAM, N., NAGARADJANE, V., CHANDRAMOULI, K. & RAVINDRAKRISHNA, M. 2010. ARTIFICIAL NEURAL NETWORK MODEL FOR PERFORMANCE EVALUATION OF RC RECTANGULAR BEAMS WITH

EXTERNALLY BONDED GLASS FIBRE REINFORCED POLYMER REINFORCEMENT. 5, 77-85.

PAY, A. C., CANBAY, E. & FROSCH, R. J. 2014. Bond strength of spliced fiber-reinforced polymer reinforcement. ACI Structural Journal, 111, 257-266.

PECCE, M., MANFREDI, G., REALFONZO, R. & COSENZA, E. 2001. Experimental and analytical evaluation of bond properties of GFRP bars. Journal of Materials in Civil Engineering, 13, 282-290.

PEPE, M., MAZAHERIPOUR, H., BARROS, J., SENA-CRUZ, J. & MARTINELLI, E. 2013. Numerical calibration of bond law for GFRP bars embedded in steel fibre-reinforced self-compacting concrete. Composites Part B: Engineering, 50, 403-412.

PLEIMANN, L. G. 1987. Tension and bond pull-out tests of deformed fiberglass rods. Marshall Vega Technologies Inc., Marshall, AK, 5-11.

PLEIMANN, L. G. Strength, modulus of elasticity, and bond of deformed FRP rods. Advanced Composites Materials in Civil Engineering Structures, 1991. ASCE, 99-110.

QUAYYUM, S. 2010. Bond behaviour of fibre reinforced polymer (FRP) rebars in concrete. MSC, University of British Columbia.

RAFI, M. M., NADJAI, A. & ALI, F. 2007. Experimental testing of concrete beams reinforced with carbon FRP bars. Journal of composite materials, 41, 2657-2673.

RILEM/CEB/FIP, R. 1982. RILEM technical recommendations for the testing and use of construction materials London : Spon, c1994.

RILEM/CEB/FIP, R. 1983. RILEM technical recommendations for the testing and use of construction materials. London : Spon, c1994.

ROBERT, M. & BENMOKRANE, B. 2010. Effect of aging on bond of GFRP bars embedded in concrete. Cement and Concrete Composites, 32, 461-467.

ROSSETTI, V. A., GALEOTA, D. & GIAMMATTEO, M. 1995. Local bond stress-slip relationships of glass fibre reinforced plastic bars embedded in concrete. Materials and Structures, 28, 340-344.

SAKLA, S. S. & ASHOUR, A. F. 2005. Prediction of tensile capacity of single adhesive anchors using neural networks. Computers & structures, 83, 1792-1803.

SALARI, M. R. & SPACONE, E. 2001. Finite element formulations of one-dimensional elements with bond-slip. Engineering structures, 23, 815-826.

SOORIYAARACHCHI, H. 2006. Tension stiffening effect in GFRP reinforced concrete elements. the degree of Doctor of Philosophy in the faculty of engineering, Sheffield University.

SORETZ, S. 1972. A comparison of beam tests and pull-out tests. Materials and Structures, 5, 261-264.

TASTANI, S. & PANTAZOPOULOU, S. 2006. Bond of GFRP bars in concrete: experimental study and analytical interpretation. Journal of Composites for Construction, 10, 381-391.

TEKLE, B. H., KHENNANE, A. & KAYALI, O. 2016. Bond Properties of Sand-Coated GFRP Bars with Fly Ash–Based Geopolymer Concrete. Journal of Composites for Construction, 20, 1-13.

TEKLE, B. H., KHENNANE, A. & KAYALI, O. 2017a. Bond behaviour of GFRP reinforcement in alkali activated cement concrete. Construction and Building Materials, 154, 972-982.

TEKLE, B. H., KHENNANE, A. & KAYALI, O. 2017b. Bond of spliced GFRP reinforcement bars in alkali activated cement concrete. Engineering Structures, 147, 740-751.

TEPFERS, R. 2006. Bond clause proposals for FRP bars/rods in concrete based on CEB/FIP Model Code 90. Part 1: Design bond stress for FRP reinforcing bars. Structural concrete, 7, 47-55.

TIGHIOUART, B., BENMOKRANE, B. & GAO, D. 1998. Investigation of bond in concrete member with fibre reinforced polymer (FRP) bars. Construction and Building Materials, 12, 453-462.

TIGHIOUART, B., BENMOKRANE, B. & MUKHOPADHYAYA, P. 1999. Bond strength of glass FRP rebar splices in beams under static loading. Construction and Building Materials, 13, 383-392.

VELJKOVIC, A., CARVELLI, V., HAFFKE, M. M. & PAHN, M. 2017. Concrete cover effect on the bond of GFRP bar and concrete under static loading. Composites Part B: Engineering, 124, 40-53.

VINT, L. & SHEIKH, S. 2015. Investigation of Bond Properties of Alternate Anchorage Schemes for Glass Fiber-Reinforced Polymer Bars. ACI Structural Journal, 112, 59.

WAMBEKE, B. W. & SHIELD, C. K. 2006. Development length of glass fiber-reinforced polymer bars in concrete. ACI Structural Journal, 103, 11-17.

WEICHEN 1997.

XUE, W., WANG, X. & ZHANG, S. 2008. Bond properties of high-strength carbon fiber-reinforced polymer strands. ACI Materials Journal, 105, 11-19.

XUE, W., ZHENG, Q., YANG, Y. & FANG, Z. 2014. Bond behavior of sand-coated deformed glass fiber reinforced polymer rebars. Journal of Reinforced Plastics and Composites, 33, 895-910.

YAN, F., LIN, Z. & YANG, M. 2016. Bond mechanism and bond strength of GFRP bars to concrete: a review. Composites Part B: Engineering, 98, 56-69.

Appendix A

Table A.1 - Experimental database of 52 pull-out specimens reinforced with GFRP (HW-SC) bars and bond strength predictions using ANNs.

Reference	d_b (mm)	L_e (mm)	f'_c (MPa)	c (mm)	$\tau_{max,exp}$ (MPa)	$\tau_{max,pred}$ (MPa)	$\frac{\tau_{max,exp}}{\tau_{max,pred}}$	Failure Mode
Baena et al. (2009)	12.7	63.5	29.15	93.65	9.838	16.30	0.60	PO
	9.5	47.5	52.28	95.25	21.808	20.41	1.07	PO
	12.7	63.5	50.91	93.65	16.983	18.68	0.91	PO
	15.9	79.5	49.55	92.05	17.362	17.31	1.00	PO
Okelo and Yuan (2005)	6	30	44.3	98.5	14.9	22.08	0.67	PO
	16	80	29.7	93.5	18.9	14.43	1.31	PO
	16	80	39	93.5	20.7	16.10	1.29	PO
	19	171	48.3	92	11.8	13.65	0.86	PO
	19	95	45.6	92	16.05	15.86	1.01	PO
	19	133	44.1	92	13.2	14.44	0.91	PO
	19	95	35	92	14.4	14.30	1.01	PO
	19	133	33.5	92	11.55	12.33	0.94	PO
	19	171	33.5	92	9.26	10.42	0.89	PO
Lee et al. (2008)	12.7	50.8	25.6	68.65	18.89	16.59	1.14	PO
	12.7	50.8	35.3	68.65	19.72	19.20	1.03	PO
	12.7	50.8	40.6	68.65	21.49	20.23	1.06	PO
	12.7	50.8	75.7	68.65	23.68	23.36	1.01	PO
	12.7	50.8	92.4	68.65	26.1	24.09	1.08	PO
Davalos et al. (2008)	9.5	47.5	63.4	70.25	19.61	20.87	0.94	PO
	12.7	63.5	62.7	68.65	21.38	20.16	1.06	PO
Sooriyaarachchi (2006)	13	65	38.25	93.5	15.67	17.61	0.89	PO
	13	130	38.25	93.5	13.5	13.15	1.03	PO
	13	65	76.5	93.5	19.89	18.76	1.06	PO
	19	190	38.25	90.5	11.74	10.37	1.13	PO
	19	95	76.5	90.5	16.62	16.99	0.98	PO
M. Baena et al. (2016)	15.9	79.5	23.34	92.05	11.57	13.07	0.88	PO
	15.9	79.5	28.99	92.05	13.87	14.49	0.96	PO
	15.9	79.5	46.14	92.05	16.22	17.08	0.95	PO
Lee et al. (2012)	12.7	63.5	24.1	69.85	12.38	13.77	0.90	PO
	12.7	63.5	39.3	69.85	16.96	17.78	0.95	PO
Lee et al. (2017)	19.1	95.5	20	100.45	11.38	10.03	1.13	PO
	19.1	95.5	40	100.45	14.93	14.58	1.02	PO
	19.1	95.5	60	100.45	17.7	16.03	1.10	PO
	25.4	127	20	137.3	8.41	8.65	0.97	PO
	25.4	127	40	137.3	12.22	13.44	0.91	PO
	25.4	127	60	137.3	14.05	15.16	0.93	PO

Reference	d_b (mm)	L_e (mm)	f'_c (MPa)	c (mm)	$\tau_{max,exp}$ (MPa)	$\tau_{max,pred}$ (MPa)	$\frac{\tau_{max,exp}}{\tau_{max,pred}}$	Failure Mode
Mesbah et al. (2017)	6.35	31.75	40	96.825	30.59	22.01	1.39	PO
	9.5	47.5	40	95.25	24.65	19.82	1.24	PO
Author	9.5	23.75	82.77	95.25	20.55	21.64	0.95	PO
	9.5	47.5	82.77	95.25	20.08	20.36	0.99	PO
	9.5	71.25	82.77	95.25	19.76	19.07	1.04	PO
	9.5	95	82.77	95.25	19.27	17.72	1.09	PO
	12.7	31.75	83.06	93.65	19.79	20.08	0.99	PO
	12.7	95.25	83.06	93.65	16.71	17.61	0.95	PO
	12.7	127	83.06	93.65	16.05	16.28	0.99	PO
	15.9	39.75	86.43	92.05	19.42	18.81	1.03	PO
	15.9	79.5	86.43	92.05	18.7	17.72	1.06	PO
	15.9	119.25	87.01	92.05	16.32	16.68	0.98	PO
	15.9	159	87.01	92.05	14.82	15.51	0.96	PO
	9.5	47.5	67.97	45.25	19.51	17.05	1.14	PO
	9.5	95	67.97	45.25	16.47	15.12	1.09	PO
	12.7	63.5	67.97	43.65	15.38	16.20	0.95	PO
						Mean	1.01	
						SD	0.13	
						COV%	13.20	

Table A.2 - Experimental database of 65 pull-out specimens reinforced with GFRP (SC) bars and bond strength predictions using ANNs.

Reference	d_b (mm)	L_e (mm)	f'_c (MPa)	c (mm)	$\tau_{max,exp}$ (MPa)	$\tau_{max,pred}$ (MPa)	$\frac{\tau_{max,exp}}{\tau_{max,pred}}$	Failure Mode
Baena et al. (2009)	12.7	63.5	26.7	93.65	11.2	10.15	1.10	PO
	15.9	79.5	27.5	92.05	12.099	13.18	0.92	PO
Lee et al. (2008)	12.7	50.8	25.6	68.65	19.75	17.86	1.11	PO
	12.7	50.8	35.3	68.65	21.5	21.53	1.00	PO
	12.7	50.8	40.6	68.65	21.17	22.61	0.94	PO
	12.7	50.8	56.3	68.65	21.39	23.95	0.89	PO
	12.7	50.8	75.7	68.65	24.41	24.28	1.01	PO
	12.7	50.8	92.4	68.65	25	24.30	1.03	PO
El Refai et al. (2014)	10	50	50	70	20.51	19.88	1.03	PO
	10	100	50	70	17.7	16.31	1.09	PO
Davalos et al. (2008)	9.5	47.5	58.7	70.25	23.42	21.30	1.10	PO
Tekle et al. (2016)	12.7	76.2	43.4	43.65	16.3	14.96	1.09	PO
	15.9	47.7	42	42.05	17.3	17.31	1.00	PO
Hossain et al. (2014)	15.9	47.7	74.2	40	19.7	18.14	1.09	PO
	15.9	111.3	74.2	40	13.1	10.57	1.24	PO

Reference	d_b (mm)	L_e (mm)	f'_c (MPa)	c (mm)	$\tau_{max,exp}$ (MPa)	$\tau_{max,pred}$ (MPa)	$\frac{\tau_{max,exp}}{\tau_{max,pred}}$	Failure Mode
Hossain et al. (2014)	15.9	47.7	74.2	60	20.6	22.32	0.92	PO
	15.9	111.3	74.2	60	14	13.49	1.04	PO
	19.1	57.3	74.2	40	17.1	14.33	1.19	PO
	19.1	133.7	74.2	40	6.7	7.17	0.93	PO
	15.9	47.7	74.2	40	17.2	18.14	0.95	PO
	15.9	111.3	74.2	40	12.2	10.57	1.15	PO
	15.9	159	74.2	40	8.3	9.24	0.90	PO
	15.9	47.7	74.2	60	20.2	22.32	0.91	PO
	15.9	111.3	74.2	60	10.7	13.49	0.79	PO
	15.9	159	74.2	60	10.1	11.82	0.85	PO
	19.1	57.3	74.2	40	12.8	14.33	0.89	PO
	19.1	133.7	74.2	40	7.1	7.17	0.99	PO
	19.1	191	74.2	40	7.6	6.57	1.16	PO
	19.1	57.3	74.2	60	15.9	17.35	0.92	PO
	19.1	133.7	74.2	60	8.2	8.67	0.95	PO
	19.1	191	74.2	60	8.1	7.59	1.07	PO
Antonietta Aiello et al. (2007)	8	52.35	44.8	96	3.79	6.78	0.56	PO
	8	52.5	44.8	121	4.23	3.98	1.06	PO
	8	55.1	44.8	96	3.66	5.58	0.66	PO
	8	55.1	44.8	121	4.26	3.15	1.35	PO
Arias et al. (2012)	9	45	23	45.5	10.08	9.05	1.11	PO
	9	45	56	45.5	13.52	19.85	0.68	PO
	16	80	23	42	8.85	8.66	1.02	PO
	16	80	56	42	10.25	10.82	0.95	PO
	16	160	23	42	4.74	5.39	0.88	PO
Lee et al. (2012)	12.7	63.5	24.2	69.85	9.08	10.73	0.85	PO
	12.7	63.5	42	69.85	13.65	17.66	0.77	PO
	12.7	63.5	70.7	69.85	16.56	19.82	0.84	PO
Lee et al. (2017)	19.1	95.5	20	100.45	9.35	8.89	1.05	PO
	19.1	95.5	40	100.45	15.93	13.89	1.15	PO
	19.1	95.5	60	100.45	13.35	15.35	0.87	PO
	25.4	127	20	137.3	8.59	9.64	0.89	PO
	25.4	127	40	137.3	11.32	12.11	0.93	PO
	25.4	127	60	137.3	14.56	12.76	1.14	PO
Author	9.5	23.75	70.61	95.25	28.91	27.43	1.05	PO
	9.5	47.5	66.03	95.25	25.51	25.52	1.00	PO
	9.5	71.25	66.03	95.25	22.15	19.06	1.16	PO
	9.5	95	66.03	95.25	19.05	18.12	1.05	PO
	12.7	31.75	67.76	93.65	28.26	27.44	1.03	PO

Reference	d_b (mm)	L_e (mm)	f'_c (MPa)	c (mm)	$\tau_{max,exp}$ (MPa)	$\tau_{max,pred}$ (MPa)	$\frac{\tau_{max,exp}}{\tau_{max,pred}}$	Failure Mode
Author	12.7	63.5	67.76	93.65	23.21	23.79	0.98	PO
	12.7	95.25	65.85	93.65	19.83	19.74	1.00	PO
	12.7	127	65.85	93.65	18.18	18.99	0.96	PO
	15.9	39.75	65.85	92.05	27.77	25.88	1.07	PO
	15.9	79.5	65.85	92.05	21.52	19.32	1.11	PO
	15.9	119.25	65.85	92.05	19.23	17.21	1.12	PO
	15.9	159	65.85	92.05	18.93	15.88	1.19	PO
	9.5	47.5	67.49	45.25	22.79	20.11	1.13	PO
	9.5	95	67.49	45.25	20.49	19.27	1.06	PO
	12.7	63.5	67.49	43.65	20.16	16.93	1.19	PO
	12.7	127	67.49	43.65	16.8	14.84	1.13	PO
						Mean	1	
						SD	0.14	
						COV%	14.06	

Note: d_b = Bar diameter (mm); L_e = Embedment length (mm); f'_c = Cylinder compressive strength of concrete (MPa); c = concrete cover (mm); $\tau_{max,exp}$ = Experimental maximum bond stress (MPa); $\tau_{max,pred}$ = Predicted maximum bond stress (MPa); HW-SC= Helical wrapping with slightly sand coating; SC= Sand coating and PO = Pull-out failure.